



Australian
National
University



Combining Fourier Plane Observables for High-contrast Imaging of Young Giant Exoplanets

A thesis submitted for the degree of Doctor of Philosophy of The
Australian National University

Jens Kammerer

`jens.kammerer@anu.edu.au`

Research School of Astronomy and Astrophysics
Australian National University

Directorate for Science
European Southern Observatory

Supervisors:

Michael J. Ireland,
Frantz Martinache,
Antoine Mérand

May 29, 2021

© Copyright by Jens Kammerer 2020
All Rights Reserved

Statement of Contribution

This thesis is submitted as a Thesis by Compilation in accordance with https://policies.anu.edu.au/ppl/document/ANUP_003405

I declare that the research presented in this Thesis represents original work that I carried out during my candidature at the Australian National University, except for contributions to multi-author papers incorporated in the Thesis where my contributions are specified in this Statement of Contribution.

Title: Kernel phase imaging with VLT/NACO: high-contrast detection of new candidate low-mass stellar companions at the diffraction limit

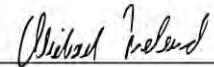
Authors: Jens Kammerer, Michael J. Ireland, Frantz Martinache and Julien H. Girard

Publication outlet: Monthly Notices of the Royal Astronomical Society, volume 486, pages 639--654

Current status of paper: Published

Contribution to paper: This paper was written by Jens Kammerer under the supervision of Michael J. Ireland and Frantz Martinache. Julien H. Girard is the PI of the archival VLT/NACO data set used in this paper.

Senior author or collaborating authors endorsement: **A./Prof. Michael Ireland**



Title: High-resolution survey for planetary companions to young stars in the Taurus molecular cloud

Authors: Alexander L. Wallace, Jens Kammerer, Michael J. Ireland, Christoph Federrath, Adam L. Kraus, Sarah T. Maddison, Aaron Rizzuto, Eloise K. Birchall and Frantz Martinache

Publication outlet: Monthly Notices of the Royal Astronomical Society, volume 498, pages 1382--1396

Current status of paper: Published

Contribution to paper: This paper was mostly written by Alexander L. Wallace in collaboration with his supervisors. Jens Kammerer conducted the close separation kernel phase analysis and wrote Section 3.4 of this paper.

Senior author or collaborating authors endorsement: **A./Prof. Michael Ireland**



Title: Mid-infrared photometry of the T Tauri triple system with kernel phase interferometry

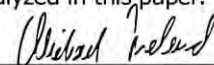
Authors: Jens Kammerer, Markus Kasper, Michael J. Ireland, Rainer Köhler, Romain Laugier, Frantz Martinache, Ralf Siebenmorgen, Mario E. van den Ancker, Roy van Boekel, Tom M. Herbst, Eric Pantin, Hans-Ulrich Käufel, Dominique J. M. Petit dit de la Roche and Valentin D. Ivanov

Publication outlet: Accepted for publication as a peer-reviewed article in Astronomy & Astrophysics

Current status of paper: Accepted

Contribution to paper: This paper was written by Jens Kammerer under the supervision of Markus Kasper, Michael J. Ireland, and Frantz Martinache. Romain Laugier helped with the development of the pupil model and the remaining co-authors contributed to the observing proposal and the VISIR-NEAR instrument which enabled the observations analyzed in this paper.

Senior author or collaborating authors endorsement: **A./Prof. Michael Ireland**



Title: Increasing the achievable contrast of infrared interferometry with an error correlation model

Authors: Jens Kammerer, Antoine Mérand, Michael J. Ireland and Sylvestre Lacour

Publication outlet: Astronomy & Astrophysics, volume 644, A110

Current status of paper: Published

Contribution to paper: This paper was written by Jens Kammerer under the supervision of Antoine Mérand, Michael J. Ireland, and Sylvestre Lacour.

Senior author or collaborating authors endorsement: Dr. Sylvestre Lacour



Title: GRAVITY K-band spectroscopy of HD 206893 B: brown dwarf or exoplanet?

Authors: Jens Kammerer, Sylvestre Lacour, Tomas Stolker, Kimberly Ward-Duong, Jason J. Wang, Mathias Nowak

Publication outlet: To be submitted as a peer-reviewed article to Astronomy & Astrophysics

Current status of paper: Not yet submitted

Contribution to paper: This paper was written by Jens Kammerer under the supervision of Sylvestre Lacour. Tomas Stolker helped with the atmospheric model fitting, Kimberly Ward-Duong provided assistance with the GPI spectra, Jason J. Wang helped with the orbit fitting, and Mathias Nowak provided assistance with the GRAVITY data reduction.

Senior author or collaborating authors endorsement: Dr. Sylvestre Lacour



Jens Kammerer

Candidate – Print Name



Signature

18 Dec 2020

Date

Endorsed

A./Prof. Michael Ireland

Primary Supervisor – Print Name



Signature

19 Dec 2020

Date

Delegated Authority – Print Name

Signature

Date

Acknowledgements

I would like to thank my supervisory panel consisting of Mike Ireland, Frantz Martinache, and Antoine Mérand for their continuous support and valuable advice over the last 3.5 years. I would also like to thank Maruša Žerjal for taking on this role in the beginning of my PhD. Furthermore, I would like to thank Markus Kasper and Sylvestre Lacour, who supported and assisted me during my time at ESO, as well as Sascha Quanz and Denis Defrère, who worked with me in the context of the LIFE project. All of you have played an important role for my PhD and without you this thesis would not have been possible. I would like to especially acknowledge your positive motivation in difficult times. I am deeply grateful that I got the chance to work with you, to learn from you, and to get to know you as colleagues and friends.

I would also like to thank my amazing colleagues and friends both in Canberra and Munich. You were extremely welcoming and lovely, and you made it very easy for me to find connection in entirely new places. Although the last year has been difficult due to the pandemic, I hope that we will stay in touch and will be able to see each other again in person in the future.

I would like to thank my parents, my sister, my grandparents, my partner, and my friends for helping me to maintain a positive work-life balance over the last 3.5 years. Even though some times were stressful, you always managed to distract my brain from work and helped me to enjoy life.

I would also like to thank the student administrators at ANU and ESO, Astrid Bardelang and Nelma Alas Silva, who helped me through the jungle of bureaucracy and policies, which was not always straightforward.

Finally, I would like to acknowledge the generous financial support from the ANU PhD Scholarship, the HDR Fee Remission Merit Scholarship, the Olin Eggen Research Award, and the ESO Studentship. I would also like to thank RSAA for funding in-person participation at the Exoplanets II conference in Cambridge and the Extreme Solar Systems IV conference in Reykjavik as well as ESO for funding in-person participation at the Spirit of Lyot conference in Tokyo and my training at the APEX and VLT(I) telescopes in San Pedro de Atacama and Paranal.

Abstract

The vast majority of the ~ 4000 exoplanets known of today have only been detected through indirect techniques, providing a limited amount of information on their physical properties and dynamical environment. On the other hand, direct techniques can provide astrometric, photometric, and spectroscopic information required to study the formation and evolution of exoplanets. However, such direct observations are challenging due to the high contrast between an exoplanet and its parent star, as well as their small apparent separation. Interferometric techniques at infrared wavelengths are able to overcome the limitation in terms of angular resolution, but are still limited in contrast at small angular separations. A further increase in contrast is necessary to make the bulk of young giant exoplanets, orbiting their parent star at Solar System scales, accessible to interferometry in general.

Here, we focus on improving our understanding of and mitigating the systematic errors which limit the sensitivity of interferometric observations. With the kernel phase technique, we survey nearby and young stars for sub-stellar companions. We develop a data reduction pipeline capable of reconstructing saturated PSFs, centering them with sub-pixel accuracy and extracting their Fourier plane observables including correlations. These correlations are then used, together with a calibration strategy based on principal component analysis, to improve the sensitivity to faint companions. In archival VLT/NACO data, we detect eight low-mass stellar companions, five of which were previously unknown, and two have angular separations of $\sim 0.8\text{--}1.2 \lambda/D$ (i.e., $\sim 80\text{--}110$ mas). Furthermore, we achieve typical $5\text{-}\sigma$ contrast limits of ~ 6 mag at separations of 0.2 arcsec and ~ 8 mag at separations of 0.5 arcsec for a Keck/NIRC2 survey of 55 single class I and class II stars in Taurus. These results clearly demonstrate that the kernel phase technique is now capable of detecting young giant exoplanets in the nearest star-forming regions.

We further utilize this technique to obtain mid-infrared photometry of the famous T Tauri triple system, including its southern binary T Tau Sa/Sb at an apparent separation of only $\sim 0.2 \lambda/D$. Our observations reveal a recent decrease in the mid-infrared brightness of T Tau Sb of ~ 2 mag. We suspect that it has moved along its orbit behind the southern circumbinary disk and now suffers from increased dust extinction. With the demonstration of the improved contrast and the unprecedented angular resolution in the mid-infrared, the kernel phase technique is a promising method for exoplanet imaging with the *James Webb Space Telescope* and the Extremely Large Telescopes.

We finally extend our study to long-baseline interferometry by extracting the correlations present in VLTI/GRAVITY data. The GRAVITY instrument has recently been used to spectroscopically characterize exoplanets in the near-infrared. We develop an analytical model to describe the correlations and show that the faint source detection limits of GRAVITY improve by a factor of ~ 2 when accounting for them in the model fitting process. Exoplanet science with GRAVITY is still in its infancy and our technical improvements will help to increase its scientific return. Moreover, future instruments such as GRAVITY+, SCIFY, or LIFE will greatly benefit from a complete treatment of the systematic errors.

Contents

Acknowledgements	iii
Abstract	iv
1 Introduction	1
1.1 A brief history of exoplanets	2
1.1.1 Preamble	2
1.1.2 Exoplanet demographics	3
1.1.3 Transit and radial velocity techniques	5
1.1.4 Microlensing techniques	6
1.1.5 Direct imaging techniques	7
1.1.6 Giant planet formation	10
1.1.7 Post-formation entropy and evolutionary tracks	15
1.2 Fourier plane techniques	19
1.2.1 Long-baseline interferometry	21
1.2.2 Aperture masking interferometry	23
1.2.3 Kernel phase interferometry	25
2 Kernel phase imaging with VLT/NACO: high-contrast detection of new candidate low-mass stellar companions at the diffraction limit	28
2.1 Introduction	30
2.2 Methods	32
2.2.1 Data reduction	32
2.2.2 Kernel phase extraction	39
2.2.3 Kernel phase calibration	44
2.2.4 Model fitting	45
2.3 Results and discussion	49
2.3.1 Target list	49
2.3.2 Detected companion candidates	50

2.3.3	Detection limits	58
2.3.4	Windowing correction	59
2.4	Conclusions	59
3	High-resolution survey for planetary companions to young stars in the Taurus molecular cloud	64
3.1	Introduction	66
3.2	Survey sample	68
3.3	Observations and image analysis	69
3.3.1	Observations	69
3.3.2	Data reduction	71
3.3.3	Image analysis using PSF subtraction	73
3.3.4	Kernel phase data reduction	75
3.3.5	Comparison of both methods	80
3.3.6	Significant features from kernel phase analysis	80
3.4	Wide separation analysis	82
3.5	The frequency of wide separation massive planets	88
3.5.1	Total probability of planet detection	88
3.5.2	Comparison with HR 8799 analogues	88
3.5.3	Planet frequency	90
3.6	Summary and conclusions	93
4	Mid-infrared photometry of the T Tauri triple system with kernel phase interferometry	95
4.1	Introduction	97
4.2	Observations	98
4.3	Data reduction	99
4.3.1	Kernel phase technique	99
4.3.2	Basic cleaning	100
4.3.3	Kernel phase extraction and calibration	101
4.3.4	Model fitting	103
4.4	Results and analysis	105
4.4.1	Binary model fits	105

CONTENTS	vii
4.4.2 Triple model fits	107
4.4.3 NEII data	110
4.4.4 Mock data	111
4.4.5 Photometry	112
4.5 Discussion	112
4.6 Conclusions	115
5 Increasing the achievable contrast of infrared interferometry with an error correlation model	118
5.1 Introduction	120
5.2 Methods	121
5.2.1 Correlations extracted from GRAVITY data	121
5.2.2 Empirical model for the correlations	126
5.2.3 Simulated and real data	129
5.2.4 Model fitting	134
5.3 Results	136
5.3.1 Model fitting to correlated noise	136
5.3.2 Injection and recovery tests (simulated data)	138
5.3.3 Injection and recovery tests (real data)	142
5.4 Conclusions	143
6 GRAVITY K-band spectroscopy of HD 206893 B: brown dwarf or exoplanet?	150
6.1 Introduction	153
6.2 Observations and data reduction	154
6.3 Orbit fitting	157
6.4 Spectral analysis	159
6.4.1 Atmospheric model fitting	160
6.4.2 Evolutionary tracks	166
6.4.3 Color-magnitude diagram	167
6.5 Discussion	169
6.6 Conclusions	171
7 Conclusions	176

Introduction

The first part of the Introduction (Section 1.1) focuses on the advancements in the field of exoplanets over the last quarter of a century, starting with radial velocity observations of the first exoplanets, continuing with exoplanet demographics inferred from transit observations, and finally motivating direct detection techniques for studying exoplanet formation and evolution. The second part of the Introduction (Section 1.2) gives a brief historical summary of long-baseline, aperture masking, and kernel phase interferometry and introduces the mathematical framework of Fourier plane imaging in the context of these three techniques. While these techniques are capable of detecting only the largest exoplanets today, they remain especially relevant for studying exoplanet formation and evolution as instrumentation improves over the next decades.

1.1 A brief history of exoplanets

1.1.1 Preamble

When Galileo Galilei pointed his **novel** telescope at the night sky for the first time in 1609 (e.g., Drake, 1990), only five planets (apart from the Earth) were known to humankind: Mercury, Venus, Mars, Jupiter, and Saturn. These five planets are all visible from the Earth with the naked **human** eye, which made them observable even before the invention of the telescope. They stand out from the background stars because of their **apparent brightness** and fast motion on the sky and played an important role in ancient mythology and astronomy.

Using his **novel telescope**, in 1610, Galilei discovered the four largest moons of Jupiter (e.g., Drake, 1978), depicting the first proof that celestial objects orbit a body different than the Earth **and causing significant tension with the medieval geocentrism**. Only two years later, he also observed **the ice giant** Neptune, noticing its high proper motion, although not realizing that it was another **Solar System** planet (e.g., Drake & Kowal, 1980). Nevertheless, Galilei's telescope heralded a new era for **observational** astronomy, with many more Solar System objects such as Vesta, Juno, Ceres, Pallas, Uranus, and Pluto being discovered **in the 19th and 20th centuries**. **Many of these newly discovered celestial objects were initially claimed to be planets, but with detection limits pushing toward smaller bodies astronomers began to wonder about the definition of a planet and a set of minimal requirements that an object had to fulfill in order to be called a planet**. This **debate** carried on for about three centuries, until Pluto was reclassified as a minor (**dwarf**) planet by the International Astronomical Union in 2006, since it has not sufficiently cleared its orbit from other small bodies¹.

By that time, the first extrasolar planets (or exoplanets) had already been known for more than **a decade** (Wolszczan & Frail, 1992; Mayor & Queloz, 1995). In 1995, Michel Mayor and Didier Queloz concluded the existence of a giant planet on a short orbit of only ~ 4 days around the main-sequence star 51 Pegasi from its periodically occurring blue- and redshifts (Mayor & Queloz, 1995), a discovery for which they were awarded the Nobel Prize in physics in 2019². Within only 15 years, the number of known exoplanets has now grown **to ~ 4400** ³, thanks to huge efforts with radial velocity and transit surveys, first and foremost NASA's *Kepler* mission. Flared up again is the debate about which objects shall be classified **as planets**, especially at the boundary between **gas giants** and brown dwarfs **subject to thermonuclear deuterium fusion**, as well as in environments that substantially differ from that of our own Earth, such as the planets orbiting a **millisecond pulsar discovered by Wolszczan & Frail (1992)**.

¹<https://www.iau.org/news/pressreleases/detail/iau0603/>

²<https://www.nobelprize.org/prizes/physics/2019/summary/>

³<https://exoplanetarchive.ipac.caltech.edu/>, retrieved on 25 May 2021

1.1.2 Exoplanet demographics

The first confirmed detection of an exoplanet was the discovery of a multi-planet system of two super-Earths orbiting the millisecond pulsar PSR1257+12 (Wolszczan & Frail, 1992). Such pulsars are extremely stable rotators and therefore emit pulses on timescales of milliseconds with extremely stable delay times. In the pulse arrival times of PSR1257+12, Wolszczan & Frail (1992) could detect a residual variation caused by two planetary-mass companions of $M_p \sin(i) = 3.4 M_\oplus$ and $2.8 M_\oplus$, where i is the system inclination. Only in 1995, Mayor & Queloz (1995) detected the first planetary-mass companion around a main-sequence star, 51 Pegasi b. Unlike the super-Earths orbiting the millisecond pulsar PSR1257+12, 51 Pegasi b was found to be a hot Jupiter orbiting its host star with an extremely short period of only 4.23 d. After these two exceptional and unexpected discoveries, for about 15 years the number of known exoplanets grew by only a few tens per year. The vast majority of these exoplanets were found with the radial velocity technique (e.g., Fischer et al., 2014), similar to observing the blue- and redshifts of 51 Pegasi, and most of them were, just like 51 Pegasi b, hot Jupiters, that is giant planets on very short orbits. The first exoplanet discovered with another technique was OGLE-TR-56 b, whose existence was inferred from periodically occurring dimming events of its host star caused by the planet occulting part of the star on its orbit around it (Konacki et al., 2003). This technique is now known as the transit technique and has proven the most fruitful way of discovering exoplanets to date thanks to NASA’s *Kepler* mission which launched in 2010 and began to monitor about 200,000 stars for such periodic dimming events (Borucki et al., 2010). For this to happen, the orbital plane of the exoplanet needs to be aligned with our line of sight, a scenario which is geometrically unlikely. By continuously monitoring such a huge sample of stars though, the *Kepler* mission could still detect thousands of dimming events and revolutionized the field of exoplanet science by providing, for the first time, robust statistics on the occurrence rate of exoplanets as a function of their size and orbital period (e.g., Fressin et al., 2013; Dressing & Charbonneau, 2013, 2015; Burke et al., 2015).

Kepler has shown that planets are ubiquitous. Recent estimates predict an occurrence rate of at least 2.57 planets per solar-type star (Kopparapu et al., 2018), with even higher numbers for M-dwarfs (Dressing & Charbonneau, 2015). These estimates are limited to planets with a radius between 0.5–6 Earth radii and an orbital period between 0.5–500 days, so there likely are even more planets outside this parameter space. Although *Kepler*’s completeness decreases strongly with decreasing planet size and increasing distance to the parent star (e.g., Fressin et al., 2013), it has been possible to constrain the frequency of Earth-like planets in the habitable zone of their parent star to $\eta_\oplus = 12.6^{+9.5\%}_{-5.5\%}$ (Bryson et al., 2020), based on the η_\oplus definition from Kopparapu et al. (2018). This is a significant achievement on the way to constraining the frequency of life in our Galaxy, as it

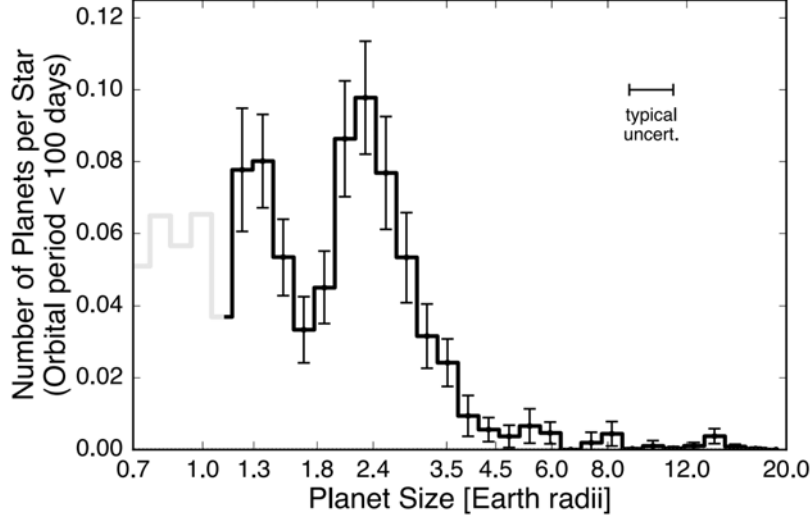


Figure 1.1: Planet occurrence rate as a function of planet size inferred from *Kepler* data. The uncertainties are increasing with decreasing planet size, and the inferred occurrence rate becomes unreliable for planets smaller than ~ 1 Earth radius (grey histogram). The distribution shows a clear dip around ~ 1.75 Earth radii, depicting the so-called evaporation valley. Adapted from [Fulton et al. \(2017\)](#).

leads us one step further toward understanding the existential Drake equation

$$N = R f_p \eta_{\oplus} f_i f_c L, \quad (1.1)$$

where N is the number of civilizations in our Galaxy with which communication is possible, R is the average star-formation rate in our Galaxy, f_p is the fraction of stars that harbour planets, f_i is the fraction of habitable planets that develop life, f_c is the fraction of developed life that becomes intelligent, f_l is the fraction of intelligent life that develops suitable communication technologies, and L is the average life time of such a civilization ([Burchell, 2006](#)). Furthermore, the planet occurrence rate inferred from *Kepler* enable planning future space missions and estimating their expected exoplanet yield ([Stark et al., 2014, 2015](#); [Kopparapu et al., 2018](#); [Kammerer & Quanz, 2018](#)).

The planet occurrence rate inferred from *Kepler* enables another important conclusion: our own Solar System is *not* a common planetary system. Figure 1.1 shows the number of planets (with orbital period < 100 days) per star as a function of the planet size ([Fulton et al., 2017](#)), revealing a significant deficit of planets around 1.75 Earth radii (R_{Earth}). There is a large population of super-Earths (~ 1.25 – $1.75 R_{\text{Earth}}$) to the left of the gap and another large population of sub-Neptunes (~ 1.75 – $4 R_{\text{Earth}}$) to the right of the gap, being the most abundant types of planets in our Galaxy. The transition between the two types is

characterized by the critical core mass required to sustain a thick envelope of H₂ and He gas (Rogers, 2015). While super-Earths have a thin atmosphere and are predominantly made up of iron and silicates, sub-Neptunes have a thick atmosphere which contributes significantly to their mass (Lopez & Rice, 2018). At the transition ($\sim 1.75 R_{\text{Earth}}$), a small change in atmosphere mass results in a large change in radius, and radiation from the parent star can quickly evaporate an envelope of H₂ and He gas. Interestingly, there is no super-Earth or sub-Neptune in our own Solar System, which might point to an uncommon formation scenario.

1.1.3 Transit and radial velocity techniques

Transit and radial velocity observations are ideal to probe short orbital periods. This is because the geometrical transit probability \mathcal{P} of an exoplanet with radius R_p on an orbit with semi-major axis a , eccentricity e and argument of periapsis ω in front of its parent star with radius R_* is

$$\mathcal{P} = 0.0045 \left(\frac{\text{au}}{a} \right) \left(\frac{R_* + R_p}{R_\odot} \right) \left(\frac{1 + e \cos(\pi/2 - \omega)}{1 - e^2} \right) \quad (1.2)$$

(Fischer et al., 2014), which decreases with increasing semi-major axis a . Similarly, the radial velocity semi-amplitude K caused by an exoplanet with mass M_p on an orbit with semi-major axis a , eccentricity e and inclination i on its parent star with mass M_* is

$$K = \frac{8.95 \text{ cm s}^{-1}}{\sqrt{1 - e^2}} \frac{M_p \sin i}{M_{\text{Earth}}} \left(\frac{M_* + M_p}{M_\odot} \right)^{-1/2} \left(\frac{a}{\text{au}} \right)^{-1/2} \quad (1.3)$$

(Fischer et al., 2014), which decreases with increasing period P . While transit observations alone only reveal the size and orbital period of an exoplanet and radial velocity observations alone only reveal its minimum mass $M_p \sin i$ and orbital period, in combination they provide information on the density of an exoplanet, since the inclination i can be assumed to be small if a transit occurs. This enables studying the bulk composition and interiors of exoplanets (e.g., Marcy et al., 2014; Weiss & Marcy, 2014). However, as will be shown in Section 1.1.6, planet formation in protoplanetary disks is believed to take place beyond the snow line (i.e., the distance to the parent star where water vapor solidifies into ice). Planets found at smaller orbital separations are believed to have migrated inward (e.g., Morbidelli & Raymond, 2016). Therefore, planet formation is best studied with techniques that are sensitive to planets beyond a few astronomical units from their parent star, such as microlensing and direct imaging (e.g., Bowler, 2016).

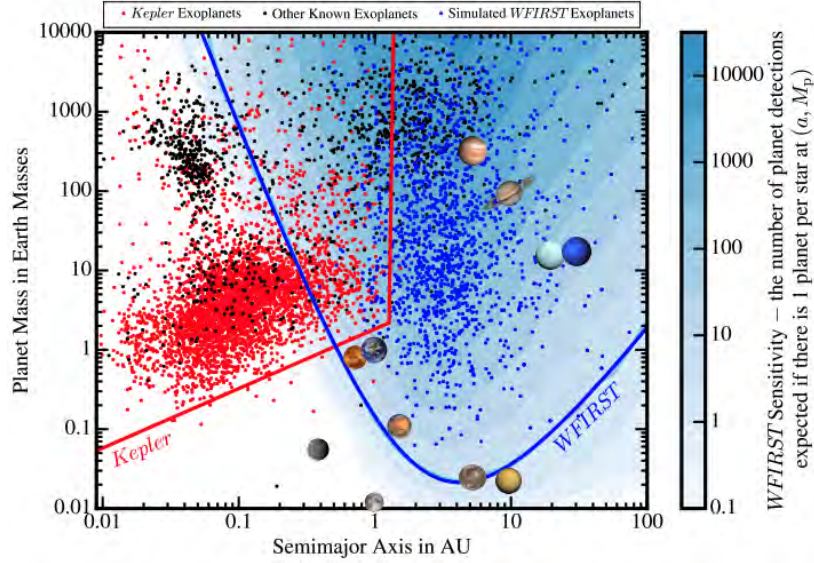


Figure 1.2: Discovery space of the *Kepler* transit and the *Roman* (here called by its former name WFIRST) microlensing surveys in the planet mass vs. semi-major axis plane. The red dots show exoplanets detected by *Kepler*, the black dots show exoplanets detected by other techniques, and the blue dots show simulated microlensing detections from *Roman*. The Solar System planets as well as the Moon, Ganymede, and Titan are shown at the semi-major axes of their parent bodies. Adapted from Penny et al. (2019).

1.1.4 Microlensing techniques

General relativity predicts that light can be gravitationally bound. When two stars come close to each other on the sky (apparent distance of ~ 1 mas), the light from the background star can be microlensed by the foreground star. If the background star is slightly offset from the foreground star, the light of the former is usually distorted into two images which appear close to the Einstein radius

$$\theta_E = \sqrt{\kappa M_L \pi_{\text{rel}}}, \quad (1.4)$$

where $\kappa = 8.14 \text{ mas } M_\odot^{-1}$, M_L is the lens mass in solar masses, and $\pi_{\text{rel}} = (1 \text{ au}/D_L) - (1 \text{ au}/D_S)$ with D_L and D_S being the lens and source distance in kpc. These two images are usually too close to each other to be resolved, although Dong et al. (2019) recently obtained the first resolved microlensing images with VLTI/GRAVITY. Even when unresolved, microlensing events can be observed as a change in the source brightness over time, as the stars approach each other on the sky and separate again. If the foreground star hosts a planet at an angular separation similar to that of the lensed images of the background star (i.e., similar to the Einstein radius), this can lead to an observable perturbation of the microlensing light curve (e.g., Fischer et al., 2014).

Gravitational microlensing events can reveal the mass and angular separation of an exoplanet (if the lens mass and the Einstein radius can be inferred), but the geometric microlensing probability makes such events rare in the Solar neighborhood. Instead, microlensing planets are usually too far away to be followed-up and characterized with other detection techniques. Nevertheless, microlensing will play an important role in mapping out the planet distribution between $\sim 1\text{--}10$ au and down to the Earth-mass regime with the *Roman Space Telescope* (Penny et al., 2019). This will bridge the gap in the planet population between transit/radial velocity and direct imaging techniques (cf. Figure 1.2) and provide a crucial test for the true occurrence of these planets which is currently inferred from the extrapolation of the known planet population (e.g., Fernandes et al., 2019).

1.1.5 Direct imaging techniques

Direct imaging observations have proven successful in exploring the outer regions of planetary systems and finding young gas giants at large orbital separations (e.g., Bowler, 2016). The technique aims at resolving an exoplanet from its parent star, at contrasts down to $\sim 12\text{--}15$ magnitudes achieved at angular separations of $0.4\text{--}0.5$ arcsec (e.g., with VLT/SPHERE, Langlois et al., 2021). Conducting such observations with dedicated instruments from the ground has only been possible through the development of extreme adaptive optics systems (e.g., SPHERE, GPI, SCExAO, Beuzit et al., 2019; Macintosh et al., 2014; Currie et al., 2017) and advanced observing and post-processing techniques that effectively remove the stellar PSF (e.g., ADI, PCA, Marois et al., 2006; Soummer et al., 2012; Amara & Quanz, 2012). Figure 1.3 shows the famous HR 8799 system with its four gas giants, one of the early discoveries of high-contrast imaging (Marois et al., 2008, 2010). Direct imaging is ideal to study the brightness, color, orbital motion, and atmospheric composition of the planets, and in combination with evolutionary models can constrain their mass, age, and formation entropy (e.g., Spiegel & Burrows, 2012; Mordasini, 2013). Moreover, it enables observations of the dynamical interaction between young planets and the protoplanetary disks in which they are born (e.g., PDS 70, Keppler et al., 2018). As such, direct imaging is vital to study planet formation and evolution.

In the past decade, there have been huge efforts to find young gas giants around nearby moving group stars. The advantage of targeting young stars is that their young planets should glow bright in the near-infrared compared to older ones due to their remaining formation heat (e.g., Spiegel & Burrows, 2012). Thousands of hours of telescope time were devoted to performing high-contrast imaging surveys of hundreds of young stars, but the overall detection rate turned out to be low. The conclusion suggests itself: wide-separation (10–100 au) gas giants ($5\text{--}13 M_{\text{Jupiter}}$) are intrinsically rare, with an overall occurrence rate of $\sim 5\%$ (Nielsen et al., 2019; Vigan et al., 2020). Brown dwarf companions ($13\text{--}80 M_{\text{Jupiter}}$) in the same semi-major axis range seem to be even more rare ($\sim 1\%$). This is in

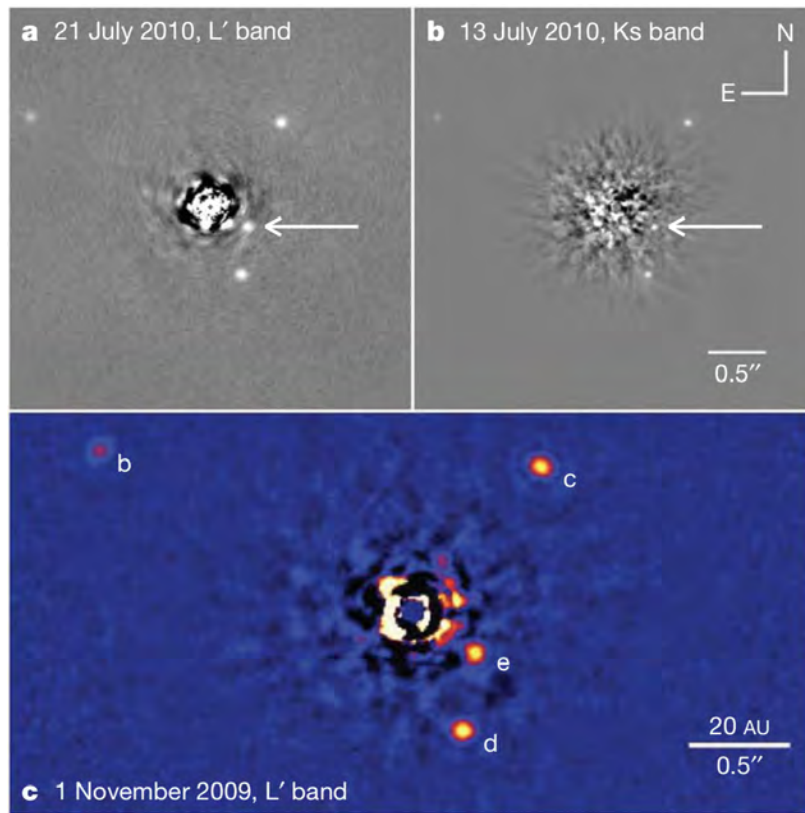


Figure 1.3: Multi-epoch Keck images of the HR 8799 planetary system processed with point-spread function (PSF) subtraction and angular differential imaging techniques. Four young and self-luminous gas giants are detected (b, c, d, and e), orbiting their parent star roughly co-planar and face-on. The parent star is located in the center, hidden behind a coronagraph and surrounded by residual speckle noise from the PSF subtraction. Adapted from [Marois et al. \(2010\)](#).

agreement with the gas giant occurrence rate inferred from radial velocity data, which suggests a peak in the giant planet distribution around the snow line ($\sim 2\text{--}5$ au around a young Sun-like star, [Mulders et al., 2015](#)) with a decline to a few percent further out (see Figure 1.4, [Fernandes et al., 2019](#)). Furthermore, most giant planets are believed to form via core accretion (see Section 1.1.6) and are thus only detectable at their youngest ages (< 5 Myr) with current instruments ([Wallace & Ireland, 2019](#)). Such young objects can only be found in the nearest star-forming regions, which are located at distances of more than 100 pc ([de Zeeuw et al., 1999](#); [Rizzuto et al., 2011](#)), where physical separations of 5 au correspond to angular separations of 50 mas. This gives current direct imaging surveys on eight-meter telescopes a hard time finding young giant planets, since they are limited by residual speckles from the PSF subtraction or occultation by coronagraphs inward of $\sim 100\text{--}200$ mas. Higher angular resolution techniques

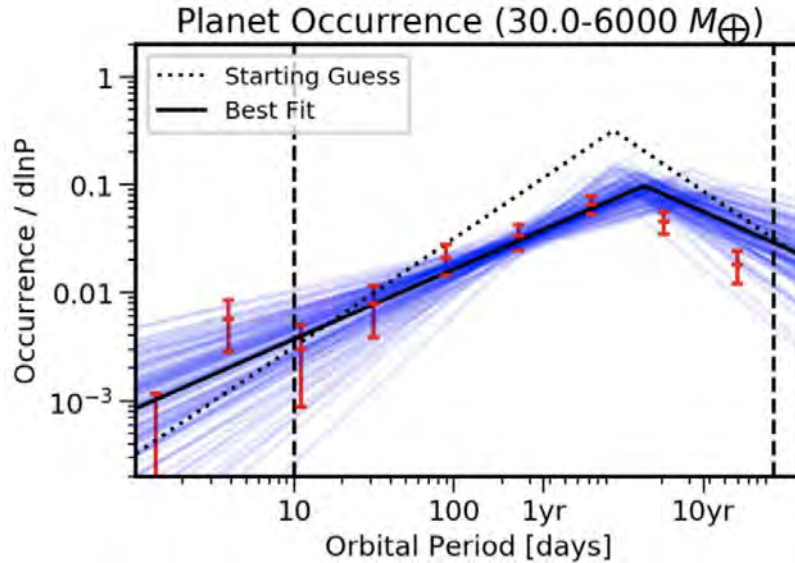


Figure 1.4: Giant planet occurrence rate as a function of orbital period inferred from radial velocity data. The red points are the data and the blue lines are randomly drawn samples from the posterior distribution of the broken power-law used to fit the data. The inferred occurrence rate suggests a peak around ~ 2 – 3 au, close to where the snow line of a young Sun-like star is located. Adapted from [Fernandes et al. \(2019\)](#).

are thus required to probe smaller orbital separations, where giant planets are more common, and to detect a sizeable sample of such objects for studying giant planet formation on a statistically relevant scale.

The present time marks an exciting period in which the planet populations from radial velocity and direct imaging begin to overlap (see Figure 1.5). As radial velocity surveys become longer and direct imaging systems become more stable, both techniques now detect planets at orbital separations of tens of astronomical units. An important step forward was the recent direct confirmation of β Pic c, a planet discovered through radial velocity observations ([Lagrange et al., 2019](#)), with long-baseline interferometry (VLTI/GRAVITY, [Nowak et al., 2020](#)). Together with a reliable mass estimate from radial velocity data, direct imaging enables the identification of a formation scenario for β Pic c. However, young and nearby field stars, such as β Pic, are rare ([Zuckerman & Song, 2004](#)) and to study giant planet formation on a statistically relevant sample, it is inevitable to aim for the nearest star-forming regions. Kernel phase and long-baseline interferometry both provide the means to access Solar System scales (~ 5 au) in these regions, where young Jupiter analogs and the tip of the giant planet distribution are located.

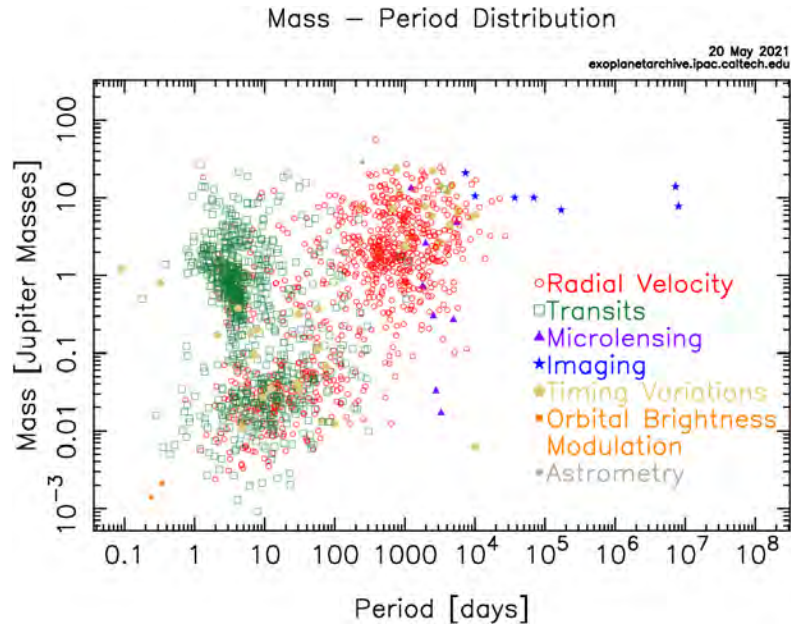


Figure 1.5: Population of known exoplanets in the mass vs. period plane, color-coded by detection technique. While transit and radial velocity are sensitive to objects at small separations ($\lesssim 10$ au), direct imaging detects companions at large separations ($\gtrsim 10$ au). However, the parameter spaces accessible with radial velocity and direct imaging are beginning to overlap significantly. Retrieved from the NASA Exoplanet Archive on 20 May 2021.

1.1.6 Giant planet formation

When stars form via gravitational collapse of a cloud made of gas and dust, the circumstellar matter settles into an accretion disk. Such circumstellar disks remain after the star-formation process and have been directly observed around T Tauri and Herbig Ae/Be stars, for example with ALMA (e.g., [ALMA Partnership et al., 2015](#)). They are believed to be the birthplaces of planets, hence also referred to as protoplanetary disks, and while spurious clumpy features have been detected in several such disks (e.g., [Kraus & Ireland, 2012](#); [Quanz et al., 2013](#); [Biller et al., 2014](#)), the PDS 70 system marks the only unambiguous proof of giant planets observed during formation in a protoplanetary disk to date ([Keppler et al., 2018](#); [Haffert et al., 2019](#)). Understanding the formation and evolution of giant planets is a fundamental goal of modern astrophysics and of particular importance for planetary systems as a whole. Giant planets accrete large amounts of matter from the protoplanetary disk and can open gaps in the disk’s radial dust distribution which form barriers for radial dust drift, limiting the amount of material available for the formation of smaller planets closer in (e.g., [Rice et al., 2006](#)). Moreover, they gravitationally interact with potential other planets in

the system causing orbital resonances and migration (e.g., D’Angelo & Marzari, 2012). Likewise, Jupiter and Saturn are believed to have played an important role for the formation and evolution of the Solar System, and have predominantly dictated its present-day architecture (Morbidelli et al., 2007).

There are two distinct channels for giant planet formation which are widely accepted in the community: (i) the core accretion model (Pollack et al., 1996) and (ii) the gravitational instability model (Boss, 2001). In the core accretion model, rocky planetary cores form through incremental growth from millimeter-sized dust particles to kilometer-sized planetesimals, which finally grow into gas giants by runaway gas accretion. In the gravitational instability model, giant planets form through gravitational collapse of an over-density in the protoplanetary disk. The two models make different predictions about the planets’ specific entropy after formation, and therefore about their luminosity as a function of age and mass. This will be discussed in detail in the following Section (Section 1.1.7). Overall, it has been estimated that roughly 90% of the known planets formed via core accretion, whereas only 10% emerged from gravitational instability (Matsuo et al., 2007). However, it is worth to point out that recent work has discovered many more planets (e.g., Hsu et al., 2019) and that high-contrast imaging surveys such as SHINE (Vigan et al., 2020) and GPIES (Nielsen et al., 2019) have found a smaller than expected number of planets at wide separations (where gravitational instability is more efficient), indicating that an even higher fraction might have formed via core accretion.

Core accretion

In the core accretion model, giant planets are believed to form via concurrent accretion of dust and gas from the protoplanetary disk (Pollack et al., 1996). The vertical motion of small dust particles in the protoplanetary disk is dominated by friction and can be described as

$$z(t) \approx z(0)e^{-\Omega^2\tau t}, \quad (1.5)$$

where $z(t)$ is the vertical dust distribution, Ω is the angular velocity of the gas, and τ is the stopping time of the gas particles (D’Angelo et al., 2010). Equation 1.5 describes an exponential decay with half life $(\Omega^2\tau)^{-1} \approx (10^{-3}\rho_{\text{dust}}R_{\text{dust}})^{-1}$, where ρ_{dust} is the density of the dust particles and R_{dust} is their size. Hence, millions of orbital periods would be required for micron-sized dust particles at a separation of ~ 5 au from a Sun-like star to settle toward the disk mid-plane. Therefore, micron-sized dust particles must first grow to centimeter-sized ices, which can only happen beyond the snow line ($\sim 2\text{--}5$ au around a young Sun-like star Mulders et al., 2015) where solidification of gas into ices is possible. This is why planet migration toward the host star is believed to be an important mechanism for the many close-in super-Earth, ice giant, and gas giant exoplanets detected by transit and radial velocity observations (e.g., Terquem &

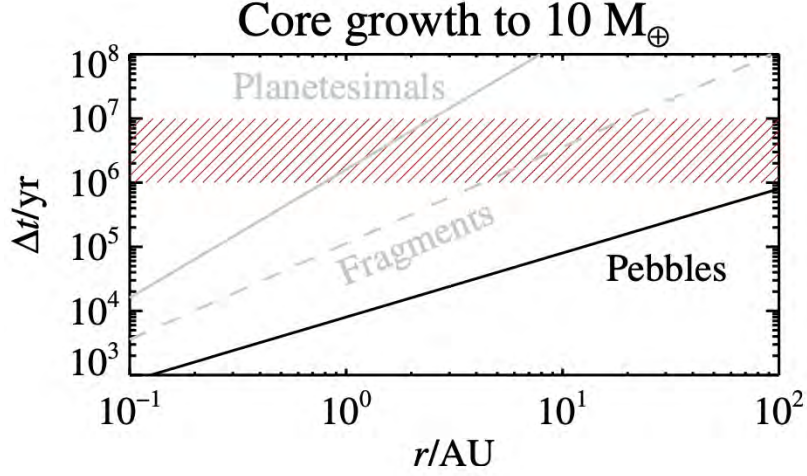


Figure 1.6: Core growth time to a core mass of 10 Earth masses as a function of separation from the host star for different accretion scenarios. Pebble accretion predicts significantly faster core growth than the accretion of larger fragments or planetesimals. Shown by dashed red hatching is the average protoplanetary disk lifetime as an upper limit to the core growth (10^6 – 10^7 years). Adapted from Lambrechts & Johansen (2012).

Papaloizou, 2007; Izidoro et al., 2017). Kilometer-sized planetesimals then form from the centimeter-sized ices in a process that is still poorly understood. The streaming instability theory (Youdin & Goodman, 2005) predicts the formation of over-densities, which could trigger planetesimal formation, only by drag forces between the gas and the dust component of the rotating protoplanetary disk and gives one possible explanation. A protoplanetary core can then form from the kilometer-sized planetesimals via collisional interactions, which predict a core growth rate of

$$\frac{dM}{dt} = \pi R^2 \Omega \Sigma F_g, \quad (1.6)$$

where R is the radius of the protoplanetary core, Ω is now the angular velocity of the protoplanetary core around the host star, Σ is the surface density of the solid material in the disk, and $F_g = (R_{\text{effective}}/R)^2$ with $R_{\text{effective}}$ being the radius out to which the protoplanetary core can gravitationally attract other planetesimals (D’Angelo et al., 2010). Since $\Omega \propto a^{-3/2}$ for a Keplerian orbit and $\Sigma \propto a^{-3/2}$ according to the phenomenological model of Hayashi (1981), core growth happens faster, the closer the core is orbiting its host star. Thus, Uranus and Neptune presumably had significantly lower core growth rates dM/dt than Jupiter and Saturn. Another approach to the formation of a protoplanetary core comes from the pebble accretion theory. Lambrechts & Johansen (2012) showed that a core of a few hundreds of kilometers in size can grow rapidly by accreting pebbles, which are intermediate-sized particles bound by drag forces to the gas component of the

disk, that also experience the drag from the core enabling kinetic energy transfer and binding to it. This theory predicts an up to four orders of magnitude faster core growth rate if compared to the planetesimal collision theory (Figure 1.6).

Once the vicinity of a protoplanetary core is cleared of planetesimals, its core growth is terminated, and the final core mass can be written as

$$M_{\text{final}} \approx \sqrt{\frac{(16\pi a^2 \Sigma)^3}{3M_\star}}, \quad (1.7)$$

where M_\star is the mass of the host star (D'Angelo et al., 2010). The core of a planet like Jupiter ($a = 5.2$ au, $\Sigma = 10$ g cm⁻²) should have a mass of $\sim 11 M_{\text{Earth}}$. Gas accretion onto the protoplanetary core can in principle begin much before its feeding zone is cleared of planetesimals, as soon as the escape velocity of the protoplanetary core exceeds the thermal velocity of the gas, which is equivalent to

$$M > \sqrt{\frac{M_\star^3}{a^3 \rho_{\text{dust}}} \frac{H^3}{a^3}} \quad (1.8)$$

and can be as small as $0.01 M_{\text{Earth}}$ at a distance of a few astronomical units from a Sun-like star. Here, H represents the vertical scale-height of the disk (D'Angelo et al., 2010). In the beginning, though, the gas accretion rate is much slower than the accretion rate of planetesimals because the gaseous envelope becomes optically thick relatively fast, which leads to a pressure gradient preventing further gas from the disk to fall inward. A long phase of slow contraction follows, dominated by the opacity of the envelope and still uncertain in its duration ($\sim 1\text{--}6$ Myr). Finally, once the protoplanetary core reaches a critical mass ($\sim 32 M_{\text{Earth}}$ for the formation of Jupiter), the gas pressure of the envelope can no longer sustain the inward gravitational pull and the protoplanet begins to rapidly accrete gas from the disk (runaway gas accretion). Its growth rate dM/dt is then given by

$$\frac{dM}{dt} \approx \frac{\Omega \Sigma}{H} R_{\text{effective}}^3 \quad (1.9)$$

(D'Angelo et al., 2010), and the timescale for doubling its mass can be as short as 100 orbital periods when the protoplanet/star mass ratio M/M_\star reaches 10^{-4} . Tidal interactions with the protoplanetary disk, however, lead to the formation of a disk gap. The timescale for the formation of such gaps is

$$\Omega \tau_{\text{gap}} \approx \pi \frac{M_\star^2 \Delta a^5}{M^2 a^5}, \quad (1.10)$$

where Δa is equal to the larger of either the Hill sphere radius R_{Hill} or the vertical scale-height of the disk H (D'Angelo et al., 2010). This timescale is usually as small as a few tens of orbital periods. Therefore, the phase of runaway gas accretion is terminated relatively fast.

Giant planet formation via core accretion and subsequent runaway gas accretion is critically limited to the life time of the gaseous component of the protoplanetary disk. The closer a planet forms to the snow line, the faster can its core reach the critical mass for runaway gas accretion and grow into a gas giant. This naturally explains the decreasing sizes of Jupiter, Saturn, Uranus, and Neptune, the gas and ice giants in our own Solar System.

Gravitational instability

In the gravitational instability model, giant planets form via gravitational fragmentation of the protoplanetary disk into clumps. The disk pressure p in radial direction can be expressed as density waves $\delta p \propto \exp(i\omega t)$, where

$$\omega^2 = \kappa^2 - \frac{4\pi^2 G \Sigma}{\lambda} + \frac{4\pi^2 c_s^2}{\lambda^2}. \quad (1.11)$$

Here, κ is the oscillating frequency of a perturbed disk particle ($\kappa = \Omega$ for a Keplerian disk), G is the gravitational constant, λ is the radial wavelength of the perturbation, and c_s is the speed of sound in the disk (D'Angelo et al., 2010). Perturbations are oscillating waves as long as $\omega^2 \geq 0$, but grow exponentially as soon as $\omega^2 < 0$. A range of unstable wavelengths occurs if

$$Q = \frac{c_s \kappa}{\pi G \Sigma} < 1, \quad (1.12)$$

where Q is called the Toomre instability parameter and the circumstellar disk becomes unstable if it is either cool enough (small c) or massive enough (large Σ). This simplification holds for axisymmetric perturbations only, but numerical simulations have shown that non-axisymmetric perturbations like spiral waves become unstable if $Q < 1.5$ – 2 already, so that spiral arms are usually the first observable feature arising from a fragmenting protoplanetary disk. If the disk temperature $T \propto a^{-1/2}$ (e.g., for an optically thin disk) and the oscillating frequency $\kappa \approx \Omega \propto a^{-3/2}$ depend on the separation to the host star a , the Toomre instability parameter is proportional to

$$Q \propto \frac{T^{1/2} \Omega}{\Sigma} \propto \frac{a^{-7/4}}{\Sigma}. \quad (1.13)$$

Therefore, if the surface density $\Sigma \propto a^{-s}$ with $s < 7/4$ and the radial extent of the disk is large enough, Q becomes less than the critical value of 1–2 at some point.

The emerging spiral waves must then fragment into clumps to form giant planets (see Figure 1.7), but in order to do so, gravitational potential energy needs to be radiated away from the over-densities. Otherwise, the sound speed c and therefore the Toomre instability parameter $Q \propto c$ increases above the critical

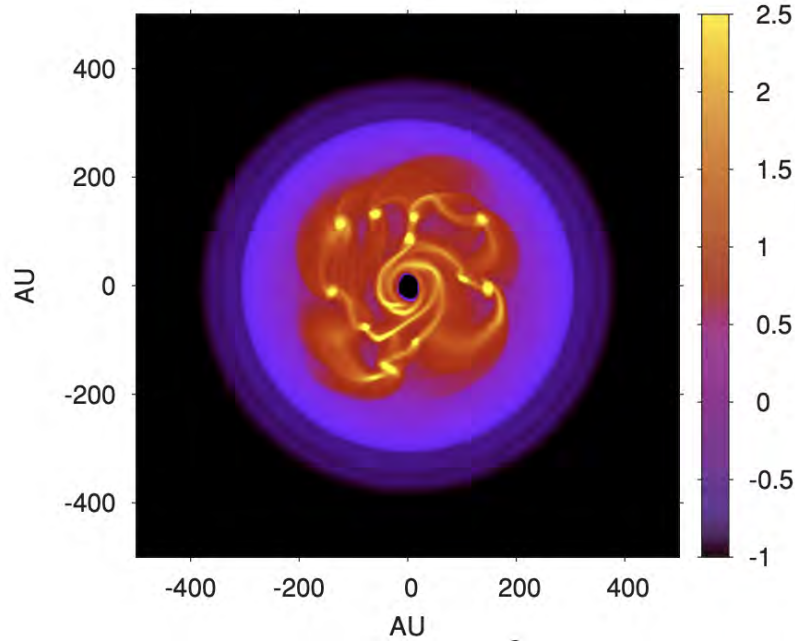


Figure 1.7: Gas surface density of a snapshot of a simulation of a gravitationally unstable protoplanetary disk leading to the formation of multiple protoplanetary cores at separations of ~ 100 – 200 au. All cores show accretion driven by spiral arms or filaments. Adapted from [Boley \(2009\)](#).

limit and the over-densities stop growing. Numerical simulations predict that

$$\frac{\tau_{\text{cooling}}}{\tau_{\text{rotation}}} \sim 1\text{--}2 \quad (1.14)$$

is required for fragmentation to occur, where τ_{cooling} is the cooling timescale of the over-densities and τ_{rotation} is their rotation timescale around the host star. At the orbital separation of Jupiter around a Sun-like star $\tau_{\text{cooling}}/\tau_{\text{rotation}} \sim 10^4 \gg 1\text{--}2$, hence planets cannot form via gravitational instability on such orbital scales. However, numerical simulations predict that outward of ~ 100 au, gravitational instability can efficiently form giant planets with typical masses of a few Jupiter masses ([Boley, 2009](#)).

1.1.7 Post-formation entropy and evolutionary tracks

The fundamentally different formation mechanisms underlying gravitational instability and core accretion predict different post-formation specific entropies for giant planets (e.g., [Spiegel & Burrows, 2012](#)). This means that for a given age and mass, the two mechanisms predict different planet luminosities, which offers the possibility to observationally distinguish between them.

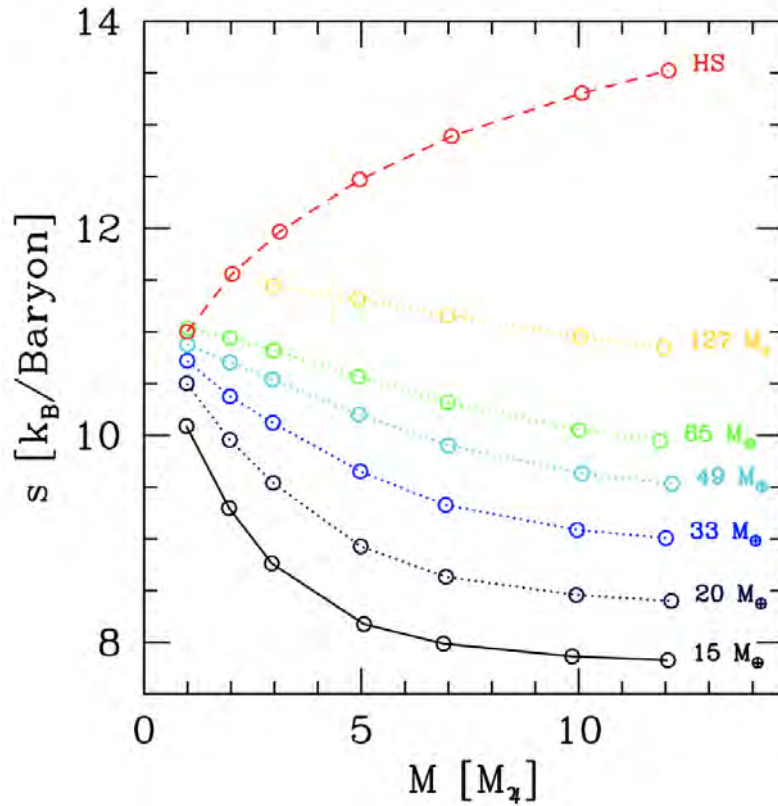


Figure 1.8: Post-formation specific entropy as a function of planet mass for giant planets formed via gravitational instability (HS, red line) and core accretion featuring different core masses (other lines). Depending on the core mass, a range of intermediate values for the post-formation specific entropy between hot and cold accretion is permitted, called the warm accretion regime. Adapted from [Mordasini \(2013\)](#).

Formation via gravitational instability is usually referred to as hot accretion, since the post-formation specific entropy is rather high and increases with increasing planet mass. This is the case since with increasing planet mass, an increasing amount of gravitational potential energy is converted to thermal energy during formation and stored in the planet. Formation via core accretion, however, is usually referred to as cold accretion and predicts a decrease in post-formation specific entropy with increasing planet mass. This is the case since with increasing planet mass, thermal energy is radiated away in stronger accretion shocks ([Marley et al., 2007](#)). While the original core accretion models assumed efficient accretion shocks, [Marleau & Cumming \(2014\)](#) have shown that more realistic dissipative accretion shocks predict an intermediate regime between hot and cold accretion, referred to as warm accretion. Figure 1.8 shows that in the core accretion scenario, the post-formation specific entropy strongly depends on

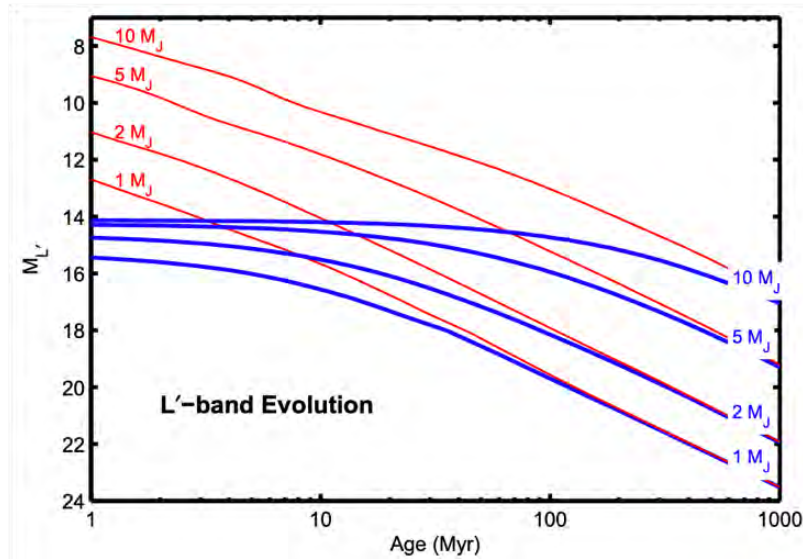


Figure 1.9: Evolutionary tracks for giant planets of different masses formed via hot (red lines) and cold (blue lines) accretion. Cold accretion predicts fainter objects for a given age and mass, but the difference to hot start objects decreases quickly with age. Hence, young objects need to be considered to be able to distinguish between different formation mechanisms. Adapted from Spiegel & Burrows (2012).

the core mass, and while hot accretion predicts post-formation specific entropies of $\sim 11\text{--}13.5 k_B/\text{baryon}$, cold and warm accretion predict values ranging from $8 k_B/\text{baryon}$ for less massive cores to $11.5 k_B/\text{baryon}$ for more massive cores.

Many of the early discoveries of direct imaging are young giant planets on large orbital separations ($\gtrsim 40$ au), such as HR 8799 b/c (Marois et al., 2008) and Fomalhaut b (Kalas et al., 2008). Traditionally, these objects were associated with hot accretion via gravitational instability, and evolutionary tracks (see Figure 1.9) could be used to infer their mass based on their luminosity and age. While the luminosity of a young giant planet is a good proxy for its post-formation specific entropy if coupled with an age estimate, the existence of the intermediate warm accretion regime makes it difficult to draw definitive conclusions on the formation mechanism. Moreover, estimating the age of giant planets is notoriously difficult itself and affected by large systematic uncertainties (e.g., Bowler, 2016). Especially for giant planets on smaller orbital separations, which could not have formed via gravitational instability at their present position, warm start core accretion represents a viable alternative to hot start gravitational instability, which furthermore does not invoke inward migration. Recent direct observations of the giant planets β Pic b and c combined with mass estimates from radial velocity data suggest good agreement with warm start core accretion models (Nowak et al., 2020), at least for β Pic c. At the youngest ages, the

picture is further complicated by the likely presence of circumplanetary accretion disks (e.g., [Shabram & Boley, 2013](#)). Even the disks around fainter core accretion planets can become considerably bright during the runaway gas accretion phase ([Zhu, 2015](#); [Wallace & Ireland, 2019](#)), lowering the contrast between an accreting giant planet and its host star to $\sim 10^{-3}$.

While direct imaging of a single giant planet can only put loose constraints on its formation, a larger, statistically relevant sample of young giant planets (e.g., [Bowler et al., 2020](#)) or other means to distinguish between the different formation channels have to be consulted. For example, [Öberg et al. \(2011\)](#) have shown that the C/O abundance ratio in the atmosphere of a giant planet depends on its formation location relative to the water and carbon-monoxide icelines of the protoplanetary disk. A stellar C/O abundance ratio points to rapid gas accretion beyond the CO iceline while a sub-stellar C/O abundance ratio suggests formation via either gravitational instability or gas and planetesimal accretion, followed by planetesimal enrichment interior to the CO iceline. The C/O abundance ratio of stars is difficult to determine (e.g., [Asplund, 2005](#)), but the C/O abundance ratio of the directly-imaged giant planet β Pic b could recently be measured via medium-resolution K-band spectroscopy with GRAVITY ([Gravity Collaboration et al., 2020](#)). The sub-solar C/O abundance ratio of β Pic b is difficult to explain with hot start gravitational instability, since the mass of accreted ices from the disk would be too small to lower the C/O abundance ratio significantly. Therefore, warm start core accretion somewhere between the water and carbon-dioxide icelines seems more likely. As mentioned before, the ability of GRAVITY to observe exoplanets at unprecedented angular resolutions gives direct access to giant planets predicted from radial velocity observations, such as β Pic c ([Lagrange et al., 2019](#); [Nowak et al., 2020](#)). Luminosity and age combined with an independent mass measurement from radial velocity data provide a direct constraint on the formation channel, at least at the youngest ages where the evolutionary tracks for hot, warm, and cold accretion are significantly different. As shown in Section 1.1.2, angular resolution is the key for studying giant planet formation, and long-baseline optical interferometry with GRAVITY is leading the field already.

1.2 Fourier plane techniques

On a first glance, optical interferometers and single-dish telescopes appear very different. From the image formation point of view, they are very similar, though, which becomes clear when considering them in Fourier space. For a single-dish telescope, the observed image $I(\vec{\alpha})$, where $\vec{\alpha}$ are the sky coordinates, can be obtained by convolution of the object intensity distribution (OID) $O(\vec{\alpha})$ with the point-spread function (PSF) $M(\vec{\alpha})$ of the telescope, that is

$$I(\vec{\alpha}) = O(\vec{\alpha}) * M(\vec{\alpha}) \quad (1.15)$$

(Ireland, 2016). For an unresolved star in the center of the field-of-view (FOV) for example, the OID is $O(\vec{\alpha}) = \delta(\vec{0})$, and additional point sources can be added with more delta functions. In the Fourier domain, convolution simplifies to multiplication and

$$\tilde{I}(\vec{u}) = \tilde{O}(\vec{u}) \times \tilde{M}(\vec{u}), \quad (1.16)$$

where the tilde denotes the Fourier transform and \vec{u} are the spatial frequencies (Ireland, 2016). Since the PSF is the square modulus of the Fourier transform of the telescope pupil $P(\vec{u})$, that is

$$M(\vec{\alpha}) = |\tilde{P}(\vec{u})|^2, \quad (1.17)$$

the image Fourier transform can also be written as

$$\tilde{I}(\vec{u}) = \tilde{O}(\vec{u}) \times (P * P)(\vec{u}) \quad (1.18)$$

according to the Wiener–Khinchin theorem (Wiener, 1930). Hence, the optical transfer function (OTF) $T(\vec{u})$ of a telescope is given by the autocorrelation of its pupil $P(\vec{u})$ (see Figure 1.10). According to the van Cittert–Zernike theorem, the Fourier transform of the OID $\tilde{O}(\vec{u})$ of a distant, incoherent source is equal to its complex visibility, that is

$$\tilde{O}(\vec{u}) = \int I(\vec{\alpha}) e^{-ik\vec{u}\cdot\vec{\alpha}} d\vec{\alpha} = V(\vec{u}), \quad (1.19)$$

where $k = 2\pi/\lambda$, λ is the observing wavelength, and \vec{u} is the distance of the two points in the pupil plane between which the spatial coherence is measured (van Cittert, 1934; Zernike, 1938). Therefore, $V(\vec{u})$ is also called the mutual spatial coherence function. As explained in Section 1.2.1, an interferometer measures this mutual spatial coherence function for the baselines between its individual telescopes. Considering Equation 1.18, it becomes clear that both optical interferometers and single-dish telescopes measure $V(\vec{u})$, spatially filtered by the autocorrelation of their pupil.

Given that both optical interferometers and single-dish telescopes measure the same quantity, the model fitting and image reconstruction process becomes

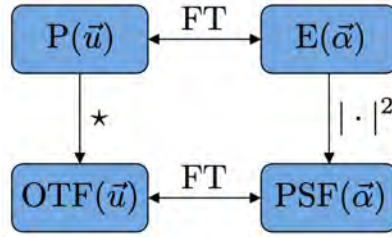


Figure 1.10: Diagram visualizing the Wiener–Khinchin or autocorrelation theorem. The point-spread function (PSF) is the square modulus of the Fourier transform (E) of the pupil (P), and can also be written as the Fourier transform of the optical transfer function (OTF), which is itself the autocorrelation of the pupil (P).

very similar in the Fourier plane. **However, one major caveat of long-baseline interferometry is the sparse spatial frequency sampling which limits the image reconstruction capabilities significantly.** For the model fitting purposes, the complex visibility is usually normalized by the total flux (e.g., Berger, 2003). Moreover, the complex visibility, as a Fourier transform, is linear. Hence, a complex object composed of a linear combination of simpler components can be described by the linear combination of the components’ complex visibilities. If the complex visibility $V(\vec{u})$ of the observed astronomical source can be parametrized, for example

$$V(\vec{u}) = \frac{1 + fe^{-2\pi i \vec{\alpha} \cdot \vec{u} / \lambda}}{1 + f} \quad (1.20)$$

in the case of two point-sources with flux ratio $0 < f < 1$ and separated on the sky by $\vec{\alpha}$ (such as an unresolved star orbited by an exoplanet), model fitting can be performed to the complex visibility measured by an interferometer or measured in the Fourier transform of an image of a single-dish telescope. If the source geometry is more complex or not known a priori, image reconstruction can be performed, for example with a maximum entropy method (Ireland, 2013).

In real observations, however, the measured complex visibility is affected by errors from atmospheric turbulence and the telescope optics themselves. This is where Fourier plane techniques can play on their real advantages over image plane techniques. In the Fourier plane, robust and unbiased estimators of the squared visibility amplitudes

$$|V|^2 \quad (1.21)$$

and the closure phases over telescope triplets

$$\angle V_1 V_2 V_3 \quad (1.22)$$

can be formed, where \angle denotes the phase of a complex number and the closure phases are independent of pupil plane phase piston noise (e.g., Monnier, 2003).

These estimators can then be calibrated using observations of a well-known point-source, obtained close in time to the observations of the science target in order to minimize quasi-static aberrations. As such, Fourier plane techniques have been used for high-angular resolution astronomy, not only with long-baseline optical interferometry, but also due to the superior PSF calibration capabilities of single-dish speckle, aperture masking, and kernel phase interferometry.

1.2.1 Long-baseline interferometry

The classical (Rayleigh) diffraction-limit of a telescope is defined as the first minimum (i.e., dark fringe) of its PSF, which is located at an angular separation of

$$\theta_{\min} \approx 1.22 \frac{\lambda}{D} \quad (1.23)$$

for a circular aperture with diameter D (e.g., Monnier, 2003). With the same definition, the diffraction-limit of a two-aperture interferometer is

$$\theta_{\min} = \frac{\lambda}{2B}, \quad (1.24)$$

where B is the distance between the two apertures (e.g., Monnier, 2003). In 1868, Fizeau proposed that a simple two-slit interferometer could be used to measure the size of astronomical objects (Fizeau, 1868). This idea was successfully demonstrated in 1891, when Michelson measured the angular diameters of the Galilean moons of Jupiter (Michelson, 1891). In 1921, Michelson and Pease went one step further and measured the angular diameter of a distant star (α Ori, Michelson & Pease, 1921). Only a decade later, Jansky (1933) discovered the first radio signals coming from space and the field of radio astronomy was born. At radio wavelengths (as opposed to at optical wavelengths), signals could be recorded electronically which made the combination of signals from multiple telescopes much easier. Moreover, at the longer wavelengths in the radio regime, single-dish antennas were strongly limited in angular resolution, so that Ryle & Vonberg (1948) constructed the first Michelson-type radio interferometer to observe discrete radio sources in the galaxy (Ryle & Hewish, 1950). It was not until the 1960s and 70s, when the importance of optical interferometry for measuring stellar diameters was strengthened, when a technique called intensity interferometry (Hanbury Brown, 1956) was developed and successfully demonstrated with baselines of up to 188 m with the Narrabri Intensity Interferometer (Hanbury Brown et al., 1967). Intensity interferometry is limited to small bandwidths, though, and therefore of limited scientific use, which pushed the development of direct beam combination techniques. The Narrabri Intensity Interferometer for instance had a limiting magnitude of ~ 2.5 mag and the achievable signal-to-noise was significantly worse than that achieved by amplitude interferometry (Tuthill, 2014). Nevertheless, modern high-energy astronomy is re-discovering the technique of intensity interferometry for the Cherenkov Telescope Array (Dravins et al., 2013).

The first direct beam combination was accomplished by Labeyrie (1975), and only a few years later Shao & Staelin (1980) could demonstrate fringe tracking on a prototype of the Mark III interferometer. These accomplishments paved the way for modern phase-referencing interferometry, which aims to preserve both the amplitude and the phase of the complex visibility in order to enable image synthesis. Today, multiple optical interferometers are spread over the world, most notably CHARA (ten Brummelaar et al., 2005), the Large Binocular Telescope Interferometer (LBTI, Hinz et al., 2012), and the Very Large Telescope Interferometer (VLTI, Bedding et al., 1994). They still enable cutting-edge science at high angular resolution, for example at the center of our galaxy (Gravity Collaboration et al., 2018) and in exoplanetary systems (Gravity Collaboration et al., 2019). In the meantime, new interferometric observing techniques such as nulling (Bracewell & MacPhie, 1979) and kernel-nulling (Martinache & Ireland, 2018) interferometry have been developed. A nulling instrument is already in operation at the LBTI (Defrère et al., 2015) and future instruments are being planned for the VLTI (Defrère et al., 2018) and for the characterization of Earth-like exoplanets from space (Lawson, 2001; Leger & Herbst, 2007; Quanz et al., 2021). Nulling interferometry is useful for high-contrast imaging applications since it achieves high attenuation of a central bright source at very small inner working angles (Guyon et al., 2013). Finally, we note that nulling of a central bright source can also be achieved by inserting a vortex phase mask into the beam of a single-dish telescope and coupling the light into a single-mode fiber, which will then reject photons coming from the bright on-axis source, but transmit photons coming from a faint off-axis source (Ruane et al., 2019). This technique is promising for the spectroscopic characterization of close-in exoplanets ($0.5\text{--}2 \lambda/D$) with the ELTs.

In Section 1.2, it was shown that the complex visibility

$$V(\vec{u}) = \int I(\vec{\alpha}) e^{-ik\vec{u}\cdot\vec{\alpha}} d\vec{\alpha} \quad (1.25)$$

is the quantity which is measured by an interferometer. This can be seen when considering a distant point-source observed by a two-telescope interferometer. For simplicity, we use the semi-classical and scalar wave approximation (i.e., only a single polarization) for quantum mechanics here. The plane waves incident on the two telescopes can be described by

$$\phi_1 \propto \exp(ik\vec{x}_1 \cdot \vec{\alpha}) \exp(-i\omega t), \quad (1.26)$$

$$\phi_2 \propto \exp(ik\vec{x}_2 \cdot \vec{\alpha}) \exp(-i\omega t), \quad (1.27)$$

where $\vec{x}_2 - \vec{x}_1 = \vec{u}$ is the baseline of the interferometer and ω is the angular frequency of the wave, which is in the THz range for optical and infrared light. The resulting interference pattern is obtained by adding the two plane waves, that is

$$\phi = \phi_1 + \phi_2 \propto (1 + \exp(-ik\vec{u} \cdot \vec{\alpha})) \exp(-i\omega t), \quad (1.28)$$

whose intensity

$$I = \phi\bar{\phi} \propto 2(1 + \cos(k\vec{u} \cdot \vec{\alpha})) \quad (1.29)$$

is recorded by the interferometer, where the bar denotes complex conjugation. For an arbitrary source, one obtains

$$I(\vec{\alpha}) = \int I(\vec{\alpha}') d\vec{\alpha}' (1 + \text{Re}(V(\vec{u}) \exp(-ik\vec{u} \cdot \vec{\alpha}))), \quad (1.30)$$

so that

$$V(\vec{u}) = \frac{\int I(\vec{\alpha}') e^{-ik\vec{u} \cdot \vec{\alpha}'} d\vec{\alpha}'}{\int I(\vec{\alpha}') d\vec{\alpha}'} \quad (1.31)$$

is the normalized complex visibility function spatially filtered through the two-telescope interferometer.

Considering again the binary model (Equation 1.20), it can be shown that

$$\text{VIS2}_{\text{bin}} \propto 1 + f, \quad (1.32)$$

$$\text{T3}_{\text{bin}} \propto f, \quad (1.33)$$

for small relative companion fluxes $f \ll 1$, where VIS2_{bin} and T3_{bin} are the squared visibility amplitudes and the closure phases of the binary model, respectively (e.g., Kammerer et al., 2020). A faint companion is thus a small perturbation in the squared visibility amplitudes and closure phases, and the dynamic range of an interferometer is the smallest relative companion flux f at which this perturbation can be detected. In order to distinguish a small perturbation from noise and correctly determine its statistical significance, the consideration of the observable covariances (i.e., the correlated errors) instead of only the observable standard deviations (as it is done frequently in the community) is necessary, as will be shown in Chapter 5. Long-baseline interferometry with GRAVITY will then be used to characterize the reddest known sub-stellar companion HD 206893 B in Chapter 6.

1.2.2 Aperture masking interferometry

One caveat of long-baseline optical interferometry is the sparse uv-plane (or Fourier plane) coverage, which complicates the image reconstruction process. A technique that achieves relatively dense Fourier plane coverage while still exploiting the superior calibration capabilities of interferometric observables is aperture masking interferometry. This technique was first applied in the late 1990s (Baldwin et al., 1986; Baldwin & Warner, 1987), and eventually brought to the 10 m Keck I telescope by Tuthill et al. (2000b). The basic idea of aperture masking interferometry is to transform a single-dish telescope into a multi-aperture interferometer by placing a mask with several holes (subapertures) into the telescope's pupil plane (see upper panel of Figure 1.11). Each hole acts as an individual

aperture, so that the mask creates interference fringes on the detector (see middle panel of Figure 1.11). The spatial Fourier transform of these interference fringes yields the observed complex visibility $V(\vec{u})$, filtered by the spatial frequencies permitted through the aperture mask. This can be seen in the power spectrum of the observed image (see lower panel of Figure 1.11). As shown in Section 1.2, the spatial frequencies permitted through the mask can be obtained by computing the mask’s autocorrelation.

An important characteristic of an aperture mask is that it is non-redundant. This means that each baseline connecting two subapertures appears only once, so that each spatial frequency in the Fourier plane can be uniquely associated with the complex visibility measured between two subapertures in the pupil plane. Since the subapertures are finite in size, the sampling of the subapertures is essentially limited by the desire to obtain a dense, but non-redundant Fourier plane coverage. Non-redundancy is crucial because in the presence of atmospheric turbulence, different realizations of the same baseline in the pupil plane will have the same spatial frequency in the Fourier plane, but with different phase offsets, hence blurring the measured complex visibility and preventing an unambiguous phase measurement. If non-redundancy is given, though, then closure phases between aperture triplets can be formed. As in long-baseline interferometry, these closure phases are independent of pupil plane phase piston noise (e.g., Ireland, 2016).

Aperture masking interferometry is ideal to perform high-angular resolution imaging of bright targets, using closure phases in order to recover asymmetries in the source. Tuthill et al. (2000b) achieved a dynamic range better than 200:1 and used aperture masking interferometry to image dust nebula, envelopes, and disks around luminous stars (Tuthill et al., 2000a, 2001, 2002, 2006; Tuthill & Lloyd, 2007; Tuthill et al., 2008) using the Keck telescope. Similar to long-baseline interferometry, the technique could also be used to study stellar diameters (e.g., Ireland, 2002). Slightly later, Kraus & Ireland (2012) were able to detect point-like features at angular separations of only $\sim 70\text{--}100$ mas in the LkCa 15 transition disk, which they interpreted as signs for on-going planet formation. While Sallum et al. (2015) presented further aperture masking interferometry observations of the LkCa 15 system and detected H_α emission from these features with the Magellan adaptive optics system, it also became clear that high-angular resolution imaging is required to study planet formation in the nearest star-forming regions. Located at distances more than ~ 100 pc (de Zeeuw et al., 1999; Rizzuto et al., 2011), the tip of the giant planet distribution is at angular separations less than ~ 100 mas (Fernandes et al., 2019). Probing this parameter space among a large sample of young stars is required in order to detect a statistically relevant sample of young giant planets in the process of formation (Wallace & Ireland, 2019).

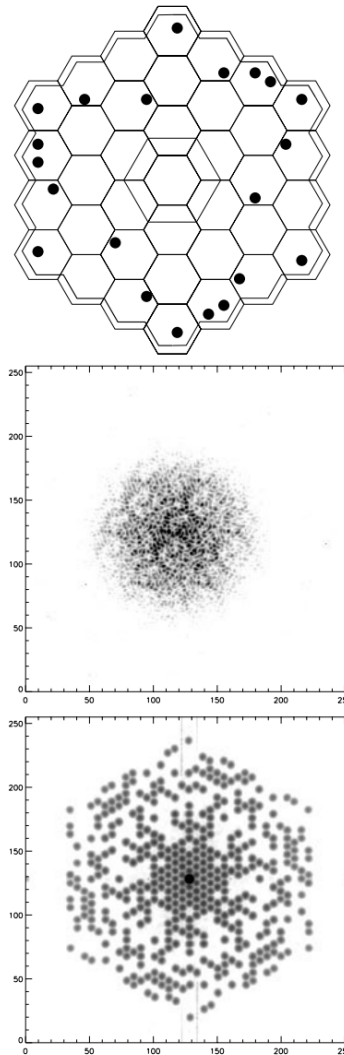


Figure 1.11: Pupil plane representation of the aperture mask at the Keck I telescope used by [Tuthill et al. \(2000b\)](#) and consisting of 21 individual subapertures (top). Interference fringes (i.e., PSF) created by the aperture mask on the detector (middle). Power spectrum of the PSF, showing the 210 unique spatial frequencies permitted through the aperture mask or, in other words, the mask’s autocorrelation (bottom).

1.2.3 Kernel phase interferometry

[Ireland \(2013\)](#) has shown that the dynamic range of aperture masking interferometry is essentially limited by higher-order phase errors. Therefore, since aperture masks block $\sim 80\text{--}90\%$ of the light, they are only suitable for high-contrast imaging around bright targets. A technique that enables studying fainter objects was

developed by [Martinache \(2010\)](#), who realized that under very good observing conditions (i.e., high Strehl), the phase information in the pupil plane is preserved and could be measured in the image Fourier transform (i.e., the Fourier plane), that is

$$\phi = \mathbf{R}^{-1} \cdot \mathbf{A} \cdot \varphi + \phi_{\text{OID}} + \mathcal{O}(\varphi^3), \quad (1.34)$$

where the full telescope pupil is discretized onto a dense grid of subapertures represented by the matrix \mathbf{A} , whose baselines have redundancies represented by the matrix \mathbf{R} , φ is the pupil plane phase, and ϕ_{OID} is the phase intrinsic to the observed source, that is the visibility phase of the object intensity distribution ([Martinache, 2010](#)). Moreover, if the higher-order pupil plane phase terms $\mathcal{O}(\varphi^3)$ are small, then multiplication of Equation 1.34 with the kernel \mathbf{K} of $\mathbf{R}^{-1} \cdot \mathbf{A}$ yields the kernel phase

$$\theta = \mathbf{K} \cdot \phi = \underbrace{\mathbf{K} \cdot \mathbf{R}^{-1} \cdot \mathbf{A} \cdot \varphi}_{=0} + \mathbf{K} \cdot \phi_{\text{OID}} = \theta_{\text{OID}} \quad (1.35)$$

([Martinache, 2010](#)). Such conditions are usually satisfied either from space or from the ground behind an (extreme) adaptive optics system. It has been noted that kernel phase is a generalization of closure phase to arbitrary pupil geometries ([Ireland, 2016](#)). While aperture masks are traditionally designed to be non-redundant, full pupil kernel phase interferometry results in a highly redundant Fourier plane. The technique is purely post-processing and can be applied to any full pupil images, and achieves superior PSF calibration capabilities by projecting the Fourier plane phase into a subspace (i.e., the kernel \mathbf{K} of $\mathbf{R}^{-1} \cdot \mathbf{A}$) which is free of pupil plane phase noise to second order ([Ireland, 2013](#)).

[Martinache \(2010\)](#) applied kernel phase interferometry to *Hubble Space Telescope* (HST) data and demonstrated high-precision astrometry of a 10:1 contrast binary star at a small angular separation (~ 90 mas), below the classical diffraction limit of the HST. The stable PSF of a space-based facility such as the HST is ideal for kernel phase observations calibrated by subtracting the kernel phase of a point-source reference from that of the science target. [Pope et al. \(2013\)](#) achieved the detection of five new brown dwarf companions, also in archival HST/NICMOS data. The first attempt to use kernel phase on a ground-based telescope was also made by [Pope et al. \(2016\)](#), who performed a benchmark experiment on the Palomar 200-inch telescope in order to compare kernel phase with aperture masking interferometry, PSF fitting, and bispectral analysis. They found that kernel phase interferometry, if combined with an adaptive optics system under good observing conditions, is a more efficient alternative to aperture masking interferometry, and opens up a new parameter space to be explored in high-resolution imaging of faint companions and circumstellar environments. To make kernel phase interferometry competitive for the detection of young giant planets from the ground, the technique will be refined with more sophisticated calibration strategies in Chapter 2 and observations at high-contrasts will be

demonstrated in Chapter 3. The first application of kernel phase interferometry to mid-infrared data will be demonstrated in Chapter 4.

Kernel phase imaging with VLT/NACO: high-contrast detection of new candidate low-mass stellar companions at the diffraction limit

This chapter was published as a peer-reviewed article in Monthly Notices of the Royal Astronomical Society, volume 486, pages 639–654. It was written by Jens Kammerer under the supervision of Michael J. Ireland and Frantz Martinache. Julien H. Girard is the PI of the archival VLT/NACO data set used in this chapter.

Jens Kammerer,¹ Michael J. Ireland,¹ Frantz Martinache² and Julien H. Girard^{3,4}

1. Research School of Astronomy & Astrophysics, Australian National University, ACT 2611, Australia
2. Laboratoire Lagrange, Université Côte d’Azur, Observatoire de la Côte d’Azur, CNRS, Parc Valrose, Bât. H. FIZEAU, 06108 Nice, France
3. Space Telescope Science Institute, 3700 San Martin Drive, Baltimore, MD 21218, USA
4. Université Grenoble Alpes, CNRS, IPAG, 38000 Grenoble, France

Preamble

In Chapter 1, it was discussed that the kernel phase technique has predominantly been used with space-based facilities before. In this chapter, it will be our goal to make this technique competitive for the detection of young giant exoplanets with ground-based facilities. Therefore, we will develop several improvements on the post-processing side and demonstrate these on an archival VLT/NACO data set of 38 nearby field stars. Firstly, looking at an archival data set is still interesting since we are going to explore a parameter space close to and below the classical diffraction-limit which has not been investigated before. Secondly, this large number of targets observed with a similar instrument setup enables us to perform self-calibration among the sample. In the end of this chapter, we will discuss our achieved detection limits in the context of directly imaging planetary-mass companions.

Abstract

Directly imaging exoplanets is challenging because quasi-static phase aberrations in the pupil plane (speckles) can mimic the signal of a companion at small angular separations. Kernel phase, which is a generalization of closure phase (known from sparse aperture masking), is independent of pupil plane phase noise to second order and allows for a robust calibration of full pupil, extreme adaptive optics observations. We applied kernel phase combined with a principal component based calibration process to a suitable but not optimal, high cadence, pupil stabilized L' band (3.8 μm) data set from the ESO archive. We detect eight low-mass companions, five of which were previously unknown, and two have angular separations of $\sim 0.8\text{--}1.2 \lambda/D$ (i.e. $\sim 80\text{--}110$ mas), demonstrating that kernel phase achieves a resolution below the classical diffraction limit of a telescope. While we reach a 5σ contrast limit of $\sim 1/100$ at such angular separations, we demonstrate that an optimized observing strategy with more diversity of PSF references (e.g. star-hopping sequences) would have led to a better calibration and even better performance. As such, kernel phase is a promising technique for achieving the best possible resolution with future space-based telescopes (e.g. JWST), which are limited by the mirror size rather than atmospheric turbulence, and with a dedicated calibration process also for extreme adaptive optics facilities from the ground.

2.1 Introduction

Direct imaging is vital for studying the outer regions of extrasolar systems which are inaccessible to transit observations and can only be revealed by decades-long, time consuming radial velocity surveys (e.g. Fischer et al., 2014). It has proven particularly successful in probing our understanding of the formation of gas giant planets (e.g. D’Angelo et al., 2010), being able to estimate their mass from their luminosity and age (e.g. Spiegel & Burrows, 2012) and resolve their orbit. Although the majority of detected companion candidates are arguably consistent with being emission or scattering from disk material (e.g. LkCa 15, Kraus & Ireland 2012, HD 100546, Quanz et al. 2013, HD 169142, Biller et al. 2014), the recent example of PDS 70 (Keppler et al., 2018) demonstrates that direct imaging of wide-separation but still solar-system scale planets is possible at relatively moderate contrasts in the vicinity of young stars. This is spurring an ongoing discussion about the nature of planet formation and the commonness of gas giant planets with large orbital distances (e.g. Bowler & Nielsen, 2018).

However, direct imaging operates at the resolution and sensitivity limit of the most powerful instruments today (e.g. Pepe et al., 2014), placing demanding requirements on the observing and the post-processing techniques which are used to uncover faint companions at high contrasts (e.g. angular differential imaging, Marois et al. 2006, point spread function subtraction, Lafrenière et al. 2007b, principal component analysis, Amara & Quanz 2012, Soummer et al. 2012). Detecting exoplanets from the ground using these techniques has only been made possible by the recent development of extreme adaptive optics systems (e.g. Milli et al., 2016) and is mainly limited by non-common path aberrations which are not sensed by the wavefront control system (e.g. Sauvage et al., 2007). These aberrations manifest themselves as quasi-static speckles on the detector images which can mimic the signal of a companion and place a strong constraint on the achievable contrast at small angular separations (e.g. Fitzgerald & Graham, 2006). Hence, directly imaging and studying the formation of gas giant planets on solar-system scales has been extremely challenging so far (e.g. Bowler, 2016) because the nearest star forming regions lie $\gtrsim 100$ pc away (e.g. Loinard et al., 2007) where such orbital distances correspond to angular separations of only $\lesssim 200$ mas.

In this paper, we explore the capabilities of the kernel phase technique (Martinache, 2010) for high-contrast imaging at the diffraction limit from the ground. This post-processing technique can be seen as refinement of sparse aperture masking and the closure phase technique (Tuthill et al., 2000b). By probing only certain linear combinations of the phase of the Fourier transformed detector images, kernel phase and sparse aperture masking allow for a robust calibration of the time-varying optical transfer function of the system and a significant mitigation of quasi-static speckles and achieve an angular resolution of $\lesssim 50$ mas in the near-infrared (i.e. the L’ band, Cheetham et al., 2016). This gives access to

objects on solar-system scales in the nearest star forming regions (i.e. projected separations of ~ 40 mas for a Jupiter analog in the Scorpius Centaurus OB association, [Preibisch & Mamajek 2008](#)) and has proven successful in directly imaging young exoplanets/disk features (e.g. [Kraus & Ireland, 2012](#)). The caveat of sparse aperture masking is that the mask blocks $\gtrsim 85$ % of the light (for VLT/NACO, [Tuthill et al., 2010](#)) and therefore significantly decreases the sensitivity and hence the contrast limit of the observations for relatively faint targets. However, kernel phase uses the light collected by the entire pupil and should perform better in the high Strehl regime and the bright limit (e.g. [Pope et al., 2016](#); [Sallum & Skemer, 2019](#)).

For sparse aperture masking, a mask is placed at the Lyot stop of an instrument in order to split the primary mirror into a discrete interferometric array of *real* sub-apertures (e.g. [Readhead et al., 1988](#)). In the Fourier transform of the detector image (hereafter referred to as Fourier plane), these sub-apertures map onto their auto-correlation (i.e. their spatial frequencies, [Ireland 2016](#)). The phase ϕ of each spatial frequency can be extracted and linearly combined in a way such that the resulting closure phase $\theta = \mathbf{K} \cdot \phi$ is independent of the pupil plane (or instrumental) phase φ to second order (i.e. terms of first and second order in φ are vanishing), where the matrix \mathbf{K} encodes this special linear combination (e.g. [Ireland, 2016](#)). For observations from the ground, the pupil plane phase φ is affected by noise from atmospheric seeing and non-common path aberrations which ultimately cause quasi-static speckles. Being more robust with respect to these systematic effects, sparse aperture masking achieves a superior angular resolution.

For full pupil kernel phase imaging, there is no mask and the entire primary mirror is discretized into an interferometric array of *virtual* sub-apertures. According to [Martinache \(2010\)](#), it is then convenient to define a transfer matrix \mathbf{A} which maps the baselines between each pair of *virtual* sub-apertures onto their corresponding spatial frequency. In the high Strehl regime, where the pupil plane phase φ can be linearized, we obtain the relationship

$$\phi = \mathbf{R}^{-1} \cdot \mathbf{A} \cdot \varphi + \phi_{\text{obj}} + \mathcal{O}(\varphi^3), \quad (2.1)$$

where \mathbf{R} is a diagonal matrix encoding the redundancy of the spatial frequencies (i.e. the baselines of the interferometric array) and ϕ_{obj} is the phase intrinsic to the observed object. Multiplication with the left kernel \mathbf{K} of $\mathbf{R}^{-1} \cdot \mathbf{A}$ yields

$$\theta = \mathbf{K} \cdot \phi \quad (2.2)$$

$$= \underbrace{\mathbf{K} \cdot \mathbf{R}^{-1} \cdot \mathbf{A}}_{=0} \cdot \varphi + \mathbf{K} \cdot \phi_{\text{obj}} + \mathcal{O}(\varphi^3) \quad (2.3)$$

$$= \theta_{\text{obj}} + \underbrace{\mathcal{O}(\varphi^3)}_{\approx 0}, \quad (2.4)$$

hence the kernel θ of the measured Fourier plane phase ϕ directly represents the kernel θ_{obj} of the phase intrinsic to the observed object ϕ_{obj} , at least in the high

Strehl regime (where $\mathcal{O}(\varphi^3)$ is negligible). This is why frame selection based on the Strehl ratio is essential. Note that the kernel phase is a generalization of the closure phase to the case of redundant apertures.

For observations from space, which do not suffer from atmospheric seeing, kernel phase has proven to be successful in resolving close companions at the diffraction limit (Martinache, 2010; Pope et al., 2013). It is our goal to determine if, under good observing conditions, kernel phase also is a competitive alternative to sparse aperture masking from the ground.

2.2 Methods

2.2.1 Data reduction

A basic direct imaging data reduction (such as dark, flat, background subtraction and bad pixel correction) is also essential for the kernel phase technique (e.g. Sallum & Eisner, 2017). For this purpose, we developed our own data reduction pipeline¹ which can be fed the raw data with their associated raw calibrators from the VLT/NACO archive². Our data reduction pipeline performs the following steps which are described in more detail in the following sections:

1. Linearize the raw frames.
2. Compute master darks and their bad pixel maps.
3. Compute master flats and their bad pixel maps.
4. Flag saturated pixels.
5. Apply dark, flat, background and bad pixel corrections.
6. Perform a dither subtraction.
7. Reconstruct saturated pixels.
8. Select frames with sufficient Strehl ratio.

In principle, the standard NACO pipeline³ would be adequate for the dark, flat, and sky subtraction steps, but additional steps like detector linearization and bad pixel correction in the Fourier plane are not performed. However, these additional steps are crucial to avoid corruption of the image Fourier phase and therefore critical to our data analysis methods.

¹<https://github.com/kammerje/PyConica>

²<http://archive.eso.org/wdb/wdb/eso/naco/form>

³https://www.eso.org/sci/facilities/paranal/decommissioned/naco/doc/VLT-MAN-ESO-14200-4038_v0.pdf

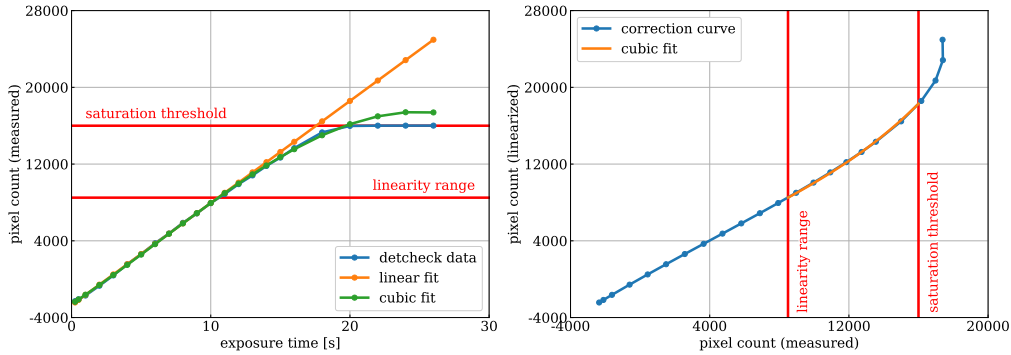


Figure 2.1: Left panel: median pixel count in dependence of the integration time t for uncorrelated high well depth mode from the detector monitoring (blue curve) and the linear (orange curve) and cubic (green curve) polynomials $f(t)$ and $g(t)$ which we fit to it. Right panel: correction curve (blue) $f(g)$ and the cubic polynomial h (orange curve) which we fit to it and use for linearizing all pixels with measured counts between 8500 and 16000. In both panels, the solid red lines mark the end of the linear regime and the saturation threshold. Note that very low (i.e. negative) pixel counts occur due to the use of a narrow-band filter ($\Delta\lambda = 0.018 \mu\text{m}$) for the detector monitoring, whereas the L' science frames are taken with a wide-band filter ($\Delta\lambda = 0.62 \mu\text{m}$).

Detector linearization correction

Like most photon counting devices, NACO’s infrared detector CONICA suffers from a non-linear response when the pixel counts approach the saturation threshold (16400 counts for uncorrelated high well depth mode⁴ according to the NACO Quality Control and Data Processing⁵, with a more conservative 16000 counts used in our analysis). As kernel phase is an interferometric technique for which the fringes are coded spatially on the detector, it is very important to characterize the pixel to pixel response. Moreover, many of the data cubes which we analyze in Section 2.3 feature saturated point spread functions (PSFs) which we want to correct for non-linearity before reconstructing their core (cf. Section 2.2.1).

In order to compute the detector linearization correction we download all frames of type “FLAT, LAMP, DETCHECK” and uncorrelated high well depth mode from 2016 March 23 and 2016 September 24 (which are closest in time to the observation of the earliest and the latest data cube which we analyze) from the VLT/NACO archive. We sort them by integration time and compute the median pixel count over all frames for each individual integration time (masking out the broken stripes in the lower left quadrant of CONICA). Then, we plot the

⁴This is the standard imaging mode in the L' band ($3.8 \mu\text{m}$) and all data cubes which we analyze have been taken in this mode.

⁵https://www.eso.org/observing/dfo/quality/NACO/qc/detmon_qc1.html

median pixel count in dependence of the integration time t , fit a linear polynomial $f(t)$ to all data points with less than 8500 counts (end of the linear regime for uncorrelated high well depth mode) and a cubic polynomial $g(t)$ to all data points with less than 16000 counts (saturation threshold, cf. left panel of Figure 2.1). We linearize the detector using a continuously differentiable piecewise polynomial approach h to the correction curve $f(g)$ with a linear function up to 8500 counts and a cubic polynomial between 8500 and 16000 counts (cf. right panel of Figure 2.1).

Master darks and master flats

For each observation block (OB) we compute master darks from the associated dark frames as the median of all dark frames with a unique set of size and exposure time. Then we compute a bad pixel map for each master dark based on the frame by frame median and variance of each pixel's count. Therefore, we first compute two frames:

1. The absolute difference between the master dark and the median filtered master dark.
2. The absolute of the median subtracted variance dark.

Then, we identify bad pixels in each of these frames based on their difference to the median of these frames. For frame (i) we classify pixels which are above 10 times the median as bad, for frame (ii) pixels which are above 75 times the median. Note that these thresholds were identified empirically. From the median subtracted dark frames, we estimate the readout noise as the mean over each frame's pixel count standard deviation.

We proceed similar for the flat frames, but also group them by filter as well as size and exposure time, subtract a master dark with matching properties (i.e. similar size and exposure time) from each master flat and normalize it by its median pixel count. **For the flat frames, thresholds of 7.5 times the median for frame (i) and 10 times the median for frame (ii) were applied.**

Saturated pixels

The data cubes which we analyze in Section 2.3 consist of 100 frames of 0.2 s exposure. For each data cube, we reject the first frame (which we find to consistently suffer from a bias), so that there are 99 frames left. Note that NACO appends the median of all 100 frames at the end of each data cube which is also rejected here. Before proceeding, we also flag the saturated pixels in each frame which are all pixels with more than $h(16000)$ counts.

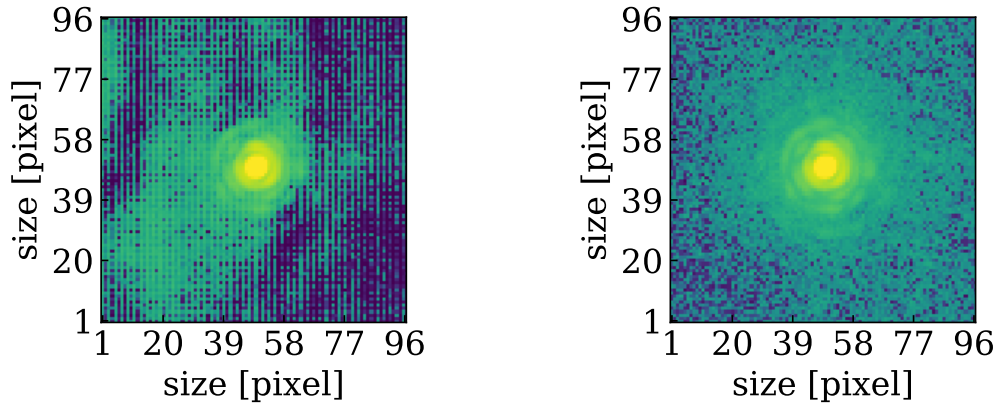


Figure 2.2: Left panel: median frame of a data cube of HIP 47425 after dark, flat and a simple background subtraction. The pixel counts are scaled by an arcsinh stretch so that both the PSF and the background are visible in the image. Right panel: same median frame after performing the dither subtraction described in Section 2.2.1. This second step is essential to remove residual systematic noise from the detector which can be seen as grid-like structure in the left panel. Note that the two panels have the same color scale.

Dark, flat, background and bad pixel correction

We clean each frame of a data cube individually by subtracting a master dark with matching properties (i.e. similar size and exposure time), dividing it by a master flat with matching properties (i.e. similar size, exposure time and filter), correcting bad pixels (which are bad pixels from the master dark or the master flat) with a median filter of size five pixels and performing a simple background subtraction by subtracting the median pixel count of the frame from each pixel. **The average fraction of bad pixels is 0.28%.** A typical result is shown in the left panel of Figure 2.2, where residual systematic noise (mainly from the detector) is still clearly visible.

Dither subtraction

In order to mitigate the residual systematic noise from the detector and the sky background we perform a dither subtraction. After cleaning all data cubes within one OB, we find for each data cube (which we will here call data cube A) the data cube B with the target furthest away (on the detector) and subtract its median frame from each frame of data cube A. The new bad and saturated pixel maps are then the logical sums of those from both involved data cubes. After this step the residual noise appears like Gaussian random noise as is shown in the right panel of Figure 2.2.

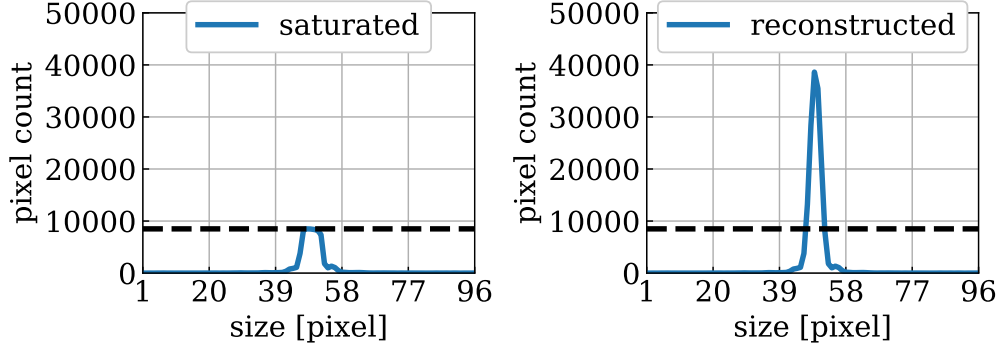


Figure 2.3: Left panel: mean over a horizontal and a vertical cross-section through the center of the median frame shown in the right panel of Figure 2.2. Right panel: same cross-section, but after reconstructing bad and saturated pixels as described in Section 2.2.1. The dashed black line marks the maximum of the cross-section in the left panel in order to illustrate the reconstruction of the peak in the PSF core.

Our typical performance is a pixel count standard deviation of $\sim 36 = 4.4 + (158/s \cdot 0.2 \text{ s})$ outside of $10 \lambda/D$ from the center of the PSF in 0.2 s exposure, where 4.4 is the detector readout noise, λ is the observing wavelength (3.8 μm for the L' band) and D is the diameter of the primary mirror (8.2 m for the VLT).

Reconstruction of saturated pixels

Our reconstruction of saturated pixels is based on an algorithm described in Section 2.5 of Ireland (2013). This technique also identifies and corrects residual bad pixels, with no more than 10 additional bad pixels corrected in a typical frame. First, we crop all frames to a size of 96 by 96 pixels ($\sim 2.6 \text{ arcsec}^2$) centered on the target. Then, we correct bad and saturated pixels for each frame separately by minimizing the Fourier plane power $|f_Z|$ outside the region of support Z permitted by the pupil geometry. Let \mathbf{B}_Z be the matrix which maps the bad and saturated pixel values x onto the Fourier plane domain Z , then

$$f_Z = \mathbf{B}_Z \cdot b + \epsilon_Z, \quad (2.5)$$

where b are the corrections to the bad and saturated pixel values x (i.e. the corrected pixel values are $x - b$) and ϵ_Z is remaining Fourier plane noise. We solve for b using the Moore-Penrose pseudo-inverse of \mathbf{B}_Z , i.e.

$$b = \mathbf{B}_Z^+ \cdot f_Z = (\mathbf{B}_Z^* \cdot \mathbf{B}_Z)^{-1} \cdot \mathbf{B}_Z^* \cdot f_Z. \quad (2.6)$$

Since a broad-band filter was used for the observations, but we use a monochromatic central filter wavelength in our analysis and also blur the edge of the pupil

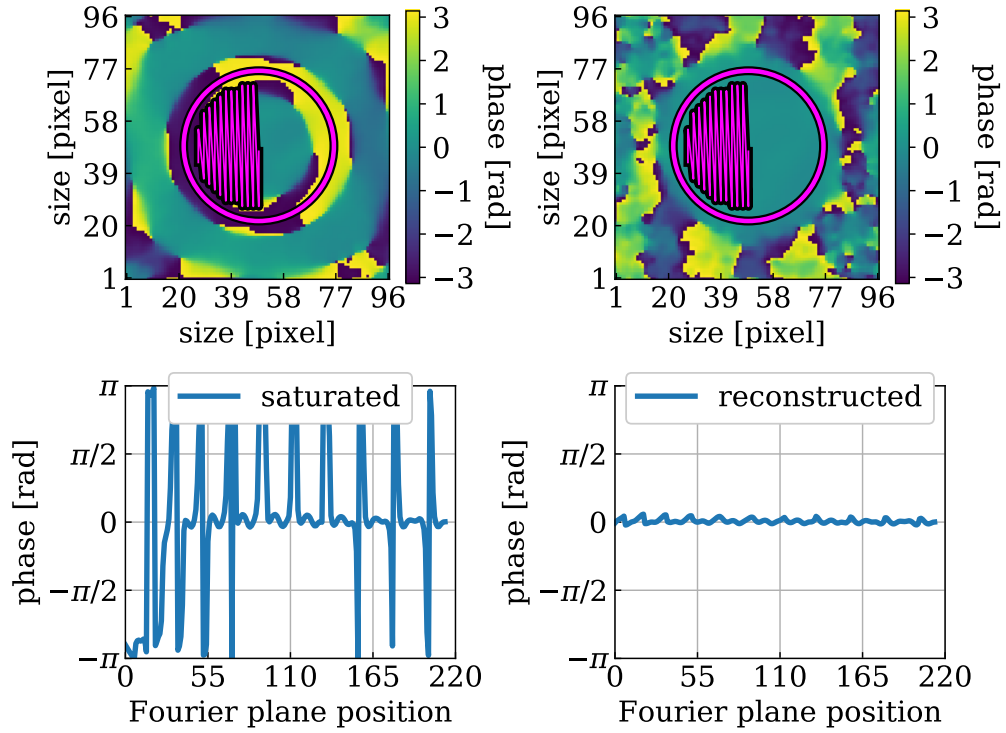


Figure 2.4: Left panels: Fourier plane phase of the median frame shown in the right panel of Figure 2.2 (top). The phase is flat in the center, but the cutoff spatial frequency is smaller than the region of support permitted by the pupil geometry (magenta circle). Median Fourier plane phase at the spatial frequencies of our pupil model (bottom). Right panels: same as in the left panels, but after reconstructing bad and saturated pixels as described in Section 2.2.1. In both upper panels, the magenta line traces out the spatial frequencies of our pupil model (from left to right) in order to illustrate how the patterns observed in the lower panels are obtained.

through the use of a windowing function, we use a slightly larger pupil diameter to define this region Z of 10 m here. In fact, the only important thing for recovering the Fourier plane phase is that the Fourier plane power *outside* the region of support permitted by the pupil geometry is minimized, so using a larger pupil diameter just assures this in case of low quality data and is a conservative choice, especially in the case of our data which is far from the Nyquist sampling criterion.

Sometimes, the remaining Fourier plane noise ϵ_Z can be significant, which is why we repeat the entire correction process up to 15 times for each frame. After each iteration, we look for remaining bad pixels by:

1. Computing the Fourier transform of the corrected frame from the previous iteration.
2. Windowing this frame by the Fourier domain Z .
3. Computing the inverse Fourier transform of this frame.
4. Identifying remaining bad pixels in this frame based on their difference to the median filtered frame.

If no remaining bad pixels are identified, we terminate the iteration.

A cross-section of a saturated PSF before and after performing the reconstruction is shown in Figure 2.3. Obviously, this reconstruction cannot reveal any structure or companions hidden behind saturated pixels, but it allows us to perform our kernel phase analysis on saturated data cubes which would otherwise suffer from high Fourier plane phase noise (cf. Figure 2.4). Please note that a method from the class of least squares spectral analysis techniques (i.e. image plane fringe fitting) may be more robust in dealing with bad pixels, but would require the simultaneous fitting of all Fourier plane phases and amplitudes and is therefore beyond the scope of this paper, although it is a promising approach for future work.

Frame selection

As explained in the Introduction, a high Strehl ratio is essential for the kernel phase technique in order for the mathematical framework (i.e. the linearization of the Fourier plane phase, cf. Equation 2.1) to be valid. Therefore, we select frames with sufficient Strehl ratio based on their peak pixel count. For each data cube, we first compute the median peak count of the 10% best frames. Then, we reject all frames with a peak count below 75% of this value. Using this dynamic threshold is better than simply rejecting a fixed fraction of the frames (e.g. Law et al., 2006) because it can correctly account for a sudden drop in the Strehl ratio like shown in Figure 2.5. Note that we consider the peak pixel count after performing the PSF reconstruction (cf Section 2.2.1) here.

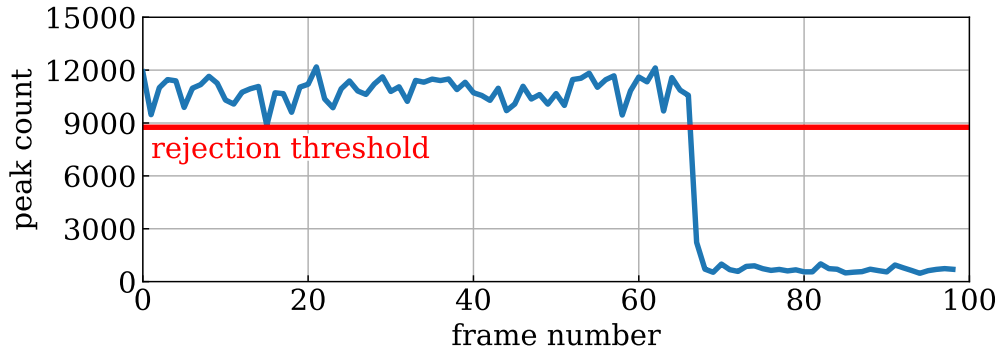


Figure 2.5: Peak count for all 99 frames of a data cube of HIP 116258. The horizontal red line marks the rejection threshold computed according to Section 2.2.1. Around frame 70 the observing conditions suddenly become worse and a clear drop in the peak count can be observed.

2.2.2 Kernel phase extraction

VLT pupil model

In order to extract the kernel phase from VLT/NACO data we first need to construct a model for the VLT pupil (i.e. split the primary mirror into an interferometric array of *virtual* sub-apertures). We sample 140 *virtual* sub-apertures on a square grid with a pupil plane spacing of 0.6 m, which is approximately half the Nyquist sampling of $\lambda/\alpha \approx 0.3$ m, where $\lambda = 3.8 \mu\text{m}$ is the observing wavelength and $\alpha = 2.610$ arcsec is the image size (96 pixels). Our VLT pupil model is shown in the left panel of Figure 2.6 and based on an 8.2 m primary mirror with a 1.2 m central obscuration. Another advantage of kernel phase over sparse aperture masking is the dense Fourier plane coverage which is shown in the right panel of Figure 2.6.

XARA

The extraction of the Fourier plane phase and the computation of the kernel phase relies on a python package called XARA⁶ (eXtreme Angular Resolution Astronomy, Martinache, 2010, 2013). XARA has been designed to process data produced by multiple instruments assuming that the images comply to the kernel phase analysis requirements of proper sampling, high-Strehl (boosted by our frame selection procedure described in Section 2.2.1), and non-saturation (restored by the procedure described in Section 2.2.1). The discrete achromatic representation of the VLT aperture (i.e. our pupil model) is used by XARA to

⁶<https://github.com/fmartinache/xara>

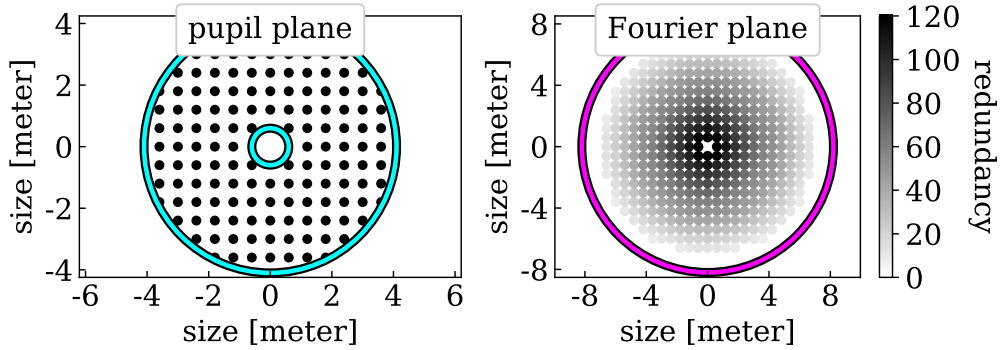


Figure 2.6: Left panel: our VLT pupil model consisting of 140 *virtual* sub-apertures sampled on a square grid with a pupil plane spacing of 0.6 m. The cyan circles show the size of the primary mirror and the central obscuration. Right panel: Fourier plane coverage of the same pupil model. The magenta circle shows the region of support permitted by the pupil geometry in the left panel. Since the Fourier transform is symmetric we only use the phase measured in one half-plane. Note that only these Fourier plane positions within 7.0 m from the origin (i.e. these which do not suffer from low power, cf. Section 2.2.2) are shown.

compute the phase transfer matrix \mathbf{A} and the associated left kernel operator \mathbf{K} via a singular value decomposition of \mathbf{A} .

With the added knowledge of the detector pixel scale and the observing wavelength, the discrete model is scaled so that the Fourier plane phase at the expected (u, v) coordinates can be extracted by a discrete Fourier transform. For the small aberration hypothesis to remain valid, the data must be properly centered prior to the Fourier transform. Failure to do so will leave a residual Fourier plane phase ramp that can wrap and lead to meaningless kernel phases (cf. left panels of Figure 2.7). XARA offers several centering algorithms. It is crucial to carefully choose from the available options depending on the requirements coming from the data. For our extensive ground-based data set for example, we find that minimizing directly the Fourier plane phase which is extracted by XARA **using a least squares optimization routine** is most robust and the offered sub-pixel re-centering is very valuable (cf. right panels of Figure 2.7) due to an increased level of pupil plane phase noise from the atmosphere and the bright background (if compared to space-borne data). **We have therefore used this centering algorithm for the entire NACO data presented in this work.**

Moreover, virtual baselines near the outer edge of the Fourier coverage suffer from low power as they are only supported by very few baselines, i.e. have small redundancy. The phase measured for these baselines is systematically noisier and needs to be excluded from the model to prevent the noise to propagate into the estimation of all kernel phases. This can be achieved using the baseline filtering

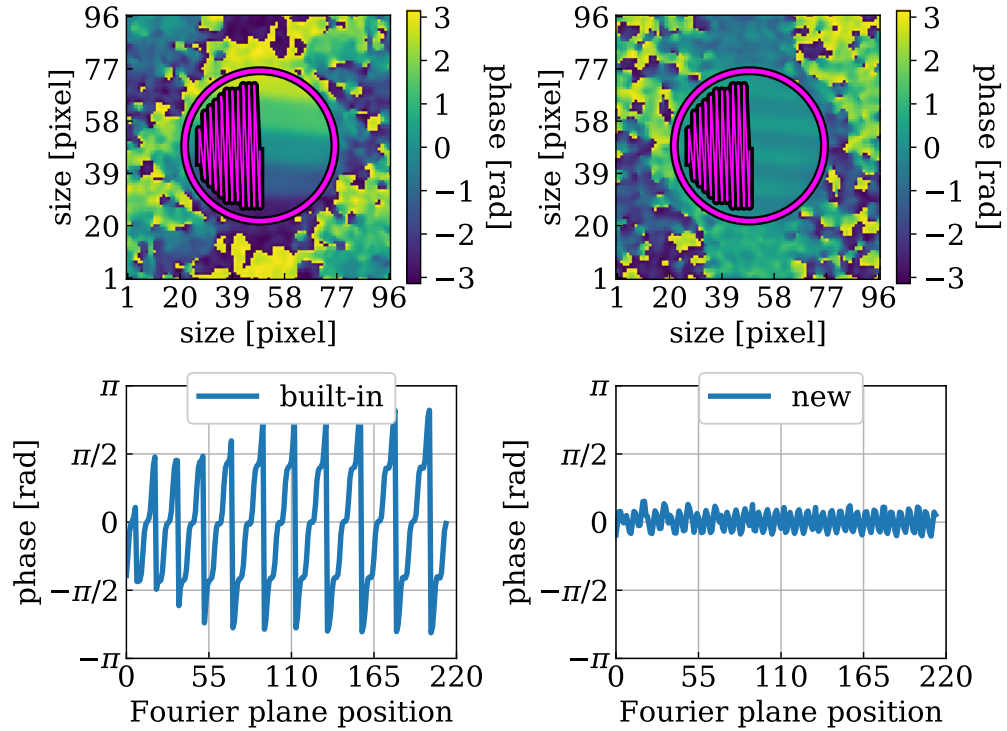


Figure 2.7: Left panels: Fourier plane phase of the median frame of a data cube of TYC 6849 1795 1 (resolved and bright binary) after imperfect re-centering of the frames (top). The phase is flat in the center, but there is an overall phase ramp from bottom to top caused by the resolved and bright companion. Median Fourier plane phase at the spatial frequencies of our pupil model (bottom). Right panels: same as in the left panels, but after proper re-centering of the frames. The residual Fourier plane phase is of considerably reduced amplitude and can be properly assembled to form meaningful kernel phases. The magenta circles and lines represent the same as in Figure 2.4.

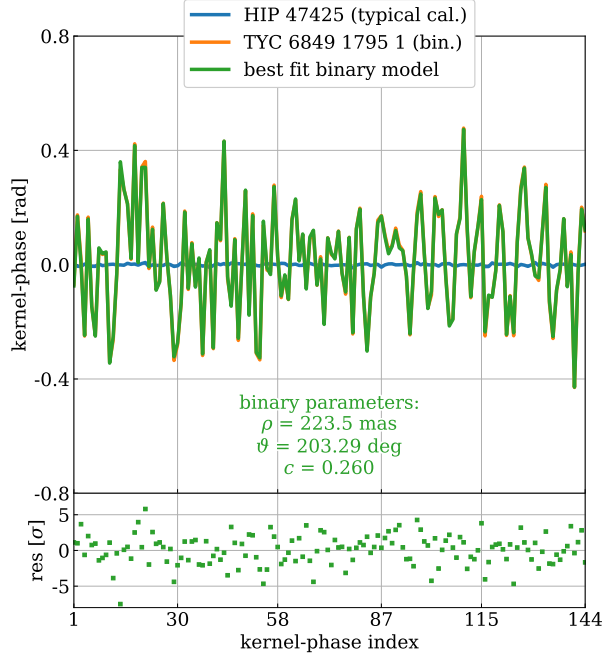


Figure 2.8: Measured mean kernel phase $\bar{\theta}$ over all data cubes of HIP 47425 (typical calibrator) and TYC 6849 1795 1 (resolved and bright binary) as well as of its best fit binary model $\theta_{\text{bin}} = \mathbf{K} \cdot \phi_{\text{bin}}$ (cf. Section 2.2.4). Data and model agree very well, so that the green curve overlaps with the orange curve. Note that we normalize each kernel phase by the norm of its corresponding row of \mathbf{K} and that the raw binary parameters reported here are not corrected for the windowing. **The lower panel shows the residuals between the TYC 6849 1795 1 data and the best fit binary model.**

option implemented in XARA. In our case, baselines of length greater than 7.0 m and the corresponding rows of \mathbf{A} are eliminated prior to the computation of \mathbf{K} . Some of the theoretically available kernel phases are lost but the remaining kernel phases can nevertheless be used just like for the complete model.

Finally, to limit the impact of readout noise in regions of the image where little signal is present, frames are windowed by a super-Gaussian ($g(r) = \exp -(r/r_0)^4$) with a radius $r_0 = 25$ pixels, effectively limiting our field of view to ~ 1000 mas. Note that Section 2.3.4 will further comment on the effect of this window and how it can affect contrast estimates for detections at large separations.

Kernel phase uncertainties

For estimating the uncertainties, we compute the kernel phase covariance Σ_{θ} for each frame \mathbf{d} from its photon count variance $\Sigma_{\mathbf{d}} = g \cdot \mathbf{w}^2 \cdot (\mathbf{d} + \mathbf{b})$ in units of

(photo-electrons)², where g is the detector gain ($g = 9.8$ for uncorrelated high well depth mode), \mathbf{w} is the super-Gaussian window, \mathbf{d} is the cleaned and re-centered frame and \mathbf{b} is its background (from the simple background subtraction, cf. Section 2.2.1). Therefore, we first need to find a linear operator \mathbf{B} which maps each frame $g \cdot \mathbf{w} \cdot \mathbf{d}$ in units of photo-electrons to its kernel phase θ . The linear discrete Fourier transform \mathbf{F} and the kernel \mathbf{K} of the pupil model $\mathbf{R}^{-1} \cdot \mathbf{A}$ are already linear operators, and the Fourier plane phase $\phi(z)$ (of a complex number z) can be approximated as $\text{Im}(z)/|z|$ for small angles. Hence, we compute

$$\mathbf{B} = \mathbf{K} \cdot \frac{\text{Im}(\mathbf{F})}{|\mathbf{F} \cdot g \cdot \mathbf{w} \cdot \mathbf{d}|}. \quad (2.7)$$

Note that $\mathbf{B} \cdot g \cdot \mathbf{w} \cdot \mathbf{d}$ would be a small-angle approximation for the kernel phase. This approximation remains valid as long as $\arctan(\phi) \approx \phi$, which holds for $\phi < 0.5$ rad which is the case for all of our data, including the resolved and bright binary shown in Figure 2.7. Then, we obtain an estimate for the kernel phase covariance by propagating the photon count variance according to

$$\Sigma_{\theta} = \mathbf{B} \cdot \Sigma_d \cdot \mathbf{B}^T. \quad (2.8)$$

Now, we have a kernel phase θ and a kernel phase covariance Σ_{θ} for each frame. In order to save computation time for the model fitting (cf. Section 2.2.4) we compute a weighted mean $\bar{\theta}$ of the kernel phase for each data cube. Therefore, we first compute the average kernel phase covariance $\bar{\Sigma}_{\theta}$ over all frames \mathbf{d}_i of a data cube via

$$\bar{\Sigma}_{\theta} = \left(\sum_i \Sigma_{\theta,i}^{-1} \right)^{-1}, \quad (2.9)$$

and then the weighted mean $\bar{\theta}$ of the kernel phase (cf. Figure 2.8) via

$$\bar{\theta} = \bar{\Sigma}_{\theta} \cdot \sum_i \Sigma_{\theta,i}^{-1} \cdot \theta_i. \quad (2.10)$$

For the rest of this paper, we omit the bar for better readability, i.e.

$$\bar{\theta} \rightarrow \theta, \quad (2.11)$$

$$\bar{\Sigma}_{\theta} \rightarrow \Sigma_{\theta}. \quad (2.12)$$

Note that this kernel phase covariance model includes the contribution of shot noise only. Any residual calibration errors not taken into account in the following section are therefore expected to increase the reduced χ^2 of any model fitting, potentially to much more than 1.0 in the case of high signal-to-noise data with highly imperfect calibration.

2.2.3 Kernel phase calibration

Under perfect conditions the closure phase of a point-symmetric source, such as an unresolved star, is zero (e.g. Monnier, 2007). The same holds for the kernel phase, which is a generalization of the closure phase (e.g. Ireland, 2016). Practically however, one is limited by systematic errors caused by third order phase residuals (e.g. Ireland, 2013) and even point-symmetric sources have non-zero kernel phase.

For this reason, calibration is of fundamental importance when analyzing interferometric measurables (like closure or kernel phase). The systematic errors are expected to be quasi-static (e.g. Ireland, 2013), i.e. slowly varying with time, and caused by mechanical or thermal drifts of the instrument on timescales of minutes to hours (e.g. Martinez et al., 2013). Hence, the kernel phase of a well-known point source measured close in time to that of the science target can serve as a calibrator. The simplest calibration technique would be to subtract the kernel phase of a well-known point source from that of the science target. This technique was for example used successfully in Martinache (2010), but here we want to go beyond this approach.

We use principal component analysis in the framework of a Karhunen-Loève decomposition (Soummer et al., 2012; Pueyo, 2016) in order to subtract the statistically most significant phase residuals of the calibrator kernel phase from that of the science target. Note that the following technique is new, but very similar to the POISE observables in Ireland (2013). We start by computing the covariance matrix \mathbf{E}_{RR} of the kernel phase $\theta_{\text{cal},i}$ of all calibrator data cubes i via

$$\mathbf{E}_{\text{RR},(i,j)} = \theta_{\text{cal},i}^T \cdot \theta_{\text{cal},j}. \quad (2.13)$$

Then, we compute an eigendecomposition of this matrix in order to obtain its sorted (in descending order) eigenvalues w_k and eigenvectors v_k . Finally, we compute the Karhunen-Loève transform \mathbf{Z} of shape (number of kernel phases, number of calibrator data cubes) via

$$\mathbf{Z}_{(n,k)} = \frac{1}{\sqrt{w_k}} \sum_p v_k^p \cdot \theta_{\text{cal},p}^n, \quad (2.14)$$

where v_k^p is the p -th component of the k -th eigenvector of \mathbf{E}_{RR} and $\theta_{\text{cal},p}^n$ is the n -th kernel phase of the p -th calibrator data cube.

From the Karhunen-Loève transform \mathbf{Z} we obtain a projection matrix \mathbf{P} via

$$\mathbf{P} = \mathbf{I} - \mathbf{Z}' \cdot \mathbf{Z}'^T, \quad (2.15)$$

where \mathbf{I} is the identity matrix and \mathbf{Z}' is obtained from the first K_{klip} columns of \mathbf{Z} . K_{klip} is an integer representing the order of the correction, i.e. how many eigencomponents of the calibrator kernel phase should be corrected for. The projection matrix \mathbf{P} is of shape (number of kernel phases, number of kernel phases),

but it has K_{klip} zero eigenvalues by construction. In order to properly represent the dimensions we compute another eigendecomposition of \mathbf{P} and obtain a new projection matrix \mathbf{P}' , whose columns are those eigenvectors of \mathbf{P} which correspond to non-zero eigenvalues. The projection matrix \mathbf{P}' is of shape (number of “good” kernel phases, number of kernel phases), where “good” means statistically independent of systematic errors, and can be used to project the measured kernel phase θ and its covariance Σ_θ into a sub-space of dimension (number of “good” kernel phases), which is more robust with respect to quasi-static errors, via

$$\theta' = \mathbf{P}' \cdot \theta, \quad (2.16)$$

$$\Sigma'_\theta = \mathbf{P}' \cdot \Sigma_\theta \cdot \mathbf{P}'^T. \quad (2.17)$$

For the rest of this paper, we omit the prime for better readability, i.e.

$$\theta' \rightarrow \theta, \quad (2.18)$$

$$\Sigma'_\theta \rightarrow \Sigma_\theta. \quad (2.19)$$

2.2.4 Model fitting

From Equations 2.2–2.4 it becomes clear that the measured kernel phase θ directly represents the kernel phase intrinsic to the observed object θ_{obj} . Hence, we can infer information about the spatial structure of the observed object by fitting models for $\theta_{\text{obj}} = \mathbf{K} \cdot \phi_{\text{obj}}$ to θ .

Binary model

In order to search for companion candidates we use the binary model

$$r_{\text{bin}} \cdot e^{i\phi_{\text{bin}}} = 1 + c \cdot \exp\left(-2\pi i \cdot \left(\frac{\Delta_{\text{RA}} \cdot u}{\lambda} + \frac{\Delta_{\text{DEC}} \cdot v}{\lambda}\right)\right), \quad (2.20)$$

where c is the contrast ratio between secondary and primary, u and v are the coordinates of the sampled Fourier plane positions (i.e. the spatial frequencies of the pupil model), λ is the observing wavelength and

$$\Delta_{\text{RA}} = -\rho \cdot \sin(\vartheta - \vartheta_0), \quad (2.21)$$

$$\Delta_{\text{DEC}} = \rho \cdot \cos(\vartheta - \vartheta_0), \quad (2.22)$$

where ρ is the angular separation between primary and secondary, ϑ is the position angle of the secondary with respect to the primary and ϑ_0 is the detector position angle during the observation. Figure 2.8 shows the best fit binary model for the measured kernel phase of TYC 6849 1795 1 (resolved and bright binary).

Uncertainties from photon noise

Using the kernel phase covariance Σ_θ estimated from photon noise according to Section 2.2.2 we compute the best fit contrast c_{fit} and its uncertainty $\sigma_{c_{\text{fit}}}$ for the binary model $\theta_{\text{bin}} = \mathbf{K} \cdot \phi_{\text{bin}}$ on each position of a discrete 500×500 mas square grid with spacing 13.595 mas (which is half the detector pixel scale of CONICA). In some cases, where we suspect a companion candidate at a larger angular separation, we also extend the grid to 1000×1000 mas.

In the high-contrast regime (where $c \ll 1$), the phase ϕ_{bin} is approximately proportional to the contrast c of the binary model, so is its kernel phase θ_{bin} (because \mathbf{K} is a linear operator). Hence, the χ^2 of the binary model χ_{bin}^2 can be approximated as

$$\chi_{\text{bin}}^2 = (\Theta - c \cdot \Theta_{\text{bin,ref}})^T \cdot \Sigma_\Theta^{-1} \cdot (\Theta - c \cdot \Theta_{\text{bin,ref}}), \quad (2.23)$$

where Θ and $\Theta_{\text{bin,ref}}$ are vertical stacks of the kernel phase θ_i and the reference binary model $\theta_{\text{bin,ref},i}$ of each data cube i and Σ_Θ^{-1} is a block-diagonal matrix whose diagonal elements are the inverse kernel phase covariances $\Sigma_{\theta,i}^{-1}$ of each data cube i , i.e.

$$\Theta = \begin{pmatrix} \theta_1 \\ \theta_2 \\ \vdots \end{pmatrix}, \quad \Sigma_\Theta^{-1} = \begin{pmatrix} \Sigma_{\theta,1}^{-1} & 0 & \cdots \\ 0 & \Sigma_{\theta,2}^{-1} & \cdots \\ \vdots & \vdots & \ddots \end{pmatrix}. \quad (2.24)$$

The reference binary model $\theta_{\text{bin,ref}}$ is the binary model θ_{bin} evaluated for and normalized by a reference contrast $c_{\text{ref}} = 0.001$, i.e.

$$\theta_{\text{bin,ref}} = \frac{\theta_{\text{bin}}(c = c_{\text{ref}})}{c_{\text{ref}}}. \quad (2.25)$$

Finally, we obtain the log-likelihood $\ln L$ for the binary model θ_{bin} as

$$\ln L = -\frac{1}{2} \chi_{\text{bin}}^2. \quad (2.26)$$

The best fit contrast c_{fit} for the binary model θ_{bin} is then obtained by maximizing $\ln L$ for each grid position, i.e.

$$\left. \frac{\partial}{\partial c} \ln L \right|_{c_{\text{fit}}} = 0, \quad (2.27)$$

$$\Rightarrow c_{\text{fit}} = \frac{\Theta_{\text{bin,ref}}^T \cdot \Sigma_\Theta^{-1} \cdot \Theta}{\Theta_{\text{bin,ref}}^T \cdot \Sigma_\Theta^{-1} \cdot \Theta_{\text{bin,ref}}}, \quad (2.28)$$

and its uncertainty is the square root of its variance, i.e.

$$\sigma_{c_{\text{fit}}} = \frac{1}{\sqrt{\Theta_{\text{bin,ref}}^T \cdot \Sigma_\Theta^{-1} \cdot \Theta_{\text{bin,ref}}}}. \quad (2.29)$$

Finally, the detection significance based on photon noise SNR_{ph} is computed for each grid position as

$$\text{SNR}_{\text{ph}} = \frac{c_{\text{fit}}}{\sigma_{\text{ph}}} = \frac{c_{\text{fit}}}{\sigma_{c_{\text{fit}}} \cdot \sqrt{\chi_{\text{r,bin,min}}^2}}, \quad (2.30)$$

where we scale the uncertainty of the best fit contrast $\sigma_{c_{\text{fit}}}$ by the square root of the minimal reduced χ^2 of the binary model of the entire grid ($\chi_{\text{r,bin,min}}^2$). Assuming that kernel phase is proportional to contrast, this is equivalent to scaling the kernel phase covariance Σ_{θ} so that the minimal reduced χ^2 is 1.0. This step is necessary because kernel phase is still affected by third (or higher) order pupil plane phase noise (cf. Equations 2.2–2.4), so that the uncertainties from photon noise $\sigma_{c_{\text{fit}}}$ significantly underestimate the true errors. Note that there can be various sources of higher order phase noise **such as temporal phase errors from uncorrected atmospheric turbulence, flat-field calibration errors, and photon, background, and readout noise** (e.g. Ireland, 2013), but studying those in detail is beyond the scope of this paper.

The final parameters p_{fit} for the best fit binary model are then obtained from a least squares search which maximizes the log-likelihood $\ln L$ of the binary model under varying angular separation, position angle and contrast simultaneously. For the least squares search, we use the grid position with the maximal log-likelihood as prior and restrict the search box for the angular separation ρ to $50 \text{ mas} \leq \rho \leq 1000 \text{ mas}$.

The uncertainties of the best fit parameters $\sigma_{p_{\text{fit}}}$ follow from the likelihood function L for Gaussian errors (which are applicable to high confidence detections)

$$\ln L(p|x) = -\frac{1}{2} \chi_{\text{bin}}^2 \quad (2.31)$$

$$= -\frac{1}{2} (\Theta - \Theta_{\text{bin}}(p))^T \cdot \Sigma_{\Theta}^{-1} \cdot (\Theta - \Theta_{\text{bin}}(p)), \quad (2.32)$$

where p represents the three-dimensional parameter space of angular separation, position angle and contrast. Differentiating twice and neglecting terms containing second order derivatives of a single parameter yields

$$\mathbf{H}_{(i,j)} = \frac{\partial^2}{\partial p_i \partial p_j} \ln L(p|x) \quad (2.33)$$

$$\approx \frac{\partial \Theta_{\text{bin}}(p)}{\partial p_i} \cdot \Sigma_{\Theta}^{-1} \cdot \frac{\partial \Theta_{\text{bin}}(p)}{\partial p_j} \quad (2.34)$$

$$= -(\mathbf{J} \cdot \Sigma_{\Theta}^{-1} \cdot \mathbf{J}^T)_{(i,j)}, \quad (2.35)$$

where \mathbf{J} and \mathbf{H} are the Jacobian and the Hessian matrix of the binary model Θ_{bin} . Hence, the covariance matrix of the model parameters Σ_p can be obtained via

$$\Sigma_p = (-\mathbf{H})^{-1} = (\mathbf{J} \cdot \Sigma_{\Theta}^{-1} \cdot \mathbf{J}^T)^{-1}, \quad (2.36)$$

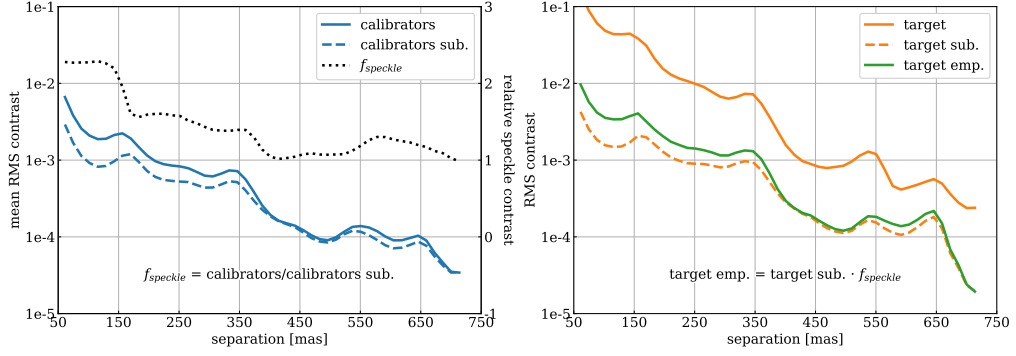


Figure 2.9: Left panel: mean of the azimuthal average c_{RMS} of the RMS best fit contrast c_{fit} of all non-detections of OB 2 (cf. column “Det” of Table 2.1) before (solid blue curve) and after (dashed blue curve) subtracting the best fit binary model from the measured kernel phase. The dotted black curve represents the correction factor for the relative contrast of the residual speckle noise f_{speckle} . Right panel: same as in the left panel, but for HIP 50156 (close binary). The empirical 1σ detection limit which we use for our analysis (solid green curve) is obtained by multiplying the azimuthal average $c_{\text{RMS}}^{\text{sub}}$ of the RMS best fit contrast $c_{\text{fit}}^{\text{sub}}$ after subtracting the best fit binary model from the measured kernel phase (dashed orange curve) with the correction factor f_{speckle} .

and the uncertainties of the model parameters for the best fit binary model $\sigma_{p_{\text{fit}}}$ are

$$\sigma_{p_{\text{fit}}} = \sqrt{\text{diag}(\Sigma_{p_{\text{fit}}})}. \quad (2.37)$$

We also compute the correlation of the best fit model parameters as

$$\text{corr} = \frac{\Sigma_{p_{\text{fit}}}}{\sigma_{p_{\text{fit}}}^T \cdot \sigma_{p_{\text{fit}}}}, \quad (2.38)$$

where \div denotes element-wise division.

Empirical uncertainties

Using only the uncertainties from photon noise, it is still difficult to distinguish between residual speckle noise (i.e. third order phase noise in the pupil plane) and real detections at small angular separations. This is the case because the data set which we analyze in Section 2.3 is very limited in terms of diversity of calibrator PSFs. For this reason, we use an empirical approach as the primary method to determine whether a detection is real or not.

First, we split our targets into candidate detections and calibrators based on their detection significance from photon noise SNR_{ph} (cf. Section 2.3.2). For each of the calibrators, we then compute two contrast curves:

1. The azimuthal average c_{RMS} of the root mean square (RMS) best fit contrast c_{fit} .
2. The azimuthal average $c_{\text{RMS}}^{\text{sub}}$ of the RMS best fit contrast $c_{\text{fit}}^{\text{sub}}$ after subtracting the best fit binary model θ_{bin} from the measured kernel phase θ .

Here, the assumption is that the calibrators are single stars, so that the ratio of the two RMS contrast curves computed above, i.e.

$$f_{\text{speckle}}(\rho) = \frac{c_{\text{RMS}}(\rho)}{c_{\text{RMS}}^{\text{sub}}(\rho)}, \quad (2.39)$$

is a correction factor for the relative contrast of the residual speckle noise. This is illustrated in the left panel of Figure 2.9.

For each of the candidate detections, we only compute the azimuthal average $c_{\text{RMS}}^{\text{sub}}$ of the RMS best fit contrast $c_{\text{fit}}^{\text{sub}}$ after subtracting the best fit binary model θ_{bin} (which might or might not be a real detection) from the measured kernel phase θ . Then, we multiply this RMS contrast curve with the mean of the relative speckle contrast f_{speckle} of all calibrators, i.e.

$$\sigma_{\text{emp}}(\rho) = \bar{f}_{\text{speckle}}(\rho) \cdot c_{\text{RMS}}^{\text{sub}}(\rho), \quad (2.40)$$

where the bar denotes the mean, in order to obtain an empirical contrast uncertainty σ_{emp} as a function of the angular separation ρ for each candidate detection (cf. right panel of Figure 2.9). We classify a candidate detection as real if its empirical detection significance SNR_{emp} is above the 5σ threshold, i.e.

$$\text{SNR}_{\text{emp}} = \frac{c_{\text{fit}}}{\sigma_{\text{emp}}} > 5. \quad (2.41)$$

Furthermore, we obtain empirically motivated uncertainties on the best fit parameters p_{fit} by multiplying the uncertainties from photon noise $\sigma_{p_{\text{fit}}}$ with the ratio f_{err} of the empirical contrast uncertainty σ_{emp} to the contrast uncertainty from photon noise σ_{ph} (at the position of the best fit binary model θ_{bin}).

The kernel phase analysis tools described in Sections 2.2.2, 2.2.3 and 2.2.4 are available on GitHub⁷. We put a strong focus on applicability to other instruments and an exchangeable kernel phase fits file format.

2.3 Results and discussion

2.3.1 Target list

We test our methods on an archival data set because the kernel phase technique is optimized for detecting companions at much smaller angular separations to their

⁷<https://github.com/kammerje/PyKernel>

host star than conventional high-contrast imaging techniques (such as ADI and reference star differential imaging, i.e. RDI). Hence, the parameter space that we are looking at is still unexplored. We search the VLT/NACO archive for L' band RDI surveys and decide to analyze program 097.C-0972(A), PI J. Girard, due to a large number of observed targets and therefore potential calibrators. A target list together with our detections is reported in Table 2.1.

2.3.2 Detected companion candidates

Before we search the targets in Table 2.1 for close companion candidates, we perform a basic vetting procedure by visually inspecting the cleaned data for wide companion candidates (cf. Section 2.3.2). In the field of view, which is limited to ~ 1 arcsec due to the windowing, we find six wide companion candidates (cf. upper section of Table 2.2). Three of them are already known and we classify our detections as confirmed, whereas the other three have not been reported before and therefore are new detections. Note that we correct the contrast of the wide companion candidates for the windowing (cf. Section 2.3.4).

After detecting and subtracting off the signal induced by the wide companion candidates, we use the kernel phase technique in order to search for closer and fainter objects (cf. Section 2.3.2). We find two companion candidates with an empirical detection significance above the 5σ threshold, i.e. $\text{SNR}_{\text{emp}}^{\text{can}} > 5$ (cf. lower section of Table 2.2). One of them is already known and we classify our detection as confirmed, whereas the other one has not been reported before and therefore is a new detection. For HIP 13008 we note that the empirical detection significance is 9.4σ when using only HIP 116384 as calibrator, but only 1.9σ when using HIP 12925 due to high residuals and a very large f_{err} correction. Therefore, HIP 12925 seems to be a bad calibrator and we do not report any best fit parameters for HIP 13008 due to a lack of credibility. Follow-up observations are required to confirm the true nature of this object. Also note that OBs 6–11 contain only one or two targets and are not analyzed with the kernel phase technique because the diversity of kernel phase amongst calibrators is essential for our empirical detection method. As there are systematic differences between the individual nights in the measured kernel phase, for this paper we are only analyzing OBs which contain at least two PSF calibrators (observed in the same night). Although this choice was made for simplicity and it might be possible to calibrate targets over longer timescales, this adds significant additional complexity which is beyond the scope of this paper.

From the targets for which we detect neither a wide nor a close companion candidate, we compute a contrast curve (i.e. the detection limit as a function of the angular separation) for the kernel phase technique (cf. Section 2.3.3).

Table 2.1: Target list grouped by OB for the VLT/NACO program 097.C-0972(A), PI J. Girard. For each target, we report the spectral type (SpT), the distance (d), the apparent K band magnitude (K) and the total integration time after frame selection (T_{int}). Whether we find any wide (visual) companion candidates, close (kernel phase) candidate detections and real detections is highlighted in columns “Vis”, “Can” and “Det”. We further report the empirical detection significance for the wide (visual) companion candidates ($\text{SNR}_{\text{emp}}^{\text{vis}}$), the detection significance from photon noise for all targets (SNR_{ph}) and the empirical detection significance for the close (kernel phase) candidate detections ($\text{SNR}_{\text{emp}}^{\text{can}}$).

OB	Target	SpT	d [pc]	K [mag]	T_{int} [s]	Vis	$\text{SNR}_{\text{emp}}^{\text{vis}}$	SNR_{ph}	Can	$\text{SNR}_{\text{emp}}^{\text{can}}$	Det	UT date
1	HIP 68994	F3/5V	71.7	6.715	395.8	N	–	46.6	Y	4.7	N	2016-03-22
	HIP 63734	F7/8V	54.1	6.436	389.2	N	–	44.3	N	–	N	2016-03-22
	HIP 55052	K7V	23.7	6.808	389.2	N	–	45.1	N	–	N	2016-03-22
2	HIP 44722	K7V	14.5	5.757	395.6	N	–	22.1	N	–	N	2016-03-23
	HD 108767 B	K0V	26.7	6.235	310.2	N	–	21.4	N	–	N	2016-03-23
	HIP 47425	M3V	9.6	6.056	388.8	N	–	32.4	Y	1.0	N	2016-03-23
	HIP 50156	M0.7V	23.4	6.261	395.2	N	–	292.7	Y	33.2	Y	2016-03-23
	HD 102982	G3V	53.2	6.605	316.6	N	–	23.9	N	–	N	2016-03-23
	HIP 58029	G7V	42.2	6.78	395.8	N	–	32.9	Y	1.4	N	2016-03-23
	HIP 61804	G3V	59.2	6.869	395.8	N	–	27.1	N	–	N	2016-03-23
	HD 110058	A0V	130.0	7.583	383.4	N	–	30.3	N	–	N	2016-03-23
	HIP 72053	G3V	59.7	6.994	382.4	N	–	29.4	N	–	N	2016-03-23
	HIP 58241	G4V	35.5	6.24	256.0	N	–	16.7	N	–	N	2016-03-24
3	TYC 8312 0298 1	K0II	804.5	6.475	162.0	N	–	18.0	N	–	N	2016-03-24
	HIP 78747	F5V	41.1	4.859	280.8	N	–	22.8	Y	2.0	N	2016-03-24
	HIP 37918	K0IV-V	34.4	6.275	389.2	N	–	336.5	Y	20.3	Y	2016-03-26
4	HIP 36985	M1.0V	14.1	5.934	334.4	Y	182.2	31.1	N	–	N	2016-03-26
	TYC 7401 2446 1	K0V	42.2	6.778	117.4	Y	195.0	14.4	N	–	N	2016-03-26
	TYC 6849 1795 1	K5V	27.6	6.911	305.4	Y	250.1	13.3	N	–	N	2016-06-15
5	HIP 92403	M3.5V	3.0	5.370	750.8	N	–	39.1	Y	2.5	N	2016-06-15
	HIP 94020 B	K5V	29.1	6.999	657.0	N	–	23.9	N	–	N	2016-06-15
	BDpl9 3532	K0	240.2	5.842	1361.2	N	–	–	N	–	N	2016-07-11
6	HIP 108085	B8IV-V	64.7	3.45	401.8	N	–	–	N	–	N	2016-07-11
	HIP 116231	B9.5III	53.4	4.611	285.2	Y	4.3	–	N	–	N	2016-07-14
	HIP 116258	K2V	34.0	6.685	367.0	N	–	–	N	–	N	2016-07-14
8	HIP 11484	B9III	60.4	4.392	279.6	N	–	–	N	–	N	2016-07-15
	HIP 3203 B	K5V	26.5	6.834	181.6	N	–	–	N	–	N	2016-07-16
	TYC 5835 0469 1	G8V	60.9	6.997	465.0	Y	95.8	–	N	–	N	2016-07-22
10	TYC 9339 2158 1	K3V	30.3	6.712	461.2	N	–	–	N	–	N	2016-07-22
	HIP 7554	M0V	22.2	6.621	637.4	N	–	–	N	–	N	2016-08-10
	HIP 13754	K2V	38.6	6.883	503.8	N	–	–	N	–	N	2016-08-10
12	HIP 116384	K7V	20.8	6.044	739.4	Y	99.7	26.2	N	–	N	2016-09-14
	HIP 12925	F8	57.1	6.52	595.4	N	–	24.0	N	–	N	2016-09-14
	HIP 13008	F5V	39.1	5.442	617.8	N	–	127.4	Y	N/A	N	2016-09-14
13	HIP 14555	M1V	19.6	6.367	609.6	N	–	35.1	N	–	N	2016-09-16
	HIP 20737	G9.5V	35.6	6.742	626.6	N	–	31.1	N	–	N	2016-09-16
	HIP 22506	G9V	50.8	6.876	620.0	N	–	35.8	Y	4.3	N	2016-09-16
	HIP 23362	B9V	60.5	4.974	311.8	N	–	28.7	N	–	N	2016-09-16

Notes. OBs 6–11 contain only one or two targets and cannot be analyzed with the kernel phase technique due to a lack of calibrators. Spectral types (SpT), distances (d) and apparent K band magnitudes (K) are taken from Simbad (Wenger et al., 2000).

Table 2.2: Wide companion candidates (CC) detected by visually inspecting the cleaned data (upper section) and close companion candidates detected only by the kernel phase technique (lower section). We estimate the apparent L' band magnitude (L') by adding the contrast (c) to the apparent K band magnitude of the host star (K, cf. Table 2.1). We report the angular separation (ρ) and the position angle (ϑ) of our best fit binary model θ_{bin} , the ratio of the empirical errors (which are reported here) to the errors from photon noise (f_{err}) and the reduced χ^2 of our best fit binary model ($\chi_{\text{r,bin}}^2$) and the raw kernel phase ($\chi_{\text{r,raw}}^2$). Whether a detection is new or known is highlighted in column “New” and a reference for known detections can be found in column “Ref”.

Target	CC	L' [mag]	c [pri/sec]	ρ [mas]	ϑ [deg]	f_{err}	$\chi_{\text{r,bin}}^2$	$\chi_{\text{r,raw}}^2$	New	Ref
HIP 36985	B	8.553 ± 0.005	$(8.96 \pm 0.04)e-2$	441.5 ± 0.2	133.77 ± 0.02	21.66	61.6	6311.3	Y	–
TYC 7401 2446 1	B	8.096 ± 0.005	$(2.97 \pm 0.01)e-1$	425.8 ± 0.3	89.23 ± 0.03	8.10	7.1	1238.9	Y	–
TYC 6849 1795 1	B	8.363 ± 0.004	$(2.63 \pm 0.01)e-1$	223.5 ± 0.4	203.29 ± 0.05	14.29	13.0	6090.0	N	G16
HIP 116231	B	9.04 ± 0.02	$(1.69 \pm 0.03)e-2$	874.6 ± 0.8	254.70 ± 0.05	58.19	667.5	696.7	N	S10
TYC 5835 0469 1	B	9.396 ± 0.003	$(1.097 \pm 0.003)e-1$	717.9 ± 0.2	37.62 ± 0.01	23.56	17.1	1883.7	Y	–
HIP 116384	C	8.732 ± 0.001	$(8.412 \pm 0.008)e-2$	842.90 ± 0.07	346.614 ± 0.004	9.18	40.6	186.4	N	M03
HIP 50156	B	8.17 ± 0.03	$(1.72 \pm 0.05)e-1$	77.3 ± 0.8	338.7 ± 0.2	19.75	22.1	1195.7	N	B15
HIP 37918	B	9.56 ± 0.05	$(4.9 \pm 0.2)e-2$	122 ± 5	9.4 ± 0.8	46.55	17.3	1104.6	Y	–

Notes. G16 = Galicher et al. (2016), S10 = Schöller et al. (2010), M03 = Martin (2003), B15 = Bowler et al. (2015).

Wide companion candidates

The wide companion candidates reported in the upper section of Table 2.2 are all detected by visually inspecting the cleaned data. When we find a companion candidate, we use a grid search followed by a least squares search in order to find its best fit binary model θ_{bin} for the measured kernel phase θ . Then, we compute the empirical detection significance $\text{SNR}_{\text{emp}}^{\text{vis}}$ for the best fit binary model θ_{bin} (cf. right panels of Figures 2.10 and 2.11). This is achieved using a simplification of the empirical detection method (cf. Section 2.2.4). Since the wide companion candidates all have a sufficiently large angular separation (i.e. $\gtrsim 200$ mas) and are sufficiently bright (otherwise we could not detect them by eye), we can skip the use of any calibrators and compute the empirical detection significance $\text{SNR}_{\text{emp}}^{\text{vis}}$ as the best fit contrast c_{fit} divided by the azimuthal average $c_{\text{RMS}}^{\text{sub}}$ of the RMS best fit contrast $c_{\text{fit}}^{\text{sub}}$ after subtracting the best fit binary model θ_{bin} from the measured kernel phase θ . Note that we do not use any Karhunen-Loève calibration for this step either, i.e. $\theta' = \theta$ (cf. Section 2.2.3).

Before we search for closer and fainter objects, we subtract the signal induced by the wide companion candidates from the measured kernel phase, i.e.

$$\theta \rightarrow \theta - \theta_{\text{bin}}, \quad (2.42)$$

so that the measured kernel phase of all targets is free of wide detections. The detected wide companion candidates are shown in the left panels of Figures 2.10 and 2.11 and are described in more detail in the following paragraphs.

HIP 36985 B, TYC 7401 2446 1 B, TYC 5835 0469 1 B. These objects are new companion candidates which were not reported before. They have L' band contrasts of $2.619 \pm 0.005^{\text{mag}}$, $1.318 \pm 0.004^{\text{mag}}$ and $2.399 \pm 0.003^{\text{mag}}$ respectively, and therefore are candidates for stellar mass companions.

TYC 6849 1795 1 B. This object was already detected in 2005 by Galicher et al. (2016) at an angular separation of ~ 220 mas, a position angle of ~ 201 deg and a H band contrast of $\sim 1.6^{\text{mag}}$. We find a L' band contrast of $1.450 \pm 0.004^{\text{mag}}$ and an angular separation (223.5 ± 0.4 mas) and a position angle (203.29 ± 0.05 deg) which are in agreement with Galicher et al. (2016), i.e. we can confirm the bound nature of the object.

HIP 116231 B. This object was already detected in 2004 by Schöller et al. (2010) at an angular separation of 641 ± 4 mas, a position angle of 240.2 ± 0.6 deg and a K band contrast of $2.75 \pm 0.01^{\text{mag}}$. We find a L' band contrast of $4.43 \pm 0.02^{\text{mag}}$, a slightly larger angular separation of 874.6 ± 0.8 mas and a slightly different position angle of 254.70 ± 0.05 deg, but (allowing for orbital motion) we can confirm the bound nature of the object. Note that there is a huge disagreement in the contrast, but a brief look at the raw data from Schöller et al. (2010) shows a significant PSF halo and confirms our result of $\sim 4^{\text{mag}}$.

HIP 116384 C. This object was first detected in 2002 by Martín (2003) who found HIP 116384 (GJ 900) to be a triple system with a 510 ± 10 mas (HIP 116384 B,

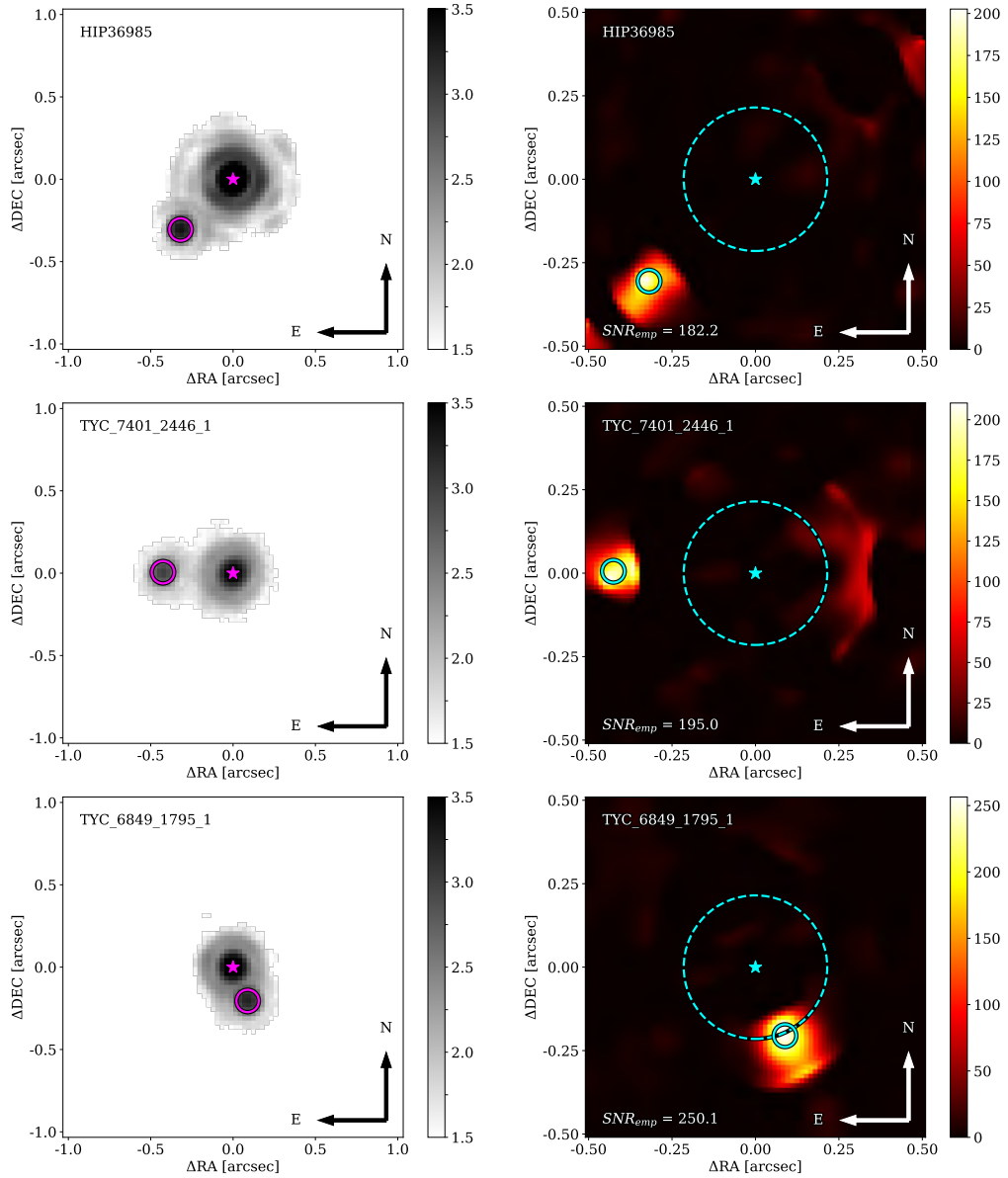


Figure 2.10: Left panels: median frame of a cleaned data cube of the targets for which we detect a wide companion candidate. The magenta star indicates the position of the host star and the magenta circle indicates the position of the companion candidate, obtained from a least squares fit of the binary model θ_{bin} to the measured kernel phase θ . Note that the color scale is logarithmic, reaching from $1e+1.5$ to $1e+3.5$ pixel counts. Right panels: map of the empirical detection significance $\text{SNR}_{\text{emp}}^{\text{vis}}$ (cf. Section 2.3.2) for the same targets as in the left panels. The number in the lower left corner of each panel reports the empirical detection significance at the position of the best fit binary model θ_{bin} (note that this is not necessarily the position with the highest detection significance) and the dashed cyan circle indicates the 99% threshold of the super-Gaussian window (i.e. the brightness of objects outside this circle is decreased by more than 1% by the windowing).

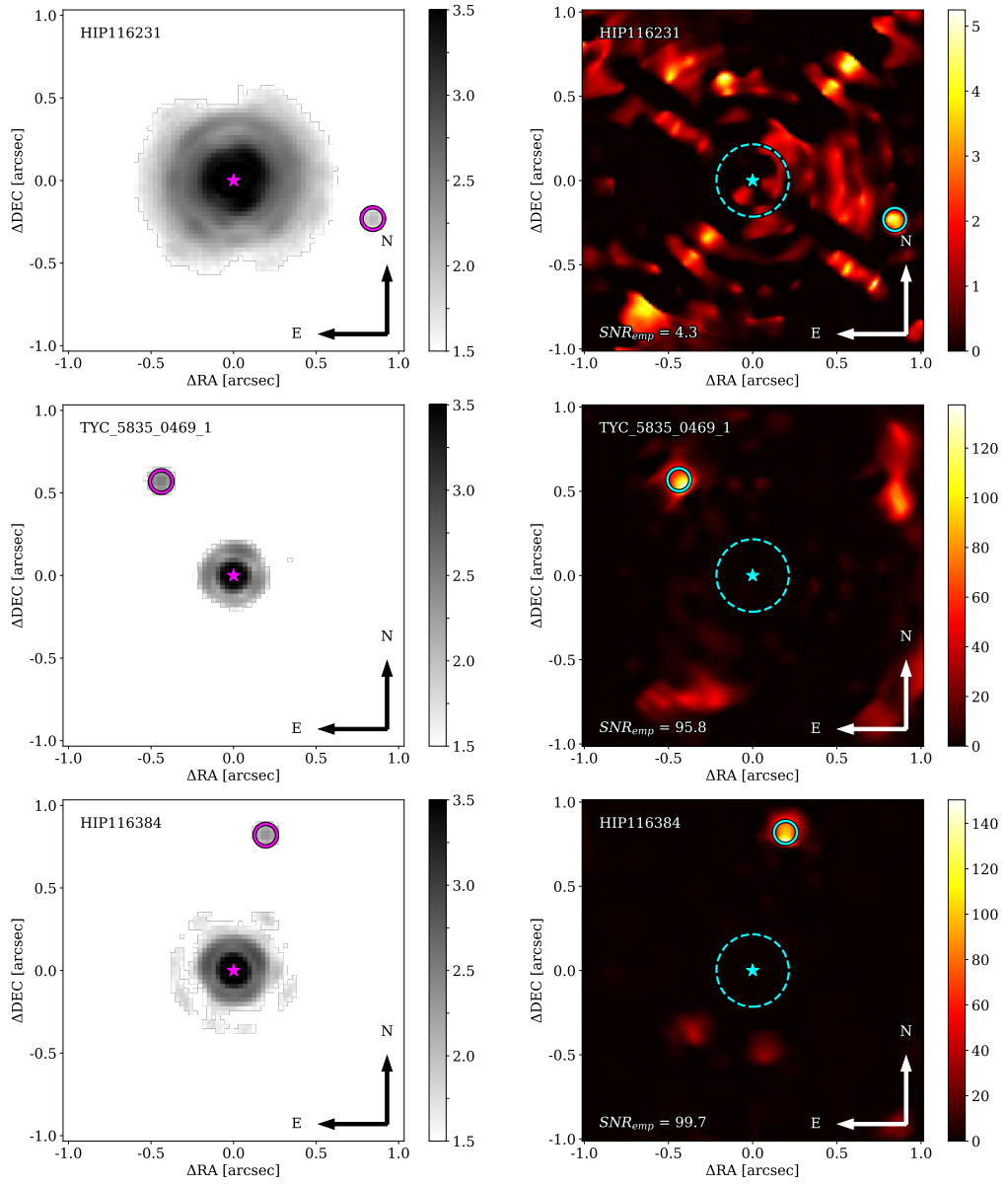


Figure 2.11: Figure 2.10 continued.

$\Delta K = 1.61 \pm 0.03^{\text{mag}}$) and a 760 ± 10 mas (HIP 116384 C, $\Delta K = 2.38 \pm 0.04^{\text{mag}}$) component. Lafrenière et al. (2007a) resolved the system again in 2004 and 2005, finding HIP 116384 B at an angular separation of 611 ± 2 mas and 673 ± 2 mas respectively, and HIP 116384 C at an angular separation of 733 ± 2 mas and 722 ± 2 mas respectively. In the cleaned data, we only find HIP 116384 C at a slightly larger angular separation of 842.90 ± 0.07 mas, but a position angle (346.614 ± 0.004 deg) and a L' band contrast ($2.688 \pm 0.001^{\text{mag}}$) which are in agreement with Martín (2003) and Lafrenière et al. (2007a), so that we can confirm the bound nature of the object. Looking at the raw data, we also find HIP 116384 B (which is the brighter of the two companions), noticing that it has moved to an angular separation of ~ 1200 mas being too far away in order to be visible in our cleaned data (due to the windowing).

Close companion candidates

The close companion candidates reported in the lower section of Table 2.2 are all detected only by the kernel phase technique. For each target in Table 2.1, we use a grid search followed by a least squares search in order to find the best fit binary model θ_{bin} for the measured kernel phase θ . Then, we compute the detection significance from photon noise SNR_{ph} (cf. Section 2.2.4) at the position of the best fit binary model θ_{bin} from the least squares search. For this step, we always use all other targets which were observed in the same OB as calibrators for the Karhunen-Loève calibration, fixing $K_{\text{klip}} = 4^8$. Knowing that the majority of VLT/NACO targets do not have any close companions, we then classify the $\sim 1/3$ of the targets with the highest SNR_{ph} in each OB as candidate detections (cf. column “Can” of Table 2.1) for the next step and the remaining targets as calibrators.

For the next step, we compute the empirical detection significance $\text{SNR}_{\text{emp}}^{\text{can}}$ (cf. Section 2.2.4) for each of the candidate detections from the previous step. For this step, we always use all remaining targets which were classified as calibrators in the previous step for the Karhunen-Loève calibration, again fixing $K_{\text{klip}} = 4$. If the empirical detection significance is above the 5σ threshold, i.e. $\text{SNR}_{\text{emp}}^{\text{can}} > 5$, we classify the candidate detection as real. If not, we add the candidate detection to the list of calibrators and redo the computation of the empirical detection significance (this time with one calibrator more than before). We repeat this process until all candidate detections are real. The detected close companion candidates are shown in Figure 2.12 and are described in more detail in the following paragraphs. Please note that we report the correlation of the

⁸For simplicity, we fix $K_{\text{klip}} = 4$ for all targets and regardless of the number of calibrators. Various testing has shown that subtracting off the four statistically most significant eigencomponents of the kernel phase of the calibrators mostly yields the smallest amount of significant detections, i.e. calibrates the data best. A more rigorous investigation of this relationship is foreseen for a future publication.

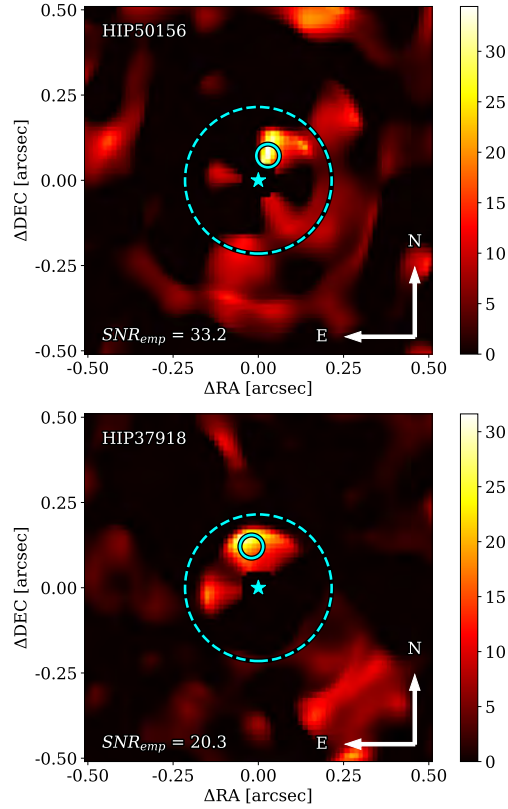


Figure 2.12: Map of the empirical detection significance $\text{SNR}_{\text{emp}}^{\text{can}}$ for the targets for which we detect a close companion candidate. The cyan star indicates the position of the host star and the solid cyan circle indicates the position of the companion candidate, obtained from a least squares fit of the binary model θ_{bin} to the measured kernel phase θ . The number in the lower left corner of each panel reports the empirical detection significance at the position of the best fit binary model θ_{bin} and the dashed cyan circle indicates the 99% threshold of the super-Gaussian window (like in Figure 2.10).

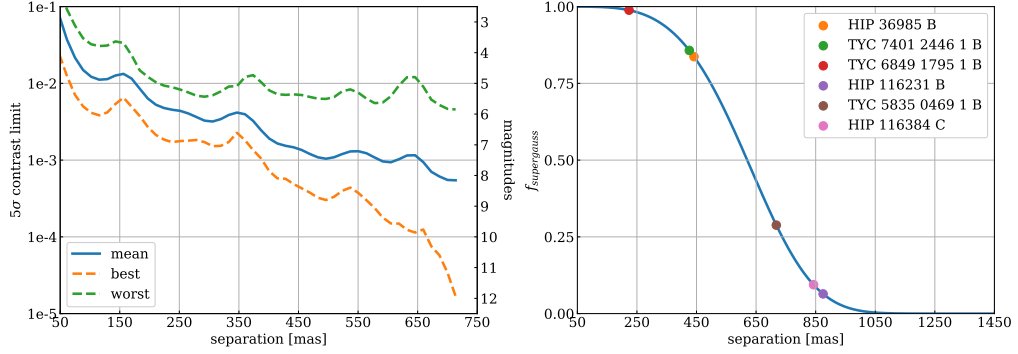


Figure 2.13: Left panel: 5σ empirical contrast limit, i.e. RMS contrast curve $c_{\text{RMS}}(\rho)$ multiplied by 5, for all non-detections (cf. column “Det” of Table 2.1). Shown are the mean, the best and the worst contrast limit. Right panel: value of the super-Gaussian windowing function depending on the angular separation. The brightness of companions outside of ~ 200 mas is decreased significantly. We use this curve to recover the true contrast of the detected wide (visual) companions (cf. upper section of Table 2.2). For reference, their position on this curve is indicated by the circles.

best fit parameters in Appendix 2.4 and present model-data correlation plots in Appendix 2.4.

HIP 50156 B. This object was already detected in 2011 by Bowler et al. (2015) at an angular separation of ~ 90 mas and a K band contrast of $\sim 1.8^{\text{mag}}$. Just nine month later, Brandt et al. (2014) cannot resolve this companion and report an upper limit of ~ 20 mas for its angular separation. We find HIP 50156 B at an angular separation of 77.3 ± 0.8 mas and an L’ band contrast of $\sim 1.91 \pm 0.03^{\text{mag}}$, confirming the detection and notable orbital motion.

HIP 37918 B. This object is a new companion candidate which was not reported before. It has a L’ band contrast of $\sim 3.29 \pm 0.05^{\text{mag}}$, and therefore is a candidate for a stellar mass companion. Furthermore, HIP 37918 ($M \approx 0.98 M_{\odot}$) is known to have a ~ 23.1 arcsec companion of almost equal mass (HIP 37923, $M \approx 0.95 M_{\odot}$, Desidera et al. 2006). Together with our companion candidate, this would make the system triple.

2.3.3 Detection limits

In Section 2.2.4, we present our empirical approach to find meaningful detection limits for the data analyzed in this paper. Based on this approach, we compute the contrast limit of the kernel phase technique as a function of the angular separation as the azimuthal mean of the RMS best fit contrast c_{RMS} of all targets for which we do not detect any companions with the kernel phase technique (i.e. all non-detections, cf. column “Det” of Table 2.1). Note that we already

subtracted off the signal induced by the wide companion candidates. The mean, the best and the worst contrast limit are shown in the left panel of Figure 2.13.

At the small angular separations which are inaccessible by classical high-contrast imaging techniques (i.e. within ~ 200 mas in the L' band), the kernel phase technique achieves contrast limits of $\sim 1e-2$. This is not yet deep enough to detect companions in the planetary-mass regime, which would start between $1e-3$ and $1e-4$ for young (~ 10 Myr) gas giants (e.g. Bowler, 2016). However, our closest detections prove that the resolution which is required to resolve solar-system scales in the nearest star forming regions can be achieved with the kernel phase technique. At larger angular separations, our best contrast limit is comparable with the limits achieved by RDI (e.g. Cantalloube et al., 2015). The large spread in the contrast limit comes from the fact that the amplitude of the background noise is nearly the same for all data cubes, whereas the peak value of the PSF varies heavily due to the PSF reconstruction (cf. Section 2.2.1).

2.3.4 Windowing correction

As mentioned in Section 2.2.2, we window all frames by a super-Gaussian (with a FWHM of 1240 mas) in order to minimize edge effects when computing their Fourier transform. Due to this windowing, the brightness of companions at angular separations $\gtrsim 215$ mas deviates by more than 1% from the true value. In order to correct for this effect, we again assume that kernel phase is proportional to contrast in the high-contrast regime, so that we can obtain the true contrast of a companion by dividing its measured contrast (i.e. the best fit contrast from the binary model) by the value of the super-Gaussian windowing function. We are aware that this method has its limits, as each PSF has a spatial extent on the detector and assuming that the entire PSF is multiplied by the same value is an over-simplification of the problem. Nevertheless, this method agrees fairly well with the contrasts which we measure in the cleaned fits files and we use it to correct the contrast of all wide companion candidates (cf. right panel of Figure 2.13). We add an additional contrast correction error in quadrature based on injection-recovery tests to companions wider than 500 mas to account for limitations in this technique.

2.4 Conclusions

We use the kernel phase technique in order to search for close companions at the diffraction limit in an archival VLT/NACO RDI L' band data set. Therefore, we develop our own data reduction pipeline for VLT/NACO data, which performs a basic dark, flat, bad pixel and background (i.e. dither) subtraction, but also reconstructs saturated PSFs in order to reduce their Fourier plane noise. Furthermore, we select frames with sufficiently high Strehl ratio, which is essential

for the kernel phase technique as it relies on a linearization of the Fourier plane phase. Then, we use XARA for extracting the kernel phase and improve its re-centering algorithm in the case of resolved and bright companions. Furthermore, we apply a principal component analysis based calibration to the data (i.e. Karhunen-Loève decomposition, Soummer et al., 2012) and develop a suite of analytic model fitting algorithms in order to search for point source companions with the kernel phase technique⁹.

For the archival data set which we analyze in Section 2.3, we find that our kernel phase covariance model (which only takes into account shot noise) is not sufficient and significantly underestimates the true errors. This is still the case after calibrating the data, because the diversity of calibrator PSFs is not sufficient. Hence, we develop an empirical method for estimating the relative contrast of the residual speckle noise and finding meaningful detection limits for the data. With this empirical approach, we detect six wide companion candidates by visually inspecting the cleaned data and two close (~ 80 – 110 mas) companion candidates which are detected only by the kernel phase technique. All eight companion candidates lie in the stellar-mass regime and five of them were previously unknown.

In order to reach the planetary-mass regime, a better library of calibrator PSFs is required. Therefore, it is extremely important that the targets and their calibrators are observed as close in time as possible. This becomes very clear from the archival data set which we analyze, where there are in fact multiple calibrators observed in one night, but not close enough in time, so that the kernel phase calibration does not reduce the quasi-static errors satisfyingly. In order to make better use of our principal component analysis based calibration, we propose star-hopping sequences of ~ 6 targets, and to revisit each target at least twice. *As we have shown with the NACO data analyzed in this paper, timescales of hours between the observations of the science and calibrator targets are too long to capture the temporal evolution of quasi-static phase errors. Instead, those observations should be spread over timescales of minutes only (for example slewing to a different target every six minutes with Keck/NIRC2 star-hopping, cf. Chapter 3).* Star-hopping is an observing strategy for which the instrument (and in particular the AO system) acquisition is only performed once at the beginning of each sequence. Then, one slews (“hops”) from target to target without interrupting the AO system. Furthermore, we aim to examine more extensive Keck data sets where we are hopeful that the significant investment of telescope resources gives adequate calibrator diversity to characterize the systematic errors and possibly use Bayesian Monte-Carlo techniques.

In this paper, we have shown that kernel phase is able to achieve a resolution below the classical diffraction limit of a telescope under good observing conditions (i.e. sufficiently high Strehl ratio). This is of particular interest for future space-based observatories, such as the JWST, as it gives access to an exciting

⁹<https://github.com/kammerje/PyKernel>

parameter space which could otherwise not be explored due to the limited mirror size (and therefore resolution). Space-based telescopes do not suffer from atmospheric turbulence, what makes the calibration much less challenging than for the ground-based VLT/NACO data (e.g. [Martinache, 2010](#)). Nevertheless, with an optimized observing strategy, kernel phase is also a competitive high-contrast imaging technique from the ground.

The application of kernel phase is of course not limited to imaging telescopes. One concept which aims to push the kernel phase technique towards higher contrasts is the VIKiNG instrument ([Martinache & Ireland, 2018](#)), which proposes kernel phase nulling interferometry with the VLTI. By combining kernel phase with a high-contrast booster (i.e. a nulling interferometer) it would allow for self-calibrating the observables and achieving a better robustness with respect to residual wavefront errors. This would in turn also be an option to reduce the demanding stability requirements on space-based nulling interferometers, such as the LIFE concept ([Kammerer & Quanz, 2018](#); [Quanz et al., 2018](#)), which aims to detect dozens of Earth-like exoplanets in the solar neighborhood.

Acknowledgements

MJI was supported by the Australian Research Council Future Fellowship (FT-130100235). This project has received funding from the European Research Council (ERC) under the European Union’s Horizon 2020 research and innovation program (grant agreement CoG #683029). JHG gratefully acknowledges support from the Director’s Research Funds at the Space Telescope Science Institute. The manuscript was also substantially improved following helpful comments from an anonymous referee.

Appendix 1: parameter correlation

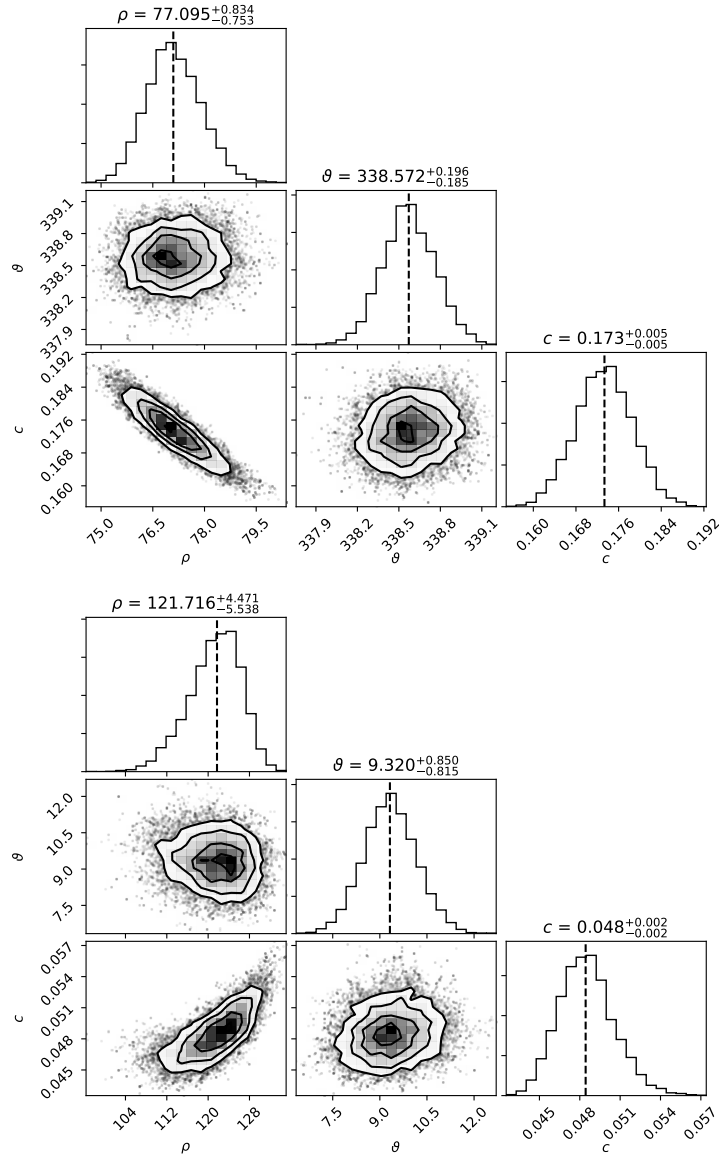


Figure 2.14: For the targets for which we detect a close companion candidate (i.e. HIP 50156, top and HIP 37918, bottom) we report the correlation of the best fit parameters using a corner plot from [Foreman-Mackey \(2016\)](#). Here, we use an MCMC technique (emcee, [Foreman-Mackey et al., 2013](#)) with six random walkers initialized at the best fit position and a temperature of f_{err}^2 in order to find the best fit parameters including their correlated uncertainties by maximizing the log-likelihood $\ln L$ of the binary model.

Appendix 2: correlation plots

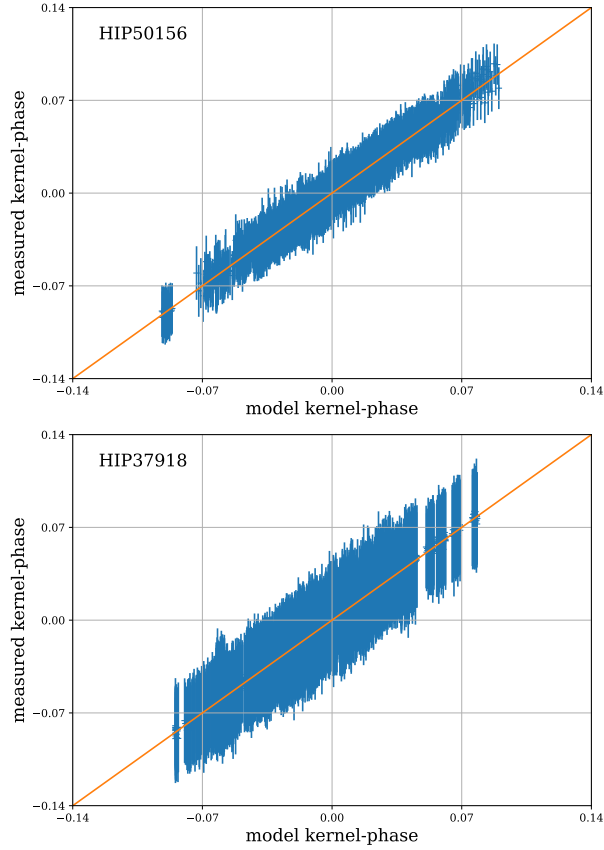


Figure 2.15: Correlation of the measured kernel phase and the best fit binary model kernel phase for the targets for which we detect a close companion candidate in blue. The presented errorbars are computed based on photon noise (cf. Section 2.2.2) and scaled up by f_{err} according to our empirical uncertainties (cf. Section 2.2.4). The orange line indicates the identity which would represent perfect agreement between measured and model kernel phase. Similar to Figure 2.8 we normalize each kernel phase by the norm of its corresponding row of $\mathbf{P}' \cdot \mathbf{K}$ since we are dealing with calibrated kernel phase here.

High-resolution survey for planetary companions to young stars in the Taurus molecular cloud

This chapter was published as a peer-reviewed article in Monthly Notices of the Royal Astronomical Society, volume 498, pages 1382–1396. It was mostly written by Alexander L. Wallace in collaboration with his supervisors. Jens Kammerer conducted the close separation kernel phase analysis and wrote Section 3.3.4 of this chapter.

Alexander L. Wallace,¹ Jens Kammerer,^{1,2} Michael J. Ireland,¹ Christoph Federrath,¹ Adam L. Kraus,³ Sarah T. Maddison,⁴ Aaron Rizzuto,³ Eloise K. Birchall¹ and Frantz Martinache⁵

1. Research School of Astronomy and Astrophysics, Australian National University, Canberra, ACT 2611, Australia
2. European Southern Observatory, Karl-Schwarzschild-Str 2, 85748, Garching, Germany
3. Department of Astronomy, University of Texas, Austin, TX 78712, United States of America
4. Centre for Astrophysics and Supercomputing, Swinburne University of Technology, Melbourne, VIC 3122, Australia
5. Laboratoire Lagrange, Université Côte d’Azur, Observatoire de la Côte d’Azur, CNRS, Parc Valrose, Bât. H. FIZEAU, 06108 Nice, France

Preamble

In Chapter 2, we presented a first approach to use the kernel phase technique for searching for faint companions among a larger sample of stars from the ground. As we have seen, the achieved detection limits were not sufficient for the detection of planetary-mass companions, though. One reason for this was a non-ideal observing strategy which lead to each individual target being affected by slightly different systematic errors at the small spatial scales that we are interested in. In this chapter, we will use the kernel phase technique on a sample of 55 young ($\lesssim 2$ Myr) stars in the Taurus star-forming region, observed with a more ideal strategy known as “star-hopping”. As will be shown, the extreme youth of these targets and the improvement of the detection limits due to the more ideal observing strategy will enable the detection of planetary-mass companions, and we will use our non-detections to derive upper limits on the frequency of giant planets as a function of mass and orbital separation.

Abstract

Direct imaging in the infrared at the diffraction limit of large telescopes is a unique probe of the properties of young planetary systems. We survey 55 single class I and class II stars in Taurus in the L' filter using natural and laser guide star adaptive optics and the near-infrared camera (NIRC2) of the Keck II telescope, in order to search for planetary-mass companions. We use both reference star differential imaging and kernel phase techniques, achieving typical 5-sigma contrasts of ~ 6 magnitudes at separations of $0.2''$ and ~ 8 magnitudes beyond $0.5''$. Although we do not detect any new faint companions, we constrain the frequency of wide separation massive planets, such as HR 8799 analogues. We find that, assuming hot-start models and a planet distribution with power-law mass and semi-major axis indices of -0.5 and -1 , respectively, less than 20% of our target stars host planets with masses $> 2 M_J$ at separations > 10 au.

3.1 Introduction

Direct imaging of exoplanets is an important method to study planetary systems and gain insight into formation scenarios. Most directly imaged exoplanets have been found in young star systems when the planets are still hot and emit in the infrared (e.g. HR 8799 (Marois et al., 2008)) while some have been found in the process of formation (Keppler et al., 2018). Most directly imaged planets are at wide separations (> 20 au) from their host stars but models of planet distributions (Fernandes et al., 2019) indicate that these systems are rare. Giant planets such as Jupiter are likely to form by core accretion which occurs closer to the star (~ 5 au.)

The Taurus Molecular Cloud (TMC) is ideal for studying planet formation due to its relative proximity (~ 140 pc) and numerous young stars (< 2 Myr) (Torres et al., 2009). Many of these young stars have prominent disc structures (ALMA Partnership et al., 2015; Huang et al., 2020), which may be indicative of planet formation. A planet in the process of formation will radiate in the near-infrared. In an optically thick disc, the planet will be hidden at these wavelengths. However, a giant planet ($\sim 0.5 M_J$ and above) is expected to clear a gap in the disc (Crida & Morbidelli, 2007). Many of the discs in our sample have gaps present in their dust distribution, as indicated by ALMA surveys (Long et al., 2018) and, although their origin is still hotly debated, one possibility is giant planet formation.

The circumstellar discs in the TMC have been extensively studied over the years in terms of their mass (Andrews & Williams, 2005; Andrews et al., 2013), structure and distribution, as have the discs in other nearby star-forming regions such as Upper Scorpius and Ophiuchus (Carpenter et al., 2014; Van Der Plas et al., 2016; Kuruwita et al., 2018). Surveys have also been conducted to detect planets in these star-forming regions (Tanner et al., 2007; Metchev & Hillenbrand, 2009) and some have found potentially planet-mass companions at wide separations (e.g., DH Tau b; Itoh et al. (2005)) as well as a close companion to CI Tau using radial velocity (Johns-Krull et al., 2016). However, these surveys were unable to achieve the necessary sensitivity for planetary-mass companions on solar-system scales. Kraus et al. (2011) managed to detect new brown dwarf companions at small separations and achieved a mass sensitivity of $\sim 20 M_J$. In part of this earlier work, emission with total luminosity comparable to a forming planet was discovered around LkCa 15 (Kraus & Ireland, 2012), although the complex transitional (or “pre-transitional”) nature of this disc has meant that a physically motivated radiative transfer model could not be made at the time. A scattering origin for the emission was, however, strongly suggested by further observations with Sphere and ZIMPOL (Thalmann et al., 2015).

The purpose of our study is to search for giant planets around young stars in the TMC still accreting from their discs, and determine dominant mechanisms for

planet formation. This study is unique because, for the first time, we attempted to probe the inner regions of these systems in search of solar-system analogues, at a time where the significant presence of disc gas means that planetary luminosities would be highest. As the TMC is the nearest star-forming region of its size (Güdel et al., 2007) and the projected separation of any planets decreases with the distance, it is the most favourable region for resolving the peak of the giant planet distribution at physical separations of < 10 au. Using planet distributions from Cumming et al. (2008) and later by Fernandes et al. (2019), it is clear that even at this close distance, the majority of planets are inside the ~ 20 -30 au limits of a typical coronagraph.

When planets form, they heat up and radiate in infrared wavelengths and are at their brightest during runaway accretion. After formation, the planets continue to radiate for some time and should still be self luminous after millions of years as shown by the HR 8799 and β -Pictoris systems (Marois et al., 2008; Lagrange et al., 2010). The evolution of planet luminosity is an important factor in this work as it determines our detection capability. However, many details of the accretion luminosity remain uncertain. The luminosity of a circum-planetary disc is dependant on the accretion rate as well as the mass and radius of the planet, and whether and where the circum-planetary disc is truncated (Zhu, 2015). The post-accretion luminosity of hot-start planets (i.e., planets which do not lose entropy in an accretion shock) has been modelled for some time as applied to brown dwarfs (e.g. Baraffe et al., 2003). "Cold" start models, where all accretion shock luminosity is radiated away, can have very different initial luminosities, especially for massive planets (e.g. Marley et al., 2007), although detailed shock models considering radiative transfer and reasonable accretion rates have recently shown that "warm" start models are much more realistic (Marleau et al., 2019). Additionally, models of post-shock gas has shown a zone of stability with initial entropies around 10 – $11 k_B$ /baryon, termed "stalling" accretion (Berardo et al., 2017).

Planets cool and fade as they age but the cooling time is very dependent on the mass and internal entropy of the planet, with high-entropy low-mass planets cooling the fastest, and e.g. a $5 M_J$ planet cooling at $0.5 k_B$ /baryon/Myr from an initial internal entropy of $1.5 k_B$ /baryon (Spiegel & Burrows, 2012). Irrespective of these uncertainties in post-formation luminosity evolution, the best time to directly image exoplanets is shortly after their formation, when they are at their highest luminosity. The canonically young age of the TMC provides a perfect environment in which to search for these planets.

In Section 3.2 we describe our survey sample of 55 stars in the TMC using the Near Infrared Camera (NIRC2) on the Keck II telescope in 2015 and 2016. In Section 3.3 we describe our observation, data reduction and small angle analysis methods. In Section 3.4 we expand our analysis to wider separations and identify companions. Section 3.5 combines our methods for all separations to place limits

on the frequency of wide planets. Our conclusions are presented in Section 3.6.

3.2 Survey sample

In choosing our sample of stars in the TMC, we decided to only select single stars, which we define as stars with no known stellar companion within $1''$. The reason for this is firstly, that multiple star systems can cause issues with adaptive optics but also for reasons of simplicity. The data reduction and analysis is simplified if there is only one bright central star to consider and there is less theoretical complexity regarding models of planet formation. **We note that at the distance of the TMC, which is ~ 140 pc (Torres et al., 2009), an angular separation of $1''$ corresponds to a physical separation of ~ 140 au. As shown by Kraus et al. (2016), stellar companions at such wide separations do not significantly impact the planet population and formation.** An exception to this is V410 Tau (Ghez et al., 1997), which we use to ensure we are correctly oriented and to verify our data processing pipelines. Note that we include close ($\lesssim 1$ au) spectroscopic binaries in our sample if they meet all other criteria, as we argue wide companions in these systems are likely to be unaffected by the dynamics of the close orbit. Two known systems are in our sample: DQ Tau (Mathieu et al., 1997) and UZ Tau A (Prato et al., 2002).

We primarily consider class II targets because, at this stage in stellar evolution, circum-stellar discs have been observed to have very low mass, between 0.2% and 0.6% of the host-star mass (Andrews et al., 2013). This indicates, if there is planet formation, the most massive planets will have already formed by this phase. We also consider class I objects such as HL Tau, which has a circumstellar disc containing notable gaps and rings, which may be indicative of planet formation (Brogan et al., 2015). Our targets were taken from Kraus et al. (2011). We selected targets based on their J-K magnitude colours and only selected targets with $J-K < 4$ and K magnitude < 10 which can be used as a guide for the approximate L' magnitude. We also made a cut on the spectral type, excluding targets listed as later than M3 in Kraus et al. (2011). This cutoff was chosen to include the relatively abundant low-mass stars in the TMC while cutting-out stars that would be too faint for AO observations and too low in mass to expect giant planets. We note that recent studies have produced updated spectral types. The spectral types shown in Table 3.1 are taken from Herczeg & Hillenbrand (2014) and include one star which is now believed to be later than M3.

All of our targets were observed with an L' filter with the exception of RY Tau, AB Aur, UX Tau and SU Aur. These stars were observed with a PAH filter as they are too bright for the method described in Section 3.3.3 to work properly. Our targets are mapped out in Figure 3.1 and shown on an H-R diagram in Figure 3.2. The map in Figure 3.1 also includes the distances taken from Gaia and a map of dust reddening from Schlafly et al. (2014). The H-R

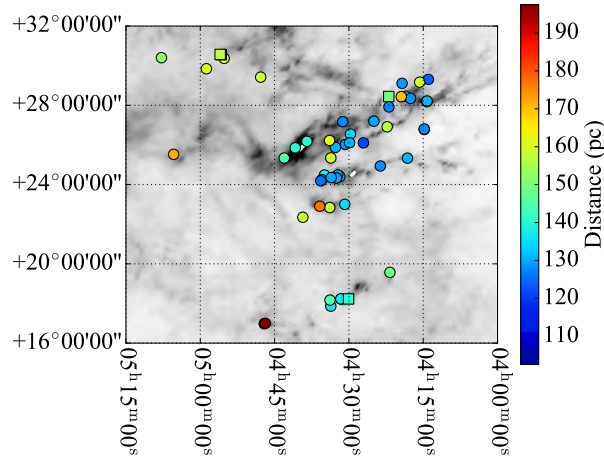


Figure 3.1: Positions of our targets superimposed on the dust reddening map from [Schlafly et al. \(2014\)](#). The squares represent the bright targets imaged with the PAH filter and circles are all other targets.

diagram in Figure 3.2 plots the absolute magnitude in the J-band (corrected for extinction using models from [Fitzpatrick & Massa \(2007\)](#)) against effective temperature. The effective temperature was calculated using spectral types from [Herczeg & Hillenbrand \(2014\)](#). Isochrones and isomass curves are shown using models from [Baraffe et al. \(2015\)](#). Note that several of our targets below 5000 K are under-luminous and appear older than 10 Myr (cf. Figure 3.2). This is due to local reddening, determined from the measured colors being inconsistent with the spectral type, which is not taken into account and should not be regarded as the actual age of the star.

As shown in Figure 3.1, most of our targets are in the main region of the TMC at distances of 130–150 pc. There are some outliers, most notably DQ Tau and DR Tau at distances of ~ 190 pc, and separated from the main group. The stellar properties for all of our targets are presented in Table 3.1. The temperature was converted to mass using the evolutionary tracks from [Baraffe et al. \(2015\)](#).

3.3 Observations and image analysis

3.3.1 Observations

Our observations were made using the NIRC2 camera of the Keck II telescope on 27, 28 November, 5 December 2015 and 7,8,9 November 2016. As the focus of these observations was to search for close companions, we used the 512x512 sub-array mode in order to minimise overheads - noting that the readout time would

Table 3.1: Properties of target stars in the TMC. The spectral types come from Herczeg & Hillenbrand (2014), the masses are calculated using evolutionary tracks from Baraffe et al. (2015) and the W_1 magnitudes are from the WISE catalog. The distance comes from the Gaia DR2. The last column shows potential stellar companions from the Washington Double Star Catalog.

Name	R. A.	Dec	Distance	Mass (M_{\odot})	SpT	Rp (mag)	K (mag)	W_1 (mag)	Stellar companions?
IRAS 04108+2910	04 13 57.38	+29 18 19.3	123.5±1.5	0.40	M3.0	14.0	9.36	7.93	N
FM Tau	04 14 13.58	+28 12 49.2	131.9±0.8	0.24	M4.5	12.5	8.76	8.00	26.2 arcsec
CW Tau	04 14 17.00	+28 10 57.8	132.4±0.7	1.00	K3.0	11.7	7.13	5.80	N
FP Tau	04 14 47.31	+26 46 26.4	128.5±0.9	0.36	M2.6	11.6	8.87	8.40	5.8 arcsec
CX Tau	04 14 47.86	+26 48 11.0	127.9±0.6	0.37	M2.5	11.5	8.81	8.52	5.8 arcsec
2MASS J04154278+2909597	04 15 42.79	+29 09 59.8	160.0±1.7	0.51	M0.6	12.8	9.38	9.04	N
CY Tau	04 17 33.73	+28 20 46.8	128.9±0.7	0.38	M2.3	11.4	8.60	7.79	N
V409 Tau	04 18 10.79	+25 19 57.4	131.4±0.7	0.54	M0.6	11.2	9.03	8.32	N
V410 Tau	04 18 31.10	+28 27 16.2	130.4±0.9	1.49	K3.0	9.5	7.63	7.36	0.1–0.3 arcsec
BP Tau	04 19 15.83	+29 06 26.9	129.1±1.0	0.45	M0.5	10.6	7.74	7.11	3.1 and 5.4 arcsec
V836 Tau	04 19 26.27	+28 26 14.3	169.6±1.2	0.45	M0.8	11.6	8.60	8.19	10.3 arcsec
IRAS 04187+1927	04 21 43.27	+19 34 13.3	148.7±2.2	0.37	M2.4	13.0	8.02	7.11	N
DE Tau	04 21 55.63	+27 55 06.2	127.4±1.1	0.37	M2.3	10.8	7.80	7.08	N
RY Tau	04 21 57.41	+28 26 35.5	149.6±5.4	2.41	G0.0	9.9	5.39	4.24	0.0 and 10.7 arcsec
2MASS J04221675+2654570	04 22 16.76	+26 54 57.1	157.6±3.4	0.52	M1.5	14.8	9.01	7.73	23.5 arcsec
UX Tau	04 23 39.19	+24 56 14.1	127.8±0.8	0.37	M2.8	12.4	8.60	7.65	2.6 arcsec
IP Tau	04 24 57.08	+27 11 56.5	130.6±0.7	0.47	M0.6	11.4	8.35	7.71	3.9 and 15.8 arcsec
DG Tau	04 27 04.69	+26 06 16.0	121.2±2.1	0.64	K7.0	10.9	6.99	6.18	16.3 and 54.4 arcsec
DH Tau	04 29 41.56	+26 32 58.3	135.4±1.3	0.37	M2.3	11.4	8.18	7.40	2.4 arcsec
IQ Tau	04 29 51.56	+26 06 44.9	131.3±1.1	0.43	M1.1	12.0	7.78	7.27	10.0, 10.0, and 10.6 arcsec
UX Tau	04 30 04.00	+18 13 49.4	139.9±2.0	0.89	K0.0	10.3	8.92	6.92	2.4 and 5.8 arcsec
DK Tau	04 30 44.25	+26 01 24.5	128.5±1.0	0.52	K8.5	11.3	7.10	6.12	3.1 arcsec
IRAS 04278+2253	04 30 50.28	+23 00 08.8	135.4±1.3	1.24	G8.0	11.4	5.86	4.53	N
JH 56	04 31 14.44	+27 10 17.9	127.5±0.7	0.64	K8.0	11.0	8.79	8.74	N
LkHa 358	04 31 36.14	+18 13 43.3	102.6±5.1	0.50	M0.9	16.1	9.69	8.21	N
HL Tau	04 31 38.44	+18 13 57.7	136.7±2.2	0.79	K3c	15.7	7.41	5.24	N
HK Tau	04 31 50.57	+24 24 18.1	133.3±1.6	0.47	M1.5	12.8	8.59	7.82	2.2 arcsec
2MASS J04321540+2428597	04 32 15.41	+24 28 59.8	130.5±3.2	0.67	K5.5	13.6	8.10	6.62	N
FY Tau	04 32 30.58	+24 19 57.3	130.2±1.2	0.51	M0.1	12.5	8.05	7.32	0.2 and 17.3 arcsec
FZ Tau	04 32 31.76	+24 20 03.0	130.0±1.3	0.50	M0.5	12.5	7.35	6.15	N
UZ Tau A	04 32 42.88	+25 52 31.9	131.2±1.6	0.39	M1.9	11.2	7.35	6.25	0.4 and 3.6 arcsec
GI Tau	04 33 34.06	+24 21 17.1	130.5±0.8	0.46	M0.4	11.5	7.89	7.09	41.8 arcsec
DL Tau	04 33 39.08	+25 20 38.1	159.3±1.2	0.99	K5.5	11.1	7.96	6.94	8.5 and 12.5 arcsec
HN Tau A	04 33 39.35	+17 51 52.4	136.6±2.9	0.79	K3c	12.5	8.38	7.23	3.2 arcsec
DM Tau	04 33 48.73	+18 10 10.0	145.1±1.1	0.35	M3.0	12.0	9.52	9.46	N
CI Tau	04 33 52.01	+22 50 30.1	158.7±1.2	0.97	K5.5	11.1	7.79	6.76	N
IT Tau	04 33 54.70	+26 13 27.5	162.0±2.0	0.89	K6.0	12.0	7.86	7.40	N
AA Tau	04 34 55.42	+24 28 53.2	137.2±2.4	0.45	M0.6	13.1	8.05	7.45	6.0 arcsec
DN Tau	04 35 27.38	+24 14 58.9	128.2±0.9	0.46	M0.3	10.5	8.02	7.66	N
2MASS J04354093+2411087	04 35 40.94	+24 11 08.8	125.2±2.3	0.58	M0.5	14.2	8.41	7.35	2.4 and 12.6 arcsec
HP Tau	04 35 52.78	+22 54 23.2	177.1±3.4	1.26	K4.0	11.8	7.62	6.02	0.0 arcsec
DO Tau	04 38 28.58	+26 10 49.4	139.4±1.0	0.46	M0.3	11.3	7.30	6.34	3.5 and 28.9 arcsec
LkCa 15	04 39 17.79	+22 21 03.4	158.9±1.2	0.97	K5.5	10.7	8.16	7.50	27.0 arcsec
JH 223	04 40 49.51	+25 51 19.2	139.9±1.1	0.38	M2.8	12.9	9.49	8.94	2.1 arcsec
GO Tau	04 43 03.08	+25 20 18.7	144.6±1.0	0.41	M2.3	12.6	9.33	8.97	N
DQ Tau	04 46 53.06	+17 00 00.1	197.4±2.0	0.43	M0.6	11.4	7.98	7.09	2.3 and 7.0 arcsec
DR Tau	04 47 06.21	+16 58 42.8	195.7±2.5	0.78	K6.0	10.7	6.87	5.83	N
DS Tau	04 47 48.60	+29 25 11.2	159.1±1.1	0.46	M0.4	11.1	8.04	7.35	5.7, 6.9, and 11.5 arcsec
GM Aur	04 55 10.98	+30 21 59.5	159.6±2.1	0.84	K6.0	10.8	8.28	8.30	28.8 arcsec
AB Aur	04 55 45.85	+30 33 04.3	162.9±1.5	1.84	A1.0	6.9	4.23	3.25	1.0 arcsec
SU Aur	04 55 59.39	+30 34 01.5	158.4±1.5	2.65	G4.0	8.8	5.99	5.07	N
MWC 480	04 58 46.26	+29 50 37.0	161.8±2.0	2.03	A3.0	7.5	4.87	4.87	N
2MASS J05052286+2531312	05 05 22.86	+25 31 31.2	171.9±2.6	0.45	M1.8	14.1	11.16	9.17	2.4 arcsec
RW Aur A	05 07 49.76	+30 24 03.7	151.9±20.8	1.77	K0c	11.4	7.02	6.25	0.1 and 1.4 arcsec
V819 Tau	05 16 22.30	+27 26 24.2	131.7±1.1	0.61	K8.0	11.1	8.42	8.27	N

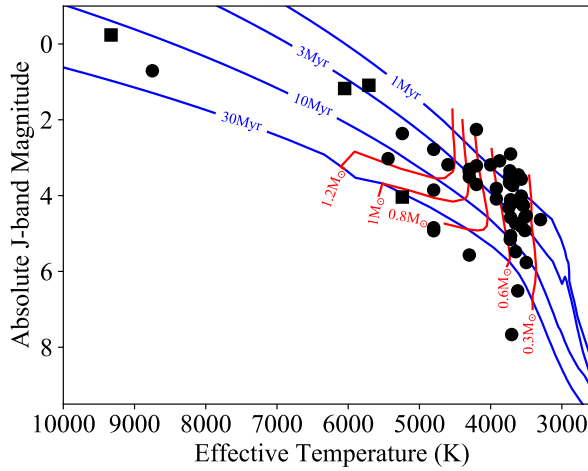


Figure 3.2: H-R diagram of our targets plotting J-band magnitude against effective temperature. As in Figure 3.1, The squares represent the bright targets imaged with the PAH filter and circles are all other targets. MWC 480 and AB Aur are A-type stars and are the only stars in our sample hotter than 5000 K, and hence they appear as outliers.

have often decreased our duty cycle by a factor of ~ 2 had we used the full array ¹.

In order to account for irregularities in the telescope PSF, at least 2 position angles were required for each object. Weather permitting, every object was observed in 4 observing blocks: 2 in the first half of the night and 2 in the second half. Where possible we avoided the highest elevations where azimuth slew rates are high and telescope vibrations can affect observations. Based on past experience with Keck, our objects were divided into groups of 4 and observed in the following sequence: A,B,C,D, A,B,C,D which gave us 2 observations of 4 objects. The members of the group are determined by their proximity to each other. This sequence is then repeated in the second half of the night. Each observation consisted of a number of frames (usually 6) with average exposure times of 30 s, which is composed of a small integration time multiplied by an appropriate number of co-adds (snapshots that make up the final image), which also varies depending on the brightness of the target. A summary of our observations is shown in Table 3.2.

3.3.2 Data reduction

Starting with our raw 512×512 pixel images, we first subtracted the master dark frame for the night and divided by the flat frame. For each observing block,

¹<https://www2.keck.hawaii.edu/inst/nirc2/ObserversManual.html>

Table 3.2: Details of observations. T_{int} refers to the integration time for each co-add. This is multiplied by the number of co-adds to get the exposure time for each frame. The # of visits column gives the number of observing blocks taken for that object each night. The number of values in this column is the number of observing nights. The # of frames column shows the number of frames for each observing block in the order they were taken. For example, IRAS 04108+2910 was observed on only one night and visited 4 times with 6 frames in each block. FM Tau was observed on 2 nights with 3 visits on the first night, and 1 on the second. The blocks taken on the first night had 12, 12 and 6 frames, while the block taken on the second night had 6.

Name	Obs. Date	T_{int} (s)	Coadds	Exposure Time (s)	# Visits	# Frames
IRAS 04108+2910	2016-11-09	0.4	80	32	4	6,6,6,6
FM Tau	2015-11-27,2015-11-28	0.3	100	30	3,1	12,12,6,6
CW Tau	2016-11-07	0.2	160	32	4	6,7,6,6
FP Tau	2016-11-07,2016-11-09	0.1	320	32	4,1	6,6,6,6,6
CX Tau	2016-11-07,2016-11-09	0.4	80	32	5,1	6,6,6,6,6
2MASS J04154278+2909597	2016-11-09	0.4	80	32	4	7,6,6,6
CY Tau	2015-11-27,2015-11-28	0.3	100	30	3,2	12,12,6,6,6
V409 Tau	2016-11-09	0.4	80	32	4	7,6,6,6,6
V410 Tau	2015-11-28,2016-11-07	0.2	160	32	1,1	16,6
BP Tau	2015-11-27,2015-11-28	0.15	200	30	3,1	12,12,6,5
V836 Tau	2015-11-27,2015-11-28	0.3	100	30	4,1	6,6,6,6,6
IRAS 04187+1927	2016-11-08	0.4	80	32	4	6,10,8,6
DE Tau	2015-11-27,2015-11-28,2015-12-05	0.3	100	30	2,2,2	6,8,6,6,8,6
RY Tau	2015-11-27,2015-11-28	1.0	30	30	1,4	12,7,6,6,6
2MASS J04221675+2654570	2016-11-08	0.4	80	32	4	9,6,6,6
FT Tau	2016-11-09	0.4	80	32	4	6,6,6,6
IP Tau	2015-11-27,2015-11-28,2015-12-05	0.3	100	30	3,1,1	12,12,6,10,6
DG Tau	2015-11-27,2015-11-28,2015-12-05	0.15	200	30	2,1,3	6,6,6,15,4,6
DH Tau	2016-11-08	0.4	80	32	4	6,11,6,6,6
IQ Tau	2015-11-27,2015-11-28	0.15	200	30	3,1	12,12,6,6,6
UX Tau	2015-11-28	1.0	30	30	5	10,6,6,6,6
DK Tau	2015-11-27,2015-11-28,2015-12-05,2016-11-08	0.15	200	30	2,2,2,4	6,8,6,6,8,6,6,6,6
IRAS 04278+2253	2016-11-08	0.053	600	31	1	7
JH 56	2015-11-27,2015-11-28	0.3	100	30	3,1	12,12,6,6,6
LkHa 358	2016-11-08,2016-11-09	0.1	80	32	4,1	6,4,6,6,6,6
HL Tau	2016-11-07,2016-11-09	0.4	320	32	5,1	6,6,6,6,14,6
HK Tau	2015-11-27,2016-11-09	0.3	160	32	1,3	9,8,6,6
2MASS J04321540+2428597	2016-11-07,2016-11-09	0.2	100	32	2,2	6,10,6,6
FY Tau	2016-11-08,2016-11-09	0.4	80	32	3,1	6,6,6,6
FZ Tau	2016-11-07	0.1	320	32	4	5,6,4,6
UZ Tau A	2016-11-09	0.1	320	32	2	6,6
GI Tau	2015-11-27,2015-11-28,2015-12-05	0.15	200	30	3,1,2	12,12,6,6,6,4
DL Tau	2015-11-27,2015-11-28,2015-12-05	0.15	200	30	2,2,1	6,6,6,6,6
HN Tau A	2016-11-08,2016-11-09	0.4	80	32	3,1	6,6,6,6
DM Tau	2015-11-27,2015-11-28	0.3	100	30	2,3	6,6,12,12,12
CJ Tau	2015-11-27,2015-11-28	0.15	200	30	3,1	12,12,6,6,6
IT Tau	2015-11-28	0.2	160	32	4	6,6,6,6,6
AA Tau	2015-11-27,2016-11-09	0.4	80	32	1,4	12,9,6,5,4
DN Tau	2015-11-28,2016-11-09	0.2	160	32	3,1	6,6,6,6
2MASS J04354093+2411087	2016-11-08,2016-11-09	0.4	80	32	3,1	6,6,6,6
HP Tau	2015-11-27,2015-11-28,2015-12-05	0.15	200	30	3,1,2	12,12,6,6,6,10
DO Tau	2016-11-07,2016-11-08	0.2	160	32	4,1	6,6,10,6,6
LkCa 15	2015-11-27,2015-11-28,2016-11-08	0.3	100	30	3,2,4	12,12,6,6,6,6,6,6
JH 223	2016-11-07,2016-11-08,2016-11-09	0.4	80	32	2,2,2	6,6,9,6,6,6
GO Tau	2016-11-07,2016-11-08,2016-11-09	0.4	80	32	2,1,1	6,6,6,6,6
DQ Tau	2015-11-27,2015-11-28	0.15	200	30	3,2	12,8,6,10,8
DR Tau	2015-11-27,2016-11-09	0.15	200	30	2,3	12,6,6,6,6
DS Tau	2015-11-27,2015-11-28	0.3	100	30	3,1	6,6,6,6,6
GM Aur	2015-11-27,2015-11-28,2016-11-08	0.2	100	30	4,2,1	6,6,6,6,12,12,6
AB Aur	2015-11-28	0.3	100	32	4	6,6,6,6,6
SU Aur	2015-11-28	1.0	30	30	5	6,6,6,6,6
MWC 480	2016-11-07,2016-11-09	0.053	600	31	4,3	6,6,6,6,6,6
2MASS J05052286+2531312	2016-11-08,2016-11-09	0.4	80	32	2,2	8,6,6,6,6
RW Aur A	2016-11-07,2016-11-09	1.0	30	30	3,4	8,6,5,6,6,6,6
V819 Tau	2015-11-27,2015-11-28	0.3	100	30	3,1	12,12,6,6,6

the target was observed in two different dither positions. Half the images had the target in the top left quarter and the other half had it in the bottom right corner. This allowed us to calculate an approximate sky background for each image. First, each image was cropped to a size of 192×192 pixels ($1.92'' \times 1.92''$) which was centred on the star by calculating the peak of the image after applying a median filter and performing a simple pixel roll. The corresponding area from the other dither position served as the sky background which was then subtracted from the cropped image.

Any “bad” pixels were fixed using the algorithm from Ireland (2013). Once identified, these pixels were set to the corresponding value in the median filtered image. In addition to bad pixels identified in the dark and flat field images, we also corrected with the same algorithm pixels near saturation which were defined as any with counts greater than $17500 \times$ the number of coadds for that image. The threshold of 17500 was chosen empirically to produce final PSF-subtracted images with the lowest residuals. Pixels above this threshold were treated as bad pixels. Once all images had been “cleaned” in this way, they were stored in a data cube containing all images for a particular observing block. The analysis was then performed on these cleaned images.

3.3.3 Image analysis using PSF subtraction

Our first method of image analysis is a form of reference star differential imaging (RDI) which focuses on simply removing the effect of the central star in order to look for planets. To achieve this, we first went back to the basics of how an image is created. When the telescope’s optical system is applied, we assumed the signal from a planet will look the same as a star but reduced by a contrast ratio. In other words, the star was represented by a PSF given by the properties of the optical system and the planet was represented by the same PSF but scaled by a contrast ratio and shifted by the planet’s relative position. In 1-D, this image function is given by

$$i(x) = p(x) + cp(x - x_0), \quad (3.1)$$

where p is the PSF representing a single star, c is the contrast ratio between a planet and the star and x is a spatial variable with the star at $x = 0$ and the planet at $x = x_0$. The first step in our analysis is the subtraction of the PSF.

For our PSF, we simply used the (cleaned) image of another star, which was taken at a similar time to our target. Another possible approach would be principal component analysis (PCA) in which the PSF is taken from a linear combination of stellar images. The number of components in the analysis is optimised, which has shown promising results in reducing background noise and finding planets (Meshkat et al., 2013; Hunziker et al., 2018). An extreme approach would be to create a linear combination using all our images. We have

tried this approach as well as an optimisation and found that there was no significant improvement in our signal-to-noise ratio, so we do not report on this here. Instead, we have opted for the opposite extreme, in which we only use 1 image that is selected by optimisation. Due to fewer degrees of freedom, this approach also subtracts a smaller fraction of the flux of a real companion than PCA.

Our targets are observed in blocks, typically consisting of 6 images each. Every target image is matched with the image of another star, which plays the role of our PSF. The PSF image for each target image was chosen from a selection of nearby observing blocks. For a given target image, we have a set of potential PSFs p_n . For each of these, we calculate the sum of the square of the differences given by

$$\Sigma_n = \sum_{ij} (t_{ij} - f_n p_{n,ij})^2, \quad (3.2)$$

where t is the target image, p_n is the image of another star, which we use as the PSF, and i and j are pixel indices. The scaling factor f_n was chosen such that the target and PSF had the same maximum value so when they are subtracted, the central star cancels out. For a given PSF this is given by

$$f_n = \frac{\max(t)}{\max(p_n)}. \quad (3.3)$$

This is calculated for all possible PSF images p_n in our sample, simply based on photon count. Whichever produces the smallest value of Σ_n is chosen as our PSF. When this PSF is chosen, we then calculate the difference between the target and the PSF that has been multiplied by the scaling factor f_n . Following on from Equation 3.1, the difference is represented in 1-D by

$$d(x) = i(x) - p(x) = cp(x - x_0). \quad (3.4)$$

We can then calculate a smooth contrast ratio as a function of position by cross-correlating the difference function with the PSF. This is then divided by the PSF cross-correlated with itself in order to normalise the contrast ratio. The contrast ratio as a function of position is given by

$$c(x_0) = \frac{(d \star p)(x_0)}{(p \star p)(x_0)}, \quad (3.5)$$

where \star denotes the cross-correlation operator given by

$$(d \star p)(x_0) = \int_{-\infty}^{\infty} d(x) p(x + x_0) dx. \quad (3.6)$$

When we apply this method to the image of one of our targets, this produces a map of the contrast ratio between any features and the central star. An example is shown in Figure 3.3 with an image of AA Tau. This star was chosen simply

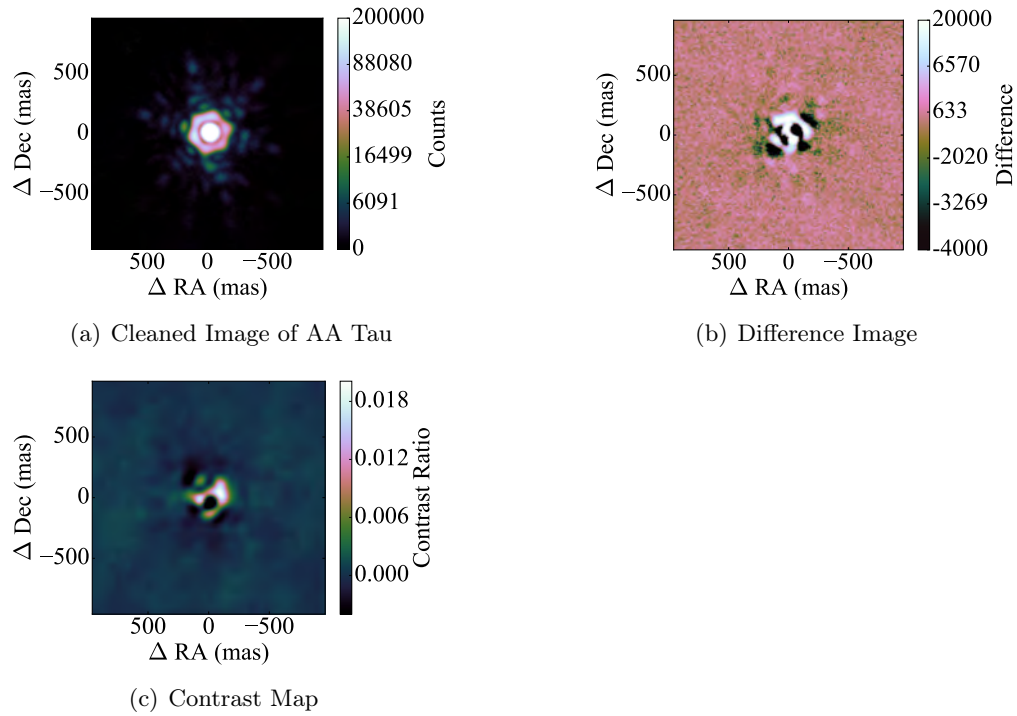


Figure 3.3: Example showing a reduced image of AA Tau (left), the difference after an image of HK Tau is subtracted (centre) and the contrast ratio map of AA Tau (right). When the contrast ratio is negative, this is due to positive features in the subtracted image. The bright feature in the middle of the contrast map is due to offsets in the position of the target and PSF central star. At wider separations, we can use this method to search for companions. While there are no obvious features in this example, the contrast values show that we should be able to detect companions more than 0.002 the brightness of the star.

because its properties are close to the average of our sample. For the PSF, we used an image of HK Tau which, as shown in Table 3.2, was taken on the same night.

This process is repeated for all images of the target, and the contrast maps are averaged. By taking the average contrast about an annulus of fixed radius, we then produce a 1-D plot of the contrast limit against separation.

3.3.4 Kernel phase data reduction

Complementary to the PSF subtraction (cf., Section 3.3.3) we use the kernel phase technique in order to search for companions close to the host star, inside of 500 mas. This analysis begins with the same 192 x 192 pixel cleaned data cubes

described in Section 3.3.3.

The kernel phase technique finds a special linear combination of the Fourier phase ϕ (i.e., the phase of the Fourier transform of the image) which is independent of pupil plane phase φ (phase aberrations in the telescope pupil which cause quasi-static speckles) to second order, similar to closure phase in non-redundant masking, but for full pupil images (i.e., highly redundant apertures). Let \mathbf{A} be the baseline-mapping matrix introduced by [Martinache \(2010\)](#), which maps the sub-apertures in the pupil plane (cf., left panel of Figure 3.4) to their corresponding Fourier plane baselines (cf., right panel of Figure 3.4), then the Fourier phase ϕ observed through the telescope is

$$\phi = \mathbf{R}^{-1} \cdot \mathbf{A} \cdot \varphi + \phi_{\text{obj}} + \mathcal{O}(\varphi^3), \quad (3.7)$$

where \mathbf{R} encodes the redundancy of the Fourier plane baselines and ϕ_{obj} is the phase intrinsic to the observed astronomical object (which is the quantity that we would like to measure). This problem is significantly simplified by multiplying Equation 3.7 with the kernel \mathbf{K} of $\mathbf{R}^{-1} \cdot \mathbf{A}$, i.e.,

$$\theta = \mathbf{K} \cdot \phi = \underbrace{\mathbf{K} \cdot \mathbf{R}^{-1} \cdot \mathbf{A}}_{=0} \cdot \varphi + \mathbf{K} \cdot \phi_{\text{obj}} + \mathcal{O}(\varphi^3), \quad (3.8)$$

so that the kernel phase observed through the telescope θ is directly equal to the kernel phase intrinsic to the observed object $\theta_{\text{obj}} = \mathbf{K} \cdot \phi_{\text{obj}}$ (except for higher order noise terms).

The kernel phase technique was first used by [Martinache \(2010\)](#) who demonstrated the detection of a 10:1 companion at $0.5 \lambda/D$ in HST/NICMOS data, clearly showing the improved speckle calibration capabilities with respect to image plane data reduction techniques. More recently, [Pope et al. \(2016\)](#) applied kernel phase to ground-based observations of α Oph with the 5.1 m Hale Telescope and showed that it outperforms PSF fitting and bispectral analysis under appropriate conditions (i.e., high Strehl). [Kammerer et al. \(2019\)](#) further developed the technique including a principal component calibration based on Karhunen-Loève decomposition ([Soummer et al., 2012](#)) for the subtraction of the residual kernel phase signal measured on calibrator stars and detected eight (candidate) low-mass stellar companions (five of which were previously unknown) in an archival VLT/NACO data set, one of which is separated by only $0.8 \lambda/D$.

Here, we use the same kernel phase data reduction pipeline as [Kammerer et al. \(2019\)](#), with slight modifications and improvements explained below.

Kernel phase extraction

For extracting the kernel phase from the images we use the Python library XARA². XARA windows the cleaned images with a super-Gaussian mask, applies

²<https://github.com/fmartinache/xara>

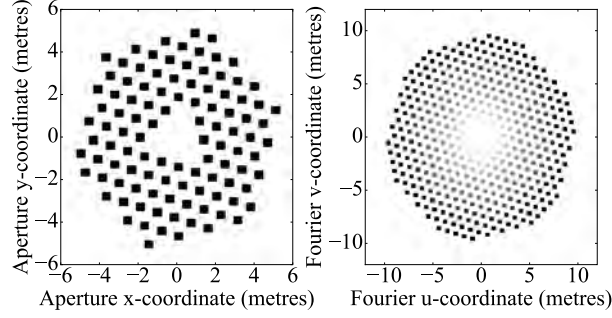


Figure 3.4: Keck pupil model consisting of 105 individual sub-apertures (left panel) and its Fourier plane coverage with 205 distinct baselines (right panel) resulting in 100 individual kernel phases. The shading in the right panel shows the redundancy (multiplicity) of the baselines with dark representing low redundancy and bright representing high redundancy. Note that the right panel is the auto-correlation of the left panel (cf., Section 2.1 of [Martinache, 2010](#)).

a linear discrete Fourier transform to them and performs a sub-pixel re-centring directly in the complex visibility space afterwards. Then, the Fourier phase ϕ of the images is extracted and multiplied by the kernel \mathbf{K} of the transfer matrix $\mathbf{R}^{-1} \cdot \mathbf{A}$ of our Keck pupil model (Figure 3.4) yielding the kernel phase θ of the images (cf., Section 2.1 of [Martinache, 2010](#)).

For the super-Gaussian mask we use a radius of 50 pixels (i.e., 500 mas) or a FWHM of 100 pixels. Our Keck pupil model consists of three individual sub-apertures per hexagonal Keck primary mirror segment in order to be sensitive to the tip-tilt orientation of each segment. Those sub-apertures that are behind the central obscuration from the secondary mirror are simply ignored. The sub-apertures are distributed uniformly in the plane of the primary mirror with a spacing of $b_{\min} = 0.9$ m resulting in a field of view of $\lambda/b_{\min} \approx 865$ mas and a maximum baseline of $b_{\max} = 9.5$ m, yielding a resolution of $\sim \lambda/(2b_{\max}) \approx 40$ mas. However, since the super-Gaussian mask has a radius of only 500 mas, we restrict our search for companions (with the kernel phase technique) to angular separations of $40 \text{ mas} \leq \rho \leq 500 \text{ mas}$.

Kernel phase frame selection

Before we feed the kernel phase extracted from the images into our calibration and model fitting pipeline (cf., Section 3.3.4 and 3.3.4), we perform a frame selection based on the sum of the squared kernel phase of each image, i.e.,

$$\text{SOSK} = \sum_i |\theta_i^2|. \quad (3.9)$$

The distribution of SOSK as a function of time is not smooth. In fact, it shows high steps when the observing conditions and thus the adaptive optics correction suddenly become worse. Hence, from each night, we only keep the 50% best images in the set of potential calibrators and the 75% best images in the set of potential targets, where best means smallest SOSK. This is motivated by the fact that a point-symmetric source (e.g., a single star) has zero Fourier phase ϕ and therefore zero kernel phase θ . Hence, a single star with a faint companion should still have a small kernel phase signal and images with a high kernel phase signal can usually be attributed to bad seeing conditions where the kernel phase technique is not valid (due to too much higher-order phase noise). Note that an unknown companion around one of our calibrators would have a small impact only, since we are averaging over a large number of calibrators and do not de-rotate them before we subtract them from the science target, so that the averaging is destructive in case of pupil-stabilised observations.

Kernel phase calibration

Similar to observations with an interferometer, we have to calibrate the kernel phase of our targets by subtracting the kernel phase of calibrators. This is done using the Karhunen-Loève projection described in Section 2.3 of Kammerer et al. (2019). We perform the Karhunen-Loève calibration separately for each night since we found this to yield a smaller reduced χ^2 than calibrating data from multiple nights together. The reason for this is likely that the quasi-static phase aberrations (for which we try to compensate with our calibration) are only stable over timescales of minutes to hours.

From the 75% best images of each night, we select one object as a target and all images of different objects from the 50% best images of the same night as calibrators. Then, we subtract the first four Karhunen-Loève components from the kernel phase of the target θ and its uncertainties Σ_θ , i.e.,

$$\theta' = \mathbf{P}' \cdot \theta, \quad (3.10)$$

$$\Sigma'_\theta = \mathbf{P}' \cdot \Sigma_\theta \cdot \mathbf{P}'^T, \quad (3.11)$$

where Σ_θ and \mathbf{P}' are obtained as described in Sections 2.2.3 and 2.3 of Kammerer et al. (2019).

Kernel phase model fitting

After calibrating the kernel phase, we fit the binary model

$$\theta'_{\text{bin}} = \mathbf{P}' \cdot \mathbf{K} \cdot \arg \left(1 + c \exp \left(-2\pi i \left(\frac{\Delta_{\text{RA}} u}{\lambda} + \frac{\Delta_{\text{DEC}} v}{\lambda} \right) \right) \right), \quad (3.12)$$

where $0 \leq c \leq 1$ is the companion contrast, Δ_{RA} and Δ_{DEC} are the on-sky separation of the companion, u and v are the Fourier coordinates of the pupil model and $\lambda = 3.776 \mu\text{m}$ is the observing wavelength, using a grid search and a least-squares routine as described in Section 2.4 of Kammerer et al. (2019) to it. We fit to all images of the same target simultaneously, also when a target was observed during multiple nights. Using the uncertainties Σ'_θ derived from the photon noise of the images this yields a RA-DEC map of best-fit companion contrasts \mathbf{c}_{fit} and their uncertainties $\sigma_{\mathbf{c}_{\text{fit}}}$ whose ratio is the photon noise-based signal-to-noise ratio SNR_{ph} . The grid position with the smallest reduced χ^2 (obtained from a least-squares routine) is our best-fit companion.

Empirical kernel phase detection limits

If the uncertainties Σ_θ derived from the photon noise would describe the underlying errors correctly (i.e., if all other errors would be negligible) we could simply classify those best-fit companions whose $\text{SNR}_{\text{ph}} > 5$ as significant detections. However, although readout noise and dark current are negligible for our dataset, there is a lot of higher-order phase noise, which leads to a high SNR_{ph} and false detections for all of our targets (cf., column “ SNR_{ph} ” of Table 3.3). Note that the kernel phase is independent of pupil plane phase noise only to second order and higher-order phase noise might be introduced by atmospheric turbulence or imperfect telescope optics.

Hence, an empirical method is necessary to derive robust detection limits. We classify the 1/3 of the targets with the highest $\text{SNR}_{\text{scaled}}$ as candidate detections and the rest of the targets as calibrators (cf., columns “Can?” and “Cal?” of Table 3.3). Here, $\text{SNR}_{\text{scaled}}$ is the photon noise-based SNR scaled by the K-band magnitude of the object, i.e.,

$$\text{SNR}_{\text{scaled}} = \text{SNR}_{\text{ph}} \sqrt{\frac{1}{10^{-(K-K_{\text{med}})/2.5}}}, \quad (3.13)$$

where K_{med} is the median K-band magnitude of our targets. This scaling is motivated by the fact that the brighter objects have higher photon noise-based SNRs due to smaller uncertainties, but similar quasi-static errors. Then, we repeat the Karhunen-Loève calibration (only allowing images of objects in the list of calibrators to be selected as calibrators) and the model fitting. Afterwards, we compute an empirical detection limit σ_{emp} and an empirical signal-to-noise ratio,

$$\text{SNR}_{\text{emp}} = \frac{\mathbf{c}_{\text{fit}}}{\sigma_{\text{emp}}} \quad (3.14)$$

for each of the candidate detections as described in Section 2.4.3 of Kammerer et al. (2019) and classify a candidate detection as significant, if $\text{SNR}_{\text{emp}} > 5$. Note that this empirical detection limit is based on azimuthally averaging the contrast maps \mathbf{c}_{fit} and therefore is primarily sensitive to point-like emission. Detecting

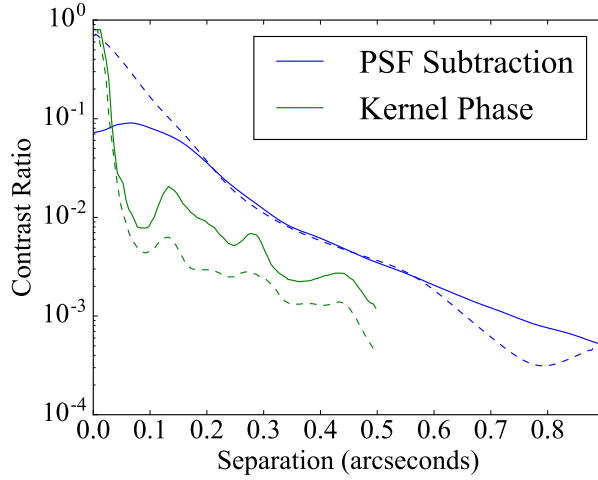


Figure 3.5: The 5σ contrast limit for AA Tau (solid curve) and CX Tau (dashed curve) as a function of separation from the star. This shows, for example, at a separation of $0.3''$ from AA Tau, the PSF subtraction method cannot detect anything less than $1/100$ the brightness of the star but kernel phase can achieve limits of $1/300$ the brightness of the star.

extended structure (such as discs) would require a more sophisticated approach, yielding higher sensitivities.

3.3.5 Comparison of both methods

The 1D contrast plot (given for each separation by averaging around an annulus of fixed radius) is shown for both the PSF subtraction and kernel phase methods at the 5σ level for 2 stars: AA Tau and CX Tau in Figure 3.5. As theoretically expected, Figure 3.5 demonstrates that the kernel phase method outperforms the PSF subtraction method over its effective range of $\sim 0.5''$ and the latter method is only useful at wider separations. This was the case for all of our targets. Our contrast limits for both methods indicate that we cannot detect objects fainter than $\sim 1/2000$ the brightness of the star even at separations of $0.5''$, which is insufficient for the detection of core-accreting giant planets (Wallace & Ireland, 2019).

3.3.6 Significant features from kernel phase analysis

The kernel phase analysis revealed several features, of which we define those with an empirical $\text{SNR}_{\text{emp}} > 5$ as significant detections. This criterion was only met by V410 Tau, which has a known brown dwarf companion (Ghez et al., 1997). We detect this known companion with both of our methods (cf., Figure 3.6). The

Table 3.3: Results of our kernel phase analysis when classifying the 1/3 most significant detections based on $\text{SNR}_{\text{scaled}}$ as candidate detections (“Can?”) and the rest as calibrators (“Cal?”) for the empirical detection method. Candidate detections with an empirical detection significance $\text{SNR}_{\text{emp}} > 5$ are classified as significant detections (“Det?”). K-band magnitudes are taken from SIMBAD.

Name	SNR_{ph}	$\text{SNR}_{\text{scaled}}$	Can?	Cal?	SNR_{emp}	Det?
IRAS 04108+2910	25.6	46.9	N	Y	–	N
FM Tau	23.5	32.8	N	Y	–	N
CW Tau	112.8	74.1	N	Y	–	N
FP Tau	23.9	35.0	N	Y	–	N
CX Tau	25.5	36.3	N	Y	–	N
2MASS J04154278+2909597	13.4	24.9	N	Y	–	N
CY Tau	25.2	32.5	N	Y	–	N
V409 Tau	21.3	33.6	N	Y	–	N
V410 Tau	450.3	372.4	Y	N	122.7	Y
BP Tau	36.5	31.7	N	Y	–	N
V836 Tau	23.6	30.4	N	Y	–	N
IRAS 04187+1927	131.8	130.5	Y	N	4.2	N
DE Tau	144.4	129.2	Y	N	2.0	N
2MASS J04221675+2654570	25.0	39.1	N	Y	–	N
FT Tau	33.3	43.0	N	Y	–	N
IP Tau	26.4	30.4	N	Y	–	N
DG Tau	1097.7	677.0	Y	N	3.5	N
DH Tau	28.3	30.2	N	Y	–	N
IQ Tau	42.2	37.4	N	Y	–	N
DK Tau	434.7	281.3	Y	N	1.8	N
JH 56	10.5	14.8	N	Y	–	N
LkHa 358	52.9	112.8	Y	N	2.1	N
HL Tau	433.7	324.3	Y	N	4.9	N
HK Tau	38.1	49.1	N	Y	–	N
2MASS J04321540+2428597	85.9	88.2	N	Y	–	N
FY Tau	66.8	67.2	N	Y	–	N
FZ Tau	194.3	141.1	Y	N	2.6	N
UZ Tau A	318.8	231.9	Y	N	1.4	N
GI Tau	43.2	40.2	N	Y	–	N
DL Tau	66.9	64.5	N	Y	–	N
HN Tau A	80.4	94.2	N	Y	–	N
DM Tau	11.6	23.0	N	Y	–	N
CI Tau	89.6	79.9	N	Y	–	N
IT Tau	37.6	34.6	N	Y	–	N
AA Tau	175.2	175.6	Y	N	2.3	N
DN Tau	46.5	45.9	N	Y	–	N
2MASS J04354093+2411087	80.1	94.9	Y	N	1.6	N
HP Tau	79.0	65.2	N	Y	–	N
DO Tau	181.2	129.0	Y	N	3.2	N
LkCa 15	117.2	124.0	Y	N	3.1	N
JH 223	15.2	29.7	N	Y	–	N
GO Tau	19.4	35.2	N	Y	–	N
DQ Tau AB	58.9	57.3	N	Y	–	N
DR Tau	272.8	159.3	Y	N	1.4	N
DS Tau	40.2	40.1	N	Y	–	N
GM Aur	39.6	44.2	N	Y	–	N
MWC 480	1244.7	391.0	Y	N	1.6	N
2MASS J05052286+2531312	13.0	54.8	N	Y	–	N
RW Aur A	571.5	357.0	Y	N	3.6	N
V819 Tau	17.1	20.4	N	Y	–	N

Name	Sep. (mas)	Pos. Ang. ($^{\circ}$)	Contrast
V410 Tau B	332.2 ± 0.2	144.11 ± 0.05	0.0542 ± 0.0004

Table 3.4: Properties of the companion to V410 Tau with uncertainties from the kernel phase analysis.

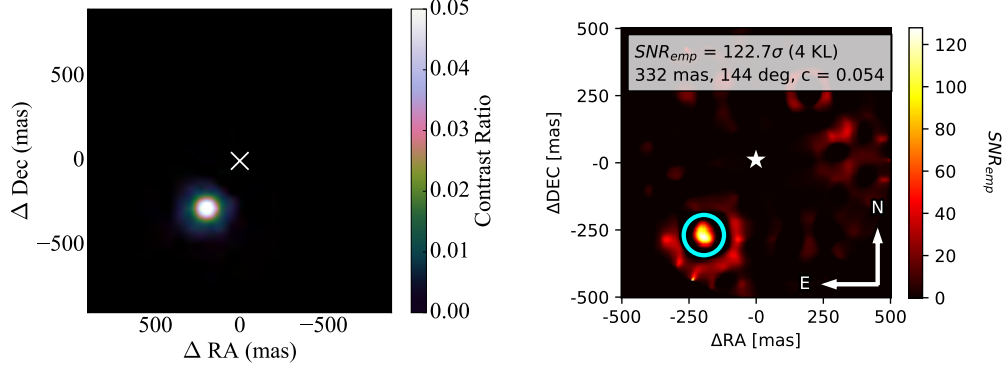


Figure 3.6: Contrast map of V410 Tau using PSF subtraction (left panel) and kernel phase detection map (right panel). The host star is in the middle of the images and is removed by both methods. The companion is clearly visible to the south-east and consistently detected with both methods. In the kernel phase detection map, V410 Tau B’s position is highlighted with a cyan circle and there is a residual halo around it which is caused by the limited Fourier coverage and model redundancies and disappears after subtracting the kernel phase signal of V410 Tau B from the data.

kernel-phase technique yields very precise constraints on its position and contrast, obtained from an MCMC fit (cf., Figure 3.7), and its best-fit parameters are listed in Table 3.4.

Note that, as shown in Table 3.3, HL Tau has a feature with $\text{SNR}_{\text{emp}} = 4.9$ so only just falls short of our detection threshold. We believe this to be a feature of HL Tau’s large protoplanetary disc (ALMA Partnership et al., 2015) and not a companion.

3.4 Wide separation analysis

Due to a focus on efficient observations at small angles (see Section 3.3.1), these data were mostly taken in a sub-array readout mode, limiting the field of view. We further extended our analysis to wider angles which were not covered by the 192×192 pixel cleaned images and analysis shown in Section 3.3.3. At these separations beyond $\sim 0.8''$, point spread function features were almost non-existent so we could use a more conventional image analysis with a simplified

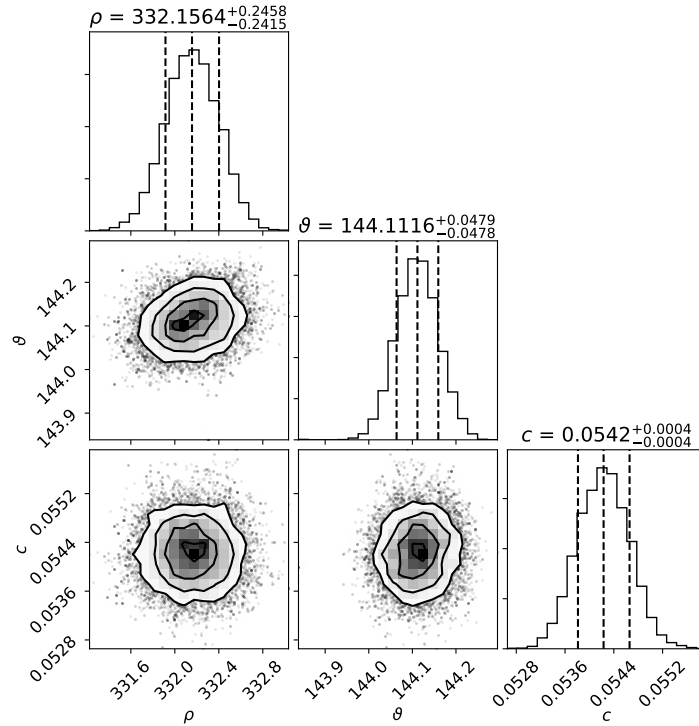


Figure 3.7: Corner plot (Foreman-Mackey, 2016) for an MCMC initialized around the best fit-position for the companion of V410 Tau. The three fitted parameters are the angular separation ρ , the position angle θ and the contrast c . The MCMC is computed from the kernel phase using emcee (Foreman-Mackey et al., 2013) with six random walkers initialized around the best-fit position and a temperature of $f_{\text{err}}^2 = (\sigma_{\text{emp}}/\sigma_{\text{ph}})^2 = 13.4 \approx \chi_{\text{red}}^2$, in order to find the best-fit parameters including their correlated uncertainties by maximizing the log-likelihood of the binary model (cf. Kammerer et al., 2019).

point-spread function model.

To clean these full images, our image reduction simply consisted of dividing by a master flat and correcting bad pixels. The master flat was created from all dithered observations for a night, using pixels significantly away from detected objects. Companions were searched for over an (ρ, θ) grid in polar sky coordinates by performing aperture photometry with a simplified Gaussian PSF model, as described below. This truncated PSF model enabled searching for companions closer to the image edge.

For each tested grid point, including the central star (i.e. separation ρ of 0), we found a least squares solution to the flux F of a model:

$$d_k = B + F g_k, \quad (3.15)$$

where d_k is the data for pixel k over a 16 x 16 pixel grid, g_k is a normalised Gaussian function with width matched to the observed PSF and B the background. This least-squares flux solution for F is simply given by:

$$F = \frac{\sum_k (g_k - \sum g_k / N) d_k}{\sum_k (g_k - \sum g_k / N) g_k}, \quad (3.16)$$

where $N = 256$, the total number of pixels. The uncertainty in pixels k was simply estimated by the root mean square residuals of the fit, and the uncertainty in F obtained by standard error propagation assuming independent background-limited uncertainties for all pixels. These fluxes were converted to contrasts by dividing by the fitted flux at a separation of 0, and these (ρ, θ) contrast maps averaged together with inverse variance weighting. Finally, uncertainties were corrected at each radius ρ to ensure that the median absolute deviation of the residuals at every radius matched that of a unit Gaussian.

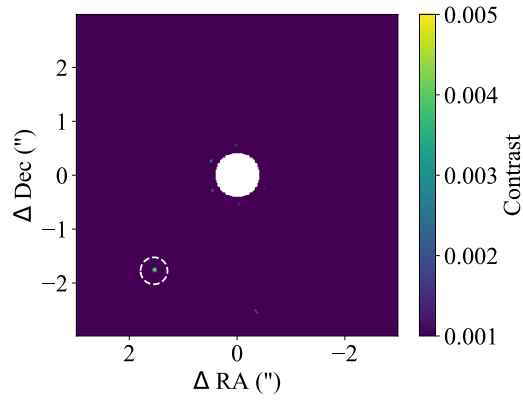
By highlighting features with significance greater than 7σ and removing those that can be explained by the few residual speckles, we are able to determine the approximate positions of companions to our targets. The contrast and position of each companion is calculated by fitting to the original reduced images. We are able to detect significant companions for 9 of our objects, the properties of which are listed in Table 3.5.

The companion of DH Tau is the only substellar-mass companion we are able to detect and our contrast is consistent with other studies such as Kraus et al. (2013). We also find a high-contrast companion to HK Tau. The fitted contrast maps for DH Tau and HK Tau are shown in Figure 3.8.

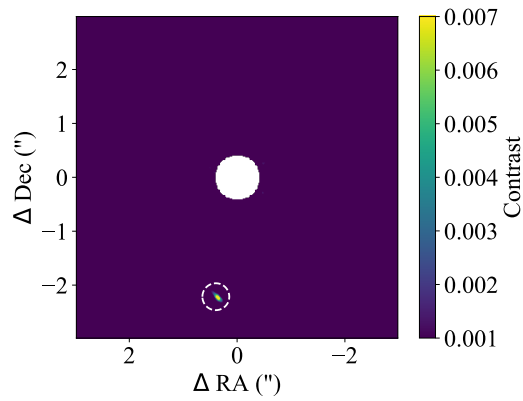
Despite the high contrast of the companion to HK Tau, previous studies have concluded that it is a stellar-mass companion of similar spectral type to the

Table 3.5: Properties of fitted companions

Name	Separation (")	Position Angle (°)	Contrast (Δm)	# Observations
2MASS J04354093	2.11	175.0	1.98 ± 0.01	1
2MASS J05052286	2.35	59.8	2.24 ± 0.01	2
DH Tau	2.35	139.0	5.75 ± 0.02	1
DK Tau	2.39	119.5	1.81 ± 0.01	4
HK Tau	2.25	169.9	5.27 ± 0.02	1
IRAS 04278+2253	1.29	95.9 ± 0.6	2.00 ± 0.02	1
IT Tau	2.43	225.8	1.64 ± 0.01	1
JH 223	2.15	342.2	2.40 ± 0.01	3
RW Aur A	1.49	254.6 ± 0.1	2.42 ± 0.01	2



(a) Fitted Contrast Map of DH Tau



(b) Fitted Contrast Map of HK Tau

Figure 3.8: Contrast Maps of DH Tau and HK Tau with the companions circled.

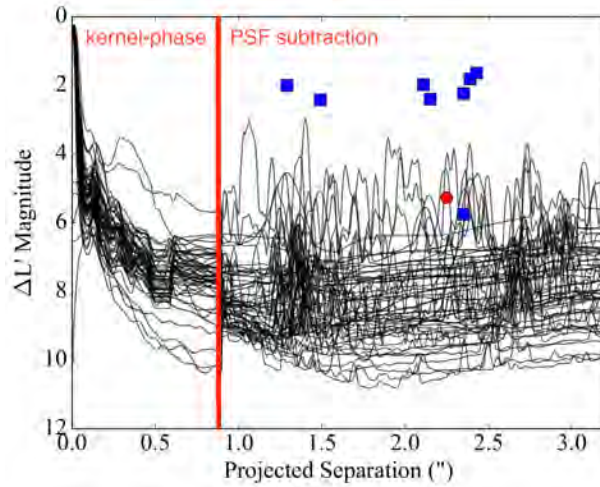


Figure 3.9: 5σ contrast curves for all targets including contrast and separation of detected companions. Each line is our contrast limit for a particular target and the markers show detected companions. The red circle indicates the companion to HK Tau. **The red vertical line separates the parameter spaces where kernel-phase and PSF subtraction were applied.**

primary and is obscured by an edge-on circumstellar disc (Stapelfeldt et al., 1998). This circumstellar disc is represented by the elongated shape of the companion. Although we did not detect any additional brown dwarf mass companions to our targets, we now have a more complete picture of our contrast limits at wide separations. These contrast limits are listed in Table 3.6. Figure 3.9 shows the contrast curves for all targets with the detected companions indicated. The companion to HK Tau is marked with a red circle and other companions are marked with blue squares.

Assuming an age of 1 Myr for our planets, which is conservative as they may still be forming in a Class II disc, we converted the contrast into a mass limit using models from Spiegel & Burrows (2012). For this conversion we need to assume an appropriate internal entropy for our planets. As mentioned previously, planet luminosity and internal entropy is highly uncertain but recent models suggest few Jupiter mass planets have initial entropy no less than $\sim 10\text{--}11 k_{\text{B}}/\text{baryon}$ (e.g. Mordasini, 2013; Berardo et al., 2017; Marleau et al., 2019). The hot-start and cold-start entropy curves take the form of a ‘tuning fork’ with hot-start entropy increasing with mass and cold-start entropy decreasing with mass (Marley et al., 2007). However, since hot-start models are expected to be more likely for high-mass planets due to the difficulty in radiating away the accretion luminosity for all but the lowest accretion rates, a reasonable assumption is that the average entropy is fairly constant at somewhere around $10\text{--}11 k_{\text{B}}/\text{baryon}$ across the $1\text{--}10 M_{\text{J}}$ range. To keep our model simple, we assume a single value of initial internal

Table 3.6: Contrast limits for our targets using all three methods.

Name	Contrast Limit (Δm)						
	0.1"	0.3"	0.5"	0.7"	1"	1.5"	2"
IRAS 04108+2910	5.09	6.03	6.79	6.52	7.40	7.66	7.13
FM Tau	5.49	6.64	7.10	6.85	7.87	7.85	7.67
CW Tau	4.94	7.14	8.41	6.58	9.24	9.82	9.87
FP Tau	5.54	7.06	8.04	7.26	7.93	7.65	7.57
CX Tau	5.84	6.55	8.31	8.06	8.15	7.85	7.64
2MASS J04154278+2909597	5.68	6.02	7.01	6.40	6.35	6.79	6.35
CY Tau	5.29	7.25	8.14	7.57	8.45	7.92	7.25
V409 Tau	5.60	6.78	7.63	7.13	7.68	7.96	7.45
V410 Tau	4.88	3.54	5.60	7.03	5.75	6.53	4.96
BP Tau	5.54	7.51	8.49	7.89	9.43	9.00	8.82
V836 Tau	5.00	6.59	7.43	7.12	8.05	7.98	7.86
IRAS 04187+1927	4.68	6.42	7.84	7.82	8.31	8.82	9.06
DE Tau	4.67	6.70	7.96	7.59	9.02	9.13	8.98
RY Tau	6.01	8.07	9.69	10.10	8.27	9.19	9.47
2MASS J04221675+2654570	5.59	6.39	7.61	7.50	8.39	8.76	8.20
FT Tau	5.61	6.36	7.41	7.20	8.28	8.64	8.17
IP Tau	6.29	7.09	8.16	6.90	7.51	7.27	7.37
DG Tau	3.91	6.26	7.11	6.84	8.30	7.39	9.80
DH Tau	6.05	6.15	7.93	7.62	8.57	8.06	8.47
IQ Tau	6.57	6.49	8.08	7.83	8.89	8.94	8.77
UX Tau	6.34	8.25	8.73	8.99	6.55	6.39	5.97
DK Tau	5.05	6.24	7.71	7.72	8.69	9.11	9.13
IRAS 04278+2253	3.29	4.33	5.13	5.45	6.62	7.43	8.73
JH 56	6.56	7.15	7.64	6.80	7.81	7.73	7.42
LkHa 358	3.92	5.59	6.61	6.94	8.39	7.39	7.58
HL Tau	4.90	6.16	7.37	7.26	8.47	10.36	10.43
HK Tau	5.21	6.57	7.66	7.47	7.29	7.36	7.13
2MASS J04321540+2428597	5.10	6.59	7.56	7.53	8.75	9.60	9.38
FY Tau	5.44	6.77	7.71	8.14	8.92	8.81	8.87
FZ Tau	5.18	6.37	7.23	7.59	9.31	10.15	9.71
UZ Tau A	3.99	5.89	7.01	7.08	9.21	9.62	9.01
GI Tau	5.48	7.23	8.30	7.39	7.41	7.50	8.51
DL Tau	5.20	7.12	8.18	8.04	9.29	9.51	9.21
HN Tau A	5.07	6.47	7.37	7.79	8.70	9.07	8.92
DM Tau	5.51	6.27	6.95	6.85	7.23	7.17	6.83
CI Tau	5.71	7.24	8.05	8.40	9.02	9.36	9.17
IT Tau	4.39	6.15	7.55	7.61	8.64	8.70	8.50
AA Tau	4.99	6.01	7.25	7.33	8.51	8.42	8.16
DN Tau	6.90	7.22	8.05	7.27	9.19	8.99	8.64
2MASS J04354093+2411087	5.21	6.13	6.87	7.63	8.91	9.07	7.51
HP Tau	5.17	6.28	7.89	7.20	6.66	6.11	5.38
DO Tau	4.86	6.05	7.88	7.34	8.62	9.36	9.70
LkCa 15	4.82	6.00	7.54	8.34	7.38	7.36	7.82
JH 223	6.11	6.92	7.36	7.16	7.44	7.10	6.71
GO Tau	5.48	6.81	7.29	6.81	7.53	7.35	7.16
DQ Tau	5.55	7.30	8.04	8.57	9.07	9.18	8.63
DR Tau	4.82	6.32	7.57	7.96	9.14	10.30	10.09
DS Tau	6.12	6.71	7.78	7.52	8.76	8.91	8.84
GM Aur	5.27	6.99	8.25	7.62	8.37	8.07	8.09
AB Aur	6.40	8.58	9.40	9.86	7.75	9.83	9.26
SU Aur	5.72	7.95	9.25	9.75	8.73	8.16	8.09
MWC 480	4.76	6.13	6.81	7.34	8.86	10.34	10.52
2MASS J05052286+2531312	5.00	6.04	6.53	6.59	6.63	6.49	6.84
RW Aur A	4.55	5.92	7.02	7.10	9.06	5.23	10.32
V819 Tau	6.07	7.08	7.92	7.63	8.42	8.36	7.97

entropy, regardless of mass. Analysis of directly imaged planets indicates β -Pic b, at the high-mass end of the planet distribution, formed with a minimum entropy of $\sim 10.5 k_{\text{B}}$ /baryon (Marleau & Cumming, 2014). We have decided to use this value to calculate mass limits as it is also close to the average initial entropy of a $1 M_{\text{J}}$ planet according to Spiegel & Burrows (2012) and can be applied to a wide temperature range of 500–1500 K (Berardo et al., 2017). Using this entropy, we calculate planet magnitude as a function of mass and age using Spiegel & Burrows (2012), and thus convert contrast ratio to mass.

Using the stellar masses shown in Table 3.1, this mass limit was also converted to a mass ratio. This is shown for all targets in Figure 3.10. As shown in Figures 3.9 and 3.10, the companion to DH Tau is close to the faintest we were able to detect. Note while the companion to HK Tau is included (shown with a red circle,) the circumstellar disc reduces its brightness **and its true mass is in the stellar-mass regime (e.g. Jensen & Akeson, 2014), much higher than that shown in Figure 3.10.** The top panel of Figure 3.10 shows that we are able to detect planetary-mass companions ($< 13 M_{\text{J}}$) for most of our targets at wide separations (> 100 au). The lack of new brown dwarf detections from our data implies these companions are rare at wide separations, providing evidence of the “brown dwarf desert” described by Marcy & Butler (2000) and Grether & Lineweaver (2006). The lack of planetary-mass detections allows us to constrain the maximum frequency of hot-start planets in the TMC.

3.5 The frequency of wide separation massive planets

3.5.1 Total probability of planet detection

Despite our lack of planet detections, Figure 3.10 shows that our limits are sufficient for the detection of young planetary-mass companions for many of our targets. This opens up the possibility of detecting wide systems analogous to HR 8799. Combining the contrast limits for all of our targets, we can determine the likelihood of detecting a planet as a function of mass and semi-major axis. We apply the same method as Figure 3.10 with an age of 1 Myr and initial entropy of $10.5 k_{\text{B}}$ /baryon to convert magnitude to mass using models from Spiegel & Burrows (2012). Using Monte-Carlo sampling, we randomise the system inclination and planet positions to get a more comprehensive view of our capabilities. This is shown in Figure 3.11. The HR 8799 planets are shown, as well as the $13 M_{\text{J}}$ planet-mass threshold.

3.5.2 Comparison with HR 8799 analogues

The result in Figure 3.11 shows that, averaged over all targets, we have a greater than 80% probability of detecting $> 10 M_{\text{J}}$ planets at separations beyond 100 au.

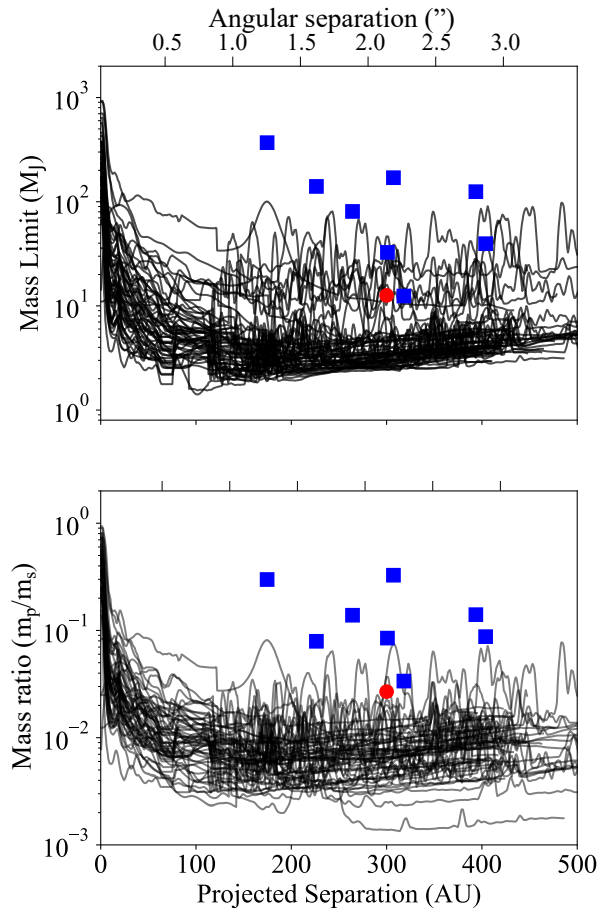


Figure 3.10: Mass and mass ratio limits for all targets. The companion to HK Tau is again represented by a red circle as the actual mass is assumed to be higher than shown here. The x-axis on the top shows the angular separation in arcseconds, obtained from the projected separation in au at an average distance of 140 pc for Taurus.

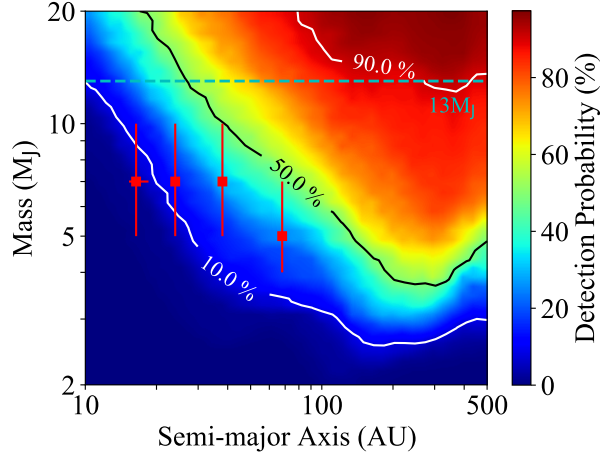


Figure 3.11: Probability of planet detection as a function of mass and semi-major axis for a planet age of 1 Myr and initial internal entropy of $10.5 k_B/\text{baryon}$. The HR 8799 planets and the planet-mass threshold of $13 M_J$ are also shown.

However, even at the lower mass and separations of an HR 8799 analogue, we still have a $\sim 20\%$ chance of detecting this system at an age of 1 Myr with an initial internal entropy of $10.5 k_B/\text{baryon}$. Applying the luminosity curves from Spiegel & Burrows (2012) to our HR 8799 analogue, we determine the probability of detecting these planets at ages of 0–3 Myr. Our detection probability of the 4 planets around HR 8799 is shown in Figure 3.12.

The curves in Figure 3.12 demonstrate how the planets around HR 8799 cool and fade over time. When the planets are newly formed, we have a greater than 40% chance of detecting HR 8799 b and c analogues. At an age of 3 Myr, we only have a 30% chance of detecting these planets.

The stars in our sample are believed to have an age of $\sim 2\text{--}3$ Myr, which implies any planets around our targets are not much older than ~ 1 Myr. Since no planets were detected in our sample, we can make a statement on the maximum frequency of wide and massive systems.

3.5.3 Planet frequency

We use the same method from Vigan et al. (2012) to calculate the maximum planet frequency in a given range. This method assumes the likelihood of the data d for a given frequency f is given by

$$L(\{d_i\} | f) = \prod_i^N (1 - fp_i)^{1-d_i} (fp_i)^{d_i}, \quad (3.17)$$

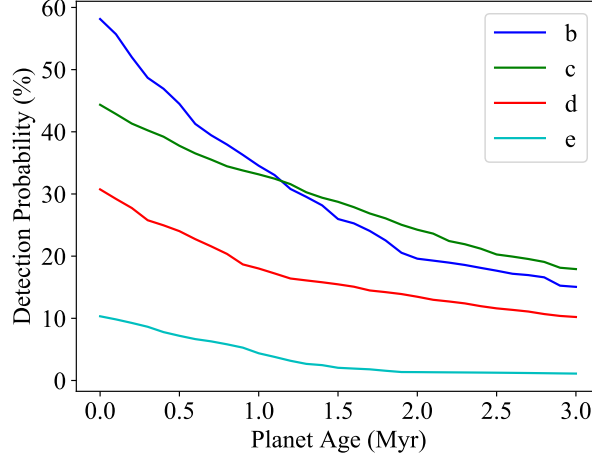


Figure 3.12: Detection probability of HR 8799 analogues (averaged over all targets) versus age of the planets. An age of 0 corresponds to the moment the planets stop accreting.

where N is the number of targets, in our case 55, d_i is 0 if no planets are detected and 1 if at least 1 planet is detected. The probability p_i is the probability of detecting planets in a given range assuming an appropriate planet distribution. We assume a power-law distribution in mass and semi-major axis such that

$$\frac{dN_{\text{planets}}}{d\ln M d\ln a} = CM^\alpha a^\beta. \quad (3.18)$$

We obtain the posterior distribution from Bayes' theorem:

$$p(f|\{d_i\}) = \frac{L(\{d_i\}|f)p(f)}{\int_0^1 L(\{d_i\}|f)p(f)df}, \quad (3.19)$$

where $p(f)$ is the priori probability density of the frequency f which we set to a uniform value of 1. For a given confidence level, the maximum frequency is obtained using

$$\text{Confidence} = \int_{f_{\min}}^{f_{\max}} p(f|\{d_i\})df. \quad (3.20)$$

We set f_{\min} to 0 and rearrange to find f_{\max} . This value was calculated over a semi-major axis range of 10–500 au, the same as Figure 3.11, and a mass range of 2–13 M_J . Since we did not detect any planets in this range, all of our values of d_i will be 0. To obtain our probabilities p_i , we try several values for the mass and semi-major axis power-law indices while keeping the range constant at [2,13] M_J and [10,500] au. The planet age is again set to be 1 Myr and the initial internal

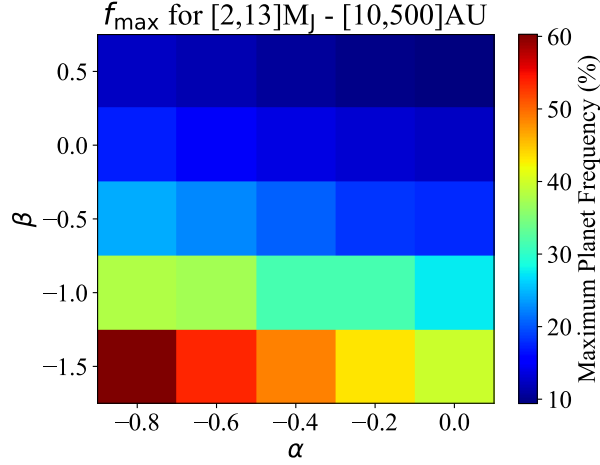


Figure 3.13: Maximum planet frequency for mass 2–13 M_J and semi-major axis 10–500 au at 90% confidence with differing mass and semi-major axis power-law indices (α and β respectively.)

entropy is $10.5 k_B$ /baryon. The maximum frequency at a 90% confidence level is shown in Figure 3.13.

As shown in Figure 3.13, the maximum frequency is better constrained at higher power-law indices but these are considered unlikely power-law indices at this mass and semi-major axis range. The symmetric power law given by Fernandes et al. (2019) has a mass index of $\alpha = -0.45$ and a semi-major axis index of $\beta = -0.95$. The study from Bowler & Nielsen (2018) has $\alpha = -0.65$ and $\beta = -0.85$. Our result shows that less than $\sim 30\%$ of stars have a planet in this mass and semi-major axis range if we assume one of these power-law distributions.

Assuming a power-law distribution in which $\alpha = -0.5$ and $\beta = -1$, we also calculate the dependence of planet frequency on mass and semi-major axis. This is shown in Figure 3.14 over a mass range of 2–13 M_J and semi-major axis range of 10–500 au at a 90% confidence level. The planets around HR 8799 are also marked.

The result from Figure 3.14 confirms that massive planets at wide separations are very rare, occurring around less than 10% of stars. Planets with the mass and semi-major axis similar to HR 8799 b, c and d are expected to occur around less than 20% of stars, while analogues to HR 8799 e may be more common, but we cannot draw a strong conclusion from our results regarding this aspect.

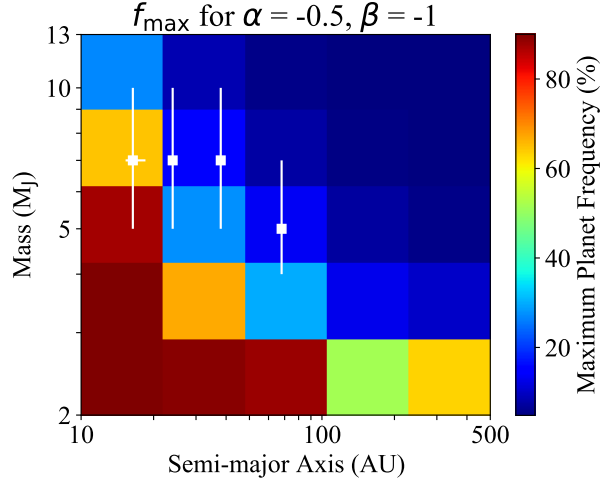


Figure 3.14: Maximum planet frequency assuming a power law with $\alpha = -0.5$ and $\beta = -1$ at 90% confidence. The white points show the planets around HR 8799.

3.6 Summary and conclusions

In this work, we have conducted a high-contrast imaging survey of the Taurus molecular cloud with the aim of finding any massive young planets and planets in the process of forming. Using the PSF subtraction technique, **we achieved sensitivity to planetary-mass companions outward of ~ 500 mas. In addition, we applied the kernel-phase method to increase the sensitivity at small separations < 500 mas and inward of ~ 70 au, but our limits remain insufficient for the detection of young solar-system analogues.** For non-accreting planets, our detection limits were similar to Kraus et al. (2011) at 20 au ($\sim 15 M_J$ median mass limit), but a factor of 10 deeper in mass at 150 au ($\sim 3 M_J$ median mass limit). Our probabilities of planet detection as a function of mass and semi-major axis are broadly comparable to the result from SHINE, the SPHERE infrared survey (Vigan et al., 2020) which used a larger sample of targets.

The continued lack of new brown dwarf companions at wide separations is further evidence of the so-called “brown dwarf desert” described by Marcy & Butler (2000) and Grether & Lineweaver (2006) extending to separations beyond that probed by radial velocity surveys. We were able to detect several known wide companions, including the roughly planetary-mass companion DH Tau b and the circumstellar disc around the companion to HK Tau.

We determined that, if the HR 8799 planets were placed in the TMC at the appropriate age, we could have detected analogues to HR 8799 b, c, and d around more than 15% of our targets at an age of 1 Myr. Assuming a similar power law to Fernandes et al. (2019), we find that planets with the mass or semi-major axis

of HR 8799 b, c, and d occur around less than 20% of stars. Generalising this to planets from 2–13 M_J at separations 10–500 au, we found that, assuming the same power law, the planet frequency in this mass and semi-major axis range is less than 30% at a 90% confidence level. Future instruments such as VIKiNG on VLTI and METIS on the E-ELT will be required to improve on our detection limits, to more precisely constrain planet frequency.

Acknowledgements

We thank the anonymous referee for their useful comments which greatly improved this study. The data presented herein were obtained at the W. M. Keck Observatory, which is operated as a scientific partnership among the California Institute of Technology, the University of California and the National Aeronautics and Space Administration. The observatory was made possible by the generous financial support of the W. M. Keck Foundation. A.L.W. would like to thank the Australian Government for their support through the Australian Postgraduate Award Scholarship and the Research School of Astronomy and Astrophysics at the Australian National University for the ANU Supplementary PhD Scholarship. M.J.I. acknowledges funding provided by the Australian Research Council (Discovery Project DP170102233 and Future Fellowship FT130100235). C. F. acknowledges funding provided by the Australian Research Council (Discovery Project DP170100603 and Future Fellowship FT180100495), and the Australia-Germany Joint Research Cooperation Scheme (UA-DAAD).

Mid-infrared photometry of the T Tauri triple system with kernel phase interferometry

*This chapter has been accepted for publication as a peer-reviewed article in *Astronomy & Astrophysics*. It was written by Jens Kammerer under the supervision of Markus Kasper, Michael J. Ireland, and Frantz Martinache. Romain Laugier helped with the development of the pupil model and the remaining co-authors contributed to the observing proposal and the VISIR-NEAR instrument which enabled the observations analyzed in this chapter.*

Jens Kammerer,^{1,2} Markus Kasper,¹ Michael J. Ireland,² Rainer Köhler,³ Romain Laugier,⁴ Frantz Martinache,⁴ Ralf Siebenmorgen,¹ Mario E. van den Ancker,¹ Roy van Boekel,⁵ Tom M. Herbst,⁵ Eric Pantin,⁶ Hans-Ulrich Käufl,¹ Dominique J. M. Petit dit de la Roche¹ and Valentin D. Ivanov¹

1. European Southern Observatory, Karl-Schwarzschild-Str. 2, 85748, Garching, Germany
2. Research School of Astronomy & Astrophysics, Australian National University, Canberra, ACT 2611, Australia
3. University of Vienna, Department of Astrophysics, Türkenschanzstr. 17 (Sternwarte), 1180 Vienna, Austria
4. Université Côte d'Azur, Observatoire de la Côte d'Azur, CNRS, Laboratoire Lagrange, Lagrange, France
5. Max Planck-Institut für Astronomie, Königstuhl 17, 69117 Heidelberg, Germany
6. Laboratoire CEA, IRFU/DAP, AIM, Université Paris-Saclay, Université Paris Diderot, Sorbonne Paris Cité, CNRS, 91191 Gif-sur-Yvette, France

Preamble

In this chapter, we move away from the very high contrast regime toward the very high angular resolution regime. We will remain in the Taurus star-forming region and study the famous T Tauri triple star system. The kernel phase technique, combined with the very high Strehl delivered by the VLT/VISIR-NEAR experiment, will enable us to obtain photometry of all three components of the T Tauri system, including its southern binary at a separation of $\sim 0.2\text{--}0.3 \lambda/D$. We will use this photometry, together with data from the literature, to learn more about the multiple misaligned circumstellar and circumbinary disks in the T Tauri system. Furthermore, this work depicts the first use of the kernel phase technique in the mid-infrared.

Abstract

T Tauri has long been the prototypical young pre-main-sequence star. However, with increasing resolution and sensitivity, T Tauri has now been decomposed into a triple system with a complex disk and outflow geometry. We aim to measure the brightness of all three components of the T Tauri system (T Tau N, T Tau Sa, and T Tau Sb) in the mid-infrared in order to obtain photometry around the $\sim 9.7 \mu\text{m}$ silicate feature. This allows us to study their variability and to investigate the distribution of dust and the geometry of circumstellar and circumbinary disks in this complex system. We observe the T Tauri system with the Very Large Telescope (VLT)/VISIR-NEAR instrument, performing diffraction-limited imaging in the mid-infrared. With kernel phase interferometry post-processing of the data, and using the astrometric positions of all three components from VLT/SPHERE, we measure the three components' individual brightnesses (including the southern binary at an angular separation down to $\sim 0.2 \lambda/D$) and obtain their photometry. In order to validate our methods, we simulate and recover mock data of the T Tauri system using the observed reference point-spread function of HD 27639. We find that T Tau N is rather stable and shows weak silicate emission, while T Tau Sa is highly variable and shows prominent silicate absorption. T Tau Sb became significantly fainter compared to data from 2004 and 2006, suggesting increased extinction by dust. The precision of our photometry is limited by systematic errors in kernel phase interferometry, which is consistent with previous studies using this technique. Our results confirm the complex scenario of misaligned disks in the T Tauri system that had been observed previously, and they are in agreement with the recently observed dimming of T Tau Sb in the near-infrared. Our mid-infrared photometry supports the interpretation that T Tau Sb has moved behind the dense region of the Sa-Sb circumbinary disk on its tight orbit around Sa, therefore suffering increased extinction.

4.1 Introduction

T Tauri (T Tau) is the historical prototype of a young and accreting low-mass star. As such, it has provided astronomers with many surprise discoveries over the past decades. While T Tau was initially believed to be a single star surrounded by a circumstellar disk (CSD), from which it accretes matter, [Dyck et al. \(1982\)](#) used near-infrared speckle interferometry to show that it is in fact a binary composed of an optically bright northern component (T Tau N) and an optically faint southern component (T Tau S). It was suspected that the optical faintness of T Tau S is caused by extinction from circumstellar material that hides the southern component behind gas and dust. Indeed, [Ghez et al. \(1991\)](#) found T Tau S to be variable at all near-infrared to mid-infrared wavelengths and concluded that its spectral energy distribution (SED) must be dominated by variable accretion from a CSD. Five years later, the detection of perpendicular jets expelled from T Tau N and S supported the theory that T Tau is composed of not one, but two young and accreting stars ([Herbst et al., 1996](#)).

When [Koresko \(2000\)](#) observed T Tau S with the Keck Near-IR Camera (NIRC) using speckle interferometry, they found that it is itself a tight binary consisting of T Tau Sa and T Tau Sb, and the detection of significant orbital motion of T Tau Sa around Sb by [Duchêne et al. \(2002\)](#) implied a high mass ratio between the two southern components. Their medium-resolution spectroscopy further revealed that T Tau Sa has a featureless spectrum and that Sb is an embedded M-type classical T Tauri star (CTTS), suggesting that both southern components are surrounded by dense material. Later, [Kasper et al. \(2002\)](#) and [Duchêne et al. \(2005\)](#) found the CSD of T Tau Sa to be oriented edge-on and attributed the strong optical extinction of ~ 15 mag around the southern components to circumbinary material (e.g., an Sa-Sb circumbinary disk). [Duchêne et al. \(2006\)](#) identified T Tau Sa to be the most massive component of the triple system, most likely a young Herbig Ae star, from orbital monitoring.

Around 2005, the triple system was first resolved in the N-band by two teams. [Ratzka et al. \(2009\)](#) used the Very Large Telescope Interferometer (VLTI) MID-infrared Interferometric instrument (MIDI) to observe T Tau in November 2004. They found that the silicate band at $9.7 \mu\text{m}$ is seen in absorption around both southern components, which confirmed a high extinction by Sa-Sb circumbinary material. Moreover, they resolved a small edge-on disk around T Tau Sa, roughly oriented from north to south. [Skemer et al. \(2008\)](#) used the Multiple Mirror Telescope (MMT) deformable secondary mirror for adaptive optics-assisted imaging in the mid-infrared in November 2006. The high Strehl ratio and the good point-spread function (PSF) stability allowed them to resolve the southern binary at one-third of the classical diffraction limit of a telescope. Their data allowed them to conclude that the material producing the strong silicate absorption toward T Tau S is entirely in front of Sa. Later, [van Boekel et al. \(2010\)](#) measured a very rapid flux increase at $12.8 \mu\text{m}$ of the unresolved T Tau S binary over just

four days, which they attributed to an increased accretion rate. Slower variations could still be well produced by variable extinction, and the most likely scenario is a combination of both processes.

Through orbital monitoring with the Very Large Telescope (VLT) Spectro-Polarimetric High-contrast Exoplanet Research instrument (SPHERE), Köhler et al. (2016) were able to precisely measure the orbits of all three components of the T Tau system, as well as their masses. They found the masses of T Tau Sa and Sb to be $\sim 2.12 M_{\odot}$ and $\sim 0.53 M_{\odot}$, respectively, using a mass of ~ 1.83 – $2.14 M_{\odot}$ for T Tau N (Loi­nard et al., 2007). Recent near-infrared polarimetry suggests an Sa-Sb circumbinary disk (CBD) with a size of ~ 150 mas and a position angle of ~ 30 deg (Yang et al., 2018). This would imply that T Tau Sb is currently moving along its orbit around Sa through the Sa-Sb CBD plane and should therefore suffer noticeable extinction for the first time since its discovery. Indeed, T Tau Sb has recently been dimming in the near-infrared (Schaefer et al., 2020), and Köhler & Kubiak (2020) proposed that this dimming is caused by Sb passing through the Sa-Sb CBD plane, based on the J-K-band photometry of the system.

In this paper, we present new mid-infrared ($\sim 10 \mu\text{m}$) photometry of all three components of the T Tau system obtained with the VLT Imager and Spectrometer for mid-IR-New Earths in the Alpha Centauri Region instrument (VISIR-NEAR) using kernel phase interferometry. Our observations were conducted in December 2019 when the southern binary was separated by only ~ 64 mas, which corresponds to $\sim 0.2 \lambda/D$ at the longest observed wavelengths. Our data allow us to study the brightness of the individual components on and off the $9.7 \mu\text{m}$ silicate feature as well as their variability. The silicate feature is interesting since it contains information about the nature of the circumstellar dust and about the orientation and geometry of the CSDs in this ever-fascinating system.

4.2 Observations

We observed T Tau with the VISIR-NEAR instrument of the European Southern Observatory’s (ESO) VLT at the summit of Cerro Paranal in Chile. VISIR-NEAR is mounted on the Cassegrain focus of Unit Telescope 4 (UT4) and consists of the VISIR instrument (Lagage et al., 2004) plus the NEAR upgrade (Käuffl et al., 2018), which enables mid-infrared imaging with extreme adaptive optics. Our observations are part of the VISIR-NEAR science demonstration program 60.A-9107(E), PI M. Kasper, and are summarized in Table 4.1.

We acquired data for both T Tau and a PSF reference (HD 27639) in pupil-tracking mode, at wavelengths of $8.98 \mu\text{m}$ (filter name ARIII), $9.81 \mu\text{m}$ (SIV_1), $10.71 \mu\text{m}$ (SIV_2), and $12.80 \mu\text{m}$ (NEII). The sky offset between T Tau and the PSF reference is ~ 1.3 deg, and the difference in average airmass is ~ 0.04 .

Table 4.1: Observing log for program 60.A-9107(E). All data were taken on December 16, 2019. Reported are the number of exposures per chopping position (NDIT), the exposure time (DIT), the number of chopping cycles (N_{chop}), the chopping frequency (ν_{chop}), the number of frames after averaging (N_{avg}), and the number of good frames (N_{good}).

Start time (UT)	Object	Filter	λ [μm]	NDIT	DIT [ms]	N_{chop}	ν_{chop} [Hz]	N_{avg}	N_{good}
02:01:24	T Tau	NEII	12.80	8	25	66	2.222	10	10
02:08:18	T Tau	SIV_1	9.81	9	22	75	2.273	12	6
02:16:51	T Tau	SIV_2	10.71	9	22	75	2.273	12	12
02:25:28	T Tau	ARIII	8.98	6	80	40	0.893	15	7
03:05:48	HD27639	NEII	12.80	8	25	66	2.222	4	3
03:08:58	HD27639	SIV_1	9.81	9	22	75	2.273	4	2
03:12:26	HD27639	SIV_2	10.71	9	22	75	2.273	8	6
03:28:05	HD27639	ARIII	8.98	6	80	40	0.893	4	2

Atmospheric turbulence was removed almost entirely by the adaptive optics facility (AOF, [Ströbele et al., 2006](#)) of UT4, leaving quasi-static aberrations (such as chromatic aberrations of the filters) as the dominant systematic error. These errors can be identified and calibrated by our kernel phase analysis.

4.3 Data reduction

At the time of our observations, the southern binary of the T Tau triple system was separated by ~ 64 mas, which is equivalent to 0.28, 0.26, 0.24, and $0.20 \lambda/D$ in the ARIII, SIV_1, SIV_2, and NEII filters, respectively. Such small separations are very challenging for high-resolution single-dish imaging. Since VISIR-NEAR is mounted at the UT4, which also hosts the AOF, the instrument achieves extremely high Strehl ratios in the mid-infrared. This makes our data set ideal for an analysis with the kernel phase technique, which models a single-dish telescope as an interferometer during the post-processing of the images. The kernel phase technique relies on a linear relationship between the pupil plane phase and the Fourier phase of the images, possible only in the high-Strehl regime. With the known astrometry of the T Tau triple system from observations at shorter wavelengths, we can use the kernel phase technique to obtain its photometry in the mid-infrared.

4.3.1 Kernel phase technique

The kernel phase technique was developed by [Martinache \(2010\)](#), who was able to achieve an angular resolution of $\sim 0.6 \lambda/D$ on the known low-contrast binary GJ 164 with the Near-Infrared Camera and Multi-Object Spectrometer (NICMOS) on the Hubble Space Telescope (HST). Later, [Pope et al. \(2013\)](#) used the technique to detect brown dwarf companions, also with HST/NICMOS, and [Pope et al. \(2016\)](#) and [Sallum & Skemer \(2019\)](#) showed that kernel phase should outperform sparse aperture masking under appropriate seeing conditions longward of $\sim 3 \mu\text{m}$ from the ground given the reduced sensitivity to sky background noise. Recently, [Kammerer et al. \(2019\)](#) used the kernel phase technique to detect eight stellar companions in an archival VLT/Nasmyth Adaptive Optics System

(NAOS) near-infrared imager and spectrograph (NACO) high-contrast imaging survey, two of which are below the classical diffraction limit at angular separations of ~ 0.8 and $\sim 1.2 \lambda/D$.

The kernel phase technique achieves its high resolution by making use of the superior calibration capabilities of the Fourier plane phase (i.e., the phase of the Fourier transform of the image) in the high-Strehl regime. Here, one can linearize the expression of the Fourier plane phase ϕ as a function of the pupil plane phase φ , that is,

$$\phi(\varphi) = \mathbf{R}^{-1} \cdot \mathbf{A} \cdot \varphi + \phi_{\text{obj}} + \mathcal{O}(\varphi^3), \quad (4.1)$$

where \mathbf{A} is the matrix of a linear map between a pair of pupil plane positions and their corresponding spatial frequency, \mathbf{R} is a diagonal matrix encoding the redundancy of the spatial frequencies, and ϕ_{obj} is the Fourier plane phase of the object intensity distribution (i.e., of the astronomical source). The first step was to model the single-dish telescope as an interferometer by discretizing the telescope pupil onto a grid of so-called subapertures in order to find a simple representation of matrix \mathbf{A} , and our VISIR-NEAR pupil model is shown in Figure 4.1. In the high-Strehl regime, the higher order pupil plane phase noise $\mathcal{O}(\varphi^3)$ is negligible and one can multiply Equation 4.1 with the kernel \mathbf{K} of $\mathbf{R}^{-1} \cdot \mathbf{A}$ to obtain the kernel phase θ , namely,

$$\theta = \mathbf{K} \cdot \phi = \underbrace{\mathbf{K} \cdot \mathbf{R}^{-1} \cdot \mathbf{A}}_{=0} \cdot \varphi + \mathbf{K} \cdot \phi_{\text{obj}} + \mathcal{O}(\varphi^3) \approx \theta_{\text{obj}}. \quad (4.2)$$

This is a very powerful finding as it means that, to the second order, the kernel phase measured in the image is directly equivalent to the kernel phase of the astronomical source.

4.3.2 Basic cleaning

Table 4.1 shows an observing log for program 60.A-9107(E). Each chopping cycle consists of two chopping positions, at each of which NDIT exposures are saved and averaged into a single frame by the instrument control software. Then, for each of the N_{chop} chopping cycles, we subtracted the two frames from the different chopping positions from each other in order to remove the mid-infrared background and averaged that over the N_{chop} background-subtracted frames; doing so, we obtained one cleaned frame for each of the N_{avg} observations. We note that we also nodded along the chopping axis during the observations but performed no nodding subtraction here for the sake of simplicity.

Next, we found the brightest PSF in the field-of-view (FOV) by looking for the brightest pixel in the median filtered (3 pixel) frame and cropped the frames to a size of 128×128 pixels around the brightest PSF, which corresponds to an FOV of 5.792 arcsec^2 . A more sophisticated sub-pixel re-centering is performed at a later stage (see Section 4.3.3).

The detector position angle of each frame was computed as the arithmetic mean of the “POSANG” and “POSANG END” fits header keywords. This approximation is feasible since the observing times are short and the field rotation per fits file is only on the order of 0.25 deg. Unfortunately, the detector position angle computed from the fits header keywords does not represent the true position angle of the detector. There is an additional rotation offset ϑ that we determined from VISIR-NEAR data of the nearby and well-known binary system α Centauri. With the known astrometry of this binary system, we obtain a rotation offset of $\vartheta = 94.02 \pm 0.10$ deg and a pixel scale of 45.25 ± 0.10 mas. The detector position angle and the rotation offset were both measured clockwise (i.e., west of north), while the position angle of the companions was measured counterclockwise (i.e., east of north), in accordance with the standard convention.

4.3.3 Kernel phase extraction and calibration

To extract the kernel phase from the cleaned frames, we used the XARA¹ package (Martinache, 2010, 2013). XARA requires a discrete pupil model of the VISIR-NEAR instrument in order to compute the kernel matrix \mathbf{K} . Figure 4.1 shows the VLT Cassegrain pupil (left-hand panel), our discrete pupil model consisting of 224 subapertures placed on a grid with a spacing of 0.5 m (middle panel), and the Fourier plane coverage of our discrete pupil model (right-hand panel). The use of subapertures with a continuous transmission between 0 and 1 (referred to as gray apertures) helps to significantly minimize residual calibration errors (Martinache et al., 2020). We note that the pupil is rotated by 81.8 deg clockwise (west of north, see Figure 4.1) with respect to the detector and we aligned the grid of subapertures with the pupil in order to obtain a symmetric pupil model and reduce calibration errors (see Martinache et al., 2020). We determined this rotation from VISIR-NEAR data of α Centauri, which feature bright diffraction artifacts from the secondary mirror (M2) support spiders.

XARA first masks the cleaned frames with an exponential windowing function m (sometimes called super-Gaussian),

$$m(x, y) = \exp \left(- \left(\frac{\sqrt{(x - x_0)^2 + (y - y_0)^2}}{r} \right)^4 \right), \quad (4.3)$$

with a radius r of 50 pixels (~ 2.263 arcsec) in order to minimize edge effects during the Fourier transform, where x and y are the x- and y-coordinates of the frame and $x_0 = 64$ and $y_0 = 64$ are the coordinates of the center of the frame. This is equivalent to a Gaussian smoothing in the Fourier plane, and a value of 50 pixels is large enough to not interfere with the spatial frequencies measured by the VLT. It then extracts the Fourier plane phase ϕ from the cleaned

¹<https://github.com/fmartinache/xara/>

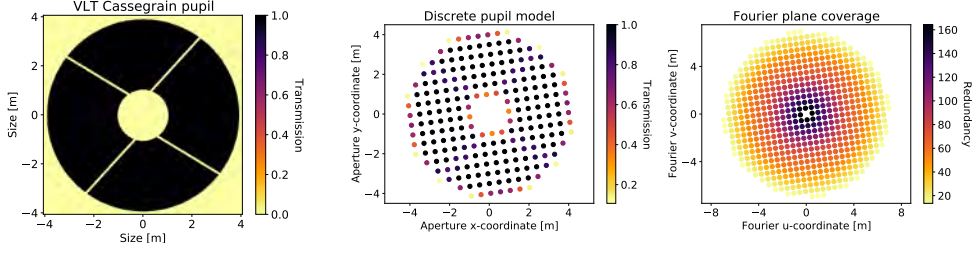


Figure 4.1: VISIR-NEAR pupil model discretized onto a grid of subapertures for the kernel phase analysis. Left: VLT Cassegrain pupil with an extended central obscuration due to the M3 baffle and four thin M2 support struts (“spiders”), rotated by 81.8 deg clockwise. Middle: Our discrete pupil model consisting of 224 subapertures, spanning 310 distinct baselines with 88 kernel phases. Right: Fourier plane coverage of our discrete pupil model.

(dither-subtracted) frames using a discrete Fourier transform at the uv-positions corresponding to the subapertures of our pupil model. Finally, it performs sub-pixel re-centering in the complex visibility space by multiplying the Fourier phase ϕ with a wedge function and computes the kernel phase $\theta = \mathbf{K} \cdot \phi$. This wedge function is determined by computing the photocenter of the brightest PSF on an iteratively shrinking window.

Furthermore, we estimated the kernel phase covariance Σ_θ based on the pixel-to-pixel background variance in the cleaned frames. Therefore, we applied the basis transform

$$\Sigma_\theta = \mathbf{B} \cdot \Sigma_d \cdot \mathbf{B}^T, \quad (4.4)$$

where

$$\mathbf{B} = \mathbf{K} \cdot \frac{\text{Im}(\mathbf{F})}{|\mathbf{F} \cdot \mathbf{d} \cdot \mathbf{g} \cdot \mathbf{m}|} \quad (4.5)$$

and Σ_d is the variance frame (see Kammerer et al., 2019). Here, we obtain the variance frame directly from the frame itself, namely,

$$\Sigma_d = \text{var}(\mathbf{d} \cdot \mathbf{g}) \cdot \mathbf{m}^2, \quad (4.6)$$

where \mathbf{d} is the frame itself and \mathbf{g} is the gain in photoelectrons per detector count. We note that we masked out the center of the frame with a circular aperture of 80 pixels (3.620 arcsec) in diameter in order to avoid confusion from the PSF of T Tau.

Before continuing with the calibration and the model fitting, we made a frame selection based on the absolute Fourier phase $|\phi|$. We rejected any frame whose absolute Fourier phase $|\phi|$ exceeds 90 deg on at least one of the 310 baselines, that is to say, vectors connecting two subapertures (see Figure 4.2). This threshold is chosen empirically and to be sufficiently high so that frames with a high-Strehl PSF of T Tau are kept (we note that T Tau is a low-contrast triple system and

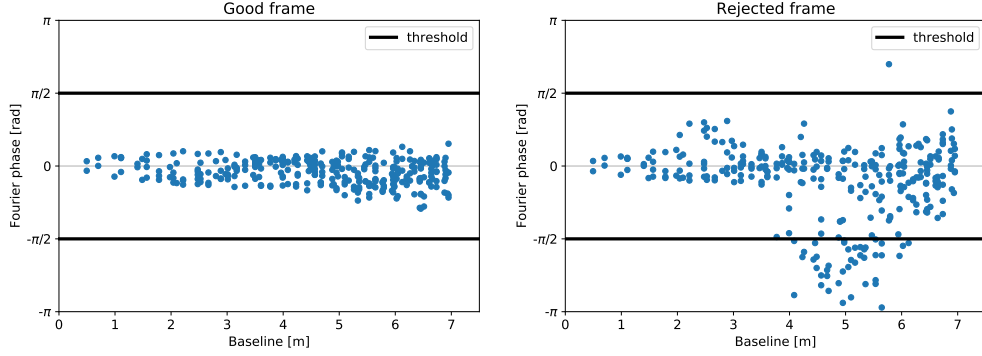


Figure 4.2: Frame selection criterion used to reject bad frames that are not suitable for a kernel phase analysis. Left: Fourier phase ϕ as a function of baseline for an example frame taken with the SIV_1 filter that passes our selection criterion ($|\phi| < 90$ deg). Right: Same, but for an example frame that does not pass our selection criterion due to seeing-driven aberrations.

therefore has a nonzero Fourier phase) but that frames suffering seeing-driven aberrations are rejected. For frames whose absolute Fourier phase $|\phi|$ exceeds 90 deg, higher order pupil plane phase errors are large and would add significant systematic errors. The number of good frames N_{good} obtained for T Tau and the PSF reference for each filter can be found in Table 4.1. The number of rejected frames can be obtained as the difference between N_{avg} and N_{good} .

In order to calibrate the kernel phase, we subtracted the average of the kernel phase measured on the calibrator from the kernel phase measured on the science target (see e.g., Martinache, 2010). The corresponding kernel phase covariance then writes as

$$\Sigma_{\theta} = \Sigma_{\theta,\text{sci}} + \frac{1}{N_{\text{good}}^2} \sum_{n=1}^{N_{\text{good}}} \Sigma_{\theta,\text{cal},n}. \quad (4.7)$$

4.3.4 Model fitting

With the kernel phase θ and its covariance Σ_{θ} , we can perform model fitting based on likelihood maximization or χ^2 minimization. For this, we used a model of N point sources,

$$\theta_{\text{mod}} = \mathbf{K} \cdot \arg \left(\sum_{n=1}^N \xi_n c_n \exp \left(-2\pi i \left(\frac{\Delta_{\text{RA},n} u}{\lambda} + \frac{\Delta_{\text{DEC},n} v}{\lambda} \right) \right) \right), \quad (4.8)$$

where ξ_n is the relative flux of the n -th component (normalized to the total flux), c_n is the complex visibility of the n -th component, $\Delta_{\text{RA},n}$ and $\Delta_{\text{DEC},n}$ are the sky offset of the n -th component from the center of the frame, u and v are the Fourier

u- and v-coordinates of our pupil model, and λ is the observing wavelength. In case of unresolved point sources (such as is the case for our observations), the complex visibility $c_n = 1$.

The N-band flux of both T Tau Sa and Sb is entirely dominated by emission from their CSDs. Both CSDs are tidally truncated by the binary's orbit, which has a semi-major axis of ~ 12.5 au and an eccentricity of ~ 0.55 (Schaefer et al., 2020). For such orbital parameters, Artymowicz & Lubow (1994) predict a ratio of the disk truncation radius to the semimajor axes that would be on the order of ~ 0.25 ($= 3.1$ au) for T Tau Sa and ~ 0.15 ($= 1.9$ au) for Sb. This corresponds to angular sizes of 21 mas and 13 mas, respectively, for the CSDs of T Tau Sa and Sb and is significantly smaller than the diffraction limit at our shortest observing wavelength of ~ 230 mas. In addition, the CSDs get warmer and brighter toward the inner disk rim, with radii of a few tenths of an au ($\lesssim 3$ mas). Therefore, we can safely assume that T Tau Sa and Sb are spatially unresolved in our data.

In the following, we used a more intuitive representation f_n of the relative flux of the individual components by normalizing it to the flux of the brightest component so that $f_1 = 1$ and $f_{n>1} \leq 1$. The ξ_n are related to the f_n according to

$$\xi_n = \frac{f_n}{\sum_{n=1}^N f_n}. \quad (4.9)$$

If we are in the high-contrast regime ($\xi_{n>1} \ll 0.5$) and only fit for two components, the model can be simplified by linearization (Kammerer et al., 2019) and by putting the brighter component into the center of the frame ($\Delta_{\text{RA},1} = \Delta_{\text{DEC},1} = 0$). Then, we can solve analytically for the relative companion flux,

$$\xi_2 = \frac{\theta_{\text{ref}}^T \cdot \Sigma_{\theta}^{-1} \cdot \theta}{\theta_{\text{ref}}^T \cdot \Sigma_{\theta}^{-1} \cdot \theta_{\text{ref}}}, \quad (4.10)$$

on an RA-DEC grid, where θ_{ref} is the binary model (Equation 4.8 for $N = 2$) evaluated on an RA-DEC grid and for a small relative reference flux $\xi_{2,\text{ref}} \ll 0.5$ (see Kammerer et al., 2019). We note that with the T Tau system, we are not in the high-contrast regime where this simplification holds. Nevertheless, such a grid search allows us to find a good first guess for the relative companion flux and its position, which we can then use as an initial position for a least-squares or a Markov chain Monte Carlo (MCMC) algorithm. Such algorithms directly minimize the χ^2 of the model, that is,

$$\chi^2 = R^T \cdot \Sigma_{\theta}^{-1} \cdot R, \quad (4.11)$$

where $R = \theta - \theta_{\text{mod}}$ is the residual kernel phase signal between the data and the model, so that no linearization is necessary.

4.4 Results and analysis

Our goal is to determine the flux of T Tau Sa and Sb relative to T Tau N in all four filters. Therefore, we first performed a binary model fit in order to find the combined flux of T Tau S (i.e., T Tau Sa and Sb) relative to T Tau N. Then, we performed a triple model fit using half of the combined relative flux of T Tau S as initial values for the fluxes of T Tau Sa and Sb relative to T Tau N (making the simple assumption that T Tau Sa and Sb are equally bright; the least-squares or MCMC algorithm will then find the true flux ratio). We note that for the NEII filter we proceeded slightly differently since T Tau S, and not T Tau N, is the brightest component (see Section 4.4.3). Finally, we created mock data with a range of different fluxes for T Tau Sa and Sb relative to T Tau N and repeated the triple model fits in order to demonstrate that our kernel phase model fitting technique correctly reproduces the mock data.

4.4.1 Binary model fits

Figure 4.3 shows the results of our binary model fits to the T Tau system, with both position and flux left as free parameters, yielding a combined flux of T Tau S relative to T Tau N of 0.546 ± 0.015 (ARIII), 0.270 ± 0.064 (SIV_1), 0.464 ± 0.051 (SIV_2), and 1.217 ± 0.047 (NEII). The position uncertainties are on the order of ~ 10 mas, constrained by the astrometric precision of the kernel phase technique; the best fit position varies slightly from filter to filter, also due to the changing flux ratio between T Tau Sa and Sb, which shifts the photocenter of the combined southern component. We note that the NEII data are centered on T Tau S, which is the brighter component at $12.80 \mu\text{m}$. This already reveals some differences compared to the values reported by Skemer et al. (2008), who found the combined southern component to be brighter than the northern component at $8.7 \mu\text{m}$ (\sim ARIII). At $10.55 \mu\text{m}$ (\sim SIV_2), our result of a flux ratio of 0.464 ± 0.051 between the southern and the northern component is more similar to the value of ~ 0.57 reported by Skemer et al. (2008), and we find the combined southern component to only be brighter than the northern component at the longest wavelength ($12.80 \mu\text{m}$).

Since T Tau N is fainter than T Tau S at $12.80 \mu\text{m}$ (NEII), the kernel phase analysis is slightly more complicated. Therefore, we only report on the analysis of the ARIII, SIV_1, and SIV_2 data in the following and treat the NEII data separately in Section 4.4.3. Furthermore, the reduced χ^2 of our binary model fits is larger than one, meaning that we are underestimating the errors. This is in agreement with previous studies that have shown that the kernel phase technique is dominated by systematic errors, usually yielding a reduced χ^2 between ~ 1 – 10 (Martinache et al., 2020; Laugier et al., 2020; Kammerer et al., 2019; Ireland, 2013).

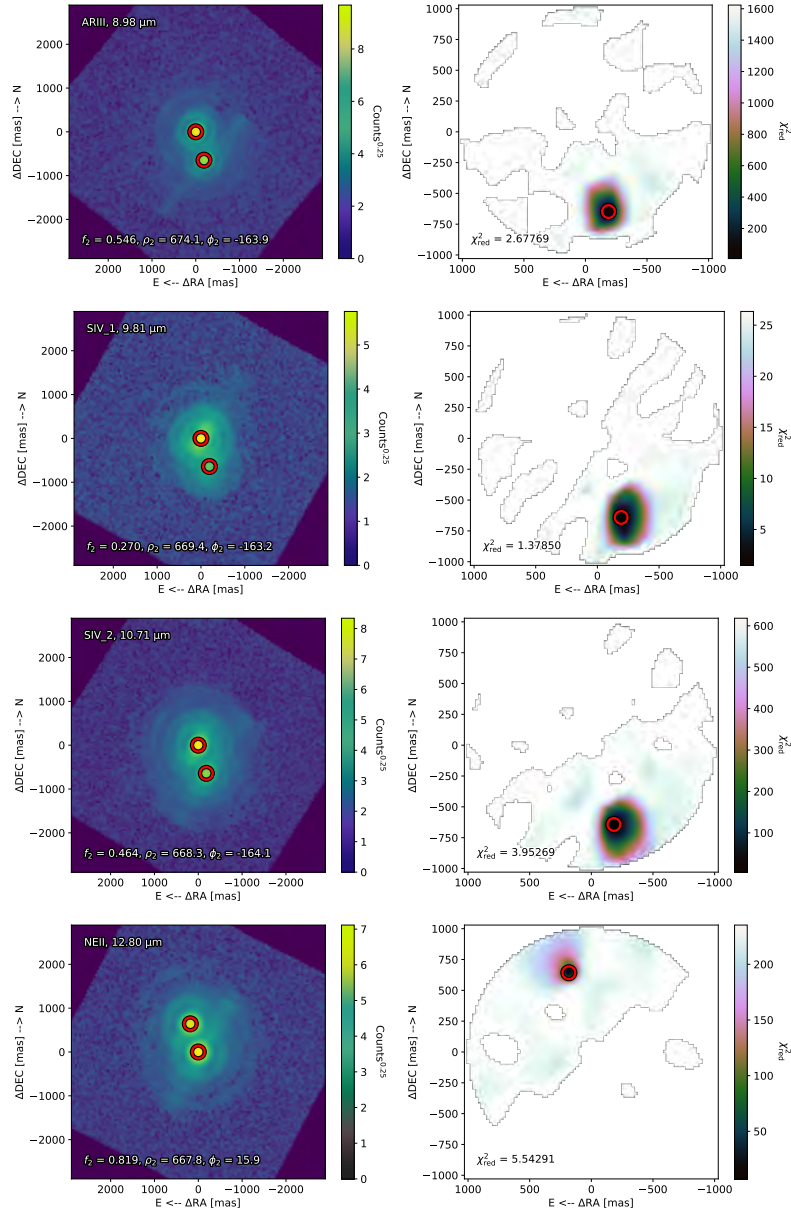


Figure 4.3: De-rotated and co-added VISIR-NEAR images of the T Tau triple system and the two-component fit (left-hand column, red circles) and the corresponding maps of the reduced χ^2 (right-hand column) in the ARIII, SIV_1, SIV_2, and NEII filters (from top to bottom). In the right-hand panels, the red circle highlights the best fit position for the companion (here, the companion is assumed to be the combined PSF of T Tau Sa and Sb). The relative flux f_2 , the angular separation ρ_2 [mas], and the position angle ϕ_2 [deg] of the best fit are printed in the left-hand panels, and its reduced χ^2 is printed in the right-hand panels. We note that the NEII data are centered on T Tau S, which is the brighter component at 12.80 μm .

4.4.2 Triple model fits

For the triple model fits, we used the known offsets of T Tau Sa and Sb relative to T Tau N, which are (-648.1 mas N, -188.5 mas E) for T Tau Sa and (-595.6 mas N, -151.4 mas E) for T Tau Sb. We obtained these values from extrapolating the orbits of the T Tau system from Köhler et al. (2016), which were obtained from VLT/SPHERE astrometry, for the date of our observations. Their accuracy is ~ 1 mas.

Figure 4.4 shows the results of our triple model fits to the T Tau system, with only the fluxes of T Tau Sa and Sb relative to T Tau N left as free parameters. We did both a simple minimization based on a Broyden–Fletcher–Goldfarb–Shanno least-squares algorithm (left-hand panels) and an MCMC fit using `emcee`² (Foreman-Mackey et al., 2013, right-hand panels). In both cases, we used half of the combined relative flux of T Tau S as initial values for the fluxes of T Tau Sa and Sb relative to T Tau N. Moreover, we restricted the search space to $0 \leq f_{2,3} \leq 1$ and normalized the log-likelihood function minimized with the MCMC algorithm by a temperature equal to the reduced χ^2 of the best fit triple model (see the left-hand panels of Figure 4.4) in order to artificially inflate the uncertainties. As can be seen in the corner plots, there is a strong anti-correlation between the relative fluxes of T Tau Sa and Sb caused by the fact that their combined flux is constrained by the data. Furthermore, T Tau Sb is fainter than T Tau Sa in all three filters, which is similar to the results from Skemer et al. (2008), and it is consistent with providing zero flux at 9.81 μm .

Since we estimated the accuracy of the fixed VISIR-NEAR position angle offset ϑ determined from α Centauri data to be ~ 0.10 deg, we repeated the MCMC fit with ϑ and the fluxes of T Tau Sa and Sb relative to T Tau N as free parameters, simultaneously for the ARIII, SIV_1, and SIV_2 data (see Figure 4.5). This approach allows us to explore the entire parameter space and to assess the errors originating from the uncertainty in the position angle offset ϑ . The results are similar to when the position angle offset ϑ is fixed and each filter is fitted separately, with similar uncertainties, suggesting that the uncertainty in the position angle offset ϑ does not significantly limit our precision. We note that the best fit position angle offset $\vartheta_{\text{fit}} = 94.07 \pm 0.02$ is consistent with our assumption of $\vartheta_{\text{prior}} = 94.02 \pm 0.10$ that is based on α Centauri data.

Finally, we repeated the simultaneous triple model fits while varying the position offsets of T Tau Sa and Sb by ± 1 mas in order to empirically estimate the errors originating from the ~ 1 mas uncertainty in these offsets. Again, we find similar results within the uncertainties, suggesting that the uncertainty in the position offsets of T Tau Sa and Sb does not significantly limit our precision either.

²<https://github.com/dfm/emcee>

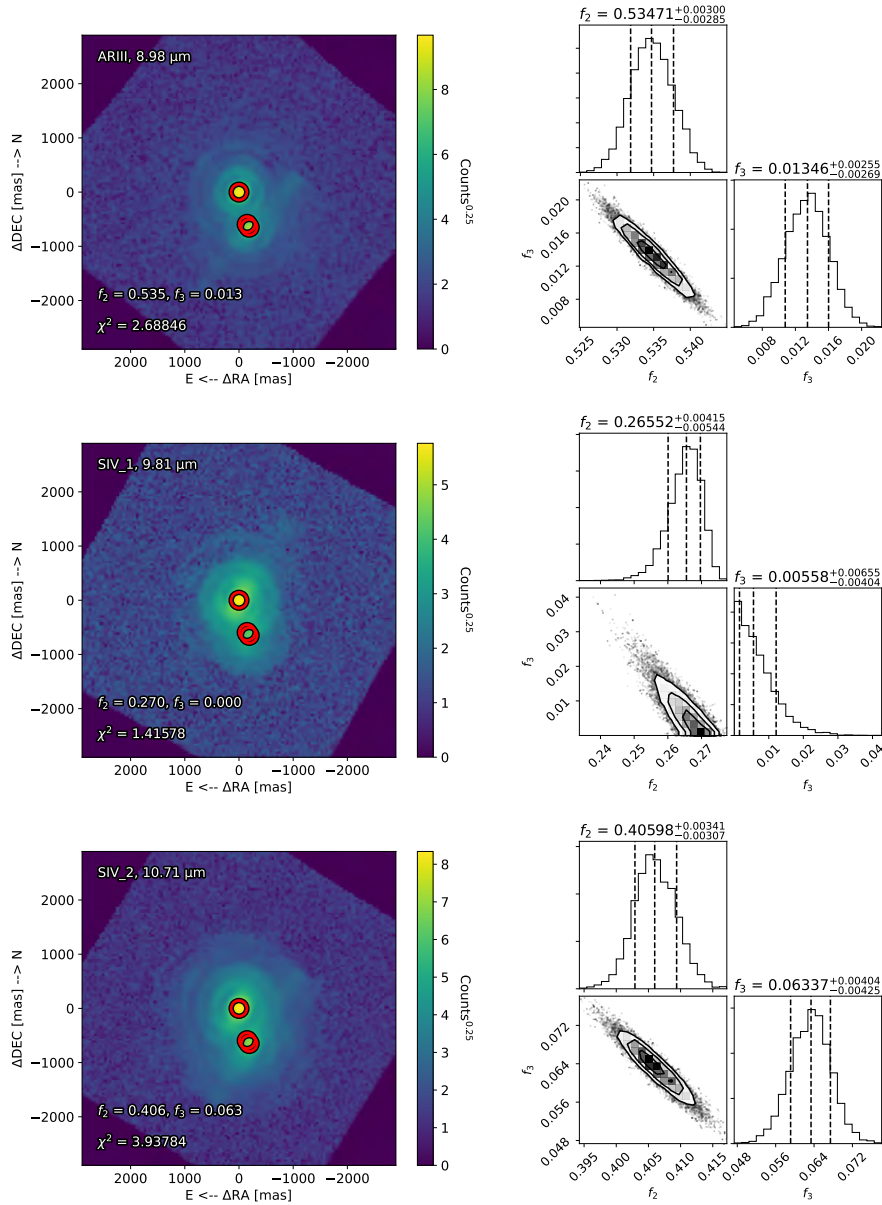


Figure 4.4: De-rotated and co-added VISIR-NEAR images of the T Tau triple system and the three-component fit (left-hand column, red circles) and the corresponding MCMC corner plots (Foreman-Mackey, 2016, right-hand column) in the ARIII, SIV_1, and SIV_2 filters (from top to bottom).

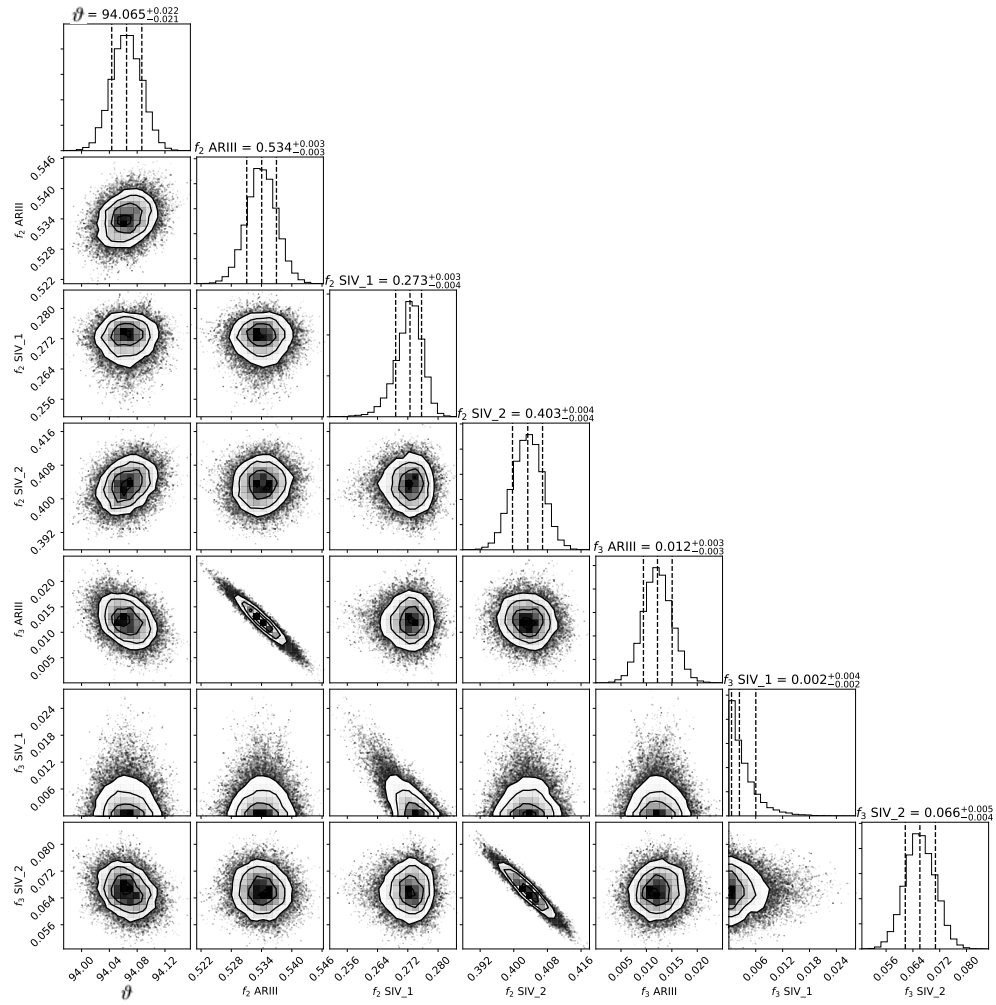


Figure 4.5: Corner plot (Foreman-Mackey, 2016) of an MCMC fit of the kernel phase triple model with the rotation offset ϕ and the relative fluxes of T Tau Sa (f_2) and Sb (f_3) as free parameters, simultaneously for the ARIII, SIV_1, and SIV_2 data.

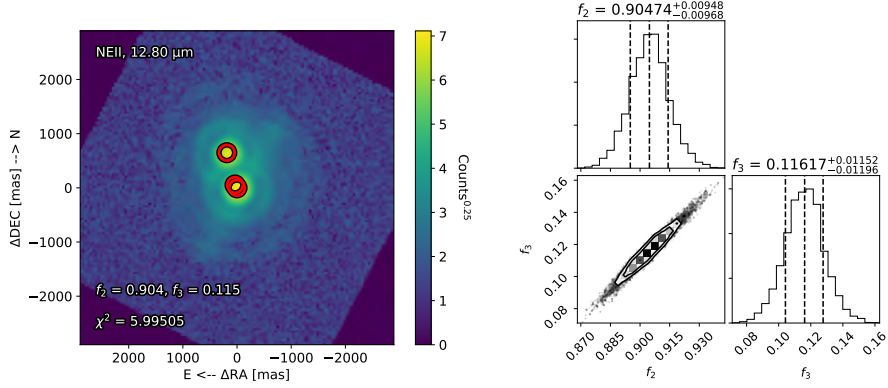


Figure 4.6: Same as Figure 4.4 but for the NEII filter and with the relative fluxes of T Tauri N (f_2) and Sb (f_3) as free parameters.

4.4.3 NEII data

In the NEII data, at 12.80 μm , the southern binary of the T Tau triple system is separated by only $0.2 \lambda/D$. Moreover, it is brighter than T Tau N, so we had to center the frames on T Tau S before extracting the kernel phase (only if the brightest PSF is in the center of the frames can we avoid the Fourier phase ϕ wrapping around $\pm\pi$ and leading to discontinuities and a corrupt kernel phase θ).

In order to perfectly center the frames on T Tau Sa, we first used XARA’s sub-pixel re-centering routine to center the frames on T Tau N. We then computed the exact shift that we have to apply to the frames in order to put T Tau Sa into the center. This is possible because we know its $(\Delta_{\text{RA}}, \Delta_{\text{DEC}})$ offset from VLT/SPHERE astrometry. Directly centering on T Tau Sa is impossible since its PSF is unresolved with the PSF of T Tau Sb; as such, XARA’s re-centering routine would only find the combined photometric center of T Tau Sa and Sb. Then, we proceeded similarly to how we treated the ARIII, SIV_1, and SIV_2 data and fit the kernel phase binary and triple models to the data. However, for the triple model fits, the offsets of T Tau N and Sb relative to the center of the frames (i.e., T Tau Sa) are now (648.1 mas N, 188.5 mas E) and (52.5 mas N, 37.1 mas E).

Our triple model fit results are shown in Figure 4.6. We note that there is now a positive correlation between the relative fluxes of T Tau N and Sb since they are both measured relative to the same PSF of T Tau Sa and are well resolved from each other.

4.4.4 Mock data

In order to validate our approach, we created mock data of the T Tau system and tried to recover it using our kernel phase model fitting techniques. Therefore, we used the calibrator HD 27639 as a reference PSF. Then, we shifted, normalized, and co-added this reference PSF so that it models the three components of the T Tau system. For each filter, we modeled one system with the observed flux ratios and three more systems with T Tau Sa/Sb flux ratios of 0.5/0.5, 0.75/0.25, and 0.9/0.1 (T Tau Sa/Sb flux ratios of 1/0.5, 1/0.25, and 1/0.1 for the NEII filter). In all scenarios, the combined flux of T Tau Sa and Sb relative to T Tau N (the flux of T Tau N for the NEII filter) is equal to the value that we obtained from the binary model fit (see Figure 4.3). We applied the kernel phase technique to the mock data in exactly the same fashion as we did to the real data (e.g., a different re-centering method for the ARIII, SIV_1, and SIV_2 data compared to the NEII data). **We note that since we created the mock data by shifting, normalizing, and co-adding real data of HD 27639, it features realistic random and systematic noise components with values similar to that of the science target.**

Table 4.3 reports the simulated and recovered relative fluxes for all scenarios and the ARIII, SIV_1, SIV_2, and NEII filters. The initial values for f_2 and f_3 were always set to half of the combined flux of T Tau S relative to T Tau N. We note that for the NEII filter, the relative flux of T Tau Sa is fixed to one and we are fitting for the relative fluxes of T Tau N and Sb.

In most cases, the recovered relative fluxes are consistent with the simulated ones within two sigma, and in all cases within three sigma. Given that the fits with mock data do not account for systematic errors and that our covariance model underestimates the uncertainties (see Section 4.4.1), differences of two to three sigma are expected. This leads us to the conclusion that the photometry obtained from our kernel phase model fitting techniques is reliable down to angular separations of $\sim 0.2 \lambda/D$ (that is the angular separation of T Tau Sa and Sb at the longest wavelength in the NEII filter). However, it is also clear that our techniques are limited by systematic errors, and not the uncertainty in the fixed position angle offset ϑ or the $(\Delta_{\text{RA}}, \Delta_{\text{DEC}})$ offset of T Tau Sa and Sb relative to T Tau N obtained from VLT/SPHERE astrometry. This can be concluded from the relatively large discrepancies between the simulated and recovered fluxes when compared to the uncertainties predicted by the MCMC fit, which accounts for the largest statistical noise (photon noise). Hence, we empirically estimated the uncertainties of the relative fluxes from the observed differences between the simulated and recovered values for the mock data (see Table 4.2). We adapted a conservative uncertainty of $\sigma_{\text{emp}} = 0.02$ for the ARIII, SIV_1, and SIV_2 filters, given that all observed differences fall within this range, and a slightly larger uncertainty of $\sigma_{\text{emp}} = 0.03$ for the NEII filter, given the slightly larger observed differences due to the longer wavelength and the different data reduction approach.

Table 4.2: Best fit relative fluxes of the T Tau system from an MCMC fit of the kernel phase triple model to the VISIR-NEAR data. We also report an empirical uncertainty (σ_{emp}) for the relative fluxes (see Section 4.4.4) as well as the final photometry of T Tau N, Sa, and Sb in all filters.

Filter	λ [μm]	Star	Rel. flux	σ_{emp}	Flux [Jy]
ARIII	8.98	N	1.000	0	8.12 ± 0.13
ARIII	8.98	Sa	$0.535^{+0.003}_{-0.003}$	0.02	4.34 ± 0.11
ARIII	8.98	Sb	$0.013^{+0.003}_{-0.003}$	0.02	0.10 ± 0.08
SIV_1	9.81	N	1.000	0	9.81 ± 0.16
SIV_1	9.81	Sa	$0.266^{+0.004}_{-0.005}$	0.02	2.68 ± 0.07
SIV_1	9.81	Sb	$0.006^{+0.007}_{-0.004}$	0.02	0.02 ± 0.05
SIV_2	10.71	N	1.000	0	10.04 ± 0.19
SIV_2	10.71	Sa	$0.406^{+0.003}_{-0.003}$	0.02	4.05 ± 0.13
SIV_2	10.71	Sb	$0.063^{+0.004}_{-0.004}$	0.02	0.66 ± 0.10
NEII	12.80	N	$0.905^{+0.009}_{-0.010}$	0.03	9.63 ± 0.43
NEII	12.80	Sa	1.000	0	10.64 ± 0.42
NEII	12.80	Sb	$0.116^{+0.012}_{-0.012}$	0.03	1.23 ± 0.32

4.4.5 Photometry

The final photometry of T Tau N, Sa, and Sb was computed from the kernel phase relative fluxes and the PSF photometry with an aperture of 70 pixels in diameter on the cleaned frames of T Tau and HD 27639 (the calibrator). HD 27639 is part of the VISIR³ photometric standards list, from which we adapted fluxes of 14.9 ± 0.3 Jy (ARIII), 13.1 ± 0.3 Jy (SIV_1), 11.3 ± 0.3 Jy (SIV_2), and 8.7 ± 0.3 Jy (NEII) with conservative uncertainties. Our final photometry for the T Tau system, using the results from Figures 4.4 and 4.6 for the relative fluxes, is reported in Table 4.2 and shown in Figure 4.7.

4.5 Discussion

Figure 4.7 shows the photometry of T Tau N, Sa, and Sb in the mid-infrared over a period of ~ 15 years. All three components were resolved with VLTI/MIDI interferometry in November 2004 (Ratzka et al., 2009), with the MMT Mid-IR Array Camera 4 (MIRAC4) using high-contrast imaging in November 2006 (Skemer et al., 2008), and VLT/VISIR-NEAR kernel phase interferometry (this work) in December 2019.

The SED of T Tau N is quite stable over time, within the uncertainties, and

³http://www.eso.org/sci/facilities/paranal/instruments/visir/tools/zerop_cohen_Jy.txt

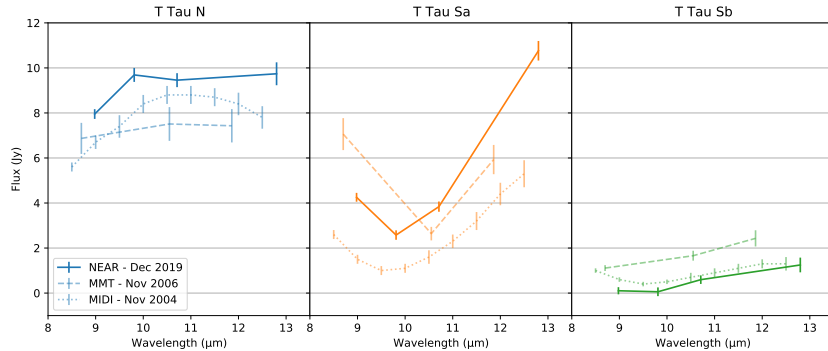


Figure 4.7: Photometry of T Tau N (blue curves), Sa (orange curves), and Sb (green curves) from $\sim 8\text{--}13\ \mu\text{m}$. There are VISIR-NEAR data from December 2019 (solid curves, this work), MMT data from November 2006 (dashed curves, Skemer et al., 2008), and MIDI data from November 2004 (dotted curves, Ratzka et al., 2009).

confirms the consistent photometry typically obtained from this star. We also confirm the detection of weak silicate emission (Ghez et al., 1991; Ratzka et al., 2009), which suggests the presence of a face-on CSD around T Tau N. Detailed modeling of this CSD performed by Ratzka et al. (2009) constrained the disk inclination to $\lesssim 30\ \text{deg}$, which is consistent with recent sub-mm observations with ALMA yielding a disk inclination of $28.3 \pm 0.2\ \text{deg}$ (Manara et al., 2019). Instead, the SED of T Tau Sa varies by up to a factor of four over the N-band, with our measurement falling approximately in between the values reported by Skemer et al. (2008) and Ratzka et al. (2009) at the shorter wavelengths. However, our $12.8\ \mu\text{m}$ flux falls significantly below the N-band fluxes measured in October 1990 ($17.1 \pm 2.3\ \text{Jy}$) and February 2008 ($12.1\text{--}16.7\ \text{Jy}$) by Ghez et al. (1991) and van Boekel et al. (2010), respectively. So, while T Tau Sa is currently rather bright in the near-infrared (Schaefer et al., 2020) when compared to the 2004–2006 period, its N-band brightness is average at best. This is the well-known "bluer when brighter" behavior typical for extinction, but it is also consistent with variable accretion from a small edge-on CSD around T Tau Sa (van Boekel et al., 2010). Variability in the $\sim 9.7\ \mu\text{m}$ silicate feature has also been observed for other strongly accreting CTTs, such as CW Tau, DG Tau, and XZ Tau (Leisenring et al., 2007).

For T Tau Sa, we also detect the silicate absorption feature known to exist in the $10\ \mu\text{m}$ spectral region around the southern component (Ghez et al., 1991). This feature was later shown to arise from extinction toward T Tau Sa and Sb, but with a greater optical depth toward Sa (Ratzka et al., 2009). As pointed out by these authors, this difference in extinction must have been rather local given the small projected separation between T Tau Sa and Sb of $\sim 0.1\ \text{arcsec}$ or

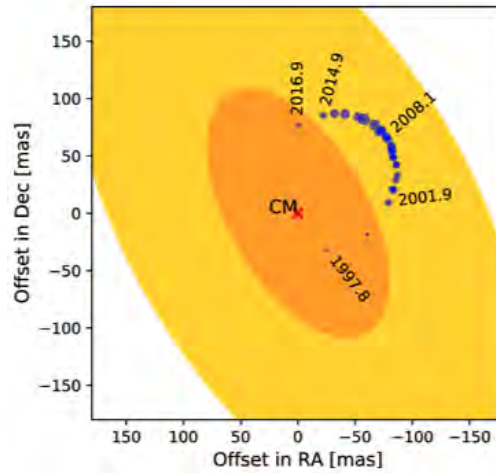


Figure 4.8: Schematic of the T Tau S binary system with its circumbinary disk. The observed positions of T Tau Sb are shown by blue dots whose size indicates the observed near-infrared brightness of the companion. CM indicates the center of mass of the T Tau S binary, which is close to the position of the more massive component T Tau Sa. The yellow and orange ellipses with an inclination of 60 deg and a position angle of 30 deg show the thin extended and the dense inner part of the circumbinary disk. Adapted from Köhler & Kubiak (2020).

~ 15 au, and they attributed it to silicate absorption caused by the outer parts of T Tau Sa’s CSD. However, van Boekel et al. (2010) showed that Sa’s tidally truncated small disk should be warm enough even in its outer parts to produce silicate emission, including when seen edge-on. Therefore, additional extinction caused by, for example, the southern CBD is necessary to explain the SED of T Tau Sa.

In contrast to T Tau Sa, our data show a significant dimming of T Tau Sb when compared to the 2004–2006 period. The effect is most prominent around the silicate feature, where Sb has been dimming by at least a factor of five or ~ 2 mag (see Figure 4.7). This is consistent with the current K-band dimming of ~ 2 – 2.5 mag observed over the same period (Schaefer et al., 2020) and enables us to infer an upper limit on the dust size by considering standard dust models (see e.g., Kruegel & Siebenmorgen, 1994) with a size distribution of $n(a) \sim a^{-3.5}$ (Mathis et al., 1977), which predict a bell-shaped silicate feature with a maximum near $9.7 \mu\text{m}$. For these, the larger the maximum grain size to cut the power-law distribution is set, the wider and shallower the silicate feature becomes. For a maximum grain size well below $1 \mu\text{m}$, which is typical for interstellar dust not processed in the dense inner regions of CSDs, the dust opacity around $10 \mu\text{m}$ would be similar to that in the K-band, and therefore the extinction would also be similar.

Köhler & Kubiak (2020) proposed that T Tau Sb has now moved along its orbit around Sa through the southern CBD and consequently suffers increased dust extinction. The Sa-Sb CBD is aligned roughly north to south, with an inclination of ~ 60 deg and a position angle of ~ 30 deg (cf. Figure 4.8). Therefore, T Tau Sb was located behind the dense inner region of the Sa-Sb CBD, which extends out to ~ 150 mas (Yang et al., 2018) from the center of mass (\sim T Tau Sa), at the time of our observations. Our photometry thus serves as evidence for increased dust extinction toward T Tau Sb caused by its orbital motion through the southern CBD and confirms the scenario proposed by Köhler & Kubiak (2020). Another possible explanation would be a cloud of dust entering the observing beam in front of T Tau Sb. Such a clumpy structure would be motivated by the strong outflows and turbulence observed in the T Tau system (e.g., Kasper et al., 2016). However, since T Tau Sb was already observed to be faint by Koresko (2000) in data from 1997 (when it was on the opposite side of T Tau Sa; see Figure 1 of Köhler & Kubiak, 2020), it seems more likely that the Sa-Sb CBD is responsible for its dimming.

Comparing our mid-infrared photometry from December 2019 to that from November 2006 and 2004, we see the silicate absorption variability of T Tau Sb that was introduced by its passage through the southern CBD, but we do not claim variability of T Tau Sa’s silicate feature. We note that van Boekel et al. (2010) measured variability at $12.8 \mu\text{m}$ (i.e., not in the silicate feature) of the unresolved T Tau S binary over just a few days and attributed this to variable accretion, where UV emission is reprocessed by the disk and shows up in the mid-infrared. These authors also modeled T Tau Sa’s truncated CSD and found that they cannot reproduce silicate absorption by the CSD alone (instead, Sa’s small and warm CSD always shows silicate in emission) and that foreground extinction by cold dust (e.g., by the CBD) is therefore needed.

4.6 Conclusions

In this paper, we measure the brightness of all three components of the iconic T Tau system in the mid-infrared, around $\sim 10 \mu\text{m}$, in order to perform photometry and study the variability caused by its dynamic and dusty environment. We confirm weak silicate emission around T Tau N, indicating a face-on CSD, and strong silicate absorption around T Tau Sa, consistent with extinction by southern circumbinary material (e.g., van Boekel et al., 2010). For T Tau Sb, we observe a dimming over the entire $\sim 8\text{--}13 \mu\text{m}$ spectral range when compared to data from 2004 and 2006, which is in agreement with recent dimming in the near-infrared (K-band) observed by Schaefer et al. (2020).

The dimming of T Tau Sb observed over a wide spectral range (near- to mid-infrared) is consistent with Sb having moved behind the dense inner region of the Sa-Sb CBD, resulting in increased dust extinction. Therefore, we can

confirm the scenario proposed by Köhler & Kubiak (2020) and the Sa-Sb CBD geometry derived by Yang et al. (2018), which, together with previous works (e.g., Duchêne et al., 2002; Skemer et al., 2008; Ratzka et al., 2009), strengthen the evidence for a significant misalignment between the CBD and the T Tau Sa CSD. Most surprisingly, these disks are also misaligned with the orbit of T Tau Sb around Sa and T Tau Sb’s non-edge-on disk, regardless of their small physical separation of ~ 15 au. At such small separations, tidal forces should align them within short timescales (Ratzka et al., 2009), challenging star-formation models and suggesting that multiple star formation can be turbulent (e.g., Whitworth, 2001; Jensen et al., 2004).

At angular separations down to $\sim 0.2 \lambda/D$, we use kernel phase interferometry (Martinache, 2010) together with the known positions of T Tau N, Sa, and Sb (Köhler et al., 2016) to robustly determine their brightnesses. We validate our methods by simulating and recovering mock data of the T Tau triple system using the observed PSF reference. We find that kernel phase interferometry, applied to high-Strehl images in the mid-infrared, is a powerful technique to achieve the highest possible angular resolution with single-dish telescopes. The adaptive optics-corrected VISIR-NEAR instrument provides a unique opportunity to perform such observations from the ground, while kernel phase will also find increased application in space-based observations with the *James Webb Space Telescope* (e.g., Ceau et al., 2019).

Acknowledgements

The NEAR project was made possible through contributions from the Breakthrough Foundation and Breakthrough Watch program, as well as through contributions from the European Southern Observatory. The manuscript was also substantially improved following helpful comments from an anonymous referee.

Appendix: tests with mock data

Table 4.3: Simulated and recovered relative fluxes for our mock data of the T Tau triple system. The values of f_2 and f_3 correspond to T Tau Sa and Sb for the ARIII, SIV_1, and SIV_2 filters and to T Tau N and Sb for the NEII filter, respectively. We perform fits using both a Broyden-Fletcher-Goldfarb-Shanno least-squares algorithm (minimize) and an MCMC algorithm (emcee).

Filter	Test no.	Sim. f_2	Rec. f_2 (minimize)	Rec. f_2 (emcee)	Sim. f_3	Rec. f_3 (minimize)	Rec. f_3 (emcee)
ARIII	1	0.534	0.530	$0.530^{+0.003}_{-0.003}$	0.012	0.009	$0.010^{+0.002}_{-0.002}$
	2	0.273	0.271	$0.271^{+0.003}_{-0.002}$	0.273	0.269	$0.269^{+0.002}_{-0.002}$
	3	0.410	0.407	$0.407^{+0.003}_{-0.003}$	0.137	0.133	$0.133^{+0.002}_{-0.002}$
	4	0.491	0.488	$0.488^{+0.002}_{-0.003}$	0.055	0.052	$0.052^{+0.002}_{-0.002}$
SIV_1	1	0.273	0.267	$0.254^{+0.011}_{-0.014}$	0.002	0.000	$0.010^{+0.011}_{-0.007}$
	2	0.135	0.143	$0.142^{+0.021}_{-0.021}$	0.135	0.121	$0.122^{+0.017}_{-0.018}$
	3	0.202	0.208	$0.208^{+0.022}_{-0.023}$	0.068	0.056	$0.056^{+0.018}_{-0.018}$
	4	0.242	0.247	$0.240^{+0.018}_{-0.020}$	0.027	0.017	$0.023^{+0.016}_{-0.014}$
SIV_2	1	0.403	0.401	$0.401^{+0.005}_{-0.005}$	0.066	0.064	$0.064^{+0.005}_{-0.006}$
	2	0.232	0.232	$0.232^{+0.005}_{-0.005}$	0.232	0.229	$0.229^{+0.005}_{-0.005}$
	3	0.348	0.347	$0.347^{+0.005}_{-0.005}$	0.116	0.113	$0.114^{+0.005}_{-0.006}$
	4	0.418	0.416	$0.416^{+0.005}_{-0.005}$	0.046	0.044	$0.044^{+0.006}_{-0.005}$
NEII	1	0.905	0.918	$0.919^{+0.009}_{-0.009}$	0.116	0.140	$0.141^{+0.012}_{-0.011}$
	2	0.905	0.920	$0.920^{+0.019}_{-0.017}$	0.500	0.535	$0.535^{+0.028}_{-0.027}$
	3	0.905	0.920	$0.921^{+0.012}_{-0.011}$	0.250	0.279	$0.281^{+0.015}_{-0.015}$
	4	0.905	0.918	$0.918^{+0.009}_{-0.008}$	0.100	0.124	$0.124^{+0.011}_{-0.011}$

Increasing the achievable contrast of infrared interferometry with an error correlation model

*This chapter was published as a peer-reviewed article in *Astronomy & Astrophysics*, volume 644, A110. It was written by Jens Kammerer under the supervision of Antoine Mérand, Michael J. Ireland, and Sylvestre Lacour.*

Jens Kammerer^{1,2} **Antoine Mérand**¹ **Michael J. Ireland**² and **Sylvestre Lacour**^{1,3}

1. European Southern Observatory, Karl-Schwarzschild-Str. 2, 85748, Garching, Germany
2. Research School of Astronomy & Astrophysics, Australian National University, ACT 2611, Australia
3. LESIA, Observatoire de Paris, Université PSL, CNRS, Sorbonne Université, Université de Paris, 5 place Jules Janssen, 92195 Meudon, France

Preamble

In the previous three chapters, we have used the kernel phase technique for high-contrast, high-angular resolution imaging from the ground. We have learned that this interferometric technique is affected by large systematic errors, and we have tried to mitigate these by estimating the correlated errors and developing a principle component-based self-calibration approach for example. In this chapter, we will transfer the study of the correlated errors to long-baseline optical interferometry. With the same goal of improving the faint-source detection limits, we will model the correlated errors of the VLTI/GRAVITY instrument. We will then show that our error correlation model improves the detection limits by a factor of ~ 2 , and that commonly used detection criteria based on χ^2 statistics become significantly more robust (i.e., yield significantly fewer false positive detections) when accounting for the correlated errors.

Abstract

Interferometric observables are strongly correlated, yet it is common practice to ignore these correlations in the data analysis process. We develop an empirical model for the correlations present in Very Large Telescope Interferometer GRAVITY data and show that properly accounting for them yields fainter detection limits and increases the reliability of potential detections. We extracted the correlations of the (squared) visibility amplitudes and the closure phases directly from intermediate products of the GRAVITY data reduction pipeline and fitted our empirical models to them. Then, we performed model fitting and companion injection and recovery tests with both simulated and real GRAVITY data, which are affected by correlated noise, and compared the results when ignoring the correlations and when properly accounting for them with our empirical models. When accounting for the correlations, the faint source detection limits improve by a factor of up to ~ 2 at angular separations > 20 mas. For commonly used detection criteria based on χ^2 statistics, this mostly results in claimed detections being more reliable. Ignoring the correlations present in interferometric data is a dangerous assumption which might lead to a large number of false detections. The commonly used detection criteria (e.g. in the model fitting pipeline CANDID) are only reliable when properly accounting for the correlations; furthermore, instrument teams should work on providing full covariance matrices instead of statistically independent error bars as part of the official data reduction pipelines.

5.1 Introduction

With the first detection and characterisation of an exoplanet by the Very Large Telescope Interferometer (VLTI) instrument GRAVITY (HR 8799 e, Gravity Collaboration et al., 2019), infrared interferometry has proven to be a powerful technique for high-contrast imaging at high angular resolution. Although initially designed for observations of the galactic centre (Bartko et al., 2009), GRAVITY’s dual-feed mode combined with the recently installed integrated optics beam combiner (Perraut et al., 2018) enable spectroscopy and micro-arcsecond astrometry of exoplanets with a wide range of angular separations (Gravity Collaboration et al., 2019).

More recently, Gravity Collaboration et al. (2020) have used GRAVITY observations of β Pic b in order to derive reliable estimates for the mass and the C/O ratio of the young giant planet using forward modelling and free retrieval of its atmosphere. In the future, infrared interferometry will be a promising opportunity for studying giant planet formation (e.g. with Hi-5, Defrère et al., 2018) and potentially even characterising terrestrial exoplanets from space (e.g. with a formation-flying nulling interferometer, Léger et al., 1996; Mennesson & Mariotti, 1997; Kammerer & Quanz, 2018; Quanz et al., 2018, 2019). However, significant improvements are required on the technical side (e.g. kernel nulling, Martinache & Ireland, 2018), in addition to on the data reduction side in order to achieve these ambitious goals.

Because they use the dual-feed mode of GRAVITY, the aforementioned observations are not conducted anywhere close to the diffraction limit of the interferometer, but rather the diffraction limit of a single telescope. Detecting a companion within the interferometer’s diffraction limit (a few λ/b_{\max}), where λ is the observing wavelength and b_{\max} is the longest baseline of the interferometer, is limited by systematic errors. While such systematic errors that are introduced by instrumental and atmospheric effects have been studied intensively (e.g. imperfect fibre coupling, Kotani et al. 2003; instrument vibrations, Le Bouquin et al. 2011; differential atmospheric piston; Colavita 1999), correlations are also introduced by the data reduction and the calibration. For instance, a systematic error might be introduced similarly to all complex visibilities measured on the science target if the instrumental transfer function obtained from the calibrator target is affected by unknown variability (Perrin, 2003) and if the closure phases measured over telescope triplets of closing triangles are not mathematically independent (Monnier, 2007). Nevertheless, most data reduction pipelines (e.g. the PIONIER data reduction pipeline, Le Bouquin et al. 2011; the GRAVITY data reduction pipeline, Lapeyrere et al. 2014) and model fitting routines (e.g. LITpro¹, Tallon-Bosc et al. 2008; CANDID², Gallenne et al. 2015) assume sta-

¹<https://www.jmmc.fr/english/tools/data-analysis/litpro>

²<https://ascl.net/1505.030>

tistically independent observables. However, in order to robustly detect faint companions, or place upper limits on their brightness, a solid understanding and description of the systematic errors is inevitable.

While [Lachaume et al. \(2019\)](#) proposed to use the bootstrapping method (i.e. sampling with replacement, [Efron & Tibshirani, 1986](#)) in order to obtain the multivariate probability density function of the squared visibility amplitudes and the closure phases, [Gravity Collaboration et al. \(2020\)](#) extracted the covariances of the complex visibilities directly from the data. Although the bootstrapping method is computationally expensive, it enables estimating the systematic errors not only between the different spectral channels, baselines and triangles, but also between different observations. This enables accounting for correlations introduced by sky rotation or the calibration method, but is only applicable at a higher level when the structure of the observing sequence is known.

In this paper, we follow a similar approach to [Gravity Collaboration et al. \(2020\)](#) by extracting the correlations between the squared visibility amplitudes and the closure phases directly from the data. Then, we develop an empirical model for these correlations which can be fitted to the correlations extracted from single GRAVITY pipeline products, even if only a small number of measurements is available. This enables the attainment of a systematic error estimate for every GRAVITY data set and could ultimately be included in the GRAVITY data reduction pipeline ([Lapeyrere et al., 2014](#)).

5.2 Methods

In Section 5.2.1 we show how we extract the correlations from individual GRAVITY pipeline products and describe their nature. In Section 5.2.2 we introduce our empirical model for these correlations and in Section 5.2.4 we present the model fitting routines with the aid of which we show the improvements that come from using our empirical correlation model. The Python code that we developed in the scope of this paper is publicly available on GitHub (<https://github.com/kammerje/InterCorr>).

5.2.1 Correlations extracted from GRAVITY data

In order to extract the correlations between the different spectral channels, baselines and triangles from GRAVITY data we use the P2VM-reduced files from the GRAVITY data reduction pipeline. These files are intermediate pipeline products which contain the individual measurements (detector read-outs) before they are averaged together. Having access to the individual measurements enables extracting the correlations from the (complex) coherent flux $VIS_{mb\lambda}$ which is stored in the P2VM-reduced file as a data cube of shape $M \times B \times \Lambda$, where $m = 1..M$ is

the number of individual measurements, $b = 1..B$ is the number of baselines and $\lambda = 1..\Lambda$ is the number of spectral channels. From the coherent flux, we compute the squared visibility amplitudes

$$\text{VIS2}_{mb\lambda} = \frac{|\text{VIS}_{mb\lambda}|^2}{\text{F1F2}_{mb\lambda}}, \quad (5.1)$$

where $\text{F1F2}_{mb\lambda}$ is the product of the total fluxes, and the closure phases

$$\text{T3}_{mt\lambda} = \mathbf{K} \cdot \angle \text{VIS}_{mb\lambda}, \quad (5.2)$$

where $t = 1..T$ is the number of triangles, \mathbf{K} is a stack of M matrices \mathbf{k} which encode how the four unique triangles can be formed from the six unique baselines of the VLTI, that is

$$\mathbf{k} = \begin{pmatrix} 1 & -1 & 0 & 1 & 0 & 0 \\ 1 & 0 & -1 & 0 & 1 & 0 \\ 0 & 1 & -1 & 0 & 0 & 1 \\ 0 & 0 & 0 & 1 & -1 & 1 \end{pmatrix}, \quad (5.3)$$

and \angle denotes the argument of a complex number (i.e. the phase).

Then, we compute the sample covariance of the squared visibility amplitudes and the closure phases according to

$$(\Sigma_X)_{ij} = \frac{1}{M-1} \sum_{m=1}^M (X_{mi} - \bar{X}_i)(X_{mj} - \bar{X}_j), \quad (5.4)$$

where X is $\text{VIS2}/\text{T3}$ and i and j run over $1..B\Lambda/1..T\Lambda$ so that we obtain covariance matrices of shape $(B\Lambda) \times (B\Lambda)/(T\Lambda) \times (T\Lambda)$ that contain the covariances between the different spectral channels and baselines/triangles. \bar{X} denotes the mean of X over the individual measurements, that is

$$\bar{X}_i = \frac{1}{M} \sum_{m=1}^M X_{mi}. \quad (5.5)$$

The correlations between the VIS2 and the T3 then follow by dividing the covariances by the standard deviation $\sigma_i = \sqrt{\Sigma_{ii}}$ of the corresponding observables, that is

$$(C_X)_{ij} = \frac{(\Sigma_X)_{ij}}{(\sigma_X)_i(\sigma_X)_j}. \quad (5.6)$$

The diagonal of the covariance matrix Σ equals the square of the standard deviation and that the diagonal of the correlation matrix \mathbf{C} equals one by definition.

For developing an empirical correlation model we use data taken with GRAVITY (Gravity Collaboration et al., 2017) at the Very Large Telescope Interferometer (VLTI) during technical time (programme 60.A-9801(U)). GRAVITY operates in the K-band (2.0–2.4 μm) and combines the light from either the four

Unit Telescopes (UTs) or the four Auxiliary Telescopes (ATs) of the VLTI in order to perform interferometric imaging and astrometry by phase referencing³. The data used here was taken with the four UTs on the object HD 82383 (ζ Ant B) in single-field medium resolution ($R = \lambda/\Delta\lambda \approx 500$) mode. This object is relatively bright (K-band magnitude of 6.698, cf. SIMBAD⁴), hence the short integration time of 0.85 ms for the fringe tracker and 1 s for the science camera. It has a companion at an angular separation of ~ 8 arcsec (cf. WDS⁵) which is well beyond the interferometric field-of-view. By choosing a bright target with a short exposure time we make sure that there is a sufficient number of frames to compute the sample covariance (cf. Equation 5.4). The short exposure time of the fringe tracker (much less than the atmospheric coherence time t_0 , which is typically ~ 20 ms in the K-band, Kellerer & Tokovinin, 2007) and spatially filtered nature of the GRAVITY beam combiner means that the fringe tracker data is less affected by systematic errors than many other beam combiners. We extract the correlations from a single P2VM-reduced file (GRAVI.2019-03-29T02-01-37.193_singlealp2vmred.fits) in order to demonstrate the direct applicability of our method to the GRAVITY data reduction pipeline. Correlations extracted from other P2VM-reduced files of the same program can be found in the Appendix (Figure 5.8).

Figure 5.1 shows the correlations of the VIS2 (left panel) and the T3 (right panel) for the GRAVITY fringe tracker. There are six different baselines and four different triangles with five spectral channels each, so 30 observables for the VIS2 and 20 observables for the T3 in total. Correlations within the same baseline/triangle are highlighted with red squares and correlations between baselines having a telescope in common are highlighted with orange squares.

The most dominant correlations of the VIS2 are between different spectral channels within the same baseline, with neighbouring spectral channels being affected most strongly. We suspect that these correlations are predominantly of both atmospheric or instrumental origin, since all five spectral channels follow the same optical path through the atmosphere and up to the dispersive element behind the beam combiner and before the science camera. Also, the five spectral channels do not correspond to individual pixels on the detector of the fringe tracker. In fact, the wavelengths of the five spectral channels lie somewhere between the wavelengths corresponding to the pixels on the detector of the fringe tracker, so that the values recorded by two neighbouring pixels on the detector need to be interpolated in order to find the values for the five spectral channels of the fringe tracker. This could explain the strong correlations between neighbouring spectral channels (one pixel above or below the diagonal) observed for the VIS2, but also for the T3. Furthermore, there are significant correlations between baselines having a telescope in common. Their strength is roughly half

³<https://www.eso.org/sci/facilities/paranal/instruments/gravity.html>

⁴<http://simbad.u-strasbg.fr/simbad/>

⁵<http://www.astro.gsu.edu/wds/>

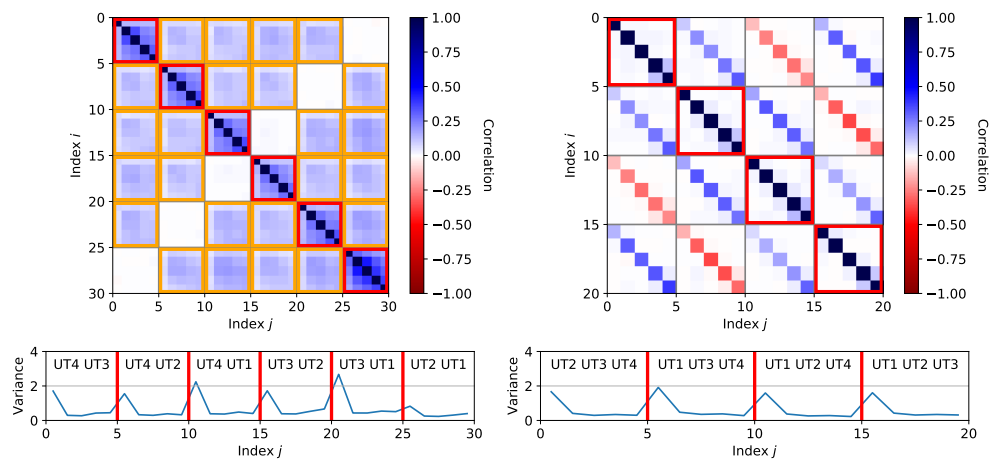


Figure 5.1: Correlations of the VIS2 (left panel) and the T3 (right panel) for the GRAVITY fringe tracker, extracted from a single P2VM-reduced file. The axes run over the different baselines/triangles, with each individual baseline/triangle comprising five spectral channels. Correlations within the same baseline/triangle are highlighted with red squares and correlations between baselines having a telescope in common are highlighted with orange squares. We note that the correlations are computed from 46592 individual measurements. Below each panel, the variance of the data and the names of the telescopes forming each baseline/triangle are shown.

the strength of the correlations within the same baseline, which makes sense if the correlations are introduced by atmospheric or instrumental effects and affect each of the four individual beams of the interferometer separately. Also, baselines having no telescope in common are essentially uncorrelated. Hence, we conclude that most of the correlations of the VIS2 are caused by atmospheric or instrumental effects.

For the T3, we observe similar correlations between neighbouring spectral channels as for the VIS2. This makes sense since the closure phases are built from a linear combination (encoded in the matrix \mathbf{k}) of the phase of the complex visibilities, whose absolute square are the squared visibility amplitudes. Moreover, there are significant correlations of $\sim \pm 1/3$ between the same spectral channels on different triangles. These are caused by the fact that each set of two different triangles has exactly one of their three baselines in common, that is each column of the matrix \mathbf{k} has exactly two non-zero entries. If the common baseline is shared between the different triangles in parallel direction (i.e. the two entries in the corresponding column of the matrix \mathbf{k} have the same sign), the correlation is $+1/3$, otherwise it is $-1/3$. This structure with the side-diagonals being $\pm 1/3$ can also be explained by assuming uncorrelated visibility phases (i.e. a diagonal correlation matrix

$$\mathbf{C}_{\angle\text{VIS}} = \begin{pmatrix} 1 & 0 & \cdots & 0 \\ 0 & \ddots & \ddots & \vdots \\ \vdots & \ddots & \ddots & 0 \\ 0 & \cdots & 0 & 1 \end{pmatrix} \quad (5.7)$$

of shape $B \times \Lambda$ for the visibility phases) and performing a basis transform

$$\mathbf{C}_{\text{T3}} = \mathbf{T} \cdot \mathbf{C}_{\angle\text{VIS}} \cdot \mathbf{T}^T, \quad (5.8)$$

where \mathbf{T} represents a matrix of shape $(T\Lambda) \times (B\Lambda)$ which maps the vector of visibility phases to the vector of closure phases and can be trivially obtained from the matrix \mathbf{k} . Also, the observed correlations between neighbouring spectral channels on different triangles (pixels next to the side-diagonals) are naturally explained by this basis transform given the correlations of the VIS2 observed between neighbouring spectral channels on the same baseline.

Figure 5.2 shows the correlations of the VIS2 (left panel) and the T3 (right panel) for the GRAVITY science camera. There are six different baselines and four different triangles with 210 spectral channels each, so 1260 observables for the VIS2 and 840 observables for the T3 in total.

Due to the much smaller number of individual measurements if compared to the fringe tracker the correlations of the science camera are more dominated by noise. Nevertheless, we observe strong positive correlations between different spectral channels within the same baseline (i.e. inside the red squares) and significant positive correlations between baselines having a telescope in common (i.e.

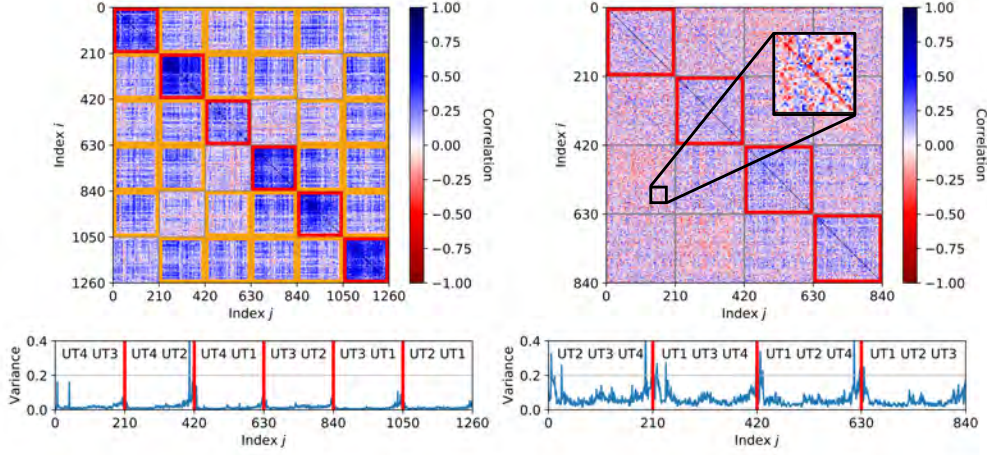


Figure 5.2: Same as Figure 5.1, but for the GRAVITY science camera. Each individual baseline/triangle comprises 210 spectral channels. We note that the correlations are computed from 32 individual measurements.

inside the orange squares) for the VIS2, similar to the correlations observed for the fringe tracker. Although the atmospheric turbulence and the optical elements (i.e. mirrors, delay lines, optical fibres, beam combiner) seen by the science camera are similar to those seen by the fringe tracker, the exposure time of the science camera is much longer than both the atmospheric coherence time t_0 and the fringe tracker inverse 3 dB bandwidth (Lacour et al., 2019), which means that the VIS2 correlations are expected to be decreased by a term proportional to the square of the fringe tracking error and the closure phase random errors are expected to be proportional to the cube of the fringe tracking error (Ireland, 2013). Therefore, since there still are significant correlations for the science camera, they must be introduced by the (correlated) fringe tracker, forwarding the correlations shown in Figure 5.1 to the science camera. For the T3, we again observe significant correlations of $\sim \pm 1/3$ between the same spectral channels on different triangles. On top of this, there are also weak positive correlations between different spectral channels on the same triangle (i.e. inside the red squares) and between different spectral channels on different triangles whose sign depends on whether the corresponding triangles share a baseline in parallel or anti-parallel direction. Again, these correlations are naturally explained by the basis transform \mathbf{T} given the correlations observed for the VIS2 of the science camera.

5.2.2 Empirical model for the correlations

An empirical VIS2/T3 sample covariance with fewer frames than the product of the number of baselines/triangles and spectral channels is necessarily singular. It

takes a number of frames much greater than this to estimate a sample covariance matrix with a condition number approaching that of the true sample covariance. For this reason, we choose to develop an analytic model for the covariance matrix Σ of the VIS2 and the T3. This model can then be fitted to the (potentially under-conditioned) covariance extracted from an arbitrary GRAVITY data set and can be used for model fitting based on log-likelihood maximisation. Most model fitting routines (e.g. LITpro, Tallon-Bosc et al. 2008; CANDID, Gallenne et al. 2015) are based on χ^2 minimisation, which is equivalent to log-likelihood maximisation, where

$$\chi^2 = R^T \cdot \Sigma^{-1} \cdot R \quad (5.9)$$

and $R = D - M$ is the residual between data and model (cf. Section 5.2.4).

Our approach is to model the correlation matrices C_{VIS2} of the VIS2 and C_{T3} of the T3 which have the relatively simple structure observed in Figures 5.1 and 5.2. Moreover, the observed structure of the correlations is consistent for different data sets with different exposure times (1 s with the UTs for programme 60.A-9801(U) and 10 s with the ATs for programme 0101.C-0907(B), cf. also Figures 5.8 and 5.9). Then, we compute

$$\Sigma_{ij} = C_{ij} \sigma_i \sigma_j, \quad (5.10)$$

where σ denotes the standard deviation of the data which can be obtained from the VIS2ERR and the T3PHIERR columns of the OIFITS files for example. We note that these standard deviations are used to build diagonal covariance matrices in LITpro and CANDID which assume uncorrelated data only. Of course, assuming uncorrelated data is a simplification and we discuss the problems that arise from this in Section 5.3.2.

A very important point is that Equation 5.10 only holds if the errors on the VIS2 (σ_{VIS2}) and the T3 (σ_{T3}) are reliably estimated by the GRAVITY data reduction pipeline. The pipeline manual⁶ explains that the uncertainties are computed by bootstrapping over ~ 10 independent samples, so that the final error on the mean measurement is estimated from the observed statistics at a slightly higher temporal frequency. There is no re-scaling or accounting for systematics in this process. In case there are less than five frames available, Monte-Carlo realisations of the theoretical photon and detector noise are added to the samples, which leads to less realistic uncertainties. However, our data sets consist of 32 frames exposures for programme 60.A-9801(U) and 20 frames exposures for programme 0101.C-0907(B), respectively. While we understand that the use of the pipeline uncertainties is a limitation and that an incorrect noise model can reduce the detection sensitivity or yield false positives (cf. e.g. Section 3 of Delisle et al., 2020), we also note that investigating and quantifying the credibility of these uncertainties is beyond the scope of this work.

⁶http://www.eso.org/sci/software/pipelines/index.html#pipelines_table

Our models for the correlation matrices equal one on the diagonal according to the definition of a correlation matrix (cf. Equation 5.6, that is every observable is 100% correlated with itself) and have one free parameter which can be determined by fitting the model to the correlations extracted from the P2VM-reduced files. For the correlation matrix of the VIS2 \mathbf{C}_{VIS2} , the free parameter x represents the correlations between spectral channels within the same baseline and between baselines having a telescope in common. There are correlations of x between different spectral channels within the same baseline, correlations of $x/2$ between baselines having a telescope in common, and no correlations between baselines having no telescope in common (cf. left panel of Figure 5.2), that is

$$\mathbf{C}_{\text{VIS2}} = \begin{pmatrix} \mathbf{X}_1 & \mathbf{X}_2 & \cdots & \cdots & \cdots & \mathbf{X}_2 & 0 \\ \mathbf{X}_2 & \ddots & \ddots & & \ddots & \ddots & \mathbf{X}_2 \\ \vdots & \ddots & \ddots & \mathbf{X}_2 & 0 & \ddots & \vdots \\ \vdots & & \mathbf{X}_2 & \ddots & \mathbf{X}_2 & & \vdots \\ \vdots & \ddots & 0 & \mathbf{X}_2 & \ddots & \ddots & \vdots \\ \mathbf{X}_2 & \ddots & \ddots & & \ddots & \ddots & \mathbf{X}_2 \\ 0 & \mathbf{X}_2 & \cdots & \cdots & \cdots & \mathbf{X}_2 & \mathbf{X}_1 \end{pmatrix}, \quad (5.11)$$

$$\mathbf{X}_1 = \begin{pmatrix} 1 & x & \cdots & x \\ x & \ddots & \ddots & \vdots \\ \vdots & \ddots & \ddots & x \\ x & \cdots & x & 1 \end{pmatrix}, \quad (5.12)$$

$$\mathbf{X}_2 = \begin{pmatrix} x/2 & \cdots & x/2 \\ \vdots & \ddots & \vdots \\ x/2 & \cdots & x/2 \end{pmatrix}. \quad (5.13)$$

The correlation matrix is a block matrix consisting of $B \times B$ blocks, where each individual block is a $\Lambda \times \Lambda$ matrix. For the correlation matrix of the T3 \mathbf{C}_{T3} , the free parameter y represents the correlations between spectral channels within the same triangle. Moreover, as illustrated by the basis transform \mathbf{T} , this naturally leads to correlations of $\pm 1/3$ between the same spectral channel of different triangles and $\pm y/3$ between different spectral channels of different triangles (cf.

right panel of Figure 5.2), that is

$$\mathbf{C}_{T3} = \begin{pmatrix} \mathbf{Y}_1 & \mathbf{Y}_2 & \cdots & \mathbf{Y}_2 \\ \mathbf{Y}_2 & \ddots & \ddots & \vdots \\ \vdots & \ddots & \ddots & \mathbf{Y}_2 \\ \mathbf{Y}_2 & \cdots & \mathbf{Y}_2 & \mathbf{Y}_1 \end{pmatrix}, \quad (5.14)$$

$$\mathbf{Y}_1 = \begin{pmatrix} 1 & y & \cdots & y \\ y & \ddots & \ddots & \vdots \\ \vdots & \ddots & \ddots & y \\ y & \cdots & y & 1 \end{pmatrix}, \quad (5.15)$$

$$\mathbf{Y}_2 = \begin{pmatrix} \pm 1/3 & \pm y/3 & \cdots & \pm y/3 \\ \pm y/3 & \ddots & \ddots & \vdots \\ \vdots & \ddots & \ddots & \pm y/3 \\ \pm y/3 & \cdots & \pm y/3 & \pm 1/3 \end{pmatrix}. \quad (5.16)$$

The correlation matrix is a block matrix consisting of $T \times T$ blocks, where each individual block is a $\Lambda \times \Lambda$ matrix. The sign is positive if the two triangles share a baseline in parallel direction and negative if they share a baseline in anti-parallel direction. **We note that this correlation model only traces intra-frame correlations, i.e., correlations occurring between different observables of the same data frame. Time-dependent effects such as detector persistence or correlations introduced by calibration errors cannot be represented in this model.**

We fit the previously described model to the correlations of the VIS2 and the T3 which we extracted from the single P2VM-reduced file of GRAVITY introduced in Section 5.2.1. Figure 5.3 shows the extracted and the model correlations (top panels) and the extracted and the model covariances (bottom panels) for the VIS2. The free parameter x takes a value of $\sim 3.2e-1$. Figure 5.4 shows the same for the T3 and the free parameter y takes a value of $\sim 7.4e-2$.

5.2.3 Simulated and real data

In order to demonstrate the improvement that comes from taking into account the correlations between the data we perform companion injection and recovery tests with simulated and real data. Therefore, we use GRAVITY data of ζ Ant B from the technical time programme 60.A-9801(U) and of HIP 78183 from the normal programme 0101.C-0907(B), PI M. J. Ireland, listed in Table 5.1. Both objects were observed in single-field medium resolution mode, but the former one with the four UTs and the latter one with the four ATs (medium configuration D0-G2-J3-K0).

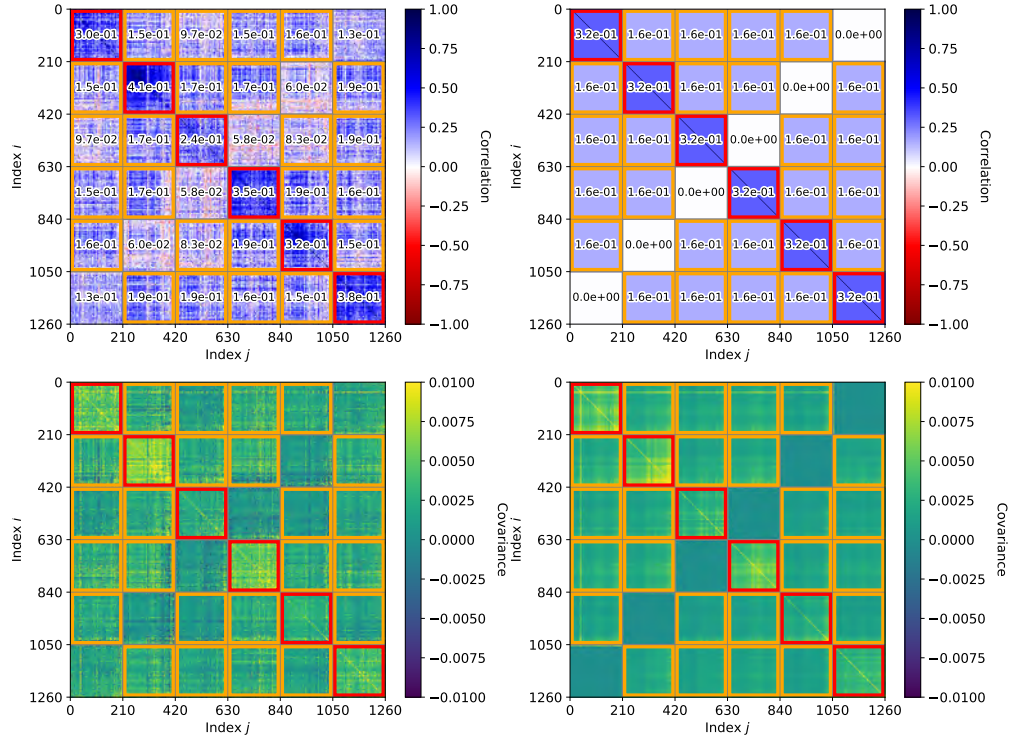


Figure 5.3: Correlations of the VIS2 for the GRAVITY science camera, extracted from a single P2VM-reduced file (upper left panel) and our one-parameter model fitted to them (upper right panel). The bottom panels show the corresponding covariances obtained by multiplying the correlation C_{ij} with the product of the standard deviations $\sigma_i\sigma_j$. Correlations/covariances within the same baseline are highlighted with red squares and correlations/covariances between baselines having a telescope in common are highlighted with orange squares.

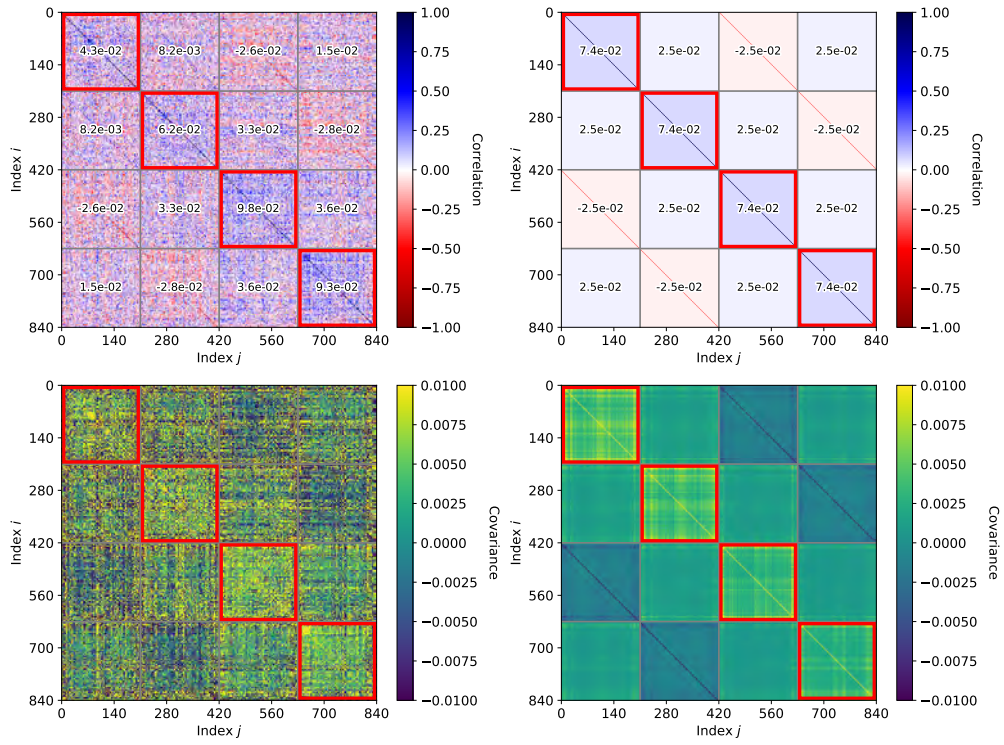


Figure 5.4: Same as Figure 5.3, but showing the correlations/covariances of the T3 and our one-parameter model fitted to them for the GRAVITY science camera.

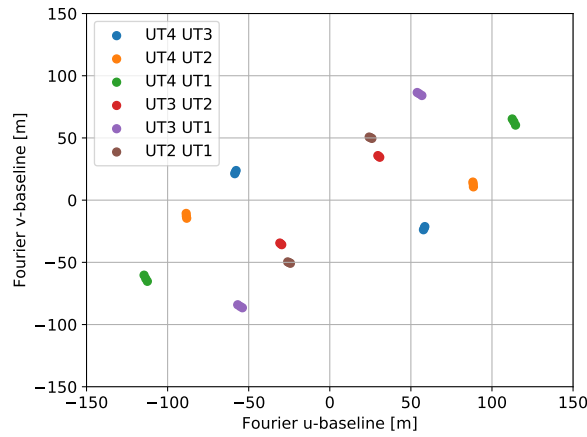


Figure 5.5: Fourier u- and v-baselines of our simulated data extracted from three on-sky observations of GRAVITY using the four UTs over ~ 20 min.

Table 5.1: GRAVITY data used for the companion injection and recovery tests. **NDIT** is the number of detector integrations averaged into a single exposure and **NEXP** is the number of exposures.

Programme	Filename	OB date	OB time (UT)	NDIT	NEXP	Airmass	Seeing
60.A-9801(U)	GRAVI.2019-03-29T01-42-55.145_singlecalvis.fits	2019-03-29	01:42:53	32	3	1.009	1.49"
	GRAVI.2019-03-29T01-51-13.167_singlecalvis.fits	2019-03-29	01:51:09	32	3	1.008	1.50"
	GRAVI.2019-03-29T02-01-37.193_singlecalvis.fits	2019-03-29	02:01:35	32	3	1.010	1.37"
0101.C-0907(B)	GRAVI.2018-04-18T08-08-19.739_single SCIP2vmred.fits	2018-04-18	08:08:16	20	6	1.044	0.60"
	GRAVI.2018-04-18T08-12-10.749_single SCIP2vmred.fits	2018-04-18	08:12:08	20	6	1.049	0.62"
	GRAVI.2018-04-18T08-20-04.769_single SCIP2vmred.fits	2018-04-18	08:20:02	20	6	1.061	0.62"

From the file GRAVI.2019-03-29T02-01-37.193_singlecalp2vmred.fits we have already extracted the covariances and correlations and fitted our empirical models to them (cf. Section 5.2.2). For the companion injection and recovery tests with simulated data, we simply use these models and the uv-tracks u and v of the files belonging to programme 60.A-9801(U) listed in Table 5.1 in order to obtain a realistic uv-coverage over ~ 20 min (cf. Figure 5.5). We simulate the complex visibility of a uniform disc with an unresolved companion according to

$$\text{VIS}_{\text{bin}} = \frac{\text{VIS}_{\text{ud}} + f \exp\left(-2\pi i \left(\frac{\Delta_{\text{RA}}u}{\lambda} + \frac{\Delta_{\text{DEC}}v}{\lambda}\right)\right)}{1 + f}, \quad (5.17)$$

$$\text{VIS}_{\text{ud}} = \frac{2J_1(\pi\theta b)}{\pi\theta b}, \quad (5.18)$$

where $0 \leq f \leq 1$ is the relative flux of the companion, Δ_{RA} and Δ_{DEC} are the on-sky separation in the direction of the celestial north and the celestial east between the companion and its host star, λ is the observing wavelength, J_1 is the first order Bessel function of first kind, θ is the angular diameter of the uniform disc and $b = \sqrt{u^2 + v^2}$ is the distance between the two telescopes observing the object. The squared visibility amplitudes and the closure phases follow according to

$$\text{VIS2}_{\text{bin}} = |\text{VIS}_{\text{bin}}|^2, \quad (5.19)$$

$$\text{T3}_{\text{bin}} = \mathbf{k} \cdot \angle \text{VIS}_{\text{bin}}. \quad (5.20)$$

Then, we add correlated noise to the VIS2_{bin} and the T3_{bin} by drawing from a multivariate normal distribution with covariance $\Sigma_{\text{VIS2,fit}}$ and $\Sigma_{\text{T3,fit}}$, which we obtain from our correlation model $\mathbf{C}_{\text{VIS2,fit}}$ and $\mathbf{C}_{\text{T3,fit}}$ (cf. Section 5.2.2) and assuming a standard deviation of $\sigma_{\text{VIS2}} = 0.01$ and $\sigma_{\text{T3}} = 1$ deg, **which is representative of the typical uncertainties obtained for on-sky GRAVITY observations (Gravity Collaboration et al., 2017)**.

For the companion injection and recovery tests with real data, we extract the correlations of the visibility amplitudes VISAMP (instead of the squared visibility amplitudes VIS2) and the closure phases T3 from the P2VM-reduced files belonging to programme 0101.C-0907(B) listed in Table 5.1, fit our empirical models to them and compute the covariances using Equation 5.10 and the errors from the corresponding final GRAVITY pipeline products (the “singleciviscalibrated” files). Using the VISAMP instead of the VIS2 can yield better results in some cases where the normalisation of the VIS2 is not done properly by the GRAVITY data reduction pipeline. From the final GRAVITY pipeline products, we also extract the VISAMP and the T3 and inject an unresolved companion according to

$$\text{VISAMP}_{\text{inj}} = \text{VISAMP} \cdot |\text{VIS}_{\text{bin}}|, \quad (5.21)$$

$$\text{T3}_{\text{inj}} = \text{T3} + \mathbf{k} \cdot \angle \text{VIS}_{\text{bin}}, \quad (5.22)$$

where we set VIS_{ud} to one. The VISAMP are simply the square root of the VIS2 , so that our correlation model and fitting routines can be equivalently applied in the high SNR regime.

5.2.4 Model fitting

We search for faint companions in the data by fitting the model for a uniform disc with an unresolved companion (cf. Equation 5.17) to it. We maximise the log-likelihood of the model by minimising its χ^2 in order to find the best fit parameters p_{fit} of the model, that is

$$p_{\text{fit}} = \operatorname{argmin}_p(\chi^2) = \operatorname{argmin}_p(R^T \cdot \Sigma^{-1} \cdot R), \quad (5.23)$$

where $R = D - M$ is the residual between data and model and $p = (f, \Delta_{\text{RA}}, \Delta_{\text{DEC}}, \theta)$ is the four-dimensional parameter vector of the model.

In order to find the global minimum of the χ^2 within a given range of companion separations, we first find a prior for the uniform disc diameter θ_0 by fitting the corresponding model (cf. Equation 5.18) to the data. **The estimated angular diameters of our two targets are ~ 0.08 mas for ζ Ant B and ~ 0.14 mas for HIP 78183 and they therefore appear essentially unresolved in the GRAVITY observations.** Then, we perform a set of minimisations with priors on a $\Delta_{\text{RA}} - \Delta_{\text{DEC}}$ grid, the uniform disc diameter θ_0 , and a small relative flux $f_0 = 1e-3$. This is necessary since the χ^2 hyper-surface is bumpy (i.e. has many local extrema) if projected onto the $\Delta_{\text{RA}} - \Delta_{\text{DEC}}$ surface and the BFGS algorithm which is used to minimise the χ^2 converges on local minima. The bumpiness is a result of the sparse uv-coverage of a long-baseline optical interferometer which causes the sensitivity to vary substantially over the FOV.

The above method relies on the covariance matrix Σ being invertible. This is not the case for a sample covariance that is estimated from a small number of frames, which is usually singular, and is the reason why we develop an empirical covariance model. However, our empirical model for the covariances of the closure phases is also singular, since the fourth triangle can be written as a linear combination of the other three. There are multiple solutions to this problem, and for simplicity we decide to completely ignore the data recorded on the fourth triangle since it theoretically is redundant anyway⁷. There are more sophisticated methods to keep the data recorded on the fourth triangle, such as the ‘‘jackknife’’ method (i.e. averaging over four model fits using data recorded on different sets of three triangles), projection into a sub-space that preserves the information in the covariance matrix (Blackburn et al., 2020), and the approach from Kulkarni (1989) which is adding a small numerical value $\epsilon \ll 1$ to the diagonal of the

⁷In practice, this is not the case since the data is affected by different errors originating from different optical paths through the instrument and different detector noise.

covariances of the closure phases, that is

$$\Sigma_{\text{T3,invertible}} = \Sigma_{\text{T3,fit}} + \epsilon \cdot \text{id}, \quad (5.24)$$

where id is the identity matrix, so that the covariance matrix becomes numerically invertible.

Finally, in order to determine the statistical significance of a detected companion, we compute the probability that the binary model is preferred over the uniform disc model according to

$$P = 1 - \text{CDF}_{N_{\text{dof}}} \left(\frac{N_{\text{dof}} \chi_{\text{red,ud}}^2}{\chi_{\text{red,bin}}^2} \right), \quad (5.25)$$

where $\text{CDF}_{N_{\text{dof}}}$ is the χ^2 cumulative distribution function with N_{dof} degrees of freedom, $\chi_{\text{red,ud}}^2$ is the reduced χ^2 of the best fit uniform disc model and $\chi_{\text{red,bin}}^2$ is the reduced χ^2 of the best fit binary model (cf. Gallenne et al., 2015).

If the host star is essentially unresolved (i.e. $\theta b \lambda \ll 1$) and the companion is at high contrast (i.e. $f \ll 1$) one can linearise the VIS2_{bin} and the T3_{bin} as a function of the relative flux of the companion f according to

$$\text{VIS2}_{\text{bin}} \propto 1 + f, \quad (5.26)$$

$$\text{T3}_{\text{bin}} \propto f. \quad (5.27)$$

A more detailed derivation of this relationship can be found in Appendix 5.4. Let D be the data, M_{ref} a reference binary model which is normalised to the relative flux of the companion f_{ref} , and Σ the covariances between the data, that is

$$D = \begin{pmatrix} \text{VIS2} - 1 \\ \text{T3} \end{pmatrix}, \quad (5.28)$$

$$M_{\text{ref}} = \begin{pmatrix} (\text{VIS2}_{\text{bin,ref}} - 1)/f_{\text{ref}} \\ \text{T3}_{\text{bin,ref}}/f_{\text{ref}} \end{pmatrix}, \quad (5.29)$$

$$\Sigma = \begin{pmatrix} \Sigma_{\text{VIS2}} & \mathbf{0} \\ \mathbf{0} & \Sigma_{\text{T3}} \end{pmatrix}, \quad (5.30)$$

where $\text{VIS2}_{\text{bin,ref}}$ and $\text{T3}_{\text{bin,ref}}$ are the binary model VIS2 and T3 evaluated at a reference relative flux $f_{\text{ref}} = 1\text{e-}3$. Then, the best fit relative flux f_{fit} and its uncertainty $\sigma_{f_{\text{fit}}}$ follow according to

$$f_{\text{fit}} = \frac{M_{\text{ref}}^T \cdot \Sigma^{-1} \cdot D}{M_{\text{ref}}^T \cdot \Sigma^{-1} \cdot M_{\text{ref}}}, \quad (5.31)$$

$$\sigma_{f_{\text{fit}}} = \frac{1}{\sqrt{M_{\text{ref}}^T \cdot \Sigma^{-1} \cdot M_{\text{ref}}}}, \quad (5.32)$$

(cf. Le Bouquin & Absil, 2012; Kammerer et al., 2019). Equation 5.31 can be computed on a $\Delta_{\text{RA}}\text{-}\Delta_{\text{DEC}}$ grid, and the best fit parameters p_{fit} follow from the grid position which minimises

$$\chi_{\text{red}}^2 = \frac{\chi^2}{N_{\text{dof}}} = \frac{R^T \cdot \Sigma^{-1} \cdot R}{N_{\text{dof}}}, \quad (5.33)$$

where N_{dof} is the number of the degrees of freedom. This grid search technique is commonly used in order to find the global minimum of the $(f, \Delta_{\text{RA}}, \Delta_{\text{DEC}}, \theta)$ parameter space and its corresponding χ_{red}^2 (e.g. Absil et al., 2011; Gallenne et al., 2015). However, the statistical structure of the grid is complex due to redundancy and periodicity in sensitivity originating from the very limited uv-coverage of a sparse interferometer such as the VLTI (cf. Figure 5.5). Therefore, the detection significance is derived using Equation 5.25 which yields the probability that the binary model is preferred over the uniform disc model (without any companion).

5.3 Results

We evaluate the impact of our full covariance model by performing model fitting and companion injection and recovery tests with both simulated and real GRAVITY data. In Section 5.3.1, we simulate data without any astronomical object, that is correlated noise only, and use model fitting to determine the fundamental detection limits when assuming uncorrelated data (i.e. a diagonal covariance) and correlated data (i.e. our full covariance model). In Sections 5.3.2 and 5.3.3 we inject companions with different relative fluxes and separations into simulated and real GRAVITY data and try to recover them, again assuming both uncorrelated and correlated data.

5.3.1 Model fitting to correlated noise

In order to compare the fundamental detection limits when assuming uncorrelated and correlated data, we simulate 100 GRAVITY data sets of an unresolved host star without any companion (i.e. $\theta = f = 0$ in Equation 5.17) affected by realistic correlated noise ($\Sigma_{\text{VIS2,fit}}$ and $\Sigma_{\text{T3,fit}}$, cf. Section 5.2.3). Then, we use Equation 5.31 in order to compute the best fit relative flux f_{fit} on a $\Delta_{\text{RA}}\text{-}\Delta_{\text{DEC}}$ grid for each of the 100 simulated data sets, first assuming uncorrelated data (i.e. a diagonal covariance $\text{diag}(\Sigma_{\text{VIS2,fit}})$ and $\text{diag}(\Sigma_{\text{T3,fit}})$) and then assuming correlated data (i.e. our full covariance model) in Equation 5.31. Since no companion was injected into the data, the best fit flux ratios of these grids represent the fundamental contrast floor. Any companion with a higher contrast (i.e. smaller flux) would not be distinguishable from the noise. By computing an azimuthal average of these grids, we obtain a fundamental $1\text{-}\sigma$ contrast curve (i.e. best fit relative flux vs. angular separation curve).

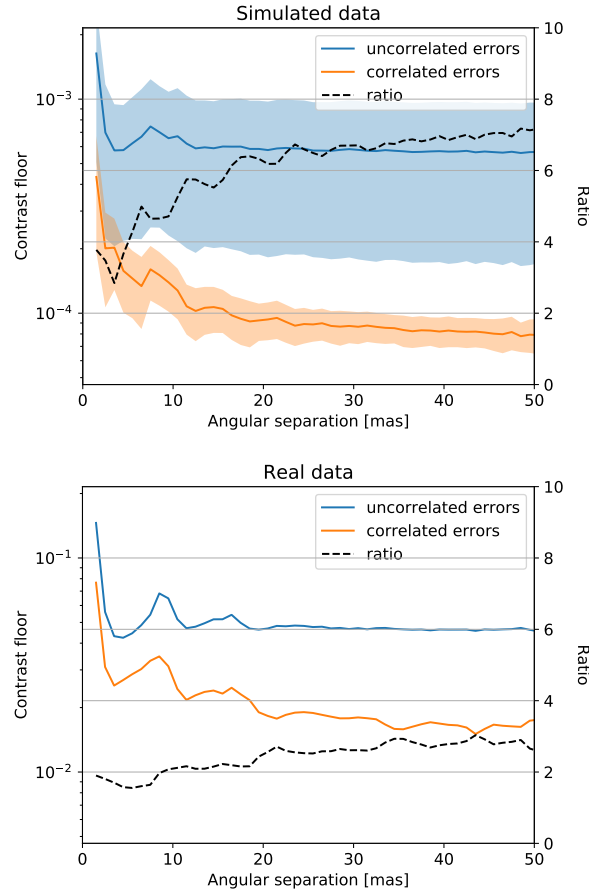


Figure 5.6: Left panel: contrast curve (i.e. azimuthal average of the best fit relative flux) for simulated data of an unresolved host star without any companion affected by correlated errors, computed with model fitting assuming uncorrelated data (blue curve) and correlated data (orange curve). Both curves show the mean contrast curve over 100 simulated data sets and the shaded region highlights its standard deviation. The dashed black line shows the ratio of the blue and the orange curve, representing the improvement (i.e. the factor by which the detection limits improve) when using our correlated error model instead of the classical uncorrelated one. Right panel: same, but for the real GRAVITY data introduced in Section 5.2.3.

The mean of the 100 azimuthal averages obtained for each of these two scenarios (model fitting assuming uncorrelated data in blue and correlated data in orange) is shown in the left panel of Figure 5.6. The contrast floor remains roughly constant at a contrast of $\sim 6e-4$ outward of an angular separation of ~ 5 mas for the scenario assuming uncorrelated data. This is because at a contrast of $\sim 6e-4$ one is dominated by the systematic (i.e. the correlated) errors. However, for the scenario assuming correlated data, the fundamental $1-\sigma$ detection limit continues to decrease with increasing angular separation. At an angular separation of ~ 10 mas it is already a factor of four better than the limit assuming uncorrelated data (cf. dashed black curve). We note that such a behaviour has already been observed by Ireland (2013) for orthogonal kernel phases and statistically independent kernel phases, which are obtained by projecting the orthogonal kernel phases into an eigenspace with zero covariances. Its reason is that at small angular separations, the detection limits rely on the average of the VIS2 and the T3 over the spectral channels, while with increasing angular separations the VIS2 and T3 vary within the spectral bands and the impact of the correlations is growing. A flat uncorrelated contrast curve (as a function of angular separation) is further consistent with previous works on interferometric observables assuming uncorrelated data (e.g. Absil et al., 2011; Gallenne et al., 2015).

Furthermore, when using our full covariance model, the contrast floor is also more stable for different representations of the noise (highlighted by the shaded regions in the left panel of Figure 5.6 which show the standard deviation of the contrast curves over the 100 simulated data sets) meaning that the derived detection limits can be regarded more robust (i.e. independent of the exact representation of the noise which is a random component). Hence, if an observer is only working with a small number of data sets, they will still be able to derive universally valid detection limits.

The right panel of Figure 5.6 shows the same plot, but for model fitting to the real GRAVITY data consisting of the three files belonging to programme 0101.C-0907(B) listed in Table 5.1. Since there is only one real GRAVITY data set we cannot compute or show any standard deviation. The plot looks similar, except for the fundamental detection limits being about two orders of magnitude worse and the ratio between the two scenarios being a lot smaller due to much weaker correlations being present in the real data if compared to the simulated data (cf. Figure 5.8).

5.3.2 Injection and recovery tests (simulated data)

As a next step, we perform companion injection and recovery tests with simulated data, in order to compare the empirical detection limits when assuming uncorrelated and correlated data. Therefore, we simulate GRAVITY data sets

(affected by correlated noise) of a 1 mas uniform disc (the host star) and inject companions with a range of relative fluxes and at different positions around the host star, that is

$$f \in [10^{-4}, 10^{-3.75}, 10^{-3.5}, \dots, 10^{-1.5}], \quad (5.34)$$

$$\Delta_{\text{RA}} \in [-30, -25, -20, \dots, 30] \text{ mas}, \quad (5.35)$$

$$\Delta_{\text{DEC}} \in [-30, -25, -20, \dots, 30] \text{ mas}, \quad (5.36)$$

using Equation 5.17. Then, we perform model fitting with priors on a Δ_{RA} - Δ_{DEC} grid in order to find the global minimum of the χ^2 (cf. Equation 5.23). We note that this method is similar to how CANDID searches for companions for example. Similar to before (cf. Section 5.3.1), we perform the model fitting once assuming uncorrelated data (i.e. a diagonal covariance $\text{diag}(\Sigma_{\text{VIS2,fit}})$ and $\text{diag}(\Sigma_{\text{T3,fit}})$) and once assuming correlated data (i.e. our full covariance model). We classify an injected companion as recovered if the best fit relative flux f_{fit} differs by no more than 10% from the injected one f_{inj} and the best fit position $(\Delta_{\text{RA,fit}}, \Delta_{\text{DEC,fit}})$ differs by no more than one resolution element of the interferometer from the injected one $(\Delta_{\text{RA,inj}}, \Delta_{\text{DEC,inj}})$, that is

$$|f_{\text{fit}} - f_{\text{inj}}|/f_{\text{inj}} < 0.1, \quad (5.37)$$

$$\sqrt{(\Delta_{\text{RA,fit}} - \Delta_{\text{RA,inj}})^2 + (\Delta_{\text{DEC,fit}} - \Delta_{\text{DEC,inj}})^2} < \frac{\lambda_{\text{mean}}}{2b_{\text{max}}}, \quad (5.38)$$

where λ_{mean} is the mean of the observed wavelength range ($\sim 2.2 \mu\text{m}$ for GRAVITY) and b_{max} is the longest baseline of the interferometer ($\sim 130 \text{ m}$ for observations with the VLTI UTs). **The allowed 10% flux difference is motivated by observations of Gallenne et al. (2015) who noted that wavelength smearing effects (for which we do not account in our injection and recovery tests) can easily cause systematic errors of $\sim 10\%$ on the measured flux ratio and the allowed spatial offset is motivated by the angular resolution of the interferometer.**

The left panel of Figure 5.7 shows the fraction of recovered companions as a function of the relative flux of the companion for model fitting assuming uncorrelated data (blue points) and correlated data (orange points). These values are summed over all positions around the host star with $5 \text{ mas} \leq \rho \leq 45 \text{ mas}$, where $\rho = \sqrt{\Delta_{\text{RA,inj}}^2 + \Delta_{\text{DEC,inj}}^2}$ is the angular separation, so to avoid any significant influence from the 1 mas uniform disc (the host star). Although one of the findings in this paper is that the contrast curve is not flat outward a few λ/b_{max} when accounting for the data correlations (cf. Figure 5.6), it is still a reasonable simplification to sum over positions with different angular separations.

The overplotted blue and orange curves are logistic growth functions

$$g(x) = \frac{L}{1 + e^{-k(x-x_0)}}, \quad (5.39)$$

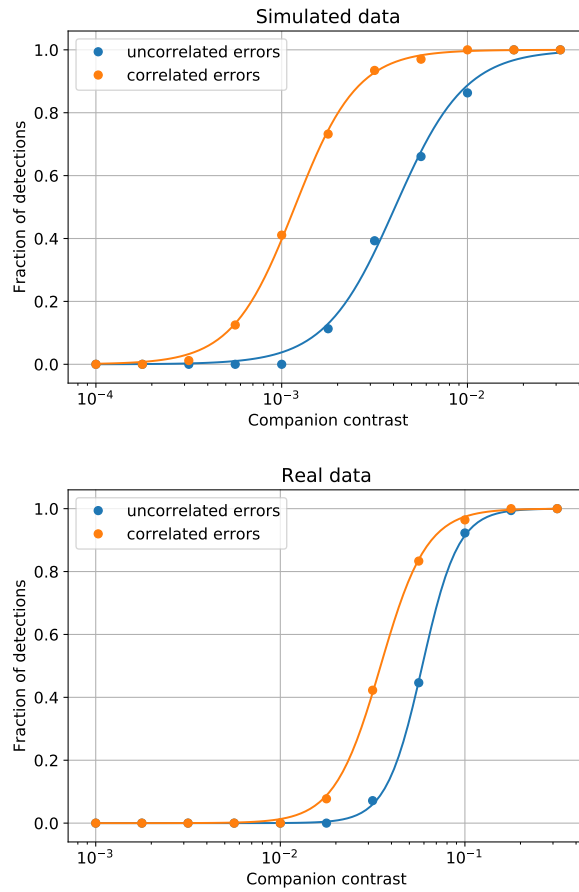


Figure 5.7: Left panel: fraction of correctly recovered companions as a function of the relative flux of the injected companion from injection and recovery tests with simulated GRAVITY data (cf. Section 5.3.2), assuming uncorrelated data (blue points) and correlated data (orange points) for the model fitting. The blue and the orange curves are logistic growth functions fitted to the data points. Right panel: same, but from injection and recovery tests with real GRAVITY data (cf. Section 5.3.3).

fitted to the data points (in log-space), where $L = 1$ is the upper growth barrier, k is the logistic growth rate and x_0 is the midpoint. The fact that the orange curve is shifted towards the left compared to the blue curve means that the detection limits are fainter when assuming correlated data instead of uncorrelated data. This could be expected since the data is affected by correlated noise and correctly accounting for these correlations in the model fitting should lead to fainter detection limits. For any given fraction of detections (i.e. any point on the y-axis), the ratio of the contrasts (i.e. the x-values) of the blue and the orange curve gives the improvement that comes from our full covariance model over the conventional diagonal covariance model. This ratio varies between ~ 3 and ~ 4 , depending on the fraction of detections, with an average value of ~ 3.5 . This means that the detection limits improve by a factor of ~ 3.5 when assuming correlated data instead of uncorrelated data.

In order to check the validity of our detection criterion (cf. Equation 5.25) we count the number of companions in different categories, which we represent in a confusion matrix

$$\zeta = \begin{pmatrix} \# \text{ of true positives} & \# \text{ of false negatives} \\ \# \text{ of false positives} & \# \text{ of true negatives} \end{pmatrix}, \quad (5.40)$$

where positive/negative refers to a detection being classified as significant/insignificant according to our detection criterion. Hence, in an ideal world, there would only be true positives or true negatives and ζ would be a diagonal matrix. Obviously, this is not the case in the real world where the data is affected by noise. If we choose an optimistic detection criterion (e.g. the significance needs to be above $1-\sigma$) there will be many false positives (i.e. many detections that are classified as significant, but which are no true companions) and if we choose a pessimistic detection criterion (e.g. the significance needs to be above $5-\sigma$) there will be many false negatives (i.e. many detections that are classified as insignificant, but which are true companions).

The confusion matrices from our companion injection and recovery tests for a $3-\sigma$ detection criterion are

$$\zeta_{\text{diag}} = \begin{pmatrix} 674 & 3 \\ 517 & 654 \end{pmatrix}, \quad (5.41)$$

$$\zeta_{\text{full}} = \begin{pmatrix} 826 & 213 \\ 12 & 797 \end{pmatrix}, \quad (5.42)$$

for assuming uncorrelated data (ζ_{diag}) and correlated data (ζ_{full}). In the former case, there is a large fraction of false detections being classified as significant ($517/1171 \approx 44\%$), whereas in the latter case this fraction ($12/809 \approx 1\%$) is roughly consistent with a $3-\sigma$ result. **We note that these false positive detections are often many resolution elements away from the position of the injected companion and can either be attributed to pure correlated noise, or to ghosts caused**

by the sparse uv-coverage of the interferometric array and the resulting periodicity in the interferometric PSF (which can be seen in Figure 5.10). If correlations are not accounted for, the best fit detection can easily jump from the position of the injected companion to another peak in the detection map that is caused by model redundancies. The number of true detections is higher when assuming correlated data ($1039 = 826+213$) than when assuming uncorrelated data ($677 = 674+3$) because the detection limits are fainter, and although the number of false negatives (i.e. true companions being classified as insignificant) is a lot higher, the number of true positives is still higher when assuming correlated data. In summary, when using our full covariance model there are less detections above $3\text{-}\sigma$ significance than when using the conventional diagonal covariance model ($838 = 826+12$ vs. $1191 = 674+517$), but the number of true positives (i.e. true companions being classified as significant) is still higher and significant detections are much more reliable since there are almost no false positives. Accounting for the correlations is therefore clearly preferred over ignoring them.

Before proceeding to the injection and recovery tests with real data we also assess the robustness of our correlation model with respect to errors in the model parameters x and y . Therefore, we repeat the injection and recovery tests with wrong correlation and covariance matrices where x and y are only 50% and 25% of their true values respectively. We find that the number of false positives or false negatives increases slightly, but not significantly. This was expected since the detection of asymmetric structure (such as a companion) is governed by the T3 whose correlations are dominated by the correlations of $\pm 1/3$ originating from shared baselines among different triangles. For scenarios where the VIS2 have a larger impact on the model (e.g. measuring stellar diameters) we expect that errors in the model parameters, especially x , have a more significant impact.

5.3.3 Injection and recovery tests (real data)

In the previous Section it is obvious that our full covariance model would outperform the conventional diagonal covariance model, since we simulated data affected by correlated noise. Therefore, the crucial next step is to validate our methods with real GRAVITY data sets. For this purpose, we extract the correlations of the VISAMP and the T3 from the files belonging to programme 0101.C-0907(B) listed in Table 5.1, fit our empirical models to them and use the VISAMP and the T3 data from the corresponding final GRAVITY pipeline products as noise model.

Since the real data is affected by bright speckles arising from an imperfect calibration, for which our correlation model does not account, we subtract the theoretical VISAMP and T3 of the best fit companion from the data before performing the injection and recovery tests. This also helps us to enter the medium-contrast regime ($f_{\text{fit}} \lesssim 10\%$) where the linearisation of the binary model

(cf. Appendix 5.4) holds. The parameters of the subtracted best fit companion are

$$p_{\text{sub}} = (f, \Delta_{\text{RA}}, \Delta_{\text{DEC}}, \theta) = (0.0383, 0.20, -5.46, 0), \quad (5.43)$$

and the corresponding detection map is shown in Figure 5.10. The parameters were obtained assuming correlated errors. An extension of our correlation model to inter-observation correlations, for instance arising from the calibration process, is left for future work.

Then, we compute the covariances from the correlations, the VISAMPERR, and the T3ERR from the final GRAVITY pipeline products using Equation 5.10 and inject companions with

$$f \in [10^{-3}, 10^{-2.75}, 10^{-2.5}, \dots, 10^{-0.5}], \quad (5.44)$$

$$\Delta_{\text{RA}} \in [-30, -25, -20, \dots, 30] \text{ mas}, \quad (5.45)$$

$$\Delta_{\text{DEC}} \in [-30, -25, -20, \dots, 30] \text{ mas}, \quad (5.46)$$

using Equations 5.21 and 5.22. In order to obtain empirical detection limits when assuming uncorrelated and correlated data, we then repeat the model fitting described in the previous Section.

The fraction of correctly recovered companions as a function of the relative flux of the companion for both scenarios (uncorrelated noise: blue points and correlated noise: orange points) is shown in the right panel of Figure 5.7, again overplotted with logistic growth functions fitted to the data points (cf. Section 5.3.2). The plot looks similar to the one from the injection and recovery tests with simulated data and confirms the applicability of our full covariance model to real GRAVITY data. Of course, the empirical detection limits are about one to two orders of magnitude worse and the improvement that comes from our full covariance model (i.e. the lateral shift of the orange curve with respect to the blue curve) is only a factor of ~ 2 (consistent with the right panel of Figure 5.6 which also shows an improvement by a factor of ~ 2) due to weaker correlations being present in the data used for the injection and recovery tests with real data. In summary, our full covariance model still brings a significant improvement over the conventional diagonal covariance model.

5.4 Conclusions

Correlated noise is placing fundamental detection limits on interferometric data. From on-sky VLTI/GRAVITY data, we extract and illustrate the correlations present in the data and develop an empirical model in order to describe them. This empirical model is sufficiently simple for it to be fitted to the correlations extracted from a single GRAVITY data product and could therefore be directly integrated into the GRAVITY data reduction pipeline and made available to the

community as part of the OIFITS 2 file (which has a well-defined standard for providing covariance matrices, [Duvert et al., 2017](#)).

Then, we evaluate the impact of our full covariance model by performing model fitting and companion injection and recovery tests with both simulated and real GRAVITY data. Our methods are based on $\chi^2 = R^T \cdot \Sigma^{-1} \cdot R$ minimisation, where we compare the scenarios assuming uncorrelated data (i.e. a diagonal covariance matrix $\text{diag}(\Sigma)$) and correlated data (i.e. a full covariance matrix Σ following from our empirical correlation model). We show that accounting for the correlations that we find to be present in GRAVITY data could yield to an improvement in the detection limits by a factor of up to ~ 3.5 over ignoring them. Moreover, the obtained detection limits (and therefore also potential detections) can be regarded more robust in the former case. We also highlight the problems which arise from ignoring the correlations, as it is done in model fitting pipelines such as LITpro ([Tallon-Bosc et al., 2008](#)) and CANDID ([Gallenne et al., 2015](#)) so far, and discuss that conventional detection criteria based on χ^2 statistics are strongly biased towards false positives (i.e. detections that are no true companions).

The empirical correlation model presented in this paper is a simple one-parameter model derived from GRAVITY data, but is arguably also applicable (with small modifications) to other instruments such as VLTI/PIONIER for example. It only treats the correlations between the different observables, but not yet between different frames or targets (such as the science and the calibrator target). We choose this approach in order to enable a simple implementation into existing data reduction and model fitting pipelines. Especially with the increasing availability of computing power, the use of full covariance matrices for describing the correlated noise in interferometric data should become a standard. Collaborations around future instruments should provide estimated data covariances as part of the official data reduction pipelines.

In the future, we aim to compare our empirical correlation model with the data covariances derived from bootstrapping (e.g. [Lachaume et al., 2019](#)) and extend our model in order to account for correlations between different frames and targets. Finally, we will re-analyse several marginal detections of companions around Cepheid stars from [Gallenne et al. \(2013, 2014, 2015\)](#) by properly accounting for the correlated noise.

Acknowledgements

The authors would like to thank Jean-Baptiste Le Bouquin for helpful feedback on the GRAVITY data reduction pipeline. MJI acknowledges support from the ESO visitor programme. This work has been partly supported by the Australian Research Council’s Discovery Projects (DP190101477). The manuscript was also

substantially improved following helpful comments from an anonymous referee.

Appendix 1: collection of correlations

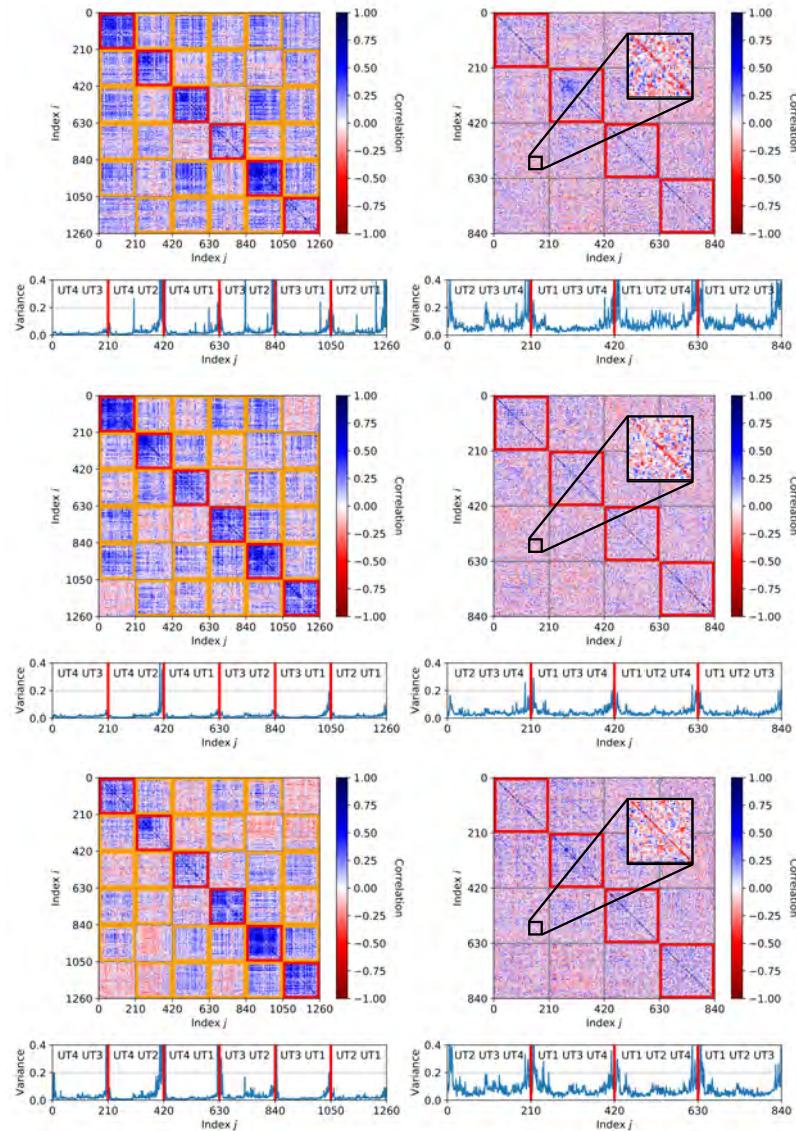


Figure 5.8: Same as Figure 5.2, but extracted from three other P2VM-reduced files from programme 60.A-9801(U). From top to bottom: GRAVI.2019-03-29T01-46-28.155_singlealp2vmred.fits, GRAVI.2019-03-29T01-57-13.182_singlealp2vmred.fits, GRAVI.2019-03-29T01-59-31.188_singlealp2vmred.fits.

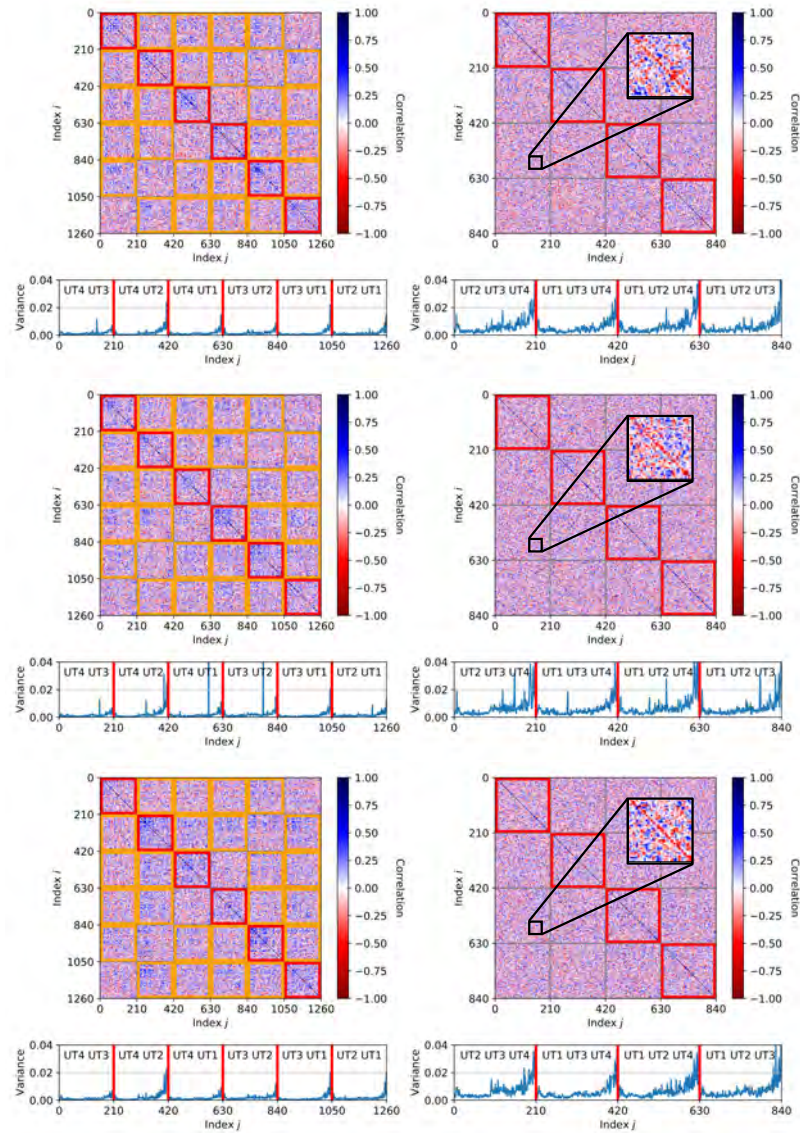


Figure 5.9: Same as Figure 5.2, but showing the correlations of the VISAMP instead of the VIS2, extracted from the three P2VM-reduced files used for the injection and recovery tests with real data in Section 5.3.3 (programme 0101.C-0907(B)). From top to bottom: GRAVI.2018-04-18T08-08-19.739_singlescip2vmred.fits, GRAVI.2018-04-18T08-12-10.749_singlescip2vmred.fits, GRAVI.2018-04-18T08-20-04.769_singlescip2vmred.fits.

Appendix 2: linearised model

If the host star is essentially unresolved (i.e. $\theta b\lambda \ll 1$) and the companion is at high contrast (i.e. $f \ll 1$) one can linearise the $\text{VIS}_{2\text{bin}}$ and the T3_{bin} as a function of the relative flux of the companion.

Consider the complex visibility of the binary model VIS_{bin} in the case where $\theta \rightarrow 0 \Leftrightarrow \text{VIS}_{\text{ud}} \rightarrow 1$ and $f \ll 1$, then the VIS_2 of this model is

$$|\text{VIS}_{\text{bin}}|^2 \approx \frac{1}{(1+f)^2} \left[(1+f \cos(x))^2 + f^2 \sin^2(x) \right] \quad (5.47)$$

$$= \frac{1}{(1+f)^2} [1 + 2f \cos(x) + f^2] \quad (5.48)$$

$$= (1 - 2f + \mathcal{O}(f^2)) [1 + 2f \cos(x) + f^2] \quad (5.49)$$

$$= 1 + 2f \cos(x) - 2f + f^2 - 4f^2 \cos(x) + \mathcal{O}(f^3) \quad (5.50)$$

$$= 1 + f(2 \cos(x) - 2) + \mathcal{O}(f^2) \quad (5.51)$$

and the phase (or argument) of this model (and therefore any linear combination of phases such as the T3) is

$$\angle \text{VIS}_{\text{bin}} = \arctan \frac{\text{Im} \text{VIS}_{\text{bin}}}{\text{Re} \text{VIS}_{\text{bin}}} \quad (5.52)$$

$$\approx \frac{\text{Im} \text{VIS}_{\text{bin}}}{\text{Re} \text{VIS}_{\text{bin}}} \quad (5.53)$$

$$= \frac{-f \sin(x)}{1 + f \cos(x)} \quad (5.54)$$

$$\approx f \frac{-\sin(x)}{1} \quad (5.55)$$

for $x = -2\pi i(\Delta_{\text{RA}} u/\lambda + \Delta_{\text{DEC}} v/\lambda)$. Hence, in the high-contrast regime, one has $\text{VIS}_{2\text{bin}} \propto 1 + f$ and $\text{T3}_{\text{bin}} \propto f$.

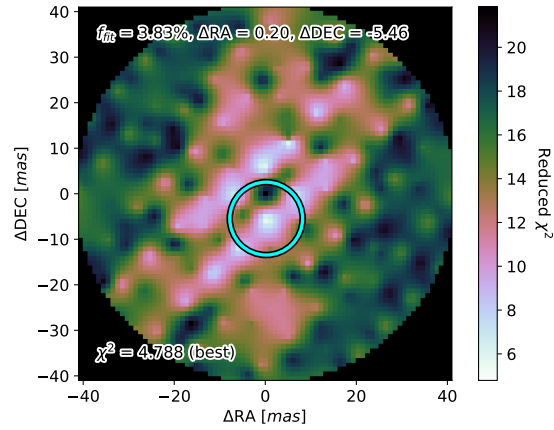
Appendix 3: detection map for real data

Figure 5.10: Detection map for the GRAVITY data used for the injection and recovery tests in Section 5.3.3. The host star is located in the centre of the map and the cyan circle highlights the position of the best fit companion. Its parameters and reduced chi-squared are shown at the top and the bottom of the map. North is up and east is left.

GRAVITY K-band spectroscopy of HD 206893 B: brown dwarf or exoplanet?

This chapter will be submitted as a peer-reviewed article to Astronomy & Astrophysics. It was written by Jens Kammerer under the supervision of Sylvestre Lacour. Tomas Stolker helped with the atmospheric model fitting, Kimberly Ward-Duong provided assistance with the GPI spectra, Jason J. Wang helped with the orbit fitting, and Mathias Nowak provided assistance with the GRAVITY data reduction.

Jens Kammerer,^{1,2} Sylvestre Lacour,^{1,3} Tomas Stolker,⁴ Kimberly Ward-Duong,⁵ Jason J. Wang⁶ and Mathias Nowak⁷

1. European Southern Observatory, Karl-Schwarzschild-Str. 2, 85748, Garching, Germany
2. Research School of Astronomy & Astrophysics, Australian National University, ACT 2611, Australia
3. LESIA, Observatoire de Paris, Université PSL, CNRS, Sorbonne Université, Université de Paris, 5 place Jules Janssen, 92195 Meudon, France
4. Leiden Observatory, Leiden University, P.O. Box 9513, 2300 RA Leiden, the Netherlands
5. Five College Astronomy Department, Amherst College, Amherst, MA 01002, USA
6. Department of Astronomy, California Institute of Technology, Pasadena, CA 91125, USA
7. Institute of Astronomy, University of Cambridge, Madingley Road, Cambridge CB3 0HA, United Kingdom

Preamble

Finally, in this chapter, we use long-baseline interferometry with VLTI/GRAVITY to characterize the orbit and the atmosphere of the directly-imaged sub-stellar companion HD 206893 B. We will study the alignment of its orbit with **respect to** the debris disk of the system and reconcile its extremely red near-infrared spectrum with atmospheric models for giant planets and brown dwarfs, by including additional extinction caused by high-altitude dust clouds made of enstatite grains. Although the observations presented in this chapter were obtained using GRAVITY’s dual feed mode and are therefore not directly affected by the systematic errors at small angular separations discussed in Chapter 5, **they benefit from a similar empirical treatment of the correlated errors introduced by Gravity Collaboration et al. (2020). Moreover, this study of HD 206893 B together with previous works on the HR 8799 (Gravity Collaboration et al., 2019), the β Pic (Gravity Collaboration et al., 2020; Nowak et al., 2020), and the PDS 70 (Wang et al., 2021) systems demonstrate the capability of long-baseline interferometry to detect and characterize exoplanets in the near-infrared. With the unprecedented angular resolution achieved by GRAVITY, an exoplanet detected with the radial velocity technique could be followed-up with direct observations for the first time (Nowak et al., 2020). This marks an important step toward closing the gap in the observed planet population between indirect and direct detection techniques. While we have seen in Chapters 2 and 3 that the kernel-phase technique struggles to reach contrasts in the planetary-mass regime with current 8 m-class telescopes, even around young stars, optical long-baseline (nulling) interferometry will be a key technique to study planet formation in the nearest star-forming regions (Defrère et al., 2018; Wallace & Ireland, 2019).**

Abstract

Near-infrared interferometry has become a powerful tool to study the orbital and atmospheric parameters of sub-stellar companions. We aim to reveal the nature of the reddest known sub-stellar companion HD 206893 B by studying its near-infrared color and spectral morphology and by investigating its orbital motion on the sky. We fit atmospheric models for giant planets and brown dwarfs to the observed SPHERE, GPI, and GRAVITY spectra of HD 206893 B. In order to recover the unusual spectral features of this companion, first and foremost its extremely red near-infrared color, we include additional extinction by high altitude dust clouds made of enstatite grains in our atmospheric model fits. Moreover, we infer the orbital parameters of HD 206893 B by combining the $\sim 100 \mu\text{as}$ -precision astrometry from GRAVITY with data available in the literature. The extremely red color and the very shallow $1.4 \mu\text{m}$ water absorption feature of HD 206893 B can be fit well with our adapted atmospheric models. However, not all of these models can reconcile the morphology of the H and K-band peaks observed with GPI and GRAVITY. By comparison with AMES-Cond evolutionary tracks we find that only some atmospheric models predict physically plausible objects. Altogether, our analysis suggests an age of $\sim 3\text{--}300$ Myr and a mass of $\sim 5\text{--}30 M_{\text{Jup}}$ for HD 206893 B, consistent with previous estimates, but extending the parameter space to younger and lower-mass objects. The GRAVITY astrometry prefers an eccentric ($e \sim 0.3$) orbit which is slightly misaligned with the debris disk of the system by ~ 6 deg. While the age and mass inferred for HD 206893 B are affected by large uncertainties, we argue that

a planetary nature has to be considered for this directly-imaged sub-stellar companion, especially in light of the previous mass estimate of $10_{-4}^{+5} M_{\text{Jup}}$ from radial velocity data and the possible Argus moving group membership of the system. Further spectroscopic or photometric observations at higher signal-to-noise are required to learn more about the composition and dust cloud properties of HD 206893 B.

6.1 Introduction

While the population of known exoplanets has been growing into the four-thousands in the last decade¹, the sample of directly imaged sub-stellar companions remains small (e.g., Bowler, 2016). Besides transit spectroscopy, which is limited to giant planets on short orbits, it are the directly-imaged giant planets whose atmospheric properties and composition can be directly studied through broad-band imaging and low-resolution spectroscopy (e.g., Biller & Bonnefoy, 2018). Together with evolutionary tracks and atmospheric models, this enables inferring their effective temperature, radius, surface gravity, age, and mass and to draw conclusions on their formation history and subsequent evolution (e.g., Bowler, 2016; Biller & Bonnefoy, 2018). Moreover, astrometric measurements from direct imaging enable deriving the orbital parameters of sub-stellar companions and studying the dynamical interactions with their environment (e.g., Kley & Nelson, 2012).

Recently, Gravity Collaboration et al. (2019) and Gravity Collaboration et al. (2020) used long-baseline interferometry to perform medium-resolution ($R \sim 500$) K-band spectroscopy of exoplanets. They could demonstrate astrometric measurements with a precision ~ 10 times better than what has been possible before, and constrain the atmospheric C/O ratio of the gas giant β Pic b. This, together with a chemical abundance framework of its protoplanetary disk based on Öberg et al. (2011), enabled them to infer a formation by core-accretion (Pollack et al., 1996) between the water and carbon-dioxide icelines. Furthermore, Nowak et al. (2020) could directly detect β Pic c, another gas giant in the same system originally discovered with the radial velocity technique (Lagrange et al., 2019). They showed that the precise mass estimate from the radial velocity data together with the K-band spectrum favors a formation by warm start core accretion (e.g., Mordasini, 2013) for β Pic c. In this regard, infrared interferometry significantly advances the field of planet formation and evolution by enabling direct observations of exoplanets discovered with the radial velocity technique for the first time ever.

Here, we present Very Large Telescope Interferometer (VLTI)/GRAVITY K-band spectroscopy of the directly imaged sub-stellar companion HD 206893 B. Located in a debris disk system (Milli et al., 2017; Marino et al., 2020) at a distance of 40.8 pc (Gaia Collaboration, 2018), astronomers are puzzled by the nature of this companion due to its unusually red near-infrared color. Delorme et al. (2017) found that an additional K-band extinction of ~ 0.5 mag is required to match the spectrum of HD 206893 B with those of other dusty, low-gravity or young brown dwarfs. Furthermore, Delorme et al. (2017) and Ward-Duong et al. (2021) showed that its extremely red color together with its very shallow 1.4 μm water absorption feature are challenging to fit with currently available at-

¹<http://exoplanet.eu/>

Table 6.1: Observing log. NEXP, NDIT, and DIT denote the number of exposures, the number of detector integrations per exposure, and the detector integration time, respectively, and τ_0 denotes the atmospheric coherence time.

Date	UT time		NEXP/NDIT/DIT		Airmass	τ_0	Seeing
	Start	End	HD 206893 B	HD 206893 A			
2019-07-17	08:52:56	09:56:06	5/12/60 s	6/64/1 s	1.17–1.54	1.5–2.2 ms	1.11–1.71''
2019-08-13	03:21:16	04:21:09	5/12/60 s	7/64/1 s	1.03–1.12	3.2–4.9 ms	0.80–1.00''

Table 6.2: Relative astrometry of HD 206893 B. The covariance matrix can be obtained using $\sigma_{\Delta\text{RA}}^2$ and $\sigma_{\Delta\text{Dec}}^2$ on the diagonal, and $\rho\sigma_{\Delta\text{RA}}\sigma_{\Delta\text{Dec}}$ off-diagonal.

MJD	ΔRA	ΔDec	$\sigma_{\Delta\text{RA}}$	$\sigma_{\Delta\text{Dec}}$	ρ
(days)	(mas)	(mas)	(mas)	(mas)	–
58681.396	130.73	198.10	0.04	0.06	-0.58
58708.165	127.03	199.27	0.09	0.13	-0.88

atmospheric models without an additional extra-photospheric source of extinction. While [Delorme et al. \(2017\)](#) argue for HD 206893 B being an extremely dusty 15–30 M_{Jup} L-dwarf, consistent with their age estimate of 50–700 Myr for the host star, [Ward-Duong et al. \(2021\)](#) note that its H and K-band spectra suggest a lower gravity and younger object. Together with the high infrared excess of the disk and a possible Argus moving group membership of the host star (membership probability $\sim 61\%$, [Ward-Duong et al., 2021](#)), there is a consistent scenario for HD 206893 B being a young (< 50 Myr) gas giant planet. This scenario is also supported by the dynamical mass estimate of $10_{-4}^{+5} M_{\text{Jup}}$ from [Grandjean et al. \(2019\)](#) based on radial velocity data of the system.

We aim to further constrain the nature of HD 206893 B. From the GRAVITY data, we extract its astrometry with a precision of $\sim 100 \mu\text{as}$ and a medium-resolution ($R \sim 500$) K-band contrast spectrum, that we convert to a spectrum of HD 206893 B with a model spectrum of its host star (cf. Section 6.2). Then, we improve the constraints on the orbital parameters of HD 206893 B (cf. Section 6.3) and perform atmospheric model fitting, with and without additional extra-photospheric extinction by high-altitude dust clouds made of enstatite grains (cf. Section 6.4.1). Moreover, we check for consistency between our best fit atmospheric models and evolutionary tracks (cf. Section 6.4.2). Finally, we discuss our findings in the context of previous works on this system (cf. Section 6.5).

6.2 Observations and data reduction

We obtained two epochs of medium-resolution ($R \sim 500$) GRAVITY data ([Gravity Collaboration et al., 2017](#)) of HD 206893 A and B combining the light of the four Unit Telescopes (UTs) at the VLTI. The observing log is presented in Table 6.1. The atmospheric conditions varied between average (atmospheric coherence time $\tau_0 = 5$ ms) and below average ($\tau_0 \approx 1.5$ ms) because both epochs

Table 6.3: Stellar parameters and 2MASS and WISE photometry of HD 206893 A from the literature.

Parameter	Unit	Value	Source
T_{eff}	K	6500 ± 100	D17
$\log g$	–	4.45 ± 0.15	D17
[Fe/H]	dex	0.04 ± 0.02	D17
R	R_{\odot}	1.26 ± 0.02	D17
π	mas	24.51 ± 0.06	G18
J _{2MASS}	mag	5.869 ± 0.023	S06
H _{2MASS}	mag	5.687 ± 0.034	S06
Ks _{2MASS}	mag	5.593 ± 0.021	S06
W1 _{WISE}	mag	5.573 ± 0.176	W10
W2 _{WISE}	mag	5.452 ± 0.052	W10
W3 _{WISE}	mag	5.629 ± 0.015	W10
W4 _{WISE}	mag	5.481 ± 0.043	W10

Notes. D17 = Delorme et al. (2017), G18 = Gaia Collaboration (2018), S06 = Skrutskie et al. (2006), W10 = Wright et al. (2010).

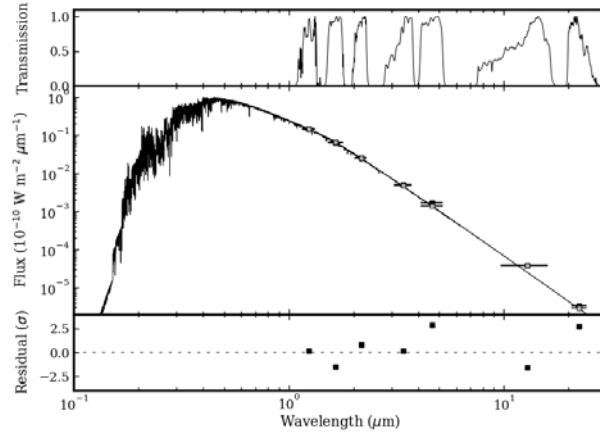


Figure 6.1: BT-NextGen model spectrum of HD 206893 A, scaled to fit the shown 2MASS and WISE photometry. The top panel shows the transmission curves corresponding to each photometric data point and the bottom panel shows the residuals between the photometry and the model spectrum. **The 2MASS filters do also include the atmospheric transmission.**

of data were obtained as bad weather backup targets for the AGN large program (PI E. Sturm, program ID 1103.B-0626).

From the GRAVITY data, we extract the coherent flux following the standard recipe of the official ESO data reduction pipeline (Lapeyrere et al., 2014). During this first step, the pipeline computes the coherent flux observed on the host star and the companion. However, the coherent flux observed on the faint companion is still contaminated by the halo of the bright host star. This contamination is removed using a Python package developed by our team². The individual steps of this package are outlined in Appendix A of Gravity Collaboration et al. (2020) and its output is the decontaminated ratio of the coherent flux between the companion and the host star. **In short, the package models the complex visibility observed on the planet as the sum of wavelength-dependent stellar leakage and the planet visibility expressed in terms of the stellar visibility and the planet-to-star contrast spectrum $C(\lambda)$. Then, assuming a model contrast spectrum, a log-likelihood map in ΔRA and ΔDEC is computed to find the best fit planet position. Given this position, the contrast spectrum is then obtained by inverting the projection of the source visibility onto the array baselines. For just one baseline and DIT, this is an underdetermined set of equations, but the projection matrix changes for each baseline and DIT enabling re-construction of the full contrast spectrum. The model contrast spectrum is then updated with the measured one and the entire process is repeated until the solution for the contrast spectrum has sufficiently converged.**

The astrometry for each epoch of data is obtained from the phase of the ratio of the coherent flux and presented in Table 6.2. The uncertainties are estimated from the scatter of the astrometric values obtained independently for each individual exposure. The typical precision is $\sim 100 \mu\text{as}$, which is well beyond the theoretical limit of $16.5 \mu\text{as}$ determined by Lacour et al. (2014). **This can be attributed to low and high frequency phase errors present in our data and introduced by instrumental and atmospheric aberrations (Gravity Collaboration et al., 2021).** The precision of our astrometry is therefore, in principle, not limited by systematic errors. Furthermore, due to the asymmetry of the uv-plane, we use the correlation coefficient ρ to properly describe the confidence intervals and the correlations between the right ascension and the declination offset.

Finally, a spectrum of the companion for each epoch is obtained from the amplitude of the ratio of the coherent flux. Before, though, this ratio is corrected for the visibility of the host star which is modelled as a uniform disk of 0.079 mas diameter (Chelli et al., 2016). Then, it is multiplied by a model spectrum of the host star, which is obtained by interpolating the BT-NextGen stellar model grid (Allard et al., 2012) for the stellar parameters presented in Table 6.3. Before, the model spectrum is scaled to match the stellar photometry presented in Table 6.3, yielding a scaling factor of ~ 1.17 . The 2MASS and WISE photometry are

²Python package available on GitHub upon request.

Table 6.4: Orbital parameters inferred for HD 206893 B. The posterior states the 68% confidence interval around the median. $\mathcal{N}(\mu, \sigma)$ denotes a normal distribution with mean μ and standard deviation σ . Scenario 1 is constrained by the data only and scenario 2 has an additional constraint on coplanarity with the debris disk.

Parameter	Prior	Posterior ¹	Posterior ²
a (au)	LogUniform(1, 100)	$9.26^{+1.82}_{-0.90}$	$11.37^{+1.09}_{-0.75}$
e	Uniform(0, 1)	$0.29^{+0.06}_{-0.12}$	$0.13^{+0.05}_{-0.03}$
i (deg)	Sine(0, 180) ¹	154^{+12}_{-10}	–
	$\mathcal{N}(140, 3)$ ²	–	142^{+2}_{-3}
ω (deg)	Uniform(0, 360)	126^{+86}_{-47}	71^{+35}_{-25}
Ω (deg)	Uniform(0, 180) ¹	55^{+48}_{-29}	–
	$\mathcal{N}(61, 4)$ ²	–	60^{+3}_{-3}
τ	Uniform(0, 1)	$0.58^{+0.09}_{-0.21}$	$0.32^{+0.11}_{-0.09}$
π (mas)	$\mathcal{N}(24.51, 0.06)$ ^(a)	$24.50^{+0.06}_{-0.06}$	$24.51^{+0.06}_{-0.06}$
M_{tot} (M_{\odot})	$\mathcal{N}(1.32, 0.02)$ ^(b)	$1.32^{+0.02}_{-0.02}$	$1.32^{+0.02}_{-0.02}$

Notes. (a) [Gaia Collaboration \(2018\)](#), (b) [Delorme et al. \(2017\)](#).

sufficient to constrain the stellar spectrum over the GRAVITY wavelength range (see Figure 6.1). This yields a spectrum of HD 206893 B for each epoch whose combination is shown in Figure 6.3.

6.3 Orbit fitting

From the interferometric observations with GRAVITY we obtain two new astrometric data points with an unprecedented precision of $\sim 100 \mu\text{as}$ for HD 206893 B (see Table 6.2). Together with astrometric data from the literature (see Table 6.7), we estimate the orbital parameters of HD 206893 B with `orbitize!`³ ([Blunt et al., 2020](#)), which infers the posterior distribution of the orbital parameters through Markov Chain Monte Carlo (MCMC) sampling with `ptemcee`⁴ ([Foreman-Mackey et al., 2013](#); [Vousden et al., 2016](#)). We initialize the sampler with 20 temperatures, 500 walkers, and 50000 steps per walker. By visual inspection of the walker chains, we assess convergence and reject the first 40000 steps before computing the posterior distribution from each walker at the lowest temperature. We note that we deploy the priors presented in Table 6.4 for the orbital parameters. These priors are chosen very conservatively in order to not constrain the posterior. The posterior distribution of the orbital parameters and the inferred orbital solutions together with the NACO, SPHERE, GPI, and

³<https://github.com/sblunt/orbitize>

⁴<https://github.com/willvousden/ptemcee>

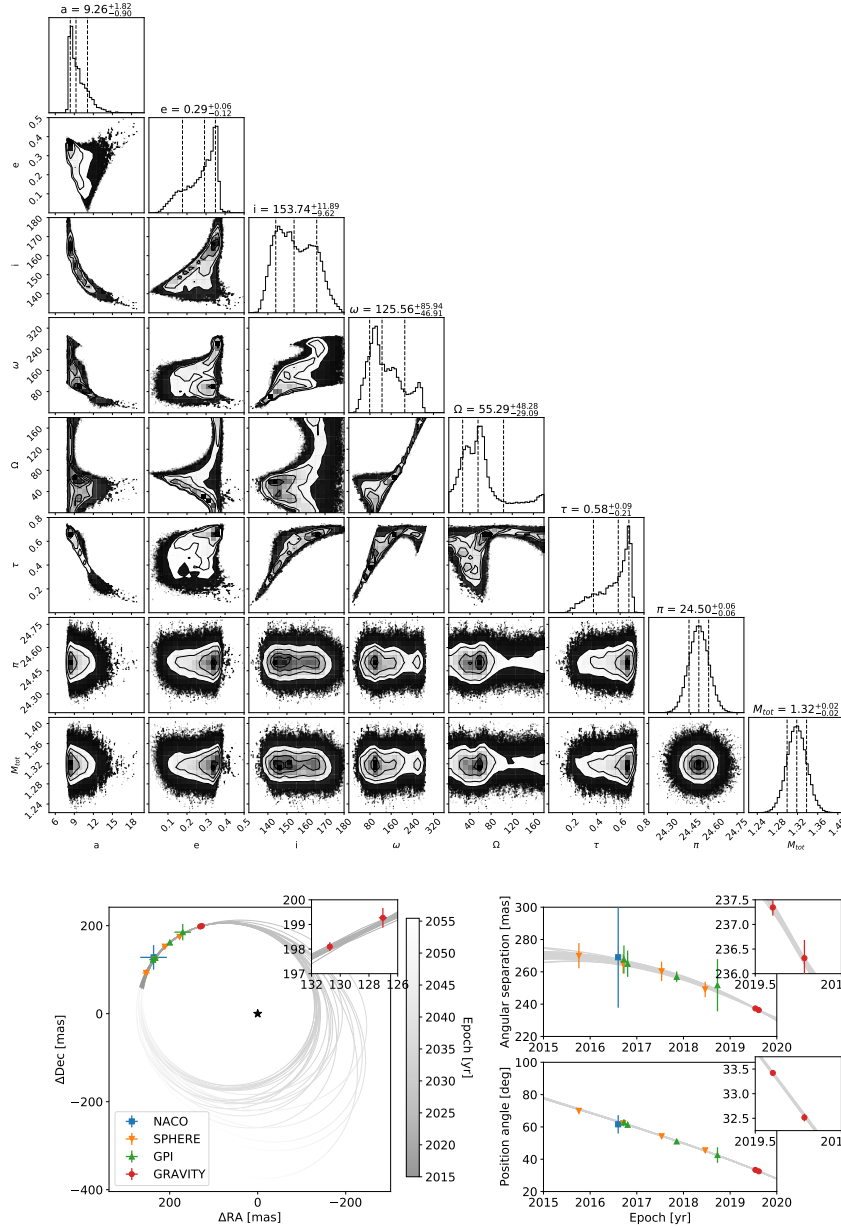


Figure 6.2: Posterior distribution of the orbital parameters (top) and orbital solutions together with the NACO, SPHERE, GPI, and GRAVITY astrometry (bottom) of HD 206893 B. In the top panel, the values state the 68% confidence intervals around the median. In the bottom panel, the black star highlights the position of HD 206893 A and all error bars show the $3-\sigma$ confidence intervals.

GRAVITY astrometry are shown in Figure 6.2.

In general, the GRAVITY astrometry is consistent with those from NACO, SPHERE, and GPI and our orbital solutions are consistent with those from Grandjean et al. (2019) and Ward-Duong et al. (2021). Both of them obtained a double-peaked semi-major axis distribution and an anti-correlation between semi-major axis a and eccentricity e . However, adding the GRAVITY astrometry disfavors small eccentricities $e \sim 0$ and removes the second peak in the semi-major axis distribution. Instead, a smaller semi-major axis of ~ 8.3 au and a higher eccentricity of ~ 0.35 are preferred. Nevertheless, the inclination i is similar to that obtained by Grandjean et al. (2019) and Ward-Duong et al. (2021) with a value of ~ 145 deg. The mutual inclination i_m between the debris disk of the system reported by Milli et al. (2017) and Marino et al. (2020) and HD 206893 B is

$$i_m = \arccos(\cos(i)\cos(i_d) + \sin(i)\sin(i_d)\cos(\Omega - \Omega_d)), \quad (6.1)$$

where $i_d = 140 \pm 3$ deg and $\Omega_d = 61 \pm 4$ deg (Marino et al., 2020). For our maximum likelihood orbital parameters we find $i_m \sim 6$ deg, which means that the debris disk and the companion are roughly (but not perfectly) aligned. We note that we used priors between 0 and 180 deg for the longitude of the ascending node Ω to enforce the debris disk and the companion orbiting in the same direction. However, the direction of rotation of the debris disk is unconstrained and there is a 180 deg ambiguity in the mutual inclination i_m between the debris disk and the companion (Heintz, 1978). Therefore, they might as well orbit in opposite directions.

Interestingly, Marino et al. (2020) found that if they enforce coplanarity between the debris disk and the companion, this would lead to the other one of the degenerate solutions being preferred, namely a larger semi-major axis of ~ 11.4 au and a smaller eccentricity of ~ 0.14 . To verify their findings, we ran another fit with Gaussian priors of 140 ± 3 deg for the inclination i and 61 ± 4 deg for the longitude of the ascending node Ω . The results are shown in Figure 6.8 and confirm the findings of Marino et al. (2020), even when adding the GRAVITY astrometry. Therefore, depending on whether coplanarity with the debris disk is assumed or not, degenerate orbital solutions are obtained for HD 206893 B.

6.4 Spectral analysis

Apart from the two astrometric data points, we also obtain two K-band contrast spectra at a resolution of $R \sim 500$, one for each epoch of GRAVITY data. These spectra measure the contrast between HD 206893 B and its host star, and with the help of a model spectrum of the host star we obtain the spectra of HD 206893 B as described in Section 6.2. The two spectra for the two different epochs are consistent with each other and we combine them into a single final spectrum,

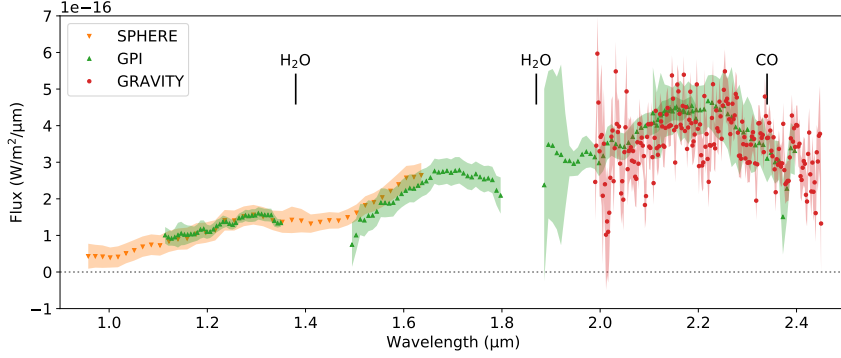


Figure 6.3: Combined GRAVITY K-band spectrum of HD 206893 B together with the SPHERE Y–H-band spectrum from [Delorme et al. \(2017\)](#) and the GPI J, H, K1, and K2-band spectra from [Ward-Duong et al. \(2021\)](#). The shaded regions highlight the $1\text{-}\sigma$ confidence intervals. For reference, absorption bands of water and carbon monoxide are indicated.

Table 6.5: Prior boundaries for the atmospheric model grids used in this work. The boundaries for the effective temperature and the radius were chosen based on previous works on HD 206893 B, while those for the other parameters exploit the maximum allowed range.

Model	T_{eff} (K)	$\log g$	[Fe/H] (dex)	C/O	R (R_{Jup})
BT-Settl-CIFIST	1000–2000	2.5–5.5	–	–	0.8–6.0
DRIFT-PHOENIX	1000–2000	3.0–5.5	-0.6–0.3	–	0.8–6.0
Exo-REM	1000–2000	3.5–4.5	-0.5–0.5	0.3–0.75	0.8–6.0

accounting for the covariances, shown in Figure 6.3 together with the SPHERE spectrum from [Delorme et al. \(2017\)](#) and the GPI spectra from [Ward-Duong et al. \(2021\)](#). In Section 6.4.1, we use these spectra for atmospheric model fitting of HD 206893 B. To constrain the fits between 3.5–5 μm , we supplement the spectra with photometry of HD 206893 B from the literature (see Table 6.8).

6.4.1 Atmospheric model fitting

By combining the GRAVITY spectrum with SPHERE and GPI spectra and photometry available in the literature, we reach a broad spectral coverage from $\sim 1\text{--}5$ μm . This spectral region contains absorption bands of water, carbon-monoxide, and methane and is broad enough to estimate the effective temperature, the radius, and the surface gravity of an object. We estimate these parameters for HD 206893 B by fitting its spectra and photometry with atmospheric model

Table 6.6: Atmospheric parameters inferred for HD 206893 B. The plain models are unmodified whereas the dusty models include additional extinction by high-altitude dust clouds made of enstatite grains. The values state the 68% confidence intervals around the median. Arrows (\uparrow or \downarrow) indicate if a parameter converges toward the upper or lower grid boundary.

Model	T_{eff} (K)	$\log g$	[Fe/H] (dex)	C/O	R ($R_{\text{J,up}}$)	M ($M_{\text{J,up}}$)	a_{mean} (μm)	σ_a	A_V (mag)	χ^2_{red}
Plain										
BT	1600^{+1}_{-1}	$3.50^{+0.00}_{-0.01}$	—	—	$0.98^{+0.01}_{-0.01}$	$1.17^{+0.02}_{-0.02}$	—	—	—	0.957
DP	1431^{+9}_{-9}	$5.14^{+0.20}_{-0.13}$	$0.27^{+0.02}_{-0.04}$ (\uparrow)	—	$1.20^{+0.03}_{-0.03}$	77^{+45}_{-21}	—	—	—	0.841
ER	1049^{+2}_{-4}	$3.50^{+0.00}_{-0.00}$ (\downarrow)	$0.49^{+0.01}_{-0.01}$ (\uparrow)	$0.65^{+0.00}_{-0.00}$	$2.32^{+0.02}_{-0.02}$	$6.58^{+0.11}_{-0.10}$	—	—	—	1.024
Dusty										
BT	1589^{+13}_{-22}	$3.83^{+0.38}_{-0.14}$	—	—	$1.17^{+0.07}_{-0.05}$	$3.55^{+5.67}_{-1.08}$	$0.33^{+0.05}_{-0.06}$	$1.30^{+0.15}_{-0.12}$	$1.99^{+0.44}_{-0.50}$	0.751
DP	1444^{+12}_{-11}	$5.02^{+0.14}_{-0.06}$	$0.26^{+0.03}_{-0.05}$	—	$1.75^{+0.25}_{-0.08}$	123^{+35}_{-35}	$2.29^{+0.11}_{-0.04}$	$1.17^{+0.07}_{-0.15}$	$0.82^{+0.23}_{-0.36}$	0.774
ER	1347^{+6}_{-7}	$3.55^{+0.06}_{-0.04}$ (\downarrow)	$0.06^{+0.09}_{-0.07}$	$0.75^{+0.00}_{-0.01}$ (\uparrow)	$2.03^{+0.08}_{-0.08}$	$5.71^{+1.01}_{-0.65}$	$0.34^{+0.04}_{-0.04}$	$1.34^{+0.11}_{-0.08}$	$2.87^{+0.36}_{-0.30}$	0.757

grids using `species`⁵ (Stolker et al., 2020). There is a variety of atmospheric model grids for giant planets and brown dwarfs, all of them being slightly different in terms of underlying physics and complexity. However, all of them assume radiative-convective equilibrium to calculate the temperature structure of the atmosphere self-consistently. Here, we use three different grids: the BT-Settl-CIFIST grid (Baraffe et al., 2015), the DRIFT-PHOENIX grid (Helling et al., 2008) (which includes metallicity as an additional free parameter), and the ExoREM grid (Baudino et al., 2015; Charnay et al., 2018) (which includes both metallicity and C/O ratio as additional free parameters). All three grids include photospheric absorption by dust clouds, but with different approaches to calculate the cloud densities, grain size distributions and compositions. We bin the grids to the spectral resolution of the respective instrument and use the spectra and filter curves to calculate the synthetic photometry and filter-weighted average flux, respectively. For all grid parameters, we deploy uniform priors whose boundaries are presented in Table 6.5. Our atmospheric model fits account for the covariances in the GRAVITY spectrum according to Greco & Brandt (2016). While fits to the GRAVITY and the SPHERE spectra alone show good photometric agreement between the two, there seems to be a significant offset between the GPI H-band and the SPHERE spectrum, which may indicate a systematic error in the absolute flux calibration. Given that the SPHERE spectrum agrees well with the GPI J-band spectrum, we decided to fit a separate scaling parameter to each of the GPI spectra while keeping the GRAVITY and the SPHERE spectra fixed in order to preserve the extremely red color of HD 206893 B. Then, we infer the posterior distribution of the model parameters with nested sampling using `PyMultiNest`⁶ (Buchner et al., 2014; Feroz et al., 2009, 2019).

The extreme redness of HD 206893 B has been tried to be explained with extinction by local dust, either extra-photospheric or in the form of a circumplanetary disk by Milli et al. (2017), Delorme et al. (2017), and Ward-Duong et al. (2021). Other possibilities like reddening by interstellar dust or extinction by the debris disk could be mostly ruled out. Ward-Duong et al. (2021) could not find any significant interstellar extinction toward the host star based on its photometry, and we can confirm this finding by visual inspection of stellar Ca-lines in high-resolution spectra of HD 206893 A (A.-M. Lagrange, private communication). It is highly unlikely that there is an interstellar dust cloud which is only obscuring HD 206893 B, but not its host star separated by only ~ 250 mas. Moreover, the debris disk of the system would need to be unrealistically optically thick ($\tau \sim 1.7$) to explain the observed reddening, even if viewed edge-on (Ward-Duong et al., 2021). Therefore, extinction by local dust is the most plausible explanation for the extremely red color of HD 206893 B, and we include additional extinction caused by high-altitude dust clouds made of crystalline enstatite (MgSiO_3) grains in our atmospheric model fits. **Since** Ward-Duong et al.

⁵<https://github.com/tomasstolker/species>

⁶<https://github.com/JohannesBuchner/PyMultiNest>

(2021) mention that common dust species such as forsterite, enstatite, corundum, and iron predict similar extinction curves for grain sizes between 0.1–1 μm , we decided to only consider enstatite grains for simplicity here. The enstatite grains are described by a log-normal size distribution

$$n(a) \propto \exp\left(\frac{(a - a_{\text{mean}})^2}{\sigma_a^2}\right) \quad (6.2)$$

where a is the grain size, a_{mean} is the geometric mean grain size, and σ_a is the grain size geometric standard deviation (which is dimensionless, Ackerman & Marley, 2001). A log-uniform prior between 0.1–10 μm is used for a_{mean} and a uniform prior between 1.1–10 is used for σ_a . Smaller grains would grow by condensation within timescales of less than a second and are therefore not considered (Charnay et al., 2018). Then, we compute the extinction cross-section $\sigma_{\text{ext}}(a_{\text{mean}}, \sigma_a)$ using PyMieScatt⁷ (Sumlin et al., 2018) and scale the observed flux F_{obs} to the de-reddened flux

$$F_{\text{der}} = F_{\text{obs}} \exp\left(\frac{A_V \sigma_{\text{ext}}}{2.5 \sigma_{\text{ext},V}}\right), \quad (6.3)$$

where A_V is the extinction in the Bessel V-band, another free parameter with a uniform prior between 0–5 mag, and $\sigma_{\text{ext},V}$ is the extinction cross-section averaged over the Bessel V-band. In total, our enstatite dust model has three free parameters (a_{mean} , σ_a , and A_V) which are inferred along with the parameters of the atmospheric model grids.

Table 6.6 summarizes the atmospheric parameters obtained for HD 206893 B based on the three different atmospheric model grids without (“plain”) and with (“dusty”) additional extinction caused by high-altitude dust clouds made of enstatite grains. The inferred effective temperatures are very similar to those obtained by Delorme et al. (2017) and Ward-Duong et al. (2021), but the surface gravities confirm the trend observed by Ward-Duong et al. (2021), namely that the H and K-band spectra prefer lower surface gravities than those obtained by Delorme et al. (2017) for the SPHERE spectrum at shorter wavelengths. Overall, the parameters inferred from the plain models are spread over a wider range of parameter space than those inferred from the dusty models. Moreover, all dusty models fit the observed data better than the plain models since they have smaller χ_{red}^2 . This is not completely surprising given that the dusty models have three more free parameters for describing the additional extinction than the plain models. Most noticeably, for both the plain and the dusty models the DRIFT-PHOENIX (DP) grid predicts a significantly higher surface gravity and mass for HD 206893 B than the BT-Settl-CIFIST (BT) and the Exo-REM (ER) grids. However, while the DP grid yields the best fit (i.e., the smallest χ_{red}^2) for the plain models, it yields the worst fit (i.e., the highest χ_{red}^2) for the dusty models.

⁷<https://github.com/bsumlin/PyMieScatt>

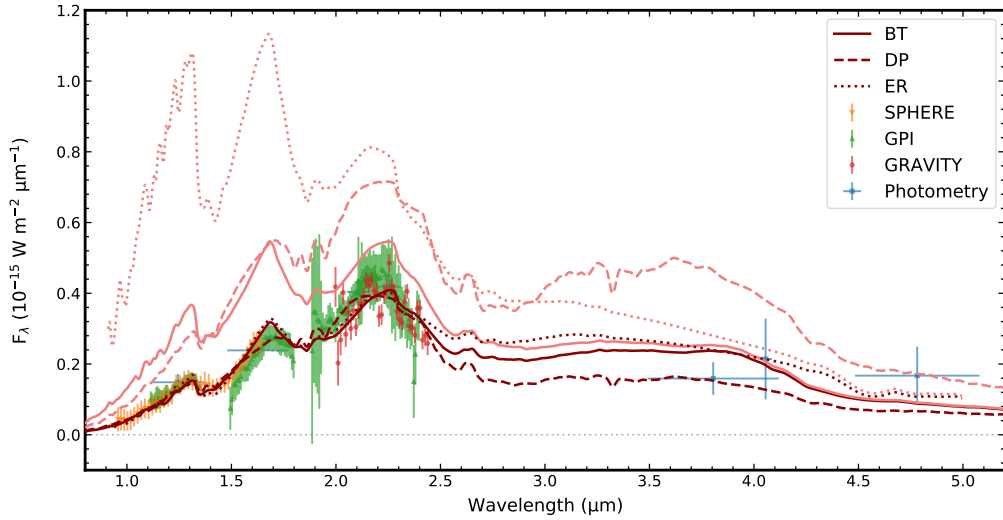


Figure 6.4: Atmospheric models fitted to the observed spectra and photometry of HD 206893 B shown in the background. Dark red lines show the best fit dusty models including additional extinction caused by high-altitude dust clouds made of enstatite grains and light red lines show the exact same models before adding the extinction. BT = BT-Settl-CIFIST, DP = DRIFT-PHOENIX, and ER = Exo-REM.

Another striking difference between the DP grid and the BT and ER grids are the extinction parameters that they predict for the dusty models. While the BT and ER grids consistently prefer small grains with a geometric mean size of $\sim 0.33\text{--}0.34\ \mu\text{m}$ and a geometric standard deviation of $\sim 1.30\text{--}1.34$ (cf. Figure 6.5), the DP grid prefers large grains with a geometric mean size of $\sim 2.29\ \mu\text{m}$ and a geometric standard deviation of ~ 1.17 . This is a difference in geometric mean grain size of almost an order of magnitude. Figure 6.4 shows the best fit model spectra for the dusty models in dark red together with the NACO, SPHERE, GPI, and GRAVITY spectra and photometry of HD 206893 B. It is noteworthy that there are significant differences between the BT and ER grids and the DP grid regarding the depth of the $1.4\ \mu\text{m}$ water absorption feature and the morphology of the H-band and K-band peaks. Moreover, they deviate significantly at longer wavelengths ($> 2.5\ \mu\text{m}$). There, the available NACO photometry is not precise enough to set meaningful constraints on the model parameters and better data, for example from the *James Webb Space Telescope*, is required.

The exact same three dusty models are shown in light red, but before the additional extinction caused by high-altitude dust clouds made of enstatite grains is added to the model spectra. Here, the striking difference in predicted grain size between the DP grid and the BT and ER grids becomes very clear. While for the BT and ER grids, the difference between unextinct (light red) and extinct

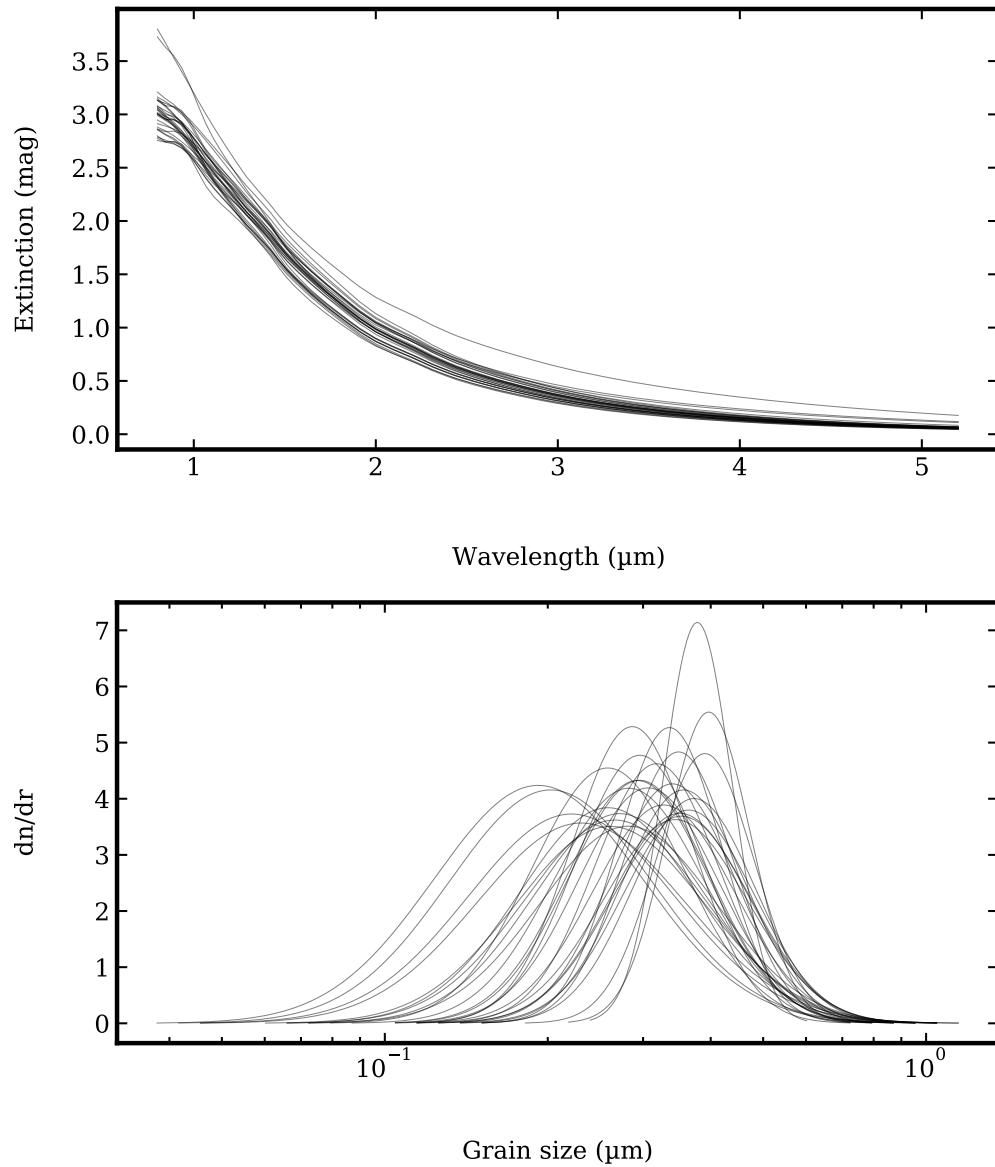


Figure 6.5: Extinction cross-section (top) and size distribution (bottom) of the enstatite dust grains for the best fit dusty ER model. The plots show 30 randomly drawn samples from the posterior distribution. Given the similar grain size parameters, the plots look similar for the best fit dusty BT model, but the extinction cross-section would be normalized to a smaller V-band extinction.

(dark red) model spectrum decreases with increasing wavelength and approaches zero over the L and M-band, the extinction reaches its maximum near the L-band (where the wavelength is of the order of the geometric mean grain size) for the DP grid. Finally, we note that the ER grid predicts a significantly higher V-band extinction than the BT grid, despite the very similar grain size parameters. This is the case because the ER grid converges toward a significantly larger radius if compared to the BT grid, resulting in a higher bolometric luminosity and therefore requiring higher extinction. **We note that similar results would be expected for other common dust species such as forsterite, corundum, and iron given their similar extinction cross-sections below 1 μm .**

6.4.2 Evolutionary tracks

Similar to Delorme et al. (2017), we compare our best fit atmospheric models to evolutionary tracks for giant planets and brown dwarfs to ensure that they correspond to physically plausible sub-stellar companions. Therefore, we use the AMES-Cond evolutionary tracks (Baraffe et al., 2003). Figure 6.6 shows these tracks for objects of different masses from 1–100 M_{Jup} in the surface gravity vs. effective temperature and the radius vs. effective temperature planes. The parameters of our best fit atmospheric models are overplotted in light red (plain models) and dark red (dusty models).

The most significant outlier is the plain ER grid, which predicts an implausibly large radius of $2.32_{-0.02}^{+0.02} R_{\text{Jup}}$ for a relatively cool (1049_{-4}^{+2} K) and low-mass ($6.58_{-0.10}^{+0.11} M_{\text{Jup}}$) object. With the additional extinction, the radius decreases and the effective temperature increases, leading to an object which is roughly consistent between the atmospheric models and the evolutionary tracks with an extremely young (< 10 Myr) planetary-mass ($< 5 M_{\text{Jup}}$) companion, given the uncertainties on the surface gravity and the radius from the atmospheric model fitting. We also note that the dusty ER grid converges toward the lower boundary of the surface gravity (~ 3.5). Other implausible objects are predicted by both the plain BT and the dusty DP grids. While the low surface gravity predicted by the plain BT grid is consistent with an extremely young object ($\sim 1\text{--}3$ Myr), its predicted small radius is consistent with a rather old object ($\sim 300\text{--}1000$ Myr). The same is observed the other way around for the dusty DP grid. Here, the predicted high surface gravity is consistent with a rather old object and the predicted large radius is consistent with an extremely young object. However, the dusty BT and the plain DP grids predict objects which are roughly consistent between the atmospheric models and the evolutionary tracks. The dusty BT grid suggests a moderately young ($\sim 3\text{--}300$ Myr) object somewhere between $\sim 5\text{--}30 M_{\text{Jup}}$. The plain DP grid suggests a rather old ($\sim 100\text{--}1000$ Myr) object somewhere between $\sim 15\text{--}75 M_{\text{Jup}}$. We note that **the parameter space predicted from the dusty BT and the plain DP grids is** also in agreement with the age and mass predicted for HD 206893 B by Delorme et al. (2017).

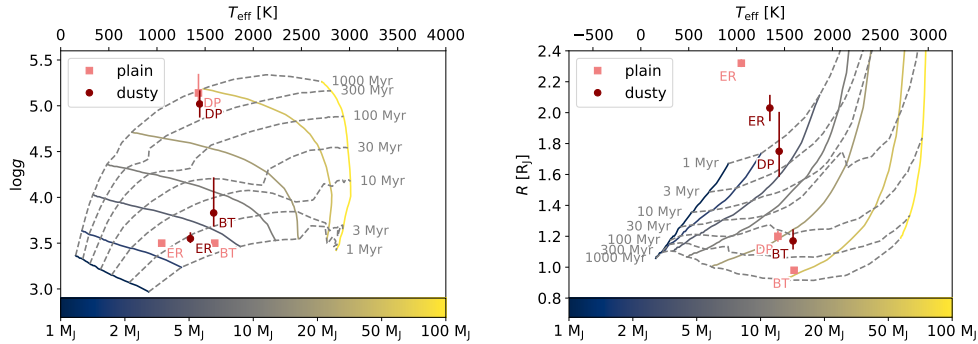


Figure 6.6: Parameters inferred for HD 206893 B from atmospheric model fitting compared to AMES-Cond evolutionary tracks. Light red points show the best fit parameters for the plain models and dark red points show the best fit parameters for the dusty models including additional extinction caused by high-altitude dust clouds made of enstatite grains. The evolutionary tracks are shown for objects with exactly those masses printed below the colorbar. Curves of constant age are shown in dashed grey. BT = BT-Settl-CIFIST, DP = DRIFT-PHOENIX, and ER = Exo-REM.

Overall, we find that the BT and the ER grids require additional extinction in order to predict physically plausible objects. This is different for the DP grid, which becomes unphysical when additional extinction is included. This could also be related to the much larger grain sizes predicted by the DP grid if compared to the BT and ER grids, which are not expected for high-altitude dust clouds (Hiranaka et al., 2016). Moreover, we find that the three different atmospheric model grids predict three degenerate objects. The (dusty) ER grid predicts an extremely young (< 10 Myr) object of $< 5 M_{\text{Jup}}$, the (dusty) BT grid predicts a moderately young ($\sim 3\text{--}300$ Myr) object of $\sim 5\text{--}30 M_{\text{Jup}}$, and the (plain) DP grid predicts a rather old (100–1000 Myr) object of $\sim 15\text{--}75 M_{\text{Jup}}$. Again, we note that this degeneracy could potentially be resolved by more precise L and M-band photometry, where the best fit plain DP model deviates significantly from the best fit dusty BT and ER models.

6.4.3 Color-magnitude diagram

In a color-magnitude diagram, it can easily be seen that HD 206893 B is the reddest known sub-stellar object (Milli et al., 2017; Delorme et al., 2017; Ward-Duong et al., 2021). Figure 6.7 shows J-K and H-K color-magnitude diagrams of HD 206893 B and other known planetary-mass companions. For reference, M, L, and T-dwarfs from the SpeX Prism Spectral Libraries⁸ are shown in the

⁸<http://pono.ucsd.edu/~adam/browndwarfs/spexprism/library.html>

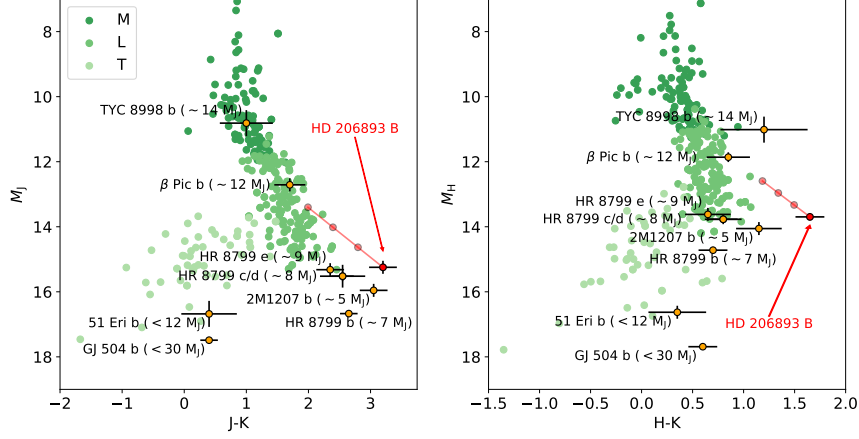


Figure 6.7: J-K and H-K color-magnitude diagrams showing HD 206893 B in red together with the reddening vectors of our best fit extra-photospheric enstatite dust model for different V-band extinctions. Other known planetary-mass objects are shown in orange and M, L, and T-dwarfs from the SpeX Prism Spectral Libraries are shown in green. For the dust model, we assume $a_{\text{mean}} = 0.33 \mu\text{m}$, $\sigma_a = 1.30$, and $A_V = 0-3$. The red dots are in steps of 1 mag.

background. The apparent magnitudes of the planetary-mass companions were taken from [Delorme et al. 2017](#) (HD 206893 B), [Currie et al. 2013](#) (β Pic b), [Skemer et al. 2016](#) (GJ 504 b), [Rajan et al. 2017](#) (51 Eri b), [Zurlo et al. 2016](#) (HR 8799 b, c, d, and e), [Patience et al. 2012](#) (2M1207 b), and [Bohn et al. 2020](#) (TYC 8998 b). Apparent magnitudes were converted to absolute magnitudes using distances (i.e., parallaxes) from [Gaia Collaboration \(2018\)](#).

The red lines show the reddening vectors of our best fit enstatite dust model for different V-band extinctions. Here, we assume $a_{\text{mean}} = 0.33 \mu\text{m}$ and $\sigma_a = 1.30$, consistent with the best fit dusty BT and ER models. We did not plot the reddening vector for the best fit dusty DP model because it corresponds to a physically implausible object (cf. Section 6.4.2). The shown reddening vectors extend from $A_V = 0-3$. For the best fit dusty BT and ER models, the predicted V-band extinction of $A_V \sim 2.0$ and $A_V \sim 2.9$, respectively, brings HD 206893 B back to the red end of the sub-stellar main-sequence, close to where other planetary-mass objects such as β Pic b and κ And b are located. This implies that HD 206893 B could indeed be a very dusty companion around a young moving group member, such as β Pic b and κ And b. Finally, compared to the interstellar reddening law applied by [Ward-Duong et al. \(2021\)](#), our enstatite dust model predicts a similar reddening slope in the M_H vs. H-K color-magnitude diagram while requiring smaller V-band extinction values of $\sim 2-3$ instead of ~ 10 in order to bring HD 206893 B back to the red end of the sub-stellar

main-sequence. The existence of the CT Cha companion (Schmidt et al., 2008) mentioned by Ward-Duong et al. (2021) and suffering from an extreme V-band extinction of ~ 5 magnitudes therefore puts the values of $A_V \sim 2\text{--}3$ obtained for HD 206893 B in a realistic regime.

6.5 Discussion

In Section 6.3, we infer the orbital parameters of HD 206893 B for two different scenarios. Scenario 1 is constrained by the data only and scenario 2 has an additional constraint on coplanarity with the debris disk of the system observed by Milli et al. (2017) and Marino et al. (2020). By comparison with earlier works from Grandjean et al. (2019) and Ward-Duong et al. (2021), we find that the GRAVITY data resolves the degeneracy between a lower eccentricity, larger semi-major axis and a higher eccentricity, smaller semi-major axis orbit by preferring the latter of these in scenario 1. This is interesting because this orbital solution is slightly misaligned with respect to the debris disk by ~ 6 deg. Marino et al. (2020) mention that a misalignment between the orbit of HD 206893 B and the debris disk should be unlikely given the system’s age of at least 50 Myr (Delorme et al., 2017). They argue that HD 206893 B should align with the debris disk due to secular interactions on timescales of only ~ 10 Myr. In scenario 2, where we enforce alignment between the orbit of HD 206893 B and the debris disk, we clearly find that the lower eccentricity, larger semi-major axis orbit is preferred. This is in agreement with Marino et al. (2020), who obtained the same result without the additional GRAVITY data, and reinforces our finding that the GRAVITY data alone prefers a slight misalignment between the orbit of HD 206893 B and the debris disk.

If this misalignment is confirmed by future GRAVITY observations, an explanation for it needs to be found. One possibility would be a significantly younger age (< 50 Myr) for the system. We note that such a young age would be in agreement with the age constraint set by comparing our best fit dusty BT and ER models with evolutionary tracks. In addition, an age of ~ 40 Myr would be expected according to Torres et al. (2008) if the system was part of the Argus moving group. Another possibility would be tidal interactions between HD 206893 B and the other putative companions predicted to exist in this system (e.g., Wu & Lithwick, 2011). There is evidence for a second, massive ($\sim 15 M_{\text{Jup}}$) and close (1.4–2.6 au) companion interior to the orbit of HD 206893 B from radial velocity data (Grandjean et al., 2019) and a third 0.4–1.7 M_{Jup} companion further out responsible for carving the gap at ~ 74 au in the debris disk observed with ALMA (Marino et al., 2020). However, a profound analysis of potential planet-planet interactions is beyond the scope of this work. Finally, we note that an eccentricity of ~ 0.3 for HD 206893 B preferred by the GRAVITY data is in better agreement with the eccentricity distribution of the brown dwarf popula-

tion than that of wide-separation (5–100 au) giant planets, the latter of which show a preference for low eccentricities (≈ 0.05 – 0.25 , Bowler et al., 2020). Still, sorting an individual companion into one or the other class of objects based on its eccentricity remains highly speculative, and as highlighted before, there might be other mechanisms responsible for an excitement of HD 206893 B’s eccentricity, such as tidal interactions with other companions in the system.

In Section 6.4, we analyze the near-infrared spectrum of HD 206893 B. We obtain a dense spectral coverage between 1–2.5 μm by combining data from SPHERE, GPI, and GRAVITY that we extend up to ~ 5 μm with VLT/NACO photometry from Stolker et al. (2020). While Delorme et al. (2017) and Ward-Duong et al. (2021) found that currently available atmospheric models for giant planets and brown dwarfs fail to predict the extremely red color and the very shallow 1.4 μm water absorption feature of HD 206893 B at the same time, they also compared the spectrum of HD 206893 B to those of other dusty, low-gravity or young M and L-dwarfs and found that none of these objects could reproduce all spectral features of HD 206893 B. Hence, both of these authors tried to reconcile the spectrum of HD 206893 B with those of other dusty, low-gravity or young M and L-dwarfs by including additional extinction caused by high-altitude dust clouds. Therefore, they explored a variety of dust species (forsterite, enstatite, corundum, and iron), grain sizes (0.05–1 μm), and extinction values. They found that reddening by forsterite or enstatite grains with sizes between 0.27–0.50 μm yields the best match to a very low-gravity L3-dwarf. Such a reddening by small (< 1 μm) dust grains in the cool upper atmosphere has been suggested before by Marocco et al. (2014) and Hiranaka et al. (2016) to match the spectra of unusually red L-dwarfs with those of spectroscopic standards. They concluded that scattering by dust clouds with grain sizes between 1–100 μm included in current atmospheric models is not sufficient to describe the peculiarly red L-dwarfs, which seem to require additional scattering by smaller grains in the cool upper atmosphere.

Here, we focussed on a slightly different approach by adding extinction caused by high-altitude dust clouds **made of enstatite grains** directly to the atmospheric model grids. Our dusty BT, DP, and ER grids fit the extremely red color as well as the very shallow 1.4 μm water absorption feature of HD 206893 B well (see Figure 6.4). However, both the plain and dusty DP grids fail to predict the pointy H-band peak observed with GPI⁹. Therefore, we obtain the best fits with our dusty BT and ER grids with $\chi^2 = 0.751$ and 0.757, respectively. In agreement with the comparison between HD 206893 B and other dusty, low-gravity or young M and L-dwarfs by Delorme et al. (2017) and Ward-Duong et al. (2021), we find a grain size distribution with a geometric mean size of ~ 0.33 – 0.34 μm for these grids.

⁹We note that since we allow for a scaling parameter for the GPI spectra, we cannot use them to obtain information about the absolute flux, but they are still useful to compare the spectral morphology between data and model.

From the comparison between our best fit atmospheric models and the AMES-Cond evolutionary tracks in Section 6.4.2, we find that the dusty ER grid would be consistent with an extremely young object and the plain DP grid would be consistent with a rather old object. In between the two, the dusty BT grid suggests a moderately young ($\sim 3\text{--}300$ Myr) object somewhere between $\sim 5\text{--}30 M_{\text{Jup}}$. While the uncertainties on HD 206893 B’s age and mass are large, it is still noteworthy that this solution is also in agreement with both the age of $\sim 40\text{--}270$ Myr estimated for the Argus moving group (Torres et al., 2008; Bell et al., 2015) and the mass of $10_{-4}^{+5} M_{\text{Jup}}$ predicted from radial velocity data of the system (Grandjean et al., 2019). Compared to Delorme et al. (2017), who report a best fit age and mass of $100\text{--}300$ Myr and $15\text{--}30 M_{\text{Jup}}$, respectively, we find that a younger, planetary-mass object would fit the data equally well.

6.6 Conclusions

We present new VLTI/GRAVITY K-band spectroscopy at a resolution of $R \sim 500$ of the reddest known sub-stellar companion HD 206893 B. From these observations we obtain two new astrometric data points with a precision of $\sim 100 \mu\text{as}$ as well as a low signal-to-noise K-band spectrum of HD 206893 B. We use the astrometry to update the orbital parameters of HD 206893 B and the spectrum to infer its atmospheric parameters with atmospheric model fitting. Given the previously observed difficulties with fitting both the extremely red color as well as the very shallow $1.4 \mu\text{m}$ water absorption feature of HD 206893 B (Delorme et al., 2017; Ward-Duong et al., 2021), we include additional extinction caused by high-altitude dust clouds made of enstatite grains in our atmospheric model fits.

From the orbit fitting, we find that the GRAVITY data resolves the previously observed degeneracy between a lower eccentricity, larger semi-major axis and a higher eccentricity, smaller semi-major axis orbit by preferring the latter of these. The orbital solution for HD 206893 B preferred by the GRAVITY data is also slightly misaligned with respect to the debris disk of the system. We argue that this misalignment could suggest a significantly younger age for the system or could be caused by tidal planet-planet interactions with other putative companions in the system. However, the slight preference for a misaligned orbit needs to be confirmed by future GRAVITY observations and a profound analysis of tidal planet-planet interactions and their impact on the alignment and eccentricity of HD 206893 B’s orbit is left for future work. **Astrometric accelerations from *Gaia* will further assist this process, but the timespan will be too small to cover a significant fraction of an orbit of B so that precision radial velocities are needed to disentangle between the inner (HD 206893 C) and outer (HD 206893 B) companion.**

From the atmospheric model fitting, we find that the BT-Settl-CIFIST (BT)

and Exo-REM (ER) grids including additional extinction (dusty models) can fit all near-infrared spectral features of HD 206893 B, namely the extremely red color, the very shallow 1.4 μm water absorption feature, and the pointy H-band peak observed with GPI. Both DRIFT-PHOENIX (DP) grids, however, these with (dusty models) and without (plain models) additional extinction, fail to reproduce the pointy H-band peak. By comparison to evolutionary tracks, we argue that only the best fit dusty BT and ER models as well as the plain DP model correspond to physically plausible objects. The best fit parameters of these three models are spread over a wide range of ages and masses, though. If the best fit dusty BT and ER models are favored over the best fit plain DP model, due to their ability to fit the pointy H-band peak observed with GPI, we predict an age of $\sim 3\text{--}300$ Myr and a mass of $\sim 5\text{--}30 M_{\text{Jup}}$ for HD 206893 B. Together with the mass estimate of $10_{-4}^{+5} M_{\text{Jup}}$ from radial velocity data (Grandjean et al., 2019) and a potential Argus moving group membership of the system (membership probability $\sim 61\%$, Ward-Duong et al., 2021), we conclude that a planetary nature has to be considered for HD 206893 B. However, further observations such as more precise L and M-band photometry from the *James Webb Space Telescope* and a broader spectral coverage or higher spectral resolution are required to make a robust statement on the nature of HD 206893 B.

Finally, it has been shown that the extreme atmospheric conditions on HD 206893 B responsible for its exceptionally red color cannot be reproduced by currently available atmospheric models for giant planets and brown dwarfs without further adaptations. The case of HD 206893 B can therefore serve as a benchmark for the further development of such atmospheric models which could ultimately lead to a more complete understanding of the objects at the boundary between exoplanets and brown dwarfs. Moreover, future radial velocity or high-contrast imaging observations might confirm the additional companions predicted to exist in this system and improve the mass estimate for HD 206893 B.

Appendix 1: orbit fitting and debris disk

Table 6.7: Relative astrometry of HD 206893 B from the literature. “Sep.” and “PA” denote the angular separation and the position angle, respectively, and “Inst.” denotes the instrument with which the data was acquired.

MJD (days)	Sep. (mas)	PA (deg)	Inst.	Band	Source
57300	270.0 ± 2.6	69.95 ± 0.55	SPHERE	H	M17
57608	269.0 ± 10.4	61.6 ± 1.9	NACO	L'	M17
57647	265 ± 2	62.25 ± 0.11	SPHERE	K1/K2	D17
57653	267.6 ± 2.9	62.72 ± 0.62	GPI	H	W20
57682	265.0 ± 2.7	61.33 ± 0.64	GPI	K1	W20
57948	260.3 ± 2.0	54.2 ± 0.4	SPHERE	H	G19
58066	256.9 ± 1.1	51.01 ± 0.35	GPI	K2	W20
58289	249.11 ± 1.60	45.50 ± 0.37	SPHERE	H2/H3	G19
58385	251.7 ± 5.4	42.6 ± 1.6	GPI	J	W20

Notes. M17 = [Milli et al. \(2017\)](#), D17 = [Delorme et al. \(2017\)](#),
G19 = [Grandjean et al. \(2019\)](#), W20 = [Ward-Duong
et al. \(2021\)](#).

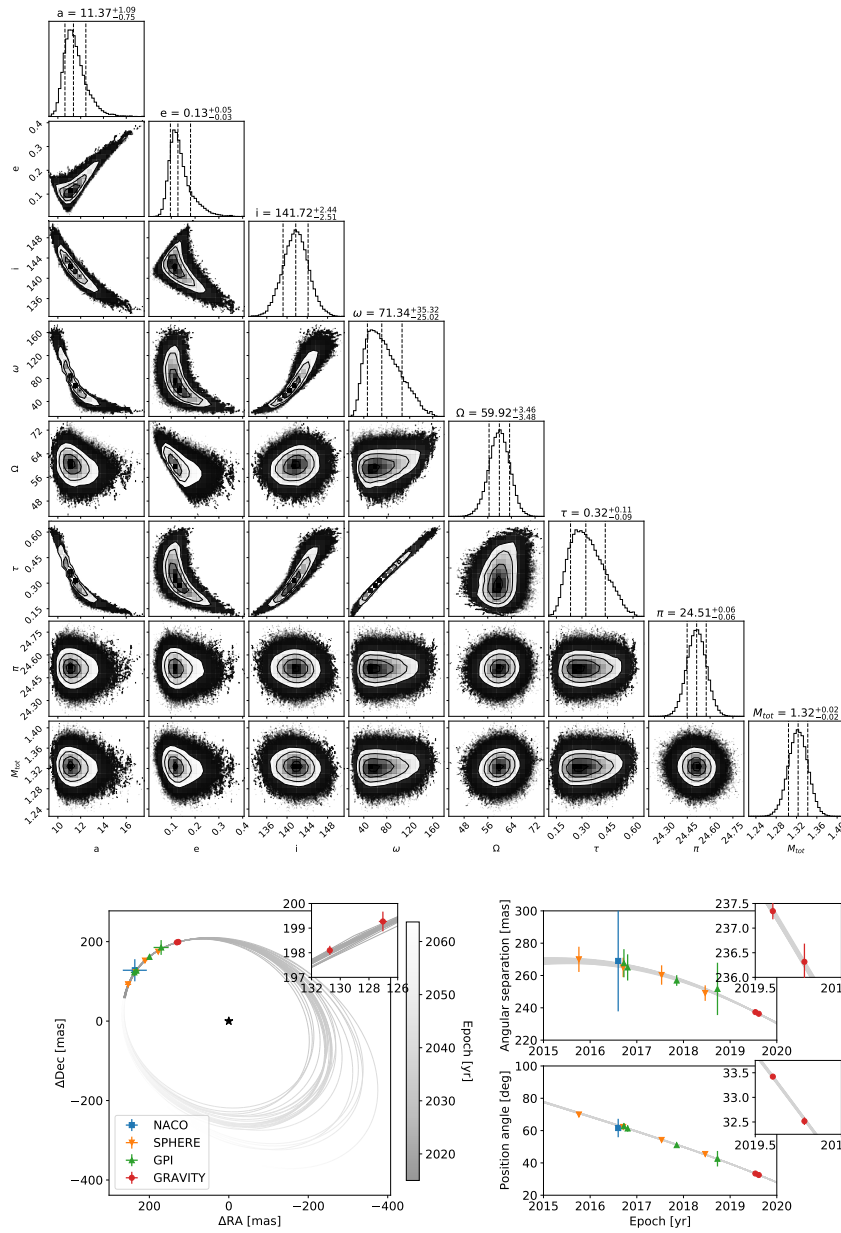


Figure 6.8: Same as Figure 6.2, but imposing Gaussian priors of 140 ± 3 deg for the inclination i and 61 ± 4 deg for the longitude of the ascending node Ω in order to enforce co-planarity between the orbit of HD 206893 B and the debris disk of the system.

Appendix 2: photometry

Table 6.8: Photometry of HD 206893 B from the literature. “Inst.” denotes the instrument with which the data was acquired.

Inst.	Band	λ (μm)	Value (mag)	Source
SPHERE	J	1.245	18.33 ± 0.17	D17
SPHERE	H	1.626	16.79 ± 0.06	D17
SPHERE	K1	2.104	15.20 ± 0.10	D17
SPHERE	K2	2.255	14.88 ± 0.09	D17
NACO	L'	3.805	13.80 ± 0.31	S20
NACO	NB405	4.056	13.17 ± 0.55	S20
NACO	M'	4.781	12.78 ± 0.51	S20

Notes. D17 = [Delorme et al. \(2017\)](#), S20 = [Stolker et al. \(2020\)](#).

Conclusions

In this thesis, we developed new methods to characterize data correlations in kernel phase and long-baseline interferometry and to account for them in the model fitting process. Furthermore, we refined the calibration process in kernel phase interferometry with a special variant of principal component analysis methods known as Karhunen-Loève decomposition. These improvements enable us to enter the high-contrast imaging regime from the ground, which we demonstrate on an archival VLT/NACO data set of nearby field stars. We detect eight low-mass stellar companions, five of which represent new discoveries, and two of which have separations below the classical (Rayleigh) diffraction-limit of the VLT, demonstrating the unprecedented angular resolution achievable with kernel phase interferometry. However, we find that the achieved contrast is limited by systematic errors due to a non-ideal observing strategy. With an observing technique called “star-hopping” we tackle this issue and enable a more accurate calibration of the stellar PSF at the smallest spatial scales ($\lesssim 1 \lambda/D$). We survey 55 young stars in the Taurus star-forming region for forming giant planets with this technique. For those, we achieve typical 5- σ contrast limits of ~ 6 mag at separations of 0.2 arcsec and ~ 8 mag at separations of 0.5 arcsec. In principle, these limits are sufficient for the detection of other young accreting protoplanets (e.g., PDS 70 b, [Keppler et al., 2018](#)), but we do not discover any new companions. Given the extreme youth of the observed targets in Taurus and based on our non-detections, we are able to put upper constraints on the giant planet frequency as a function of mass and orbital separation. As a next step, we apply kernel phase interferometry to mid-infrared data of the enigmatic T Tauri triple system. Once thought to be a prototypical single T Tauri-star with a circumstellar disk from which it accretes matter, it is today known to be a complex triple system with multiple misaligned circumstellar and circumbinary disks. At relatively low contrast, we obtain photometry of all three components of T Tauri, including the southern binary at an angular separation of down to $\sim 0.2 \lambda/D$ in our longest wavelength filter at $\sim 12.8 \mu\text{m}$.

Our empirical correlation model for VLTI/GRAVITY data enables a gain in contrast of a factor of up to ~ 2 at small angular separations, where detections are limited by systematic errors. We highlight the importance of accounting for these correlations by investigating the probability of false positive or false negative detections with and without our correlation model, finding that widely

used detection criteria based on χ^2 statistics are only valid when accounting for the correlations. Not doing so can lead to an excessive number of false positive detections. On the one hand, our correlation model enables observing fainter companions or circumstellar disks at small angular separations ($\lesssim 50$ mas) and the sensitivity to asymmetric features of observations such as those presented in Varga et al. (2020) could be improved by a factor of ~ 2 . On the other hand, accounting for the correlated errors yields a remarkable boost in the robustness of the detections (i.e., significantly fewer false positive detections). Therefore, a re-analysis of marginal companion (non)-detections from the archive, such as those presented in multiplicity studies of Cepheid stars from Gallenne et al. (2013, 2014, 2015), would greatly benefit from our correlation model and potentially yield new insights into the true nature of these companions.

Finally, we demonstrate the capabilities of optical long-baseline interferometry in terms of exoplanet and brown dwarf characterization. We obtain medium-resolution VLTI/GRAVITY spectroscopy of the reddest known sub-stellar companion HD 206893 B (Milli et al., 2017; Delorme et al., 2017) and infer its orbital and atmospheric parameters by model fitting. From the orbital fitting, we find that HD 206893 B orbits roughly co-planar with the debris disk of its parent star and therefore likely formed from its circumstellar disk. However, the GRAVITY astrometry prefers an eccentric orbit ($e \sim 0.3$) slightly misaligned with the debris disk, as opposed to the low-eccentricity orbit ($e < 0.1$) which is preferred if co-planarity with the debris disk is assumed. From the atmospheric fitting, we find that HD 206893 B is relatively hot, small, and low-mass, probably residing at the lower end of the brown dwarf regime. However, its extreme redness, most likely caused by high-altitude dust clouds in the cool upper atmosphere, complicates the model fitting process. More precise photometry in the L and M-band (e.g., with the *James Webb Space Telescope*) is required to draw a definitive conclusion on the nature of HD 206893 B and the extinction and dust grain properties of its clouds. Further insights could come from higher signal-to-noise or higher resolution near-infrared spectroscopy, which would enable measuring elemental abundances and linking them to chemical enrichment during formation (e.g., Öberg et al., 2011; Lavie et al., 2017).

Our work enables high-contrast imaging at extremely high resolution with kernel phase interferometry. While Martinache (2010) and Pope et al. (2013) reported $5\text{-}\sigma$ detection limits of ~ 5.75 mag at $\sim 1 \lambda/D$ with the *Hubble Space Telescope*, we achieve better limits of ~ 6 mag at separations of 0.2 arcsec and ~ 8 mag at separations of 0.5 arcsec with Keck/NIRC2 from the ground. This enables the detection of the youngest hot start giant planets (Wallace et al., 2020) and cold and warm start giant planets during the runaway gas accretion phase (Wallace & Ireland, 2019). Besides using a larger telescope, the gain in contrast if compared to earlier works is achieved by various improvements in the data reduction process, such as propagating uncertainties in the image plane to covariances in the Fourier plane and applying a calibration approach based

on principal component analysis methods. While kernel phase interferometry has mostly been used with space-based facilities before (Martinache, 2010; Pope et al., 2013), due to their exquisite PSF stability, our work enables using the technique with adaptive-optics-fed instruments from the ground. Kernel phase interferometry opens up the parameter space of young accreting protoplanets in the nearest star-forming regions, both in terms of contrast and resolution. However, as shown by Wallace & Ireland (2019), a further increase in contrast is required to access the bulk of young giant planets rather than just those which are particularly bright due to brief runaway gas accretion from a hot circumplanetary disk (e.g., Zhu, 2015). Such an increase in contrast could come either from the next generation of Extremely Large ground-based Telescopes (ELTs), improved adaptive optics systems delivering higher Strehl ratios, or from further developments on the post-processing side. Recently, Martinache et al. (2020) have shown that the previously used binary representation (i.e., either 0% or 100% transmission) of the pupil model introduced systematic errors to the kernel phase observables, which could be significantly mitigated by using a grey representation (i.e., continuous transmission between 0–100%) of the pupil model. Laugier et al. (2019) developed a method for reconstructing saturated PSFs complementary to the one applied in Kammerer et al. (2019) and Laugier et al. (2020) constructed a subset of kernel phases, the so-called angular differential kernel phases, which are robust with respect to static biases by making use of the field rotation. Further improvements could come from a treatment of higher-order atmospheric noise, for example by making use of the telemetry of adaptive optics systems, and mitigating remaining systematic errors will be key for high-contrast kernel phase observations of exoplanets.

We have further shown that (ground-based) kernel-phase observations require a careful data post-processing before the actual kernel-phases and their uncertainties can be extracted. Most important are the correction of bad or saturated pixels and the selection of “good” frames which fulfill the small-angle Fourier phase approximation on which the kernel-phase formalism is based. For the frame selection, we have presented three different methods in Chapters 2, 3, and 4; one based on the peak pixel count of each frame, one based on the sum of the squared kernel-phase signal of each frame, and one based on the Fourier phase signal of each frame. To first order, all of these methods are equivalent, since the peak pixel count is a function of the Strehl ratio, which directly impacts the non-zero Fourier phase signal and the higher-order terms in the kernel-phase formalism. However, considering directly the Fourier or kernel-phase signal is preferred over rejecting frames based on their peak pixel count, since this quantity is difficult to compare among different targets with different brightnesses. The kernel-phase signal, however, is independent of the target brightness and enables comparison of the data quality throughout an entire observing run. Finally, when the observed target is expected to have a significant kernel-phase signal because it is a low-contrast binary or multiple system, rejecting frames based on the Fourier

phase can be more robust to ensure compatibility with the small-angle approximation. We have also shown that using a large library of calibrator PSFs is only beneficial over using a single one when these calibrators were observed close in time to the science target, since the quasi-static phase errors which dominate the systematic error budget of kernel-phase observations from the ground evolve over timescales of tens of minutes.

In the near future, kernel phase interferometry will complement the aperture masking interferometry (AMI) mode of the *James Webb Space Telescope* (JWST). While AMI is ideal for high-resolution imaging around bright targets, since the aperture mask blocks 85% of the light, kernel phase will yield similar performance around fainter targets (Ceau et al., 2019). This enables searching for young giant planets in the nearest star-forming regions, although we highlight that the resolution achievable with JWST will not be sufficient to probe the tip of the giant planet distribution. Nevertheless, there might be a compelling science case which makes use of JWST’s large FOV. In a dense stellar region, multiple targets could be observed at the same time and kernel phase interferometry could be used to search for faint companions around all of them. This is because unlike with a coronagraph or an aperture mask, off-axis targets can be studied with kernel phase interferometry. Apart from that, both kernel phase interferometry and AMI can be used to obtain 3–5 μm photometry of sub-stellar companions. This wavelength regime contains absorption features of methane and carbon-monoxide and enables to constrain the metallicity, especially the C/O abundance ratio, of exoplanet and brown dwarf companions (e.g., Stolker et al., 2020). These parameters are tightly linked to the formation of these objects, and can be used to infer the formation mechanism and location in the protoplanetary disk (Öberg et al., 2011; Gravity Collaboration et al., 2020).

However, until the ELTs go online, studying planet formation will be limited to a few exquisite cases. Even then, Wallace & Ireland (2019) have shown that the probability of detecting young giant planets is limited rather by resolution than sensitivity. Only in an optimistic migration scenario, in which giant planets form and stay at larger orbital periods, the yield predicted for E-ELT/METIS is of a few percent ($\sim 2\text{--}3\%$) and comparable to that of VIKiNG, a potential high-contrast kernel nuller for the VLTI (Martinache & Ireland, 2018). In this regard, kernel phase interferometry would be a solution to overcome the limitation of the ELTs in terms of angular resolution, while still achieving high-contrasts suitable for the detection of young giant planets. Other possibilities can come from the development of novel coronagraphs, such as (vector) apodizing phase plates (e.g., Kenworthy et al., 2007; Otten et al., 2014) or vortex coronagraphs (e.g., Mawet et al., 2012), which reach smaller inner working angles than classical Lyot coronagraphs and are planned to be installed in E-ELT/METIS.

Optical/near-infrared long-baseline interferometry will be another key player in the field, and next-generation nulling instruments (SCIFY, VIKiNG, DeFrère

et al., 2018; Martinache & Ireland, 2018) will be able to detect a sizeable sample of young giant exoplanets (Wallace & Ireland, 2019). At present, long-baseline interferometry is limited in sensitivity due to poorly understood systematic errors at the smallest spatial scales. We contribute to the understanding of these errors by studying the correlations present in VLTI/GRAVITY data and developing an empirical correlation model in order to account for them in the model fitting process. This yields a gain in sensitivity by a factor of up to ~ 2 and greatly improves the reliability of the technique. Recently, Gravity Collaboration et al. (2019) have shown the capability of GRAVITY to detect known exoplanets, and the direct confirmation of β Pic c (Nowak et al., 2020), a giant exoplanet discovered through radial velocity observations (Lagrange et al., 2019), marks an important step toward high-resolution surveys for young giant exoplanets with long-baseline interferometry. GRAVITY+, the adaptive-optics and fringe tracker upgrade for GRAVITY, will further improve the sensitivity and contrast of GRAVITY and enable follow-up spectroscopy of giant planets detected via Gaia astrometry (Perryman et al., 2014). As a consequence, studying the age-luminosity relationship and inferring the formation entropy of giant planets will be possible on a statistically relevant scale. However, as statistical uncertainties decrease, systematic errors will become more important and our work on correlations in GRAVITY data will be a useful starting point for mitigating their impact on GRAVITY+.

The application of high-contrast imaging techniques to single-dish kernel-phase and multi-aperture long-baseline interferometry throughout this work has shown significant differences and complementarity between these methods. Kernel-phase is efficient in searching for new sub-stellar companions because it features a dense uv-plane coverage and can easily be applied at small angular separations in combination with PSF subtraction methods at larger angular separations. Contrast detection limits of ~ 6 – 8 mag at angular separations of ~ 0.2 – 0.5 arcsec can be readily achieved in half an hour with an optimized observing strategy (such as star-hopping) capable of tracing quasi-static phase errors varying on timescales of tens of minutes. Compared to aperture masking interferometry, kernel-phase also achieves a higher throughput and can thus be used to search for companions around fainter targets, with the drawback of requiring better observing conditions. While optical long-baseline single-field interferometry pushes the resolution down to a few milli-arcseconds (e.g., Gallenne et al., 2015), it is still limited in contrast to $\lesssim 6$ mag, even with our novel error correlation model. In between these two methods, GRAVITY dual-field interferometry achieves faint source detection limits of ~ 18 mag apparent magnitude in the K-band in three hours, suitable for detecting even the faintest known directly-imaged exoplanets (e.g., 51 Eri b, Macintosh et al., 2015). However, the diameter of the optical fibers used in these dual-field observations limits the angular resolution and the field-of-view to about 50 mas so that this method is only useful if the position of the companion can be constrained a priori (e.g., Lacour et al., 2020). In summary, while GRAVITY dual-field interferometry is a powerful method for

following-up and characterizing already known sub-stellar objects, kernel-phase is more suitable for searching for new companions.

In the far future, long-baseline interferometry could become a dominant technique in optical and infrared imaging, similar to radio and sub-millimeter astronomy today. We are at a point in time where constructing larger single-dish telescopes has become impossible, and even large-aperture segmented telescopes comprise immense challenges to be overcome. Segmented mirrors need to be co-phased, very similar to the phase-referencing of an interferometer, and while co-phasing the E-ELT still has to be demonstrated, fringe tracking with baselines of ~ 100 m is already daily practice at the VLTI. Advancements in optical fiber and integrated optics technology greatly aid long-baseline interferometry (Perraut et al., 2018) and even put a large space-based nulling interferometer (Cockell et al., 2009) in reach. With such an instrument, a sizeable sample of nearby terrestrial worlds could be searched for signs of habitability and biological activity for the first time in human history (Kammerer & Quanz, 2018; Quanz et al., 2018, 2019). This would be a significant advancement toward answering the question whether alien life exists – a question that might also have been on Galilei’s mind when he pointed his telescope to the night sky in 1609.

Bibliography

- Absil, O., Le Bouquin, J. B., Berger, J. P., et al. 2011, *A&A*, 535, A68
- Ackerman, A. S. & Marley, M. S. 2001, *ApJ*, 556, 872
- Allard, F., Homeier, D., & Freytag, B. 2012, *Philosophical Transactions of the Royal Society of London Series A*, 370, 2765
- ALMA Partnership, Brogan, C. L., Pérez, L. M., et al. 2015, *Astrophysical Journal Letters*, 808, L3
- Amara, A. & Quanz, S. P. 2012, *MNRAS*, 427, 948
- Andrews, S. M., Rosenfeld, K. A., Kraus, A. L., & Wilner, D. J. 2013, *The Astrophysical Journal*, 771, 129
- Andrews, S. M. & Williams, J. P. 2005, *The Astrophysical Journal*, 631, 1134
- Artymowicz, P. & Lubow, S. H. 1994, *ApJ*, 421, 651
- Asplund, M. 2005, *Annual Review of Astronomy & Astrophysics*, 43, 481
- Baldwin, J. E., Haniff, C. A., Mackay, C. D., & Warner, P. J. 1986, *Nature*, 320, 595
- Baldwin, J. E. & Warner, P. J. 1987, *Nature*, 328, 694
- Baraffe, I., Chabrier, G., Allard, F., & Hauschildt, P. 2003, in *Symposium-International Astronomical Union*, Vol. 211, Cambridge University Press, 41–50
- Baraffe, I., Chabrier, G., Barman, T. S., Allard, F., & Hauschildt, P. H. 2003, *Astronomy & Astrophysics*, 402, 701
- Baraffe, I., Homeier, D., Allard, F., & Chabrier, G. 2015, *A&A*, 577, A42
- Bartko, H., Perrin, G., Brandner, W., et al. 2009, *New Astron. Rev.*, 53, 301
- Baudino, J. L., Bézard, B., Boccaletti, A., et al. 2015, *A&A*, 582, A83
- Bedding, T. R., Beckers, J. M., Faucherre, M., et al. 1994, in *Very High Angular Resolution Imaging*, ed. J. G. Robertson & W. J. Tango, Vol. 158, 143
- Bell, C. P. M., Mamajek, E. E., & Naylor, T. 2015, *MNRAS*, 454, 593

- Berardo, D., Cumming, A., & Marleau, G.-D. 2017, *The Astrophysical Journal*, 834, 149
- Berger, J. P. 2003, in *EAS Publications Series*, Vol. 6, *EAS Publications Series*, ed. G. Perrin & F. Malbet, 23
- Beuzit, J. L., Vigan, A., Mouillet, D., et al. 2019, *Astronomy & Astrophysics*, 631, A155
- Biller, B. A. & Bonnefoy, M. 2018, *Exoplanet Atmosphere Measurements from Direct Imaging*, ed. H. J. Deeg & J. A. Belmonte, 101
- Biller, B. A., Males, J., Rodigas, T., et al. 2014, *Astrophysical Journal Letters*, 792, L22
- Blackburn, L., Pesce, D. W., Johnson, M. D., et al. 2020, *ApJ*, 894, 31
- Blunt, S., Wang, J. J., Angelo, I., et al. 2020, *AJ*, 159, 89
- Bohn, A. J., Kenworthy, M. A., Ginski, C., et al. 2020, *MNRAS*, 492, 431
- Boley, A. C. 2009, *Astrophysical Journal Letters*, 695, L53
- Borucki, W. J., Koch, D., Basri, G., et al. 2010, *Science*, 327, 977
- Boss, A. P. 2001, *Astrophysical Journal Letters*, 551, L167
- Bowler, B. P. 2016, *PASP*, 128, 102001
- Bowler, B. P., Blunt, S. C., & Nielsen, E. L. 2020, *Astronomical Journal*, 159, 63
- Bowler, B. P., Liu, M. C., Shkolnik, E. L., & Tamura, M. 2015, *ApJS*, 216, 7
- Bowler, B. P. & Nielsen, E. L. 2018, *Handbook of Exoplanets*, 1
- Bracewell, R. N. & MacPhie, R. H. 1979, *Icarus*, 38, 136
- Brandt, T. D., Kuzuhara, M., McElwain, M. W., et al. 2014, *ApJ*, 786, 1
- Brogan, C., Pérez, L., Hunter, T., et al. 2015, *The Astrophysical Journal Letters*, 808, L3
- Bryson, S., Coughlin, J., Batalha, N. M., et al. 2020, *Astronomical Journal*, 159, 279
- Buchner, J., Georgakakis, A., Nandra, K., et al. 2014, *A&A*, 564, A125
- Burchell, M. J. 2006, *International Journal of Astrobiology*, 5, 243
- Burke, C. J., Christiansen, J. L., Mullally, F., et al. 2015, *Astrophysical Journal*, 809, 8

- Cantalloube, F., Mouillet, D., Mugnier, L. M., et al. 2015, *A&A*, 582, A89
- Carpenter, J. M., Ricci, L., & Isella, A. 2014, *The Astrophysical Journal*, 787, 42
- Ceau, A., Mary, D., Greenbaum, A., et al. 2019, *Astronomy & Astrophysics*, 630, A120
- Charnay, B., Bézard, B., Baudino, J. L., et al. 2018, *ApJ*, 854, 172
- Cheetham, A. C., Girard, J., Lacour, S., et al. 2016, in *Proc. SPIE*, Vol. 9907, Optical and Infrared Interferometry and Imaging V, 99072T
- Chelli, A., Duvert, G., Bourguès, L., et al. 2016, *A&A*, 589, A112
- Cockell, C. S., Léger, A., Fridlund, M., et al. 2009, *Astrobiology*, 9, 1
- Colavita, M. M. 1999, *PASP*, 111, 111
- Crida, A. & Morbidelli, A. 2007, *Monthly Notices of the Royal Astronomical Society*, 377, 1324
- Cumming, A., Butler, R. P., Marcy, G. W., et al. 2008, *Publications of the Astronomical Society of the Pacific*, 120, 531
- Currie, T., Burrows, A., Madhusudhan, N., et al. 2013, *ApJ*, 776, 15
- Currie, T., Guyon, O., Tamura, M., et al. 2017, *Astrophysical Journal Letters*, 836, L15
- D'Angelo, G., Durisen, R. H., & Lissauer, J. J. 2010, *Giant Planet Formation*, ed. S. Seager, 319–346
- D'Angelo, G. & Marzari, F. 2012, *Astrophysical Journal*, 757, 50
- de Zeeuw, P. T., Hoogerwerf, R., de Bruijne, J. H. J., Brown, A. G. A., & Blaauw, A. 1999, *Astronomical Journal*, 117, 354
- Defrère, D., Absil, O., Berger, J. P., et al. 2018, *Experimental Astronomy*, 46, 475
- Defrère, D., Hinz, P. M., Skemer, A. J., et al. 2015, *Astrophysical Journal*, 799, 42
- Delisle, J. B., Hara, N., & Ségransan, D. 2020, *A&A*, 635, A83
- Delorme, P., Schmidt, T., Bonnefoy, M., et al. 2017, *Astronomy & Astrophysics*, 608, A79
- Desidera, S., Gratton, R. G., Lucatello, S., & Claudi, R. U. 2006, *A&A*, 454, 581

- Dong, S., Mérand, A., Delplancke-Ströbele, F., et al. 2019, *Astrophysical Journal*, 871, 70
- Drake, S. 1978, *Galileo at work : his scientific biography*
- Drake, S. 1990, *Galileo : pioneer scientist*
- Drake, S. & Kowal, C. T. 1980, *Scientific American*, 243, 74
- Dravins, D., LeBohec, S., Jensen, H., Nuñez, P. D., & CTA Consortium. 2013, *Astroparticle Physics*, 43, 331
- Dressing, C. D. & Charbonneau, D. 2013, *Astrophysical Journal*, 767, 95
- Dressing, C. D. & Charbonneau, D. 2015, *Astrophysical Journal*, 807, 45
- Duchêne, G., Beust, H., Adjali, F., Konopacky, Q. M., & Ghez, A. M. 2006, *A&A*, 457, L9
- Duchêne, G., Ghez, A. M., & McCabe, C. 2002, *ApJ*, 568, 771
- Duchêne, G., Ghez, A. M., McCabe, C., & Ceccarelli, C. 2005, *ApJ*, 628, 832
- Duvert, G., Young, J., & Hummel, C. A. 2017, *A&A*, 597, A8
- Dyck, H. M., Simon, T., & Zuckerman, B. 1982, *ApJ*, 255, L103
- Efron, B. & Tibshirani, R. 1986, *Statistical Science*, 1, 54
- Fernandes, R. B., Mulders, G. D., Pascucci, I., Mordasini, C., & Emsenhuber, A. 2019, *Astrophysical Journal*, 874, 81
- Feroz, F., Hobson, M. P., & Bridges, M. 2009, *MNRAS*, 398, 1601
- Feroz, F., Hobson, M. P., Cameron, E., & Pettitt, A. N. 2019, *The Open Journal of Astrophysics*, 2, 10
- Fischer, D. A., Howard, A. W., Laughlin, G. P., et al. 2014, in *Protostars and Planets VI*, ed. H. Beuther, R. S. Klessen, C. P. Dullemond, & T. Henning, 715
- Fitzgerald, M. P. & Graham, J. R. 2006, *ApJ*, 637, 541
- Fitzpatrick, E. & Massa, D. 2007, *The Astrophysical Journal*, 663, 320
- Fizeau, H. 1868, *Comptes Rendus Hebdomadaires des Seances de l'Academie des Sciences*, 66, 932
- Foreman-Mackey, D. 2016, *The Journal of Open Source Software*, 1, 24
- Foreman-Mackey, D., Hogg, D. W., Lang, D., & Goodman, J. 2013, *PASP*, 125, 306

- Fressin, F., Torres, G., Charbonneau, D., et al. 2013, *Astrophysical Journal*, 766, 81
- Fulton, B. J., Petigura, E. A., Howard, A. W., et al. 2017, *Astronomical Journal*, 154, 109
- Gaia Collaboration. 2018, *VizieR Online Data Catalog*, I/345
- Galicher, R., Marois, C., Macintosh, B., et al. 2016, *VizieR Online Data Catalog*, 359
- Gallenne, A., Mérand, A., Kervella, P., et al. 2014, *Astronomy & Astrophysics*, 561, L3
- Gallenne, A., Mérand, A., Kervella, P., et al. 2015, *Astronomy & Astrophysics*, 579, A68
- Gallenne, A., Monnier, J. D., Mérand, A., et al. 2013, *Astronomy & Astrophysics*, 552, A21
- Ghez, A., White, R. J., & Simon, M. 1997, *The Astrophysical Journal*, 490, 353
- Ghez, A. M., Neugebauer, G., Gorham, P. W., et al. 1991, *AJ*, 102, 2066
- Grandjean, A., Lagrange, A. M., Beust, H., et al. 2019, *A&A*, 627, L9
- Gravity Collaboration, Abuter, R., Accardo, M., et al. 2017, *A&A*, 602, A94
- Gravity Collaboration, Abuter, R., Amorim, A., et al. 2018, *Astronomy & Astrophysics*, 615, L15
- Gravity Collaboration, Abuter, R., Amorim, A., et al. 2021, *Astronomy & Astrophysics*, 647, A59
- Gravity Collaboration, Lacour, S., Nowak, M., et al. 2019, *Astronomy & Astrophysics*, 623, L11
- Gravity Collaboration, Nowak, M., Lacour, S., et al. 2020, *Astronomy & Astrophysics*, 633, A110
- Greco, J. P. & Brandt, T. D. 2016, *ApJ*, 833, 134
- Grether, D. & Lineweaver, C. H. 2006, *The Astrophysical Journal*, 640, 1051
- Güdel, M., Briggs, K. R., Arzner, K., et al. 2007, *Astronomy & Astrophysics*, 468, 353
- Guyon, O., Mennesson, B., Serabyn, E., & Martin, S. 2013, *PASP*, 125, 951
- Haffert, S. Y., Bohn, A. J., de Boer, J., et al. 2019, *Nature Astronomy*, 3, 749

- Hanbury Brown, R. 1956, *Nature*, 178, 1046
- Hanbury Brown, R., Davis, J., Allen, L. R., & Rome, J. M. 1967, *MNRAS*, 137, 393
- Hayashi, C. 1981, *Progress of Theoretical Physics Supplement*, 70, 35
- Heintz, W. D. 1978, *Double stars*, Vol. 15
- Helling, C., Dehn, M., Woitke, P., & Hauschildt, P. H. 2008, *ApJ*, 675, L105
- Herbst, T. M., Beckwith, S. V. W., Glindemann, A., et al. 1996, *AJ*, 111, 2403
- Herczeg, G. J. & Hillenbrand, L. A. 2014, *The Astrophysical Journal*, 786, 97
- Hinz, P., Arbo, P., Bailey, V., et al. 2012, in *Society of Photo-Optical Instrumentation Engineers (SPIE) Conference Series*, Vol. 8445, *Optical and Infrared Interferometry III*, ed. F. Delplancke, J. K. Rajagopal, & F. Malbet, 84450U
- Hiranaka, K., Cruz, K. L., Douglas, S. T., Marley, M. S., & Baldassare, V. F. 2016, *ApJ*, 830, 96
- Hsu, D. C., Ford, E. B., Ragozzine, D., & Ashby, K. 2019, *Astronomical Journal*, 158, 109
- Huang, J., Andrews, S. M., Dullemond, C. P., et al. 2020, *The Astrophysical Journal*, 891, 48
- Hunziker, S., Quanz, S. P., Amara, A., & Meyer, M. R. 2018, *Astronomy & Astrophysics*, 611, A23
- Ireland, M. J. 2002, Master's thesis, University of Sydney
- Ireland, M. J. 2013, *MNRAS*, 433, 1718
- Ireland, M. J. 2016, *Aperture Masking Imaging*, ed. H. M. J. Boffin, G. Hussain, J.-P. Berger, & L. Schmidtbreick, Vol. 439, 43
- Itoh, Y., Hayashi, M., Tamura, M., et al. 2005, *The Astrophysical Journal*, 620, 984
- Izidoro, A., Ogiwara, M., Raymond, S. N., et al. 2017, *MNRAS*, 470, 1750
- Jansky, K. G. 1933, *Nature*, 132, 66
- Jensen, E. L. N. & Akeson, R. 2014, *Nature*, 511, 567
- Jensen, E. L. N., Mathieu, R. D., Donar, A. X., & Dullighan, A. 2004, *ApJ*, 600, 789

- Johns-Krull, C. M., McLane, J. N., Prato, L., et al. 2016, *The Astrophysical Journal*, 826, 206
- Kalas, P., Graham, J. R., Chiang, E., et al. 2008, *Science*, 322, 1345
- Kammerer, J., Ireland, M. J., Martinache, F., & Girard, J. H. 2019, *MNRAS*, 486, 639
- Kammerer, J., Mérand, A., Ireland, M. J., & Lacour, S. 2020, *Astronomy & Astrophysics*, 644, A110
- Kammerer, J. & Quanz, S. P. 2018, *Astronomy & Astrophysics*, 609, A4
- Kasper, M., Santhakumari, K. K. R., Herbst, T. M., & Köhler, R. 2016, *A&A*, 593, A50
- Kasper, M. E., Feldt, M., Herbst, T. M., et al. 2002, *ApJ*, 568, 267
- Käuff, H.-U., Kasper, M., Arsenaault, R., et al. 2018, in *Society of Photo-Optical Instrumentation Engineers (SPIE) Conference Series*, Vol. 10702, Proc. SPIE, 107020D
- Kellerer, A. & Tokovinin, A. 2007, *A&A*, 461, 775
- Kenworthy, M. A., Codona, J. L., Hinz, P. M., et al. 2007, *Astrophysical Journal*, 660, 762
- Keppler, M., Benisty, M., Müller, A., et al. 2018, *Astronomy & Astrophysics*, 617, A44
- Kley, W. & Nelson, R. P. 2012, *ARA&A*, 50, 211
- Köhler, R., Kasper, M., Herbst, T. M., Ratzka, T., & Bertrang, G. H. M. 2016, *A&A*, 587, A35
- Köhler, R. & Kubiak, K. 2020, *Research Notes of the American Astronomical Society*, 4, 73
- Konacki, M., Torres, G., Jha, S., & Sasselov, D. D. 2003, *Nature*, 421, 507
- Kopparapu, R. K., Hébrard, E., Belikov, R., et al. 2018, *Astrophysical Journal*, 856, 122
- Koresko, C. D. 2000, *ApJ*, 531, L147
- Kotani, T., Nishikawa, J., Sato, K., et al. 2003, in *Society of Photo-Optical Instrumentation Engineers (SPIE) Conference Series*, Vol. 4838, Proc. SPIE, ed. W. A. Traub, 1370–1377
- Kraus, A. L. & Ireland, M. J. 2012, *Astrophysical Journal*, 745, 5

- Kraus, A. L., Ireland, M. J., Cieza, L. A., et al. 2013, *The Astrophysical Journal*, 781, 20
- Kraus, A. L., Ireland, M. J., Huber, D., Mann, A. W., & Dupuy, T. J. 2016, *AJ*, 152, 8
- Kraus, A. L., Ireland, M. J., Martinache, F., & Hillenbrand, L. A. 2011, *The Astrophysical Journal*, 731, 8
- Kruegel, E. & Siebenmorgen, R. 1994, *A&A*, 288, 929
- Kulkarni, S. R. 1989, *AJ*, 98, 1112
- Kuruwita, R. L., Ireland, M., Rizzuto, A., Bento, J., & Federrath, C. 2018, *Monthly Notices of the Royal Astronomical Society*, 480, 5099
- Labeyrie, A. 1975, *Astrophysical Journal Letters*, 196, L71
- Lachaume, R., Rabus, M., Jordán, A., et al. 2019, *MNRAS*, 484, 2656
- Lacour, S., Dembet, R., Abuter, R., et al. 2019, *A&A*, 624, A99
- Lacour, S., Eisenhauer, F., Gillessen, S., et al. 2014, *A&A*, 567, A75
- Lacour, S., Wang, J. J., Nowak, M., et al. 2020, in *Society of Photo-Optical Instrumentation Engineers (SPIE) Conference Series*, Vol. 11446, *Society of Photo-Optical Instrumentation Engineers (SPIE) Conference Series*, 114460O
- Lafrenière, D., Doyon, R., Marois, C., et al. 2007a, *ApJ*, 670, 1367
- Lafrenière, D., Marois, C., Doyon, R., Nadeau, D., & Artigau, É. 2007b, *ApJ*, 660, 770
- Lagage, P. O., Pel, J. W., Authier, M., et al. 2004, *The Messenger*, 117, 12
- Lagrange, A.-M., Bonnefoy, M., Chauvin, G., et al. 2010, *Science*, 329, 57
- Lagrange, A. M., Meunier, N., Rubini, P., et al. 2019, *Nature Astronomy*, 3, 1135
- Lambrechts, M. & Johansen, A. 2012, *Astronomy & Astrophysics*, 544, A32
- Langlois, M., Gratton, R., Lagrange, A. M., et al. 2021, *arXiv e-prints*, arXiv:2103.03976
- Lapeyrere, V., Kervella, P., Lacour, S., et al. 2014, in *Society of Photo-Optical Instrumentation Engineers (SPIE) Conference Series*, Vol. 9146, *Proc. SPIE*, 91462D
- Laugier, R., Martinache, F., Ceau, A., et al. 2019, *Astronomy & Astrophysics*, 623, A164

- Laugier, R., Martinache, F., Cvetojevic, N., et al. 2020, *Astronomy & Astrophysics*, 636, A21
- Lavie, B., Mendonça, J. M., Mordasini, C., et al. 2017, *Astronomical Journal*, 154, 91
- Law, N. M., Mackay, C. D., & Baldwin, J. E. 2006, *A&A*, 446, 739
- Lawson, P. 2001, in 2001 IEEE Aerospace Conference Proceedings (Cat. No.01TH8542), Vol. 4, 4/2005–4/2011 vol.4
- Le Bouquin, J. B. & Absil, O. 2012, *A&A*, 541, A89
- Le Bouquin, J. B., Berger, J. P., Lazareff, B., et al. 2011, *A&A*, 535, A67
- Leger, A. & Herbst, T. 2007, arXiv e-prints, arXiv:0707.3385
- Léger, A., Mariotti, J. M., Mennesson, B., et al. 1996, *Icarus*, 123, 249
- Leisenring, J., Bary, J., & Skrutskie, M. 2007, in American Astronomical Society Meeting Abstracts, Vol. 211, American Astronomical Society Meeting Abstracts, 62.12
- Loinard, L., Torres, R. M., Mioduszewski, A. J., et al. 2007, *ApJ*, 671, 546
- Long, F., Pinilla, P., Herczeg, G. J., et al. 2018, *The Astrophysical Journal*, 869, 17
- Lopez, E. D. & Rice, K. 2018, *MNRAS*, 479, 5303
- Macintosh, B., Graham, J., Barman, T., et al. 2015, *Science*, 350, 64
- Macintosh, B., Graham, J. R., Ingraham, P., et al. 2014, *Proceedings of the National Academy of Science*, 111, 12661
- Manara, C. F., Tazzari, M., Long, F., et al. 2019, *A&A*, 628, A95
- Marcy, G. W. & Butler, R. P. 2000, *Publications of the Astronomical Society of the Pacific*, 112, 137
- Marcy, G. W., Isaacson, H., Howard, A. W., et al. 2014, *Astrophysical Journal Supplement*, 210, 20
- Marino, S., Zurlo, A., Faramaz, V., et al. 2020, *MNRAS*, 498, 1319
- Marleau, G. D. & Cumming, A. 2014, *MNRAS*, 437, 1378
- Marleau, G.-D., Mordasini, C., & Kuiper, R. 2019, *ApJ*, 881, 144
- Marley, M. S., Fortney, J. J., Hubickyj, O., Bodenheimer, P., & Lissauer, J. J. 2007, *Astrophysical Journal*, 655, 541

- Marocco, F., Day-Jones, A. C., Lucas, P. W., et al. 2014, *MNRAS*, 439, 372
- Marois, C., Lafrenière, D., Doyon, R., Macintosh, B., & Nadeau, D. 2006, *Astrophysical Journal*, 641, 556
- Marois, C., Macintosh, B., Barman, T., et al. 2008, *Science*, 322, 1348
- Marois, C., Zuckerman, B., Konopacky, Q. M., Macintosh, B., & Barman, T. 2010, *Nature*, 468, 1080
- Martín, E. L. 2003, *AJ*, 126, 918
- Martinache, F. 2010, *Astrophysical Journal*, 724, 464
- Martinache, F. 2013, *PASP*, 125, 422
- Martinache, F., Ceau, A., Laugier, R., et al. 2020, *Astronomy & Astrophysics*, 636, A72
- Martinache, F. & Ireland, M. J. 2018, arXiv preprint arXiv:1802.06252
- Martinache, F. & Ireland, M. J. 2018, *Astronomy & Astrophysics*, 619, A87
- Martinez, P., Kasper, M., Costille, A., et al. 2013, *Astronomy & Astrophysics*, 554, A41
- Mathieu, R. D., Stassun, K., Basri, G., et al. 1997, *AJ*, 113, 1841
- Mathis, J. S., Rumpl, W., & Nordsieck, K. H. 1977, *ApJ*, 217, 425
- Matsuo, T., Shibai, H., Ootsubo, T., & Tamura, M. 2007, *Astrophysical Journal*, 662, 1282
- Mawet, D., Pueyo, L., Lawson, P., et al. 2012, in *Society of Photo-Optical Instrumentation Engineers (SPIE) Conference Series*, Vol. 8442, *Space Telescopes and Instrumentation 2012: Optical, Infrared, and Millimeter Wave*, ed. M. C. Clampin, G. G. Fazio, H. A. MacEwen, & J. Oschmann, Jacobus M., 844204
- Mayor, M. & Queloz, D. 1995, *Nature*, 378, 355
- Mennesson, B. & Mariotti, J. M. 1997, *Icarus*, 128, 202
- Meshkat, T., Kenworthy, M. A., Quanz, S. P., & Amara, A. 2013, *The Astrophysical Journal*, 780, 17
- Metchev, S. A. & Hillenbrand, L. A. 2009, *The Astrophysical Journal Supplement Series*, 181, 62
- Michelson, A. A. 1891, *Nature*, 45, 160
- Michelson, A. A. & Pease, F. G. 1921, *Astrophysical Journal*, 53, 249

- Milli, J., Hiben, P., Christiaens, V., et al. 2017, *Astronomy & Astrophysics*, 597, L2
- Milli, J., Mawet, D., Mouillet, D., Kasper, M., & Girard, J. H. 2016, in *Astrophysics and Space Science Library*, Vol. 439, *Astronomy at High Angular Resolution*, ed. H. M. J. Boffin, G. Hussain, J.-P. Berger, & L. Schmidtobreick, 17
- Monnier, J. D. 2003, *Reports on Progress in Physics*, 66, 789
- Monnier, J. D. 2007, *New Astron. Rev.*, 51, 604
- Morbidelli, A. & Raymond, S. N. 2016, *Journal of Geophysical Research (Planets)*, 121, 1962
- Morbidelli, A., Tsiganis, K., Crida, A., Levison, H. F., & Gomes, R. 2007, *Astronomical Journal*, 134, 1790
- Mordasini, C. 2013, *Astronomy & Astrophysics*, 558, A113
- Mulders, G. D., Ciesla, F. J., Min, M., & Pascucci, I. 2015, *Astrophysical Journal*, 807, 9
- Nielsen, E. L., De Rosa, R. J., Macintosh, B., et al. 2019, *Astronomical Journal*, 158, 13
- Nowak, M., Lacour, S., Lagrange, A. M., et al. 2020, *Astronomy & Astrophysics*, 642, L2
- Öberg, K. I., Murray-Clay, R., & Bergin, E. A. 2011, *Astrophysical Journal Letters*, 743, L16
- Otten, G. P. P. L., Snik, F., Kenworthy, M. A., Miskiewicz, M. N., & Escuti, M. J. 2014, *Optics Express*, 22, 30287
- Patience, J., King, R. R., De Rosa, R. J., et al. 2012, *A&A*, 540, A85
- Penny, M. T., Gaudi, B. S., Kerins, E., et al. 2019, *Astrophysical Journal Supplements*, 241, 3
- Pepe, F., Ehrenreich, D., & Meyer, M. R. 2014, *Nature*, 513, 358
- Perraut, K., Jocu, L., Berger, J. P., et al. 2018, *Astronomy & Astrophysics*, 614, A70
- Perrin, G. 2003, *A&A*, 400, 1173
- Perryman, M., Hartman, J., Bakos, G. Á., & Lindegren, L. 2014, *Astrophysical Journal*, 797, 14

- Pollack, J. B., Hubickyj, O., Bodenheimer, P., et al. 1996, *ICARUS*, 124, 62
- Pope, B., Martinache, F., & Tuthill, P. 2013, *Astrophysical Journal*, 767, 110
- Pope, B., Tuthill, P., Hinkley, S., et al. 2016, *MNRAS*, 455, 1647
- Prato, L., Simon, M., Mazeh, T., Zucker, S., & McLean, I. S. 2002, *ApJ*, 579, L99
- Preibisch, T. & Mamajek, E. 2008, *The Nearest OB Association: Scorpius-Centaurus (Sco OB2)*, ed. B. Reipurth, 235
- Pueyo, L. 2016, *ApJ*, 824, 117
- Quanz, S. P., Absil, O., Angerhausen, D., et al. 2019, arXiv e-prints, arXiv:1908.01316
- Quanz, S. P., Amara, A., Meyer, M. R., et al. 2013, *Astrophysical Journal Letters*, 766, L1
- Quanz, S. P., Kammerer, J., Defrère, D., et al. 2018, in *Society of Photo-Optical Instrumentation Engineers (SPIE) Conference Series*, Vol. 10701, *Optical and Infrared Interferometry and Imaging VI*, ed. M. J. Creech-Eakman, P. G. Tuthill, & A. Mérand, 107011I
- Quanz, S. P., Ottiger, M., Fontanet, E., et al. 2021, arXiv e-prints, arXiv:2101.07500
- Rajan, A., Rameau, J., De Rosa, R. J., et al. 2017, *AJ*, 154, 10
- Ratzka, T., Schegerer, A. A., Leinert, C., et al. 2009, *A&A*, 502, 623
- Readhead, A. C. S., Nakajima, T. S., Pearson, T. J., et al. 1988, *AJ*, 95, 1278
- Rice, W. K. M., Armitage, P. J., Wood, K., & Lodato, G. 2006, *MNRAS*, 373, 1619
- Rizzuto, A. C., Ireland, M. J., & Robertson, J. G. 2011, *MNRAS*, 416, 3108
- Rogers, L. A. 2015, *Astrophysical Journal*, 801, 41
- Ruane, G., Echeverri, D., Jovanovic, N., et al. 2019, in *Society of Photo-Optical Instrumentation Engineers (SPIE) Conference Series*, Vol. 11117, *Society of Photo-Optical Instrumentation Engineers (SPIE) Conference Series*, 1111716
- Ryle, M. & Hewish, A. 1950, *MNRAS*, 110, 381
- Ryle, M. & Vonberg, D. D. 1948, *Proceedings of the Royal Society of London Series A*, 193, 98
- Sallum, S. & Eisner, J. 2017, *ApJS*, 233, 9

- Sallum, S., Follette, K. B., Eisner, J. A., et al. 2015, *Nature*, 527, 342
- Sallum, S. & Skemer, A. 2019, arXiv e-prints [[arXiv]1901.01266]
- Sauvage, J.-F., Fusco, T., Rousset, G., & Petit, C. 2007, *Journal of the Optical Society of America A*, 24, 2334
- Schaefer, G. H., Beck, T. L., Prato, L., & Simon, M. 2020, *AJ*, 160, 35
- Schlafly, E., Green, G., Finkbeiner, D., et al. 2014, *The Astrophysical Journal*, 789, 15
- Schmidt, T. O. B., Neuhäuser, R., Seifahrt, A., et al. 2008, *A&A*, 491, 311
- Schöller, M., Correia, S., Hubrig, S., & Ageorges, N. 2010, *A&A*, 522, A85
- Shabram, M. & Boley, A. C. 2013, *Astrophysical Journal*, 767, 63
- Shao, M. & Staelin, D. H. 1980, *Applied Optics*, 19, 1519
- Skemer, A. J., Close, L. M., Hinz, P. M., et al. 2008, *ApJ*, 676, 1082
- Skemer, A. J., Morley, C. V., Zimmerman, N. T., et al. 2016, *ApJ*, 817, 166
- Skrutskie, M. F., Cutri, R. M., Stiening, R., et al. 2006, *AJ*, 131, 1163
- Soummer, R., Pueyo, L., & Larkin, J. 2012, *Astrophysical Journal Letters*, 755, L28
- Spiegel, D. S. & Burrows, A. 2012, *Astrophysical Journal*, 745, 174
- Stapelfeldt, K. R., Krist, J. E., Ménard, F., et al. 1998, *The Astrophysical Journal Letters*, 502, L65
- Stark, C. C., Roberge, A., Mandell, A., et al. 2015, *Astrophysical Journal*, 808, 149
- Stark, C. C., Roberge, A., Mandell, A., & Robinson, T. D. 2014, *Astrophysical Journal*, 795, 122
- Stolker, T., Quanz, S. P., Todorov, K. O., et al. 2020, *Astronomy & Astrophysics*, 635, A182
- Ströbele, S., Arsenault, R., Bacon, R., et al. 2006, *Society of Photo-Optical Instrumentation Engineers (SPIE) Conference Series*, Vol. 6272, *The ESO Adaptive Optics Facility*, 62720B
- Sumlin, B. J., Heinson, W. R., & Chakrabarty, R. K. 2018, *Journal of Quantitative Spectroscopy and Radiative Transfer*, 205, 127

- Tallon-Bosc, I., Tallon, M., Thiébaud, E., et al. 2008, in Society of Photo-Optical Instrumentation Engineers (SPIE) Conference Series, Vol. 7013, Proc. SPIE, 70131J
- Tanner, A., Beichman, C., Akeson, R., et al. 2007, Publications of the Astronomical Society of the Pacific, 119, 747
- ten Brummelaar, T. A., McAlister, H. A., Ridgway, S. T., et al. 2005, *Astrophysical Journal*, 628, 453
- Terquem, C. & Papaloizou, J. C. B. 2007, *Astrophysical Journal*, 654, 1110
- Thalmann, C., Mulders, G. D., Janson, M., et al. 2015, *ApJ*, 808, L41
- Torres, C. A. O., Quast, G. R., Melo, C. H. F., & Sterzik, M. F. 2008, *Young Nearby Loose Associations*, ed. B. Reipurth, Vol. 5, 757
- Torres, R. M., Loinard, L., Mioduszewski, A. J., & Rodríguez, L. F. 2009, *The Astrophysical Journal*, 698, 242
- Tuthill, P., Lacour, S., Amico, P., et al. 2010, in Proc. SPIE, Vol. 7735, *Ground-based and Airborne Instrumentation for Astronomy III*, 77351O
- Tuthill, P., Monnier, J., Tanner, A., et al. 2006, *Science*, 313, 935
- Tuthill, P. G. 2014, in Society of Photo-Optical Instrumentation Engineers (SPIE) Conference Series, Vol. 9146, *Optical and Infrared Interferometry IV*, ed. J. K. Rajagopal, M. J. Creech-Eakman, & F. Malbet, 91460C
- Tuthill, P. G., Danchi, W. C., Hale, D. S., Monnier, J. D., & Townes, C. H. 2000a, *Astrophysical Journal*, 534, 907
- Tuthill, P. G. & Lloyd, J. P. 2007, *Science*, 316, 247
- Tuthill, P. G., Monnier, J. D., & Danchi, W. C. 2001, *Nature*, 409, 1012
- Tuthill, P. G., Monnier, J. D., Danchi, W. C., Hale, D. D. S., & Townes, C. H. 2002, *Astrophysical Journal*, 577, 826
- Tuthill, P. G., Monnier, J. D., Danchi, W. C., Wishnow, E. H., & Haniff, C. A. 2000b, *PASP*, 112, 555
- Tuthill, P. G., Monnier, J. D., Lawrance, N., et al. 2008, *Astrophysical Journal*, 675, 698
- van Boekel, R., Juhász, A., Henning, T., et al. 2010, *A&A*, 517, A16
- van Cittert, P. 1934, *Physica*, 1, 201
- Van Der Plas, G., Ménard, F., Ward-Duong, K., et al. 2016, *The Astrophysical Journal*, 819, 102

- Varga, J., Hogerheijde, M., van Boekel, R., et al. 2020, arXiv e-prints, arXiv:2012.05697
- Vigan, A., Fontanive, C., Meyer, M., et al. 2020, arXiv e-prints, arXiv:2007.06573
- Vigan, A., Fontanive, C., Meyer, M., et al. 2020, arXiv preprint arXiv:2007.06573
- Vigan, A., Patience, J., Marois, C., et al. 2012, *Astronomy & Astrophysics*, 544, A9
- Vousden, W. D., Farr, W. M., & Mandel, I. 2016, *MNRAS*, 455, 1919
- Wallace, A. & Ireland, M. 2019, *Monthly Notices of the Royal Astronomical Society*, 490, 502
- Wallace, A. L. & Ireland, M. J. 2019, *MNRAS*, 490, 502
- Wallace, A. L., Kammerer, J., Ireland, M. J., et al. 2020, *MNRAS*, 498, 1382
- Wang, J. J., Vigan, A., Lacour, S., et al. 2021, *Astronomical Journal*, 161, 148
- Ward-Duong, K., Patience, J., Follette, K., et al. 2021, *AJ*, 161, 5
- Weiss, L. M. & Marcy, G. W. 2014, *Astrophysical Journal Letters*, 783, L6
- Wenger, M., Ochsenbein, F., Egret, D., et al. 2000, *A&AS*, 143, 9
- Whitworth, A. P. 2001, in *IAU Symposium*, Vol. 200, *The Formation of Binary Stars*, ed. H. Zinnecker & R. Mathieu, 33
- Wiener, N. 1930, *Acta Math.*, 55, 117
- Wolszczan, A. & Frail, D. A. 1992, *Nature*, 355, 145
- Wright, E. L., Eisenhardt, P. R. M., Mainzer, A. K., et al. 2010, *AJ*, 140, 1868
- Wu, Y. & Lithwick, Y. 2011, *ApJ*, 735, 109
- Yang, Y., Mayama, S., Hayashi, S. S., et al. 2018, *ApJ*, 861, 133
- Youdin, A. N. & Goodman, J. 2005, *Astrophysical Journal*, 620, 459
- Zernike, F. 1938, *Physica*, 5, 785
- Zhu, Z. 2015, *Astrophysical Journal*, 799, 16
- Zuckerman, B. & Song, I. 2004, *Annual Review of Astronomy & Astrophysics*, 42, 685
- Zurlo, A., Vigan, A., Galicher, R., et al. 2016, *A&A*, 587, A57